frontiers | Research Topics

Reviews in geochemistry 2022

Edited by
Salvatore Inguaggiato, Qingqiang Meng, Erfan Mondal, Yi-Xiang Chen and Luiz Drude Lacerda

Published in
Frontiers in Earth Science

ISSN 1664-8714
ISBN 978-2-8325-4261-3
DOI 10.3389/978-2-8325-4261-3

About Frontiers

Frontiers is more than just an open access publisher of scholarly articles: it is a pioneering approach to the world of academia, radically improving the way scholarly research is managed. The grand vision of Frontiers is a world where all people have an equal opportunity to seek, share and generate knowledge. Frontiers provides immediate and permanent online open access to all its publications, but this alone is not enough to realize our grand goals.

Frontiers journal series

The Frontiers journal series is a multi-tier and interdisciplinary set of open-access, online journals, promising a paradigm shift from the current review, selection and dissemination processes in academic publishing. All Frontiers journals are driven by researchers for researchers; therefore, they constitute a service to the scholarly community. At the same time, the *Frontiers journal series* operates on a revolutionary invention, the tiered publishing system, initially addressing specific communities of scholars, and gradually climbing up to broader public understanding, thus serving the interests of the lay society, too.

Dedication to quality

Each Frontiers article is a landmark of the highest quality, thanks to genuinely collaborative interactions between authors and review editors, who include some of the world's best academicians. Research must be certified by peers before entering a stream of knowledge that may eventually reach the public - and shape society; therefore, Frontiers only applies the most rigorous and unbiased reviews. Frontiers revolutionizes research publishing by freely delivering the most outstanding research, evaluated with no bias from both the academic and social point of view. By applying the most advanced information technologies, Frontiers is catapulting scholarly publishing into a new generation.

What are Frontiers Research Topics?

Frontiers Research Topics are very popular trademarks of the *Frontiers journals series*: they are collections of at least ten articles, all centered on a particular subject. With their unique mix of varied contributions from Original Research to Review Articles, Frontiers Research Topics unify the most influential researchers, the latest key findings and historical advances in a hot research area.

Find out more on how to host your own Frontiers Research Topic or contribute to one as an author by contacting the Frontiers editorial office: frontiersin.org/about/contact

Reviews in geochemistry: 2022

Topic editors

Salvatore Inguaggiato — National Institute of Geophysics and Volcanology (INGV), Italy

Qingqiang Meng — SINOPEC Petroleum Exploration and Production Research Institute, China

Erfan Mondal — Aligarh Muslim University, India

Yi-Xiang Chen — University of Science and Technology of China, China

Luiz Drude Lacerda — Federal University of Ceara, Brazil

Citation

Inguaggiato, S., Meng, Q., Mondal, E., Chen, Y.-X., Lacerda, L. D., eds. (2024). *Reviews in geochemistry: 2022*. Lausanne: Frontiers Media SA.

doi: 10.3389/978-2-8325-4261-3

Table of contents

05 Research on the efficiency of green development of industry in Chinese prefecture-level oil and gas cities based on super-efficient SBM-DEA model and Malmquist index
Sun Fei, Sun Chongliang, Luo Jie, An Yana and Sun Haiyan

16 Hydrogeochemical characteristics and genesis of Hongshuilantang Hot Spring and its water temperature anomalies during the Rushan earthquake swarm in Eastern China
Guilin Du, Shujuan Su, Xiangchun Chang, Hongwei Ren, Zhuqing Huo and Xiaohui Zhang

26 TOC interpretation of lithofacies-based categorical regression model: A case study of the Yanchang formation shale in the Ordos basin, NW China
Jintao Yin, Chao Gao, Ming Cheng, Quansheng Liang, Pei Xue, Shiyan Hao and Qianping Zhao

44 Prediction of hydrocarbon source rock distribution using logging curves: A case study of Es_3^2 source rock in Nanpu Sag, Huanghua depression, Bohai Bay Basin
Qianwen Guo, Shan Jiang, Jianwei Wang, Quanzhen Zhou, Yongliang Gao, Lin Ye and Jie Yin

60 Thermodynamic analysis of the difference in adsorption characteristics of CH_4 and CO_2 on continental shale
Pei Xue, Quansheng Liang, Chao Gao, Jintao Yin, Shiyan Hao and Qianping Zhao

70 Hydrogeochemical characteristics and the genesis of the No. Lu 32 well in the Jiaodong Peninsula, China
Guilin Du, Bin Zhai, Shujuan Su, Lailun Sui, Xiangchun Chang, Hongwei Ren, Maiyu Sun and Lili Wang

78 Dynamic background on formation, evolution, and later reformation of the Late Paleozoic–Early Mesozoic Basin in Songliao and its significance for hydrocarbon exploration
Lijun Song, Yongqi Ruan, Yonghe Sun, Fenquan Xie, Junlong Li and Yulong Yuan

89 Geological characteristics and exploration potential of the coal measure gas from Shan 2 of the Shanxi formation in the eastern Ordos Basin
Wei-Bo Zhao, Hui Zhang, Yun-He Shi, Xun-Xun Fu, Jie Hui and Xue-Yuan Jing

100 Radon on Mt. Etna (Italy): a useful tracer of geodynamic processes and a potential health hazard to populations
Salvatore Giammanco, Pietro Bonfanti and Marco Neri

114 Review on metal contamination in equatorial estuaries in the Brazilian Northeast
Thays Thayanne Luz Santos, Rozane Valente Marins and Letícia Paulino Alves

137 Review on detection method, main source and geological application of diamondoids in crude oil
Chenchen Fang, Guoyi Hu, Yilin Yuan and Deyu Gong

frontiers | Frontiers in Earth Science

TYPE Original Research
PUBLISHED 11 January 2023
DOI 10.3389/feart.2022.1121071

OPEN ACCESS

EDITED BY
Qingqiang Meng,
SINOPEC Petroleum Exploration and Production Research Institute, China

REVIEWED BY
Jia Qiang,
Shandong University of Science and Technology, China
Hognqi Liu,
Southwest Petroleum University, China

*CORRESPONDENCE
Sun Chongliang,
sunchongliang@petrochina.com.cn

SPECIALTY SECTION
This article was submitted to Geochemistry, a section of the journal Frontiers in Earth Science

RECEIVED 11 December 2022
ACCEPTED 30 December 2022
PUBLISHED 11 January 2023

CITATION
Fei S, Chongliang S, Jie L, Yana A and Haiyan S (2023), Research on the efficiency of green development of industry in Chinese prefecture-level oil and gas cities based on super-efficient SBM-DEA model and Malmquist index.
Front. Earth Sci. 10:1121071.
doi: 10.3389/feart.2022.1121071

Research on the efficiency of green development of industry in Chinese prefecture-level oil and gas cities based on super-efficient SBM-DEA model and Malmquist index

Sun Fei[1], Sun Chongliang[2]*, Luo Jie[1], An Yana[1] and Sun Haiyan[3]

[1]School of Economics and Management, Northeast Petroleum University, Daqing, Heilongjiang, China, [2]Daqing Oilfield Design Institute Ltd., Daqing, Heilongjiang, China, [3]Institute of Petroleum Economics and Management, Northeast Petroleum University, Daqing, Heilongjiang, China

With the proposal of Industrial Green Development Plan (2016–2020), it is particularly urgent to focus on the industrial green development of oil and gas cities, actively promote industrial energy efficiency, reduce pollution emissions, and measure the efficiency of their industrial green development. Based on the actual situation of oil and gas cities, we apply the Super-SBM model to measure the industrial green development efficiency of oil and gas cities in 15 years from 2004 to 2018, analyze the spatial and temporal evolution trends and characteristics of industrial green development efficiency, and also calculate the Malmquist index to dynamically analyze the industrial green development efficiency of oil and gas cities. The results show that the industrial green development efficiency of oil and gas cities as a whole is not high from 2004 to 2018, showing a gentle "W" type fluctuation change. From the spatial dimension, there are significant differences in industrial green development efficiency among oil and gas cities in the east, central and west, with the efficiency value is relatively higher in the west. The total factor productivity of industrial green development is most influenced by the changes of technical efficiency and technological progress. In view of the above problems, it is recommended to broaden green technology innovation channels, increase green technology innovation investment, build a new mechanism for regional synergistic development, and formulate regional graded development strategies.

KEYWORDS

oil and gas cities, industrial green development efficiency, super-SBM model, industrial energy consumption, comprehensive environmental pollution index

1 Introduction

Oil and gas cities are resource-based cities with oil and gas extraction and processing as their pillar industries, which have a large share of resource extraction and related industries in their industrial structure. However, long-term oil and gas exploitation has brought comparatively large impact on the ecology. For example, the oilfield development can cause air pollution in oil and gas cities. The pollutants mainly include SO_2, smoke, dust, NO_X, CO and total hydrocarbons. Oil development under the direction of the latest geology research (Ma et al., 2021; Zou et al., 2021; Feng et al., 2022; Meng, 2022; Wang et al., 2022; Wang et al., 2022) will also pollute the soil, with the large amounts of pollutants, such as NaCL, NaOH, and Na_2Co_3. Now the resulting environmental problems have gradually attracted attention. Under the new normal, with the tightening of China's resources and environment, the industrial green development of oil and gas

cities has become inevitable under the constraint of resources and environmental carrying capacity. The "14th Five-Year Plan" for Industrial Green Development clearly puts forward that by 2025, the green and low-carbon transformation of industrial structure and production methods will achieve significant results, green and low-carbon technologies and equipment will be widely used, energy and resource utilization efficiency will be greatly improved, and the level of green manufacturing will be comprehensively enhanced. The report of the 20th National Congress of the Communist Party of China also proposed to accelerate the green transformation of the development mode, and put forward a series of clear requirements in this regard, emphasizing to "develop green and low-carbon industries," "accelerate the research and development, promotion and application of advanced technologies for energy conservation and carbon reduction," *etc.* It can be seen that promoting the industrial green development of oil and gas cities means taking the concept of green development as an important development goal throughout the whole process and field of industry, with "efficient, sustainable, recycling, low-carbon" as the core, effectively using resources and energy, and reducing pollutant emissions. Therefore, the key is to improve "industrial green development efficiency." In view of this, it is especially urgent to pay attention to the industrial green development efficiency of oil and gas cities, actively promote industrial energy efficiency, reduce pollution emissions, and measure the industrial green development efficiency of oil and gas cities.

2 Literature review

Research on the efficiency of industrial green development originated from green technical efficiency, which was first measured by Pittman (1983) using an index that included non-desired outputs. After that, German scholar Schaltegger (1990) proposed the concept of industrial eco-efficiency, and Hoh et al. (2001) used productivity indicators in the EEA model to evaluate industrial eco-efficiency in Germany. Considering the slack problem of non-desired output and input-output variables arising from production, Tone (2001) proposed a non-radial and non-angular SBM model that can effectively solve the slackness problem of non-desired output and input-output variables, and the model was widely used for measuring environmental and resource efficiency. Ramarkrishnan (2006), Ugur Soytasa et al. (2009) used data envelopment analysis to examine the dependence between variables such as energy use, income and carbon emissions and found a significant correlation between energy consumption and income. Quariguasi et al. (2019) used the ecological topology approach to further expand the evaluation index of industrial green development efficiency to include multiple aspects such as energy consumption and consumption of specific substances to measure industrial green development efficiency. The current studies on industrial green development efficiency at home and abroad are generally conducted from the input-output perspective, selecting appropriate models to measure the study, focusing on analyzing the current situation and making predictions for the future. Some studies have also used DEA models under variable returns to scale and super-efficient SBM models in conducting efficiency assessments. Scholars represented by Wang et al. (2019), Zhang et al. (2020), Wang (2020), Wu et al. (2018), Ding et al. (2019), and Zhao et al. (2022) used a global super-efficiency SBM model, selecting capital, labor, technology, and resources as input indicators, regional GDP as desired output indicators, and industrial wastewater, industrial waste gas, and industrial solid waste emissions as non-desired outputs. With this method, the industrial green development efficiency of 30 provinces (autonomous regions and municipalities directly under the central government), Yangtze River Economic Belt and Yellow River Basin were measured. The results of the study showed that the industrial green development efficiency of Chinese provinces showed a general trend of fluctuating increase in the time dimension, and the regional differences of industrial green development efficiency were obvious, and the industrial green development efficiency measured by provinces was in a state of fluctuating growth (Wu et al., 2018; Ding et al., 2019; Wang et al., 2019; Wang et al., 2020; Zhang et al., 2020).

In summary, foreign studies have been able to balance normative and econometric analysis. Although domestic studies started late, we have made great progress in terms of research objects and methods, such as focusing on national, provincial and municipal areas to measure the efficiency of industrial green development, focusing on the use of traditional CCR and BCC models, as well as super-efficient SBM models and other quantitative analysis tools to measure the efficiency of industrial green development and analyze its influencing factors. Although the measurement of industrial green development efficiency is becoming more and more accurate, the measurement of industrial green development efficiency in oil and gas cities has not been covered yet. Therefore, this paper adopts the Super-SBM model to measure the industrial green development efficiency of prefecture-level oil and gas cities in China during the 15-year period from 2004 to 2018, analyzes the spatial and temporal evolution trends and characteristics of industrial green development efficiency, calculates the Malmquist index to dynamically analyze the industrial green development efficiency of oil and gas cities, and proposes measures to improve the industrial green development efficiency of oil and gas cities.

3 Research methodology and data sources

3.1 Super-SBM model

The current efficiency evaluation methods commonly used in academia mainly include non-parametric analysis and parametric analysis, among which, non-parametric analysis is based on data envelopment analysis (DEA) and parametric analysis is based on stochastic frontier analysis (SFA). Since SFA assumes that random errors obey a specific probability distribution and relies on the production function under multiple constraints, it is difficult to meet the requirements of realistic data and conditions (Dong and Wu, 2017), so the SFA method is seldom chosen by academics for efficiency evaluation. The DEA method, on the other hand, based on the idea of linear programming with the help of input-output data, compares the deviation of each decision unit from the production frontier to measure and evaluate its relative efficiency, which is accepted and improved by a wide range of scholars (Li and Xia, 2017). Tone has improved the SBM model based on the proposed non-radial, non-angle SBM model (slacks-based measure) and proposed the Super-SBM model that allows the efficiency value of the decision unit to be greater than one (Tone, 2001). In this paper, the Super-SBM model is used to measure the efficiency of green development in oil and gas urban industries considering non-desired outputs, and the model is as follows.

Tone defines a finite set of production possibilities that exclude the decision unit (x_o, y_0).

$$P\backslash(x_0, y_0) = \left\{(\bar{x}, \bar{y}) | \bar{x} \geq \sum_{j=1, \neq 0}^{n} \lambda_j \lambda_j, \bar{y} \leq \sum_{j=1, \neq 0}^{n} \lambda_j y_j, \bar{y} \geq 0, \lambda \geq 0\right\} \tag{1}$$

where p\(x_0, y_0) is the set of production inputs excluding (x_0,y_0), and on top of this set of inputs a subset $\bar{p}\backslash(x_o, y_0)$ is defined as

$$\bar{p}\backslash(x_0, y_0) = P\backslash(x_0, y_0) \cap \{\bar{x} \geq x_0, \bar{y} \leq y_0\} \tag{2}$$

since X>0, Y>0, therefore, $\bar{p}\backslash(x_o, y_0)$ is a non-empty set. It is the average distance from (x_0, y_0) to the $(\bar{x}, \bar{y}) \in \bar{p}\backslash(x_o, y_0)$. According to this distance the index δ is defined.

$$\delta = \frac{\frac{1}{m}\sum_{i=1}^{m} \overline{x_i} / x_{i0}}{\frac{1}{s}\sum_{r=1}^{s} \overline{y_r} / y_{r0}} \tag{3}$$

where the δ's numerator represents the average distance from x_0 to the point $\bar{x}$ in the set space $(\bar{x}, \bar{y}) \in \bar{p}\backslash(x_o, y_0)$, the δ's denominator represents the average distance from y_0 to the $\bar{y}$ point in the set space $(\bar{x}, \bar{y}) \in \bar{p}\backslash(x_o, y_0)$. δ is usually used to interpret as the average distance between the production frontier surface and the production cell in the input and output space. The super-efficient SBM planning form for the production cell (x_0, y_0) is as follows:

$$\delta^* = \min \delta = \frac{\frac{1}{m}\sum_{i=1}^{m} \overline{x_i} / x_{i0}}{\frac{1}{s}\sum_{r=1}^{s} \overline{y_r} / y_{r0}} \tag{4}$$

$$st \quad \bar{x} \geq \sum_{j=1, \neq 0}^{n} \lambda_j x_j$$

$$\bar{y} \leq \sum_{j=1, \neq 0}^{n} \lambda_j y_j$$

$$\bar{x} \geq x_0, \bar{y} \leq y_0, y \geq 0, \lambda \geq 0 \tag{5}$$

Translating the above equation into a linear program that can be solved:

$$\tau^* = \min \tau = \frac{1}{m}\sum_{i=1}^{m} \frac{\tilde{x_i}}{x_{i0}}$$

$$st \quad 1 = \frac{1}{s}\sum_{i=1}^{s} \frac{\tilde{y}_r}{y_{r0}}$$

$$\bar{x} \geq \sum_{j=1, \neq 0}^{n} \Delta_j x_j$$

$$\bar{y} \geq \sum_{j=1, \neq 0}^{n} \Delta_j y_j$$

$$\bar{x} \geq t x_0, \bar{y} \geq t y_0, \Delta \geq 0, \bar{y} \geq 0, t \geq 0 \tag{6}$$

The optimal solution of the original plan can be obtained from the optimal solution $(\tau^*, \tilde{x}^*, \tilde{y}^*, \Delta^*, t^*)$ obtained by the above equation:

$$\delta^* = \tau^*, \ \lambda^* = \Delta^* / t^*, \ \bar{x}^* = \bar{x}^* / t^*, \ \bar{y}^* = \bar{y}^* / t^* \tag{7}$$

3.2 Indicator system construction

As the green development of urban industry is not only to achieve urban economic development, but also needs to carry out urban environmental pollution control and improve and restore urban ecology. Therefore, the efficiency of oil and gas city on industrial green development will reflect the coordinated development relationship among economic growth, social development, environmental protection and resource conservation. The measurement of efficiency generally chooses DEA method, and the evaluation index delineation is usually divided into two categories: input and output. Considering the relationship between the number of input and output indicators and the number of decision units (the decision units in this paper are 14 prefecture-level oil and gas cities), the final choice is to use resources, capital and labor as input indicators, and use urban industrial added value and environmental pollution composite index (calculated based on the emissions of industrial wastewater, industrial sulfur dioxide and industrial soot) as output indicators (Zhao, 2019; Sun and Yang, 2021). Based on the principles of data availability, operability, scientificity, representativeness and independence, and by reference to the index construction methods in relevant literature, the input-output index system of industrial green development efficiency of oil and gas cities in China is established, and the specific input and output indicators are shown in Table 1.

3.3 Data sources

Based on the National Plan for Sustainable Development of Resource-based Cities (2013–2020) and the List of 262 Resource-based Cities in China, referring to the oil and gas cities defined in the existing literature, this paper defines a total of 29 oil and gas cities in China (see Table 2), including eight in the east, five in the center, and 16 in the west. Among them, 18 cities are prefecture-level cities. And Xinjiang has the largest distribution of oil and gas cities, with seven oil and gas cities, accounting for about 1/4 of the country.

In order to measure the efficiency of industrial green development in oil and gas cities better, the time selected for this study are 15 years from 2004 to 2018. Considering the comparability of data of each city, this paper takes prefecture-level oil and gas cities as the object of empirical evaluation, and there are 18 prefecture-level cities among 29 oil and gas cities, as shown in Table 2. Due to the serious lack of data on research indicators in Hami, Qingyang, Zhaotong and Fushun, considering the availability of data, this paper collects the indicator data of 14 representative oil and gas cities in the eastern, central and western regions for the study. The data are obtained from EPS database, China City Statistical Yearbook, provincial and municipal statistical yearbooks and official websites, and this paper uses OLS trend analysis to fill in the missing data.

4 Measurement results and analysis

4.1 Analysis of the spatial and temporal evolution of the industrial green development efficiency of oil and gas city

4.1.1 Time dimension analysis of industrial green development efficiency of oil and gas city

In this paper, we measure the industrial green development efficiency of 14 prefecture-level oil and gas cities from the year of 2004–2018 based on the Super-SBM model using DEA-Solver Pro 5.0 (Table 3), and the trend of industrial green development efficiency of each oil and gas city is shown in Figure 1.

TABLE 1 Evaluation index system of green development efficiency of oil and gas city industry.

Type	Category	Specific indicators and units
Invest	Capital	Total fixed assets of industrial enterprises above the scale (RMB ten thousand)
	Labor	Number of employees in urban industrial units (10,000 people)
	Resources	Energy consumption of industrial enterprises (10,000 tons of standard coal)
Outputs	Expected output	Urban industrial added value (RMB 100 million)
	Unexpected output	Comprehensive index of environmental pollution (%)

TABLE 2 Distribution areas and types of oil and gas cities in China.

Region	Province	Oil and gas city	City level
Eastern	Heilongjiang	Daqing	City at prefecture level
	Hebei	Renqiu	County-level city
		Tangshan	City at prefecture level
	Liaoning	Panjin	City at prefecture level
		Fushun	City at prefecture level
	Shandong	Dongying	City at prefecture level
	Jilin	Songyuan	City at prefecture level
	Hainan	Dongfang	County-level city
Central	Inner Mongolia	Ordos	City at prefecture level
		Xilinhot	County-level city
	Henan	Nanyang	City at prefecture level
		Puyang	City at prefecture level
	Hubei	Qianjiang	County-level city
Western	Sichuan	Nanchong	City at prefecture level
		Luzhou	City at prefecture level
		Dazhou	City at prefecture level
	Shaanxi	Yan'an	City at prefecture level
		Yulin	City at prefecture level
	Gansu	Qingyang	City at prefecture level
		Yumen	County-level city
	Ningxia	Lingwu	County-level city
	Yunnan	Zhaotong	City at prefecture level
	Xinjiang	Hami	City at prefecture level
		Shanshan	County
		Fukang	County-level city
		Bayingolin	Autonomous prefecture
		Korla	County-level city
		Karamay	City at prefecture level
		Baicheng	County

The results show that from the time dimension (Figure 1), the overall industrial green development efficiency of oil and gas cities from 2004 to 2018 is not high, and the efficiency value fluctuates and rises from 2004 to 2012, reaching a high point in 2012, after which the efficiency value decreases to the lowest in 2015, and then slowly rebounds. Among them, the industrial green development efficiency of oil and gas cities in the western region is higher than that in the eastern and central regions before 2014 and 2017, and the efficiency value in the western region is above the average. And the industrial green development efficiency of oil and gas cities in the eastern region show a fluctuating increasing trend before 2014, then fluctuating decreases, with the lowest efficiency value of .89 in 2017, and rebounds to .96 in 2018. In contrast, the central region shows a fluctuating increasing trend until 2016, reaching the maximum efficiency value of 1.22 in 2016, after which the efficiency value falls back to 1.17 in 2018. During 2004–2014, the efficiency value of industrial green development in western oil and gas cities is higher than that in the eastern and central regions, and the efficiency value in the western region is lower than that in the eastern and central regions in 2015–2016, with the rebound in 2017 is still higher than that in other two regions, and between the two regions in 2018. The efficiency value of the eastern region has been lower than the other two regions except for 2016, when it is between the western and central regions. The efficiency value of the central region is between the eastern and western regions until 2015, and is higher than other two regions from 2015 to 2018, except for 2017. The reason for this is that the eastern region has a developed industrial economy, with a higher average urban industrial added value than the central and western regions (Figure 2), and has long been both the main force of industrial production and energy consumption in China (Figure 3), with economic growth, a large number of pollutants are discharged, resulting in more serious environmental pollution than the central and western regions (Figure 4), and its industrial green development efficiency is naturally low (Figure 1). The high efficiency value in the western region is due to the fact that the oil and gas cities that have reached effective development in the western region account for a larger proportion than those in the eastern and central regions, with only Karamay city among the six oil and gas cities having an average efficiency value less than 1. This is mainly because the average energy consumption of oil and gas cities in the western region is lower than that in the central and eastern regions, with the eastern oil and gas cities having the highest average energy consumption (Figure 3), and the integrated environmental pollution index of oil and gas cities in

TABLE 3 Measured values of industrial green development efficiency in prefecture-level oil and gas cities 2004–2018.

Region	City	2004	2005	2006	2007	2008	2009	2010	2011	2012	2013	2014	2015	2016	2017	2018	Average
Eastern	Daqing	1.21	1.13	1.14	1.12	1.21	1.11	1.26	1.33	1.28	1.29	1.29	1.11	1.01	.88	.70	1.14
	Tangshan	1.39	1.30	1.26	1.28	1.29	1.38	1.22	1.28	1.28	1.28	1.35	1.44	1.53	1.40	1.32	1.33
	Panjin	.59	.48	.55	.64	.69	.65	.66	.75	.84	.79	.70	.58	.48	.49	.56	.63
	Dongying	1.17	1.18	1.17	1.11	1.05	1.00	.71	.61	.56	.60	.70	1.09	1.12	1.10	1.21	.96
	Songyuan	.47	.55	.67	.70	.84	1.06	1.04	1.04	1.08	1.13	1.17	.81	1.03	.58	1.00	.88
	Mean	.97	.93	.96	.97	1.01	1.04	.98	1.00	1.01	1.02	1.04	1.00	1.03	.89	.96	
central	Ordos	1.17	1.15	1.14	1.09	1.10	1.17	1.17	1.01	1.07	1.05	1.20	1.36	1.42	1.10	1.06	1.15
	Nanyang	1.30	1.19	1.20	1.26	1.28	1.26	1.17	1.12	1.03	1.01	1.02	1.00	1.09	1.11	1.12	1.14
	Puyang	.50	.56	.69	.75	.81	.85	1.02	1.01	1.03	1.10	1.06	1.17	1.15	1.14	1.34	.95
	Mean	.99	.96	1.01	1.03	1.06	1.09	1.12	1.05	1.04	1.05	1.09	1.18	1.22	1.12	1.17	
Western	Nanchong	1.12	1.23	1.16	1.20	1.15	1.16	1.13	1.13	1.10	1.09	1.05	.56	.57	1.18	1.00	1.06
	Luzhou	1.21	1.06	1.11	1.12	1.20	1.51	1.42	1.52	1.56	1.37	1.44	1.43	1.49	1.49	1.19	1.34
	Dazhou	1.05	1.02	1.01	.39	1.07	1.00	1.01	1.07	1.10	1.06	1.13	1.13	1.05	1.00	1.01	1.01
	Yan'an	1.15	1.24	1.31	1.32	1.38	1.29	1.24	1.31	1.41	1.32	1.33	1.24	1.22	1.12	1.13	1.27
	Yulin	1.55	1.47	1.51	1.44	1.35	1.16	1.19	1.11	1.28	1.20	1.07	1.07	1.02	1.11	1.13	1.24
	Karamay	.48	.50	.50	.46	.60	.51	.60	1.06	1.06	1.10	.58	.55	.52	1.02	1.01	.70
	Mean	1.09	1.09	1.10	.99	1.12	1.10	1.10	1.20	1.25	1.19	1.10	1.00	.98	1.15	1.08	
Nationwide		1.03	1.00	1.03	.99	1.07	1.08	1.06	1.10	1.12	1.10	1.08	1.04	1.05	1.05	1.06	

10.3389/feart.2022.1121071

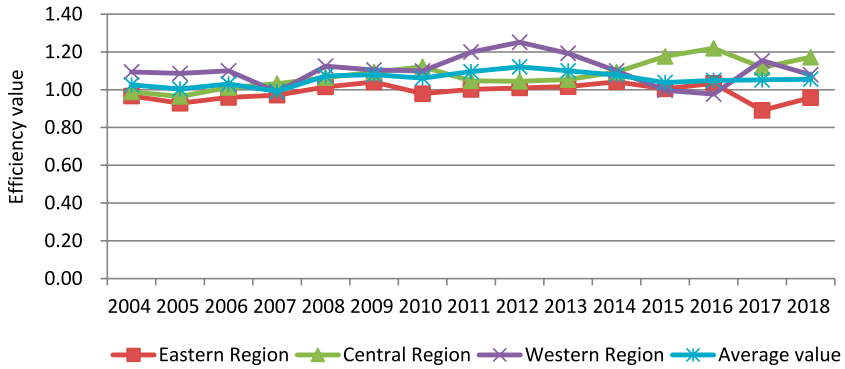

FIGURE 1
Temporal evolution of industrial green development efficiency in prefecture-level oil and gas cities 2004–2018.

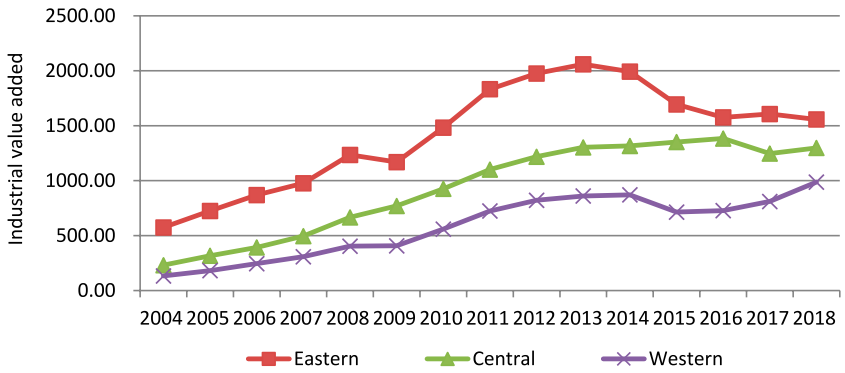

FIGURE 2
Trends in industrial value added in oil and gas cities, 2004–2018 (unit: RMB one hundred million).

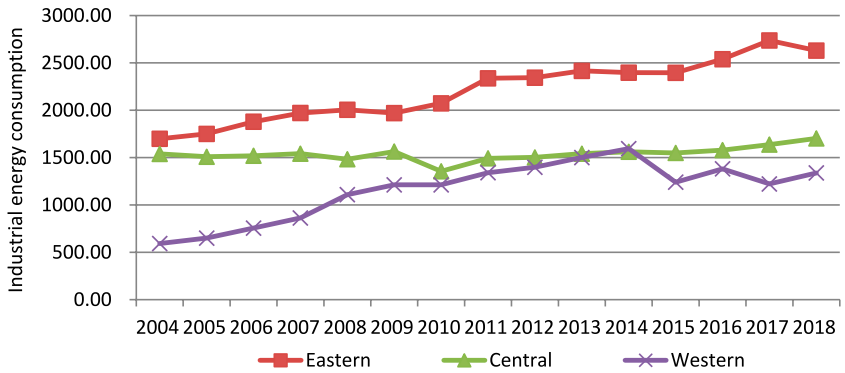

FIGURE 3
Trends in industrial energy consumption in oil and gas cities, 2004–2018 (unit: ten thousand tons of coal equivalent).

the western region is also significantly lower than that of the other two regions. Index is also significantly lower than the other two regions (Figure 4), so the efficiency of industrial green development in the western region is significantly higher than that in the central and eastern regions. The efficiency value of the central region is basically higher than the other two regions after 2014, because the environmental pollution in the central region was more serious during 2004–2007, and its environmental pollution level

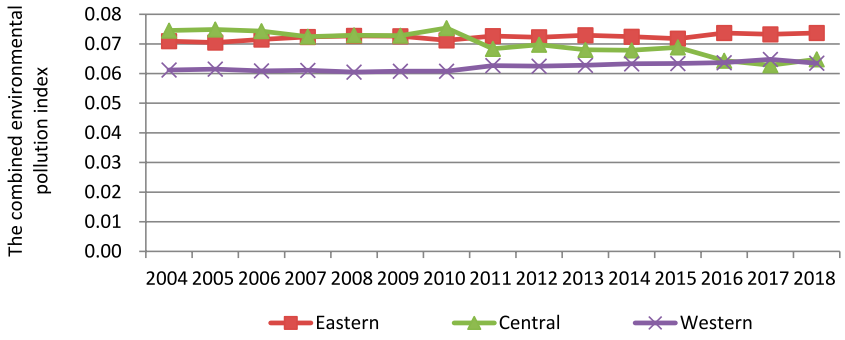

FIGURE 4
Trends in the combined environmental pollution index in oil and gas cities, 2004–2018 (unit: %).

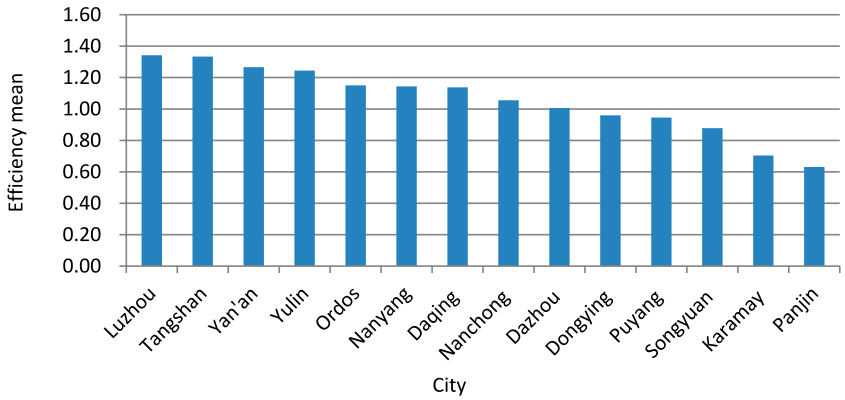

FIGURE 5
Average value of green development efficiency of oil and gas urban industries during 2004–2018.

improved during 2007–2014, and the environmental pollution management has been effective after 2015.

4.1.2 Spatial dimensional analysis of green development efficiency in oil and gas city industry

From the spatial dimension (Figure 5), Luzhou (1.342), Tangshan (1.334), Yan'an (1.267), Yulin (1.244), Ordos (1.151), Nanyang (1.144), Daqing (1.138), Nanchong (1.055), and Dazhou (1.007) are at the forefront of industrial green development in oil and gas cities, with efficiency values greater than 1 belonging to the efficiency effective zone, and Dongying (.959), Puyang (.946), Songyuan (.878), Karamay (.704) and Panjin (.631) are the cities with lower level of industrial green development in oil and gas cities, with efficiency values less than 1 and no effective development. Panjin, the city with the lowest efficiency value, has an efficiency value of .631, compared with Luzhou, the city with the highest efficiency value of industrial green development. It is only half of Luzhou's efficiency, and there is still much room for improvement. It can be seen that the western region has a high concentration of oil and gas cities with high efficiency in industrial green development, while the eastern and central regions have more oil and gas cities with low efficiency.

4.2 Dynamic analysis of green development efficiency of oil and gas urban industry

For the evaluation of industrial green development efficiency, from the micro level, the ratio relationship between inputs and outputs is considered, for which it has been analyzed in the temporal and spatial dimensions. From the macro level, it mainly involves technical efficiency, scale efficiency and total factor productivity, *etc.* (Zhang, 2018). In this paper, DEAP 2.1 software is used to measure and decompose the input-output index data of 14 prefecture-level oil and gas cities from 2004 to 2018 using Malmquist index to dynamically analyze the relationship between total factor productivity and each efficiency of industrial green development in prefecture-level oil and gas cities.

4.2.1 Analysis of dynamic changes in the efficiency of industrial green development in oil and gas cities at various levels

Based on the results of the Malmquist index run, the annual average Malmquist index of industrial green development efficiency and its decomposition for each oil and gas city at each level from 2004 to 2018 are obtained, as shown in Table 4.

TABLE 4 Malmquist index of annual average industrial green development efficiency and its decomposition in 14 prefecture-level oil and gas cities in 2004–2018.

Region	Oil and gas city	Technical efficiency	Technology progress	Pure technical efficiency	Scale efficiency	Total factor productivity
Eastern	Daqing	.983	1.036	.990	.993	1.019
	Tangshan	1.000	1.009	1.000	1.000	1.009
	Panjin	1.010	1.018	1.013	.997	1.028
	Dongying	1.000	1.012	1.000	1.000	1.012
	Songyuan	1.029	.989	1.033	.996	1.017
Central	Ordos	1.016	.962	1.000	1.016	.978
	Nanyang	1.000	1.005	1.000	1.000	1.005
	Puyang	1.041	1.010	1.041	1.001	1.052
Western	Nanchong	.991	.925	1.000	.991	.917
	Luzhou	1.000	.964	1.000	1.000	.964
	Dazhou	1.007	.947	1.000	1.007	.953
	Yan'an	1.000	1.017	1.000	1.000	1.017
	Yulin	1.000	.974	1.000	1.000	.974
	Karamay	1.032	1.017	1.033	.998	1.050
	Mean	1.008	.991	1.008	1.000	.999

According to the measurement results in Table 4, it can be seen that the Malmquist efficiency index of 14 prefecture-level oil and gas cities in Northeast China from 2004 to 2018 has an index less than 1 except for Tangshan, Panjin, Dongying, Nanyang, Puyang, and Yan'an, and the geometric mean of total factor productivity of each oil and gas city is .999, which indicates that the level of industrial green development in each oil and gas city is in a declining trend and the overall average annual decline is 1%. Overall, the relationship between industrial green development and resources and environment in oil and gas cities in this period needs to be improved. From the decomposition of total factor productivity of industrial green development, the average value of the technical efficiency index is 1.008, indicating that technical efficiency keeps increasing year by year at an average annual rate of .8%, with the average value of the technical progress index is .991, indicating that the contribution of technical progress to total factor productivity decreases by .9% annually compared with the previous year. This indicates that the decline in total factor productivity of green development in oil and gas urban industries from 2004 to 2018 is dominated by the decline in technical progress.

By analyzing the changes of total factor productivity of industrial green development in each oil and gas city, it is found that Puyang has the fastest increase with an average annual increase of 5.2%, followed by Karamay and Panjin, and the average annual increase is 5% and 2.8% respectively. Total factor productivity of industrial green development in Ordos, Nanchong, Luzhou, Dazhou and Yulin is in decline, and the fastest decline is in Nanchong, with an average annual decline of 8.3%. From the decomposition indicators, the total factor productivity of industrial green development in oil and gas cities is greatly influenced by two factors: technical efficiency and technical progress. According to the data in Table 4, it can be seen that oil and gas cities with increased total factor productivity, such as Panjin, Puyang, and Karamay, have higher technical efficiency or technical progress index, while oil and gas cities with decreased total factor productivity generally also have lower technical efficiency or technical progress index, among which Nanchong has the fastest rate of decrease in total factor productivity, and its technical progress index and technical efficiency index are also the lowest, therefore, for Nanchong, its technical efficiency and technical progress need to be improved. During the study period, the technical efficiency of all oil and gas cities at all levels rose and fell, among which Puyang has the fastest increase in technical efficiency with an average annual increase of 4.1%, Daqing has the fastest decrease in technical efficiency with an average annual decrease of 1.7%, and in a comprehensive view, 14 oil and gas cities rose at an average annual rate of .8%. In terms of pure technical efficiency, only Daqing is in a declining state, with an average annual decline of 1%, and other cities are in a static or rising state. The scale efficiency of each oil and gas city, except for Daqing, Panjin, Songyuan, Nanchong and Karamay, which are in a declining state, and other oil and gas cities are in a stationary or rising state all oil and gas cities are in a stationary state in general. It indicates that the scale system of these oil and gas cities has tended to be perfect.

4.2.2 Analysis of dynamic changes in the efficiency of industrial green development of the overall oil and gas city

Using the Malmquist index to measure and decompose the input-output data of oil and gas cities, we can also obtain the average Malmquist index and its decomposition for each year of oil and gas cities, which are shown in Table 5.

From the interannual variation of industrial green development total factor productivity in oil and gas cities, there is a general trend of fluctuating variation in industrial green development total factor productivity from 2004 to 2018. Except for 2004–2005, 2007–2008,

TABLE 5 Average Malmquist index and its decomposition by year in oil and gas cities in 2004–2018.

Year	Technical efficiency	Technology progress	Pure technical efficiency	Scale efficiency	Total factor productivity
2004–2005	1.006	1.030	1.011	.995	1.036
2005–2006	.984	1.010	.991	.993	.994
2006–2007	1.023	.973	1.017	1.006	.995
2007–2008	1.076	.933	1.050	1.025	1.004
2008–2009	1.039	.902	1.036	1.003	.937
2009–2010	.961	1.089	.974	.986	1.047
2010–2011	1.012	1.078	1.013	.999	1.091
2011–2012	.998	1.004	1.007	.991	1.001
2012–2013	1.013	.963	1.008	1.005	.975
2013–2014	.956	.972	1.000	.955	.929
2014–2015	.985	.962	.990	.995	.947
2015–2016	1.035	.936	1.026	1.009	.969
2016–2017	1.032	1.005	.986	1.047	1.037
2017–2018	.995	1.041	1.003	.992	1.036
Average	1.008	.991	1.008	1.000	.999

2009–2012, and 2016–2018 when the total factor productivity of industrial green development is greater than 1, all other years show negative growth.

The increase of total factor productivity of industrial green development in 2004–2005 should be influenced by the western development strategy, because about half of the oil and gas cities studied are located in the west, and the negative growth of total factor productivity of industrial green development in 2005–2007 is mainly due to the economic downturn in the northeast, and the industrial economic development of oil and gas cities located in the northeast is affected, with the implementation of the northeast revitalization strategy increases the efficiency of industrial green development in 2007–2008. However, in mid-2008, due to the international financial crisis, the total factor productivity of industrial green development in 2008–2009 is negative. Affected by the financial crisis, the Chinese government implements the "four trillion" investment to boost economic development, and the total factor productivity of industrial green development in 2009–2012 has increased. This should be a brief stimulation brought by the "four trillion" investment. After that, under the dual influence of the global financial crisis and domestic economic restructuring, the negative effects of the previous blind expansion of production capacity, the pursuit of rapid economic recovery begin to appear, and the national demand for oil, coal and other resource-based products falls, resulting in a decline in the prices of resource-based products, while the "four trillion" investment leads to overcapacity in the industry. In particular, the industries of iron and steel, electricity, coal and cement caused serious waste of resources, and the oil and gas industry are also affected, resulting in negative total factor productivity growth in the green development of oil and gas city industry from 2012 to 2016. As China's economic development enters a new normal, in the context of continuous downward economic growth and CPI continues to run low, China proposed in November 2015"supply-side structural reform," that is, starting from the production side and supply-side to adjust the supply structure, in order to achieve high-quality economic development to find a new way. As a result, oil and gas cities have actively eliminated backward production capacity and taken relevant measures to seek green and low-carbon transformation of the oil and gas industry on the basis of the existing foundation, and the total factor productivity of industrial green development has increased from 2016 to 2018. The industrial green development of oil and gas cities has begun to bear fruit.

Analyzed from the perspective of composition, the technical progress index was the largest during 2009–2010, and the technical efficiency index and technical progress index are greater than 1 in 2004–2005, 2010–2011, and 2016–2017, and they are in an increasing state, which is the main reason for their high Malmquist productivity index. As can be seen from Table 5, the annual average industrial green development total factor productivity of oil and gas cities during the study period is .999, and the technical efficiency index, technical progress index, pure technical efficiency index and scale efficiency index are 1.008, .991, 1.008, and 1, respectively, all of which are greater than or equal to 1 except for the technical progress index. It is concluded that both pure technical efficiency and technical efficiency promote the total factor productivity of industrial green development in cities, of which technical efficiency and pure technical efficiency have the greatest role in promoting it. The technical progress index is less than 1, which hinders the improvement of total factor productivity of industrial green development, indicating that oil and gas cities should focus on the introduction and application of senior talents and advanced technologies, and also further improve the scale of industrial green development.

5 Conclusion and recommendations

5.1 Conclusion

Industrial green development is the only way for oil and gas cities to carry out industrial green transformation, which can promote the harmonious integration of industrial and ecological civilizations. Green industrial development in oil and gas cities can reduce excessive consumption of oil and gas resources and damage to the environment, actively promote Efficiency of industrial energy, reduce pollution emissions, and achieve a "win-win" situation between industrial growth and resource environmental protection in cities. In this paper, we use the Super-SBM model to measure the efficiency of green development in oil and gas cities, and use the Malmquist index to dynamically analyze its total factor productivity, and draw the following conclusions.

(1) From the time dimension, the overall industrial green development efficiency of oil and gas cities is not high during the 15 years, showing a gentle "W" type fluctuation change. Among them, the industrial green development efficiency of oil and gas cities in the western region is higher than that in the eastern and central regions before 2014 and 2017, and the efficiency value in the western region is above the average.
(2) From the spatial dimension, there are significant differences in industrial green development efficiency among oil and gas cities in the east, central and west, with the western region having relatively high efficiency values and being the target for other regions to catch up, while the industrial green development efficiency in the eastern and central oil and gas cities continues to be at a relatively low level and many oil and gas cities are in a state of low efficiency of industrial green development.
(3) Dynamic analysis of the total factor productivity of industrial green development in oil and gas cities, it can be seen by decomposing the indicators that changes in technical efficiency and technical progress have the greatest impact on the total factor productivity of industrial green development. Among them, technical efficiency and pure technical efficiency promote the improvement of total factor productivity of industrial green development in oil and gas cities, and hindered technical progress hinders the improvement of total factor productivity of industrial green development. It indicates that oil and gas cities should focus on the introduction and application of senior talents and advanced technologies, while further improvements in the scale of industrial green development should also be made.
(4) Regional differences in the industrial green development efficiency of oil and gas cities are significant. The better the environmental protection being done, the lower pollutant emission and the lower the comprehensive energy consumption will be achieved, and the higher industrial green development efficiency of oil and gas cities will be achieved.

5.2 Recommendations

Based on the above findings, this paper proposes recommendations for improving the efficiency of green development in oil and gas urban industries.

5.2.1 Broadening green technology innovation channels

For oil and gas cities with low efficiency of industrial green development such as Songyuan and Panjin, the channels of green technology innovation should be broadened in the future development. Firstly, cooperation with outstanding foreign oil and gas companies can be launched to introduce their advanced technologies. Secondly, advanced and efficient green technology transfer mechanisms can be established through contact or cooperation with developed countries or regions to promote the transfer and diffusion of green technologies. Besides, the construction of a collaborative platform among industry, academia and research institutes should be accelerate to break through a number of green technologies with independent intellectual property rights. Finally, we should increase investment in green technology innovation, establish a sound incentive mechanism for employees, vigorously develop low-carbon technologies and promote the application of green technologies, so as to improve energy utilization efficiency and transform and eliminate backward production capacity.

5.2.2 Building a new mechanism for regional synergistic development

The efficiency of industrial green development in the western region has increased significantly in recent years, but compared to the eastern region by the degree of economic development, the western region is lagging clearly behind the eastern region, leading to the flow of high-quality factors cultivated in the region to the developed eastern region due to the siphon effect. To this end, a new mechanism of regional synergistic development should be constructed, the advantages of location should be utilized, open cooperation experimental zones should be built, oil and gas cities in the east, central and west should cooperate in introducing industrial projects such as new materials, modern logistics, culture and entertainment, developing service and tourism industries, breaking down regional barriers, improving the ability of the region itself to absorb talent, technology, products and other factors, and improving the institutional system to realize the flow of regional high-quality elements from the east to the central and west. Eventually, the balanced distribution of industrial green development factors in the east, central and west regions will be realized.

5.2.3 Developing regional graded development strategies

The government should not formulate policies to guide the industrial green development of cities in a generalized manner, but pay more attention to the differences in the development of each city, formulate graded development policies, and implement linkage development of oil and gas cities at the same level. For oil and gas cities such as Yulin, Yan'an, Ordos and Tangshan with high efficiency of industrial green development, the government should encourage enterprises to carry out independent innovation and provide a relatively relaxed technological innovation environment, so as to improve the economic structure, form new economic growth points and seek new impetus for promoting the industrial green development of the cities; for cities such as Daqing and Dongying with medium level of industrial green development efficiency, the government should actively adopt high and new technologies to improve and upgrade traditional enterprises with high pollution

and high energy consumption, and optimize the industrial structure, so as to enhance the degree of industrial green development of the cities. While for cities such as Songyuan and Panjin, which have low industrial green development efficiency, they should guide oil and gas cities with high degree of industrial green development to flow advanced production technologies to low-efficiency cities to form a new situation of radiation-driven and mutual support, so as to jointly promote the industrial Green development.

Data availability statement

The original contributions presented in the study are included in the article/supplementary material, further inquiries can be directed to the corresponding author.

Author contributions

SF takes the paper's idea, data collection, fund support, and paper writing; SC contributes to data handling and the paper writing; LJ contributes to the work of figure drawing and data handling; AY contributes to data verification; SH contributes to the paper writing.

Funding

Chinese Social Sciences Fund: Research on mechanism analysis, efficiency measurement and path exploration of digital enabling low-carbon transformation on traditional energy industry (22BTJ046).

Conflict of interest

Author SC was employed by Daqing Oilfield Design Institute Ltd.

The remaining authors declare that the research was conducted in the absence of any commercial or financial relationships that could be construed as a potential conflict of interest.

Publisher's note

All claims expressed in this article are solely those of the authors and do not necessarily represent those of their affiliated organizations, or those of the publisher, the editors and the reviewers. Any product that may be evaluated in this article, or claim that may be made by its manufacturer, is not guaranteed or endorsed by the publisher.

References

Ding, X. Y., Xiao, W., and Tian, Z. (2019). Research on the efficiency of industrial green innovation development and its synergistic effect in the Yangtze River Delta city cluster. *J. Industrial Technol. Econ.* 38 (7), 67–75.

Dong, X., and Wu, C. Q. (2017). A study on the spatial and temporal evolution and influencing factors of total factor productivity in Chinese cities-empirical evidence from 35 major cities from 2000-2014. *Study Pract.* 5, 5–16.

Feng, D. H., Liu, C. L., Tian, J. X., et al. (2022). Erosion thickness recovery and its significance to hydrocarbon accumulation in northwestern Qaidam Basin. *Petroleum Geology & Experiment* 44 (1), 188–198. doi:10.11781/sysydz202201188

Hoh, H., Scoer, K., and Seibel, S. (2001). Eco-efficiency indicators in German environmental economic accounting. *Stat. J. U. N. Econ. Comm. Eur. Ger.* 19 (1/2), 41–52. doi:10.3233/sju-2002-191-205

Li, J. B., and Xian, X. F. (2017). Empirical analysis of energy DEA efficiency in Chongqing under green low-carbon constraints. *J. Chongqing Univ.* 40 (02), 26–36.

Meng, Q. Q. (2022). Identification method for the origin of natural hydrogen gas in geological bodies. *Petroleum Geology & Experiment* 44 (3), 552–558. doi:10.11781/sysydz202203552

Ma, Y. S., Li, M. W., Cai, X. Y., et al. (2021). Advances in basic research on the mechanism of deep marine hydrocarbon enrichment and key exploitation technologies. *Petroleum Geology & Experiment* 43 (5), 737–748. doi:10.11781/sysydz202105737

Pittman, R. W. (1983). Multilateral productivity comparisons with undesirable outputs. *Econ. J.* 93, 883–891. doi:10.2307/2232753

Quariguasi, J. F. N., Walther, G. J., and Bloemhof, J. (2019). A methodology for assessing eco-efficiency in logistics networks. *Eur. J. Operational Res.* 193, 670–683.

Ramakrishnan, Ramanathan. (2006). A multifact or efficiency perspective to the relationships among world GDP, energy consumption and carbon dioxide emissions. *Technol. Forecasting&Social Change* 73, 483–494. doi:10.1016/j.techfore.2005.06.012

Schaltegger, S., and Sturm, A. (1990). Kologische rationalitt:ansatzpunktezur ausgestaltung you okologieorienttierten management instrumenten. *Die Unternehm.* 4, 273–290.

Sun, F., and Yang, X. L. (2021). Measurement of green development efficiency in resource-based cities in Northeast China-an empirical study based on 2008-2017 data. *J. China Univ. Petroleum* 37 (3), 18–25. doi:10.13216/j.cnki.upcjess.2021.03.0003

Tone, K. (2001). A slacks-based measure of efficiency in data envelopment analysis. *Eur. J. Operational Res.* 130, 498–509. doi:10.1016/s0377-2217(99)00407-5

Ugur, S., and Ramazan, S. (2009). Energy consumption economic growth and carbon emissions:Challenges faced by an EU candidate member. *Ecol. Econ.* 68, 1667–1675. doi:10.1016/j.ecolecon.2007.06.014

Wang, J. M., Qiu, D. S., Jiang, Q. Y., Zhang, M., et al. (2019). Research on the measurement and improvement path of industrial green development efficiency in Yangtze River Economic Belt. *Sci. Technol. Manag. Res.* 39 (12), 46–52.

Wang, X. P., and Li, Y. M. (2020). Industrial green development measurement and its differential evolution in the perspective of sustainable development. *J. Industrial Technol. Econ.* 39 (7), 83–91.

Wang, Y. G., Sheng, X. J., Yang, S., et al. (2022). Method of post-drilling assessment for the prospect evaluation of petroleum exploration. *Petroleum Geology & Experiment* 44 (6), 1088–1091. doi:10.11781/sysydz2022061088

Wang, Z. Q., Ge, H. K., Guo, H. Y., et al. (2022). Experimental study on the mobility of Junggar Basin's Jimsar shale oil by CO_2 huff and puff under different temperatures and pressures. *Petroleum Geology & Experiment* 44 (6), 1092–1099. doi:10.11781/sysydz2022061092

Wu, C. Q., and Huang, L. (2018). Research on the performance assessment of industrial green development in Yangtze River Economic Belt and its synergistic effect. *J. China Univ. Geosciences Soc. Sci. Ed.* 18 (03), 46–55.

Zhang, H. C. (2018). A review of research on green transformation of resource-based cities at home and abroad. *Resour. Industries* 20 (05), 9–15.

Zhang, R. J., and Dong, H. Z. (2020). Spatial and temporal evolution and influencing factors of industrial eco-efficiency in China based on provincial scale. *Econ. Geogr.* 40 (7), 124–132. doi:10.15957/j.cnki.jjdl.2020.07.014

Zhao, J. J., Zhan, R., and Wang, Y. (2022). Spatial temporal pattern and influencing factors of industrial green development efficiency in the Yellow River Basin. *Yellow River* 44 (09), 56–63.

Zhao, Y., Liu, D., Li, J., Zhang, X., and Wang, X. (2019). L-NBP, a multiple growth factor activator, attenuates ischemic neuronal impairments possibly through promoting neuritogenesis. *Inq. into Econ. Issues* 7, 94–105. doi:10.1016/j.neuint.2019.01.002

Zou, Y., Wang, G. J., Lu, L., et al. (2021). Simulation experiment and mathematical model analysis for shale gas diffusion in nano-scale pores. *Petroleum Geology & Experiment* 43 (5), 844–854. doi:10.11781/sysydz202105844

frontiers | Frontiers in Earth Science

TYPE Original Research
PUBLISHED 17 January 2023
DOI 10.3389/feart.2022.1088240

OPEN ACCESS

EDITED BY
Qingqiang Meng,
SINOPEC Petroleum Exploration and Production Research Institute, China

REVIEWED BY
Rijun Hu,
Ocean University of China, China
Maosheng Gao,
Qingdao Institute of Marine Geology (QIMG), China

*CORRESPONDENCE
Shujuan Su,
shujuan_su@163.com

SPECIALTY SECTION
This article was submitted to Geochemistry, a section of the journal Frontiers in Earth Science

RECEIVED 03 November 2022
ACCEPTED 14 November 2022
PUBLISHED 17 January 2023

CITATION
Du G, Su S, Chang X, Ren H, Huo Z and Zhang X (2023), Hydrogeochemical characteristics and genesis of Hongshuilantang Hot Spring and its water temperature anomalies during the Rushan earthquake swarm in Eastern China.
Front. Earth Sci. 10:1088240.
doi: 10.3389/feart.2022.1088240

Hydrogeochemical characteristics and genesis of Hongshuilantang Hot Spring and its water temperature anomalies during the Rushan earthquake swarm in Eastern China

Guilin Du[1,2], Shujuan Su[3]*, Xiangchun Chang[1], Hongwei Ren[4], Zhuqing Huo[5] and Xiaohui Zhang[2]

[1]College of Earth Science and Engineering, Shandong University of Science and Technology, Qingdao, China, [2]Weihai Earthquake Monitoring Center, Weihai, China, [3]Yantai Earthquake Monitoring Center Station, Shandong Earthquake Agency, Yantai, China, [4]National Institute of Natural Hazards, Ministry of Emergency Management of China, Beijing, China, [5]Jiangsu Earthquake Agency, Nanjing, China

Water temperatures of hot springs close to tectonic fault zones often show some variations before earthquakes, and analyses of earthquake precursors in hot springs have significant referential meaning for earthquake monitoring and forecasting. This study measured the concentration of major ions in water from the Hongshuilantang Hot Spring in 2017 and 2020. The ion composition was classified by hydrochemistry into the HCO_3·SO_4-Na chemical type. The composition of hydrogen and oxygen isotopes in the Hongshuilantang Hot Spring were located near the global meteoric water line (GMWL), indicating that the recharge source of the hot spring was meteoric water. The δD and δ18O values were not plotted on the Glogal Meteroric Water Line (GMWL), and there were some deviations, which suggested that hot spring water underwent water–rock interactions. Deep circulation water played an important role during the evolution process of thermal water. Water temperature showed a decreasing trend from October 2013 to June 2015 during the Rushan earthquake swarm in eastern China. Because of the occurrence of the earthquake swarm, we inferred that regional stress in this area began to be released, allowing continuous rebalancing. Free surface water appeared in some aquifers, and the seepage of low-temperature underground water into the upper aquifer led to a drop in water temperature in the hot spring. The Hongshuilantang Hot Spring and the epicenter of the Rushan earthquake swarm were located on the Muping–Jimo seismological fault zone, with the same seismotectonic system and some genesis relationships.

KEYWORDS

Hongshuilantang Hot spring, anomaly analysis, Rushan earthquake swarm, genesis, hydrogeochemistry

Introduction

Geothermal resources have significant economic and social value and are clean and recyclable (Tiwari et al., 2020; Lai et al., 2021; Verma et al., 2021). The study of hot springs is important and indispensable for the development and utilization of geothermal resources (Luan and Li, 1993; Wang et al., 2011). In recent years, hot springs have been widely used for seismic monitoring and forecasting, including the observation and analysis of ion concentrations and isotope compositions in hot springs that are close to fault zones (Gao et al., 2015; Che et al., 2016; Zhang et al., 2021). Seismic precursors, co-seismic responses, and the tidal effects of water temperatures have been recorded in a number of hot springs and geothermal wells (Mogi et al., 1989; Che et al., 2014; Liu et al., 2015; Ma et al., 2015; Miyakoshi et al., 2020). Anomalies in the water temperature of thermal water can be critical and especially useful earthquake precursors (Ma, 2016). For seismic fluid geochemistry, the determination of hydrogeochemical characteristics and measurement of stable hydrogen and oxygen isotopes is a promising and important method for earthquake monitoring and forecasting (Favara et al., 2001; Claesson et al., 2004; Pope et al., 2014; Skelton et al., 2014; Li et al., 2019; Miyakoshi et al., 2020). A large amount of useful information on the origins and migrations of thermal water can be obtained from hydrochemical compositions and environmental isotopes, which provides the basis for determining geochemical characteristics, such as hydrochemical type, genesis, and stage of water–rock reactions (Tiwari et al., 2020; Lai et al., 2021; Sasaki et al., 2021; Song et al., 2021; Su et al., 2021; Verma et al., 2021; Zhang et al., 2021; Duan et al., 2022).

The Jiaodong Peninsula, Shandong Province, eastern China, is located in the eastern part of the Penglai–Weihai fault zone with extensive distributions of metamorphic rocks and granites that have relatively high terrestrial heat flow values. Hot springs are widely distributed in the Jiaodong Peninsula (Jin et al., 2000). The Hongshuilantang Hot Spring is located in the eastern part of the Jiaodong Peninsula, which is a continental margin region of the Middle-Cenozoic crustal tectonic activity zone (Luan and Li, 1993; Jin et al., 2000; Zhou et al., 2002). A great number of moderate-to-strong earthquake swarms have occurred in the vicinity of these areas (Chen et al., 2006; Gu et al., 2020); therefore, Hongshuilantang Hot Spring has been explored as a potential seismic monitoring well by the local earthquake administration in order to capture valuable information related to earthquake precursors. A total of 7420 earthquakes with magnitude >1.0 occurred during the Rushan earthquake swarm from 1 October 2013 to 30 June 2015; the strongest earthquake was M_L 5.0 on 22 May 2015. Earthquakes caused cracks in some houses in local rural areas and had a great impact on the residents of Rushan city. During the Rushan earthquake swarm, the water temperature of Hongshuilantang Hot Spring appeared to decrease, so it is very important to study the relationship between earthquake swarm and water temperature. Due to the relatively abundant hot springs and frequent seismic activities in this region, it is an ideal site for research on the relationship between deep geofluids and earthquakes. Much research on the geochemistry of hot springs for the purposes of geothermal development has been carried out in the study area and its surroundings (Luan and Li, 1993; Shangguang et al., 1998; Jin et al., 2000; Wang et al., 2011). However, few studies on hot spring geochemistry have been carried out on seismic monitoring and forecasting. In this paper, the anomalies in water temperatures in the hot spring during the period of the Rushan earthquake swarm were analyzed, and possible relationships between temperature changes in the Hongshuilantang Hot Spring and the Rushan earthquake swarm were discussed together with background information on the geological structure. Combined with hydrochemical compositions, environmental isotopes, and geological and geomorphological investigations, a model map of the genesis of the hot spring was built. The results of this paper provide an important reference for exploring the genesis and earthquake precursor anomalies of geothermal wells and hot springs in other areas.

Settings

Geological settings

The Jiaodong Peninsula, with its many northeast-trending tectonic faults, is located in the northeastern part of the North China Block. It is not only an area with frequent moderate-to-strong earthquakes in the North China Earthquake Zone but also a continental margin zone exhibiting Middle-Cenozoic crustal tectonic activities (Figure 1). The Tanlu fault zone, a NE-trending deep fault zone running through the western part of the Jiaodong Peninsula in eastern China, crosses the Bohai Sea in the north, connects to the lower Liaohe fault zone, and ends at the Yangtze River in the south. The main tectonic evolution pattern of the Tanlu fault zone in recent years has largely comprised compressional activity with right-sided strike–slip characteristics (Pan et al., 2015; Qu et al., 2021). The largest earthquake along the Tanlu fault zone was the 1668 Tancheng 8.5 earthquake. The Penglai–Weihai fault zone, an NW-trending deep fault, is located in the northern part of the Jiaodong Peninsula and controls the distribution of seismic activities (Chen et al., 2006; Zhu G.et al., 2018; Gu et al., 2020). The western segment of the Penglai–Weihai fault zone was active in the late Pleistocene, and the eastern part of it was active in the mid-Pleistocene with no late-Pleistocene offset found. It is considered that the intersection of the Penglai–Weihai fault zone and the NE-striking branch faults of the Tanlu fault zone is the epicenter for medium-to-strong earthquakes, such as the Weihai M6 and the Bohai M7 (Figure 2B, Wang et al., 2006).

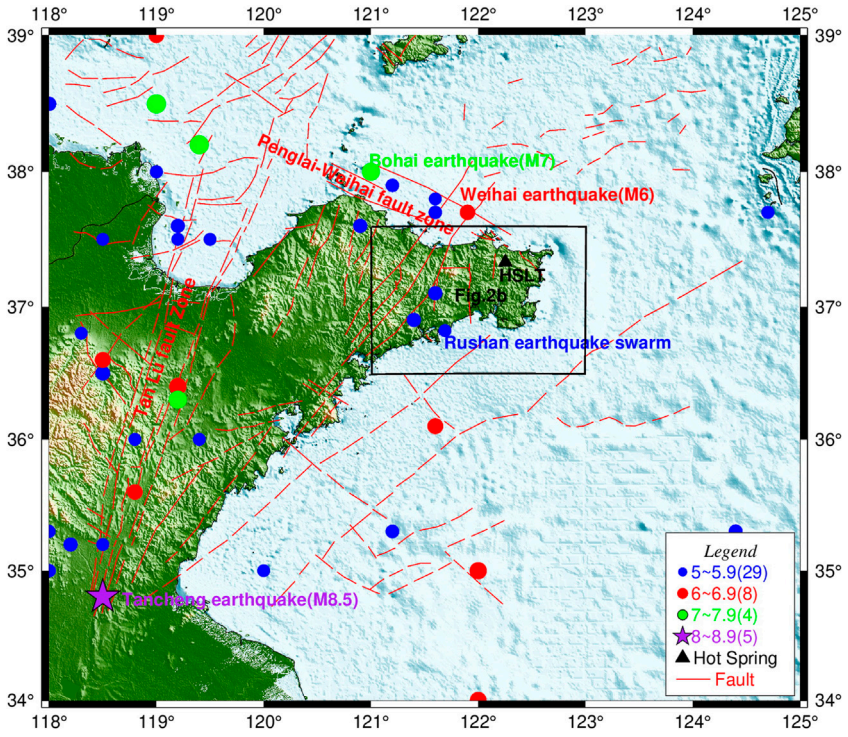

FIGURE 1
Seismotectonic settings of the Hongshuilantang Hot Spring in Jiaodong Peninsula, China. (Data of faults and earthquakes are from Chao et al., 1997).

The NE-trending fault zone in the study area includes the Wulian–Yantai fault zone, a northern boundary of the Sulu orogenic belt, and the Muping–Jimo fault zone, an important NE-oriented fracture (Zhou et al., 2002).

Hongshuilantang Hot Spring, on the east side of the Qilitang–Hengshan fault and close to the Muping–Jimo fault zone, is located in the eastern part of the Jiaodong Peninsula (Luan and Li, 1993; Jin et al., 2000; Zhou et al., 2002). (Figure 2A). The NW-trending Qilitang–Hengshan fault (F1) and the three inferred faults (F2, F3, and F4) may control the development of the Hongshuilantang Hot Spring.

Climatic settings

The hot spring explored in this study is located in the northeast of Shandong Province in northern China (Figure 1). It has a marine monsoon climate, with an average annual precipitation of 740 mm and an average annual temperature of about 12.0°C. Because of the influence of its land and sea location, topography, and other factors, there is more precipitation in summer. As it is surrounded by the sea on three sides and traversed by mountains from east to west, there is a large amount of strong convective weather and heavy snowfall in winter. The amount of precipitation in spring (from March to May), summer (from June to August), autumn (from September to November), and winter (from December to February) accounts for 15%, 53%, 25%, and 7% of total annual precipitation, respectively (Liu, 2021).

Methods and data

Hydrochemical characteristics and δD and $\delta^{18}O$ stable isotopes

To determine the genesis of water temperature anomalies, water samples were collected from the Hongshuilantang Hot Spring in March 2017 and June 2020. Chemical ion concentrations and δD and $\delta^{18}O$ stable isotope compositions of water samples were measured simultaneously. High-density polyethylene bottles with a 50 ml capacity were used as sample containers. Before sampling, the bottles were rinsed three times with the water samples, and at least three bottles of each water sample were collected for analysis. The bottles were filled with water samples, making sure there were no air bubbles, and the bottle mouths were sealed with a sealing film as quickly as possible. The chemical ion concentrations and δD and $\delta^{18}O$

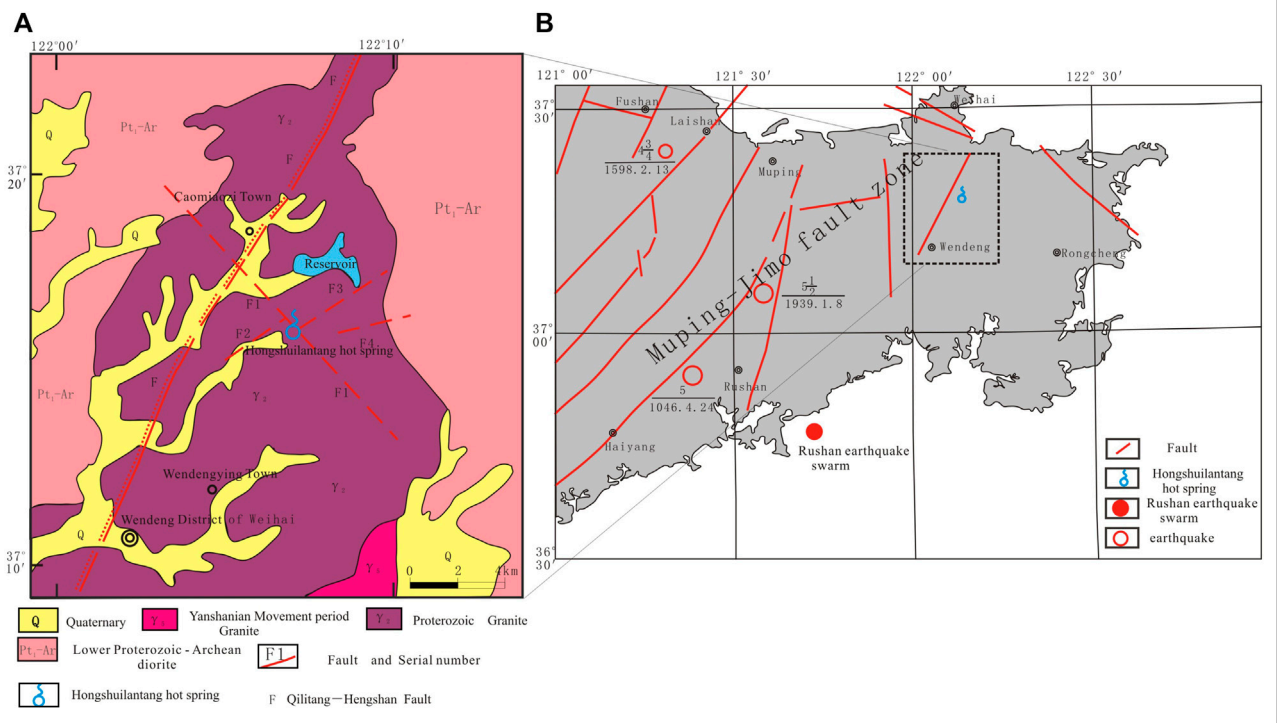

FIGURE 2
Geological settings and regional location of Hongshuilantang Hot Spring. **(A)** Geological settings; **(B)** regional location.

stable isotope compositions were measured in the Underground Fluid Dynamics Laboratory Unit, Key Laboratory of Crustal Dynamics of the China Earthquake Administration. Volumetric methods and CIC-200 ion chromatography were used for hydrochemistry analysis. δD and $\delta^{18}O$ stable isotopes were measured with an LGR 912-0008 hydrogen–oxygen stable isotope analyzer calibrated with water standards GBW04458, GBW04459, and GBW04460.

Long-term observation of water temperature

Before seismological observations were begun, the Hongshuilantang Hot Spring was an artesian well. The hot spring cannot flow on its own because of the decrease in the water table. However, when pumped, the hot spring can flow on its own. At present, water from the hot spring is mainly used for freshwater aquaculture by local residents. The Hongshuilantang Hot Spring is a seismic observation well belonging to the Weihai Earthquake Monitoring Center. The station observer uses a thermometer to measure and record the water temperature of the hot spring once a day. Temperature observations began in 2001, meaning we have data covering 21 years.

Thermometry

In this study, Na/K, K/Mg, and SiO_2 thermometries were selected to calculate the temperature of thermal reservoirs (Jiang et al., 2022).

Na/K thermometry used the following formula (Tian, 2012; Shi et al., 2019; Jiang et al., 2022):

$$t = \frac{933}{\left(\lg\frac{C1}{C2} + 0.933\right)} - 273.15. \quad (1)$$

K/Mg thermometry used the following formula (Tian, 2012; Jiang et al., 2022):

$$t = \frac{4418}{\left(13.95 - \lg\frac{C2}{C3}\right)} - 273.15. \quad (2)$$

Silica thermometry used the following formula (Tian, 2012; Jiang et al., 2022; Shi et al., 2022):

$$t = \frac{1522}{\left(5.75 - \lg C\right)} - 273.15 \quad (3)$$

where *C* is the concentration of SiO_2 in thermal waters, *C1* is the concentration of Na^+, *C2* is the concentration of K^+, and *C3* is the concentration of Mg^{2+}.

TABLE 1 Hydrochemistry characteristics of the Hongshuilantang Hot Spring in Jiaodong Peninsula.

No.	T °C	K^+ mg·L^{-1}	Na^+ mg·L^{-1}	Ca^{2+} mg·L^{-1}	Mg^{2+} mg·L^{-1}	Cl^- mg·L^{-1}	SO_4^{2-} mg·L^{-1}	HCO_3^- mg·L^{-1}	Date	Data source
1	63	287.96		25.05	2.33	177.76	176.58	323.77	1994	Jin et al. (2000)
2	76	19	222	24	2.4	56	230	329	2007	Tian (2012); Wang et al. (2011)
3	73	5.77	151.27	10.92	n.d.	52.98	102.10	258.41	2017	This study
4	74	12.7	161.74	23.55	1.4	11.93	114.06	284.745	2020	

"n.d." denotes that no data were collected.

TABLE 2 δD and $\delta^{18}O$ stable isotope characteristics of different waters in Weihai city.

No.	Type of water	δD	δ^2O	Data	Data source
a	Rainfall	−105	−14	1992	Tian (2012)
b	Seawater	−13.8	−2.34	2006	
c	Stream water	−52.63	−7.98	2006	
d		−56.70	−8.01	2007	
e	Hongshuilantang Hot Spring	−59.00	−8.20	2012	Tian (2015)
f		−55.80	−7.47	2017	This study
g		−59.72	−8.52	2020	

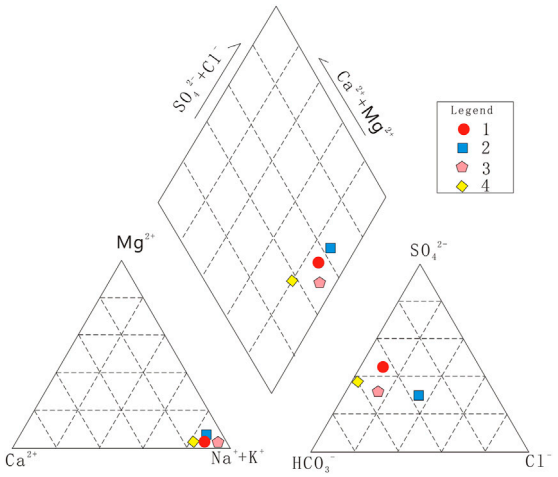

FIGURE 3
Piper diagram of waters from Hongshuilantang Hot Spring. The numbers in the figure correspond to those in Table 1.

Estimation of circulation depth

The circulation depth of the Hongshuilantang Hot Spring is given by the following formula (Jin et al., 2000; Tian, 2012):

$$H = \frac{t - t_0}{r} + h \quad (4)$$

where H is the circulation depth of hot spring water (m), r is the geothermal gradient, t is the temperature of the reservoir, t_0 is the average annual temperature of the recharge area, and h is the depth of the local normal temperature zone over a period of many years.

Results

The hydrochemical characteristics and the δD and $\delta^{18}O$ stable isotope compositions are shown in Table 1 and Table 2. To determine the genesis of the Hongshuilantang Hot Spring, we used data from other published studies (Jin et al., 2000; Wang et al., 2011; Tian, 2012; Tian, 2015).

Chemical type of hot spring water

Based on data measured in this paper and collected from published studies (Jin et al., 2000; Tian, 2012), a Piper diagram was plotted (Figure 3). The spring water was classified as an HCO_3·SO_4-Na type. The content of HCO_3^- in hot springs is relatively high; therefore, we hypothesized that the recharge source may be from surface water. The concentrations of Cl^- and SO_4^{2-} also have implied meanings for the depth of groundwater circulation, retention time, and recharge path.

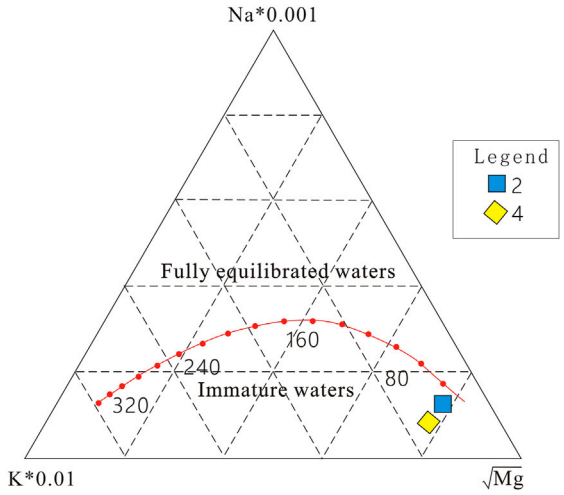

FIGURE 4
Na–K–Mg diagram of the Hongshuilantang Hot Spring. The numbers in the figure correspond to those in Table 1.

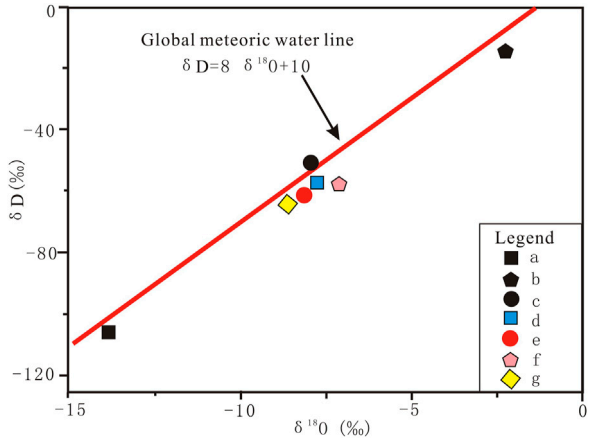

FIGURE 5
Relationships between δD and $\delta^{18}O$ values of the hot spring and the global meteoric water line (GMWL). The numbers in the diagram correspond to those in Table 2 and the GMWL is from Craig (1961).

Water–rock reaction characteristics

The Na–K–Mg diagram shows that water samples from the studied hot spring are near the Mg-end (Figure 4) and the equilibrium line, which indicates that the hot spring waters can be classified as immature. The water–rock interactions have not yet reached the state of ion equilibrium, indicating that the water is from a shallow, cold pool.

δD and $\delta^{18}O$ stable isotope characteristics

Environmental isotope analysis has been widely used in hydrogeological research. Measuring hydrogen and oxygen isotope levels is an effective method for ascertaining the origin and migration of water and other fluids circulating within the Earth (Tiwari et al., 2020; Li et al., 2021; Sasaki et al., 2021; Duan et al., 2022). Evaporation and precipitation can result in significant discrepancies in the isotopic composition of the mass of water molecules (Li et al., 2021; Duan et al., 2022). The δD and $\delta^{18}O$ values of freshwater and seawater in Weihai vary significantly from place to place, while the isotope levels in the river and thermal water were similar (Table 2).

Based on data obtained in this study and from other published work by Tian (2012) and Tian (2015), the values of the stable isotopes, δD and $\delta^{18}O$, in the hot spring water fell into the GMWL, and a rightward drift occurred to some extent (Figure 5). The GMWL could reflect the hydrogen and oxygen isotopic composition of precipitation in many marine monsoon climate areas. The nearer the origin is to the coastal areas, the closer its δD and $\delta^{18}O$ stable isotope values are to the GMWL; therefore, the GMWL was used as a reference for the δD and $\delta^{18}O$ stable isotope characteristics in the study (Craig, 1961; Li et al., 2011). There may be two reasons for the rightward drift of δD and $\delta^{18}O$ stable isotope compositions seen in the δD and $\delta^{18}O$ value graph. One is that Rayleigh fractionation occurs in arid and semi-arid areas of low precipitation and strong evaporation, which leads to an increase in $\delta^{18}O$ values. The other is that water–rock reactions between groundwater and siliceous or carbonate rocks cause oxygen drift and equilibrium exchange between hydrogen and oxygen isotopes. Combined climatic and geological conditions around the studied hot spring revealed that water–rock interactions in deep circulation systems may be the main reason for the appearance of $\delta^{18}O$ drift. To sum up, the main recharge resources of the Hongshuilantang Hot Springs are meteoric water, surface water, and groundwater.

Circulation depth of hot spring water

Na/K thermometries of thermal waters from the hot spring were 193°C and 185°C. K/Mg thermometries were 66°C and 68°C. Silica thermometry was 135°C (Shi et al., 2019; Shi et al., 2022). Since Na^+ and K^+ ions do not reach equilibrium easily and water–rock interactions were still in process, the temperatures calculated by the Na/K temperature scale were higher than the true values; therefore, silica thermometry was used to estimate the thermal reservoir temperatures, which should be closer to the actual value (Shi et al., 2019; Shi et al., 2022). In this study, formula (4) was used to estimate the circulation depth in the Hongshuilantang Hot Spring (Jin et al., 2000; Tian, 2012). In the equation, r is the geothermal gradient (4.4°C/100 m close to Huangxian basin in Jiaodong Peninsula), t is the selected silica

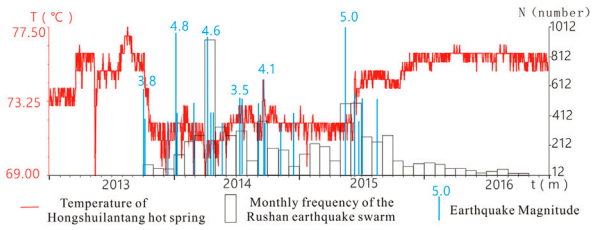

FIGURE 6
Comparison chart of daily temperature variations of the Hongshuilantang Hot Spring and monthly frequency of the Rushan earthquake swarm from 1 Jan 2013 to 31 Dec 2016.

thermometry of 135°C, and t_0 is the annual average temperature in the recharge areas; adopting 12.1°C, h is the depth of the local normal temperature zone for multiple years, which is equal to 25 m. Based on the aforementioned assumptions, the circulation depth was calculated to be about 2793 m.

Response to earthquakes

The water temperatures in the hot spring dropped from 76 to 70°C between October 2013 and June 2015, representing a maximum decrease of 6°C. After June 2015, the water temperature gradually began to increase, returning to September 2013 values by November 2015, when the whole water temperature oscillation process was over (Figure 6). The Rushan earthquake swarm was accompanied by continuous aftershocks from the M_L 3.2 earthquake on 1 October 2013. As of 30 June 2015, Rushan had experienced 5997 earthquakes with magnitudes of $0.0 \leq M_L \leq 0.9$, 1216 earthquakes with a magnitude of $1.0 \leq M_L \leq 1.9$, 182 earthquakes with a magnitude of $2.0 \leq M_L \leq 2.9$, 21 earthquakes with a magnitude of $3.0 \leq M_L \leq 3.9$, three earthquakes with a magnitude of $4.0 \leq M_L \leq 4.9$, and one earthquake with a magnitude of $M_L \geq 5.0$. The M_L 5.0 earthquake hit Rushan on 22 May 2015.

Discussion

Genesis model of the Hongshuilantang Hot Spring

Considering the hydrochemical characteristics, the Na–K–Mg diagram, and the δD and $\delta^{18}O$ stable isotope levels, we concluded that the Hongshuilantang Hot Spring possesses properties of both shallow and deep circulation water. The reason for this complex origin is that the chemical composition of hot spring water is closely related to burial conditions, surrounding rock lithology, recharge conditions of the hot spring, etc., (Shangguang et al., 1998; Jin et al., 2000). Combining the results of the geological and geomorphological investigations, a genesis model map of the Hongshuilantang Hot Spring was created (Figure 7), illustrating that it is not only affected by shallow meteoric water but also by deep circulation water.

Relative motion of the blocks in the vicinity

Based on continuous GPS observation data, Zhu et al. (2018) analyzed the relative motion state of the block continuum on both sides of the Tanlu fault zone after the 2011 Mw 9.0 earthquake in Japan through a sliding block model. The study suggested that the occurrence of the Rushan earthquake swarm may be related to the local regional stress adjustment promoted by the relative motion of the blocks on each side of the Tanlu fault zone. The enhanced relative motion from September 2013 to September 2015, which is vertical to the deep fault zone, promoted the release of the concentrated energy by means of the Rushan earthquake swarm. The vertical motion of the blocks on each side of the Tanlu Fault Zone has decelerated since February 2016, and at the same time, the activity of the Rushan earthquake swarm was also significantly weakened (Zhu C.et al., 2018). The epicenter of the Rushan earthquake swarm and the Hongshuilantang Hot Spring are both located in the Muping–Iimo Fault Zone on the eastern side of the Tanlu Fault Zone and belong to the Muping–Iimo Fault Zone, implying that they should be affected by the same stress conditions. Local stress adjustments also contributed to the variations in pore pressure of ground fluids, which affected the water temperature of the Hongshuilantang Hot Spring (Igarashi and Wakita, 1990; Lai et al., 2021).

Relationships between water temperature anomalies and the Rushan earthquake swarm

As shown in Figure 3, the water temperature of the hot spring declined from 76°C to approximately 70°C, with a maximum drop of 7°C after the Rushan M_L3.8 earthquake on 1 October 2013. After the Rushan M_L 5.0 earthquake on 22 May 2015, the number of earthquakes showed a decreasing trend. The data indicated that the water temperature began to increase from June 2015 and slowly returned to 76°C. As of the end of March 2017, the water temperature had remained stable. There appeared to be a temporal correlation between the Rushan earthquake swarm and the temperature drop in the hot spring. In addition, there was a close relationship between the monthly earthquake frequency during the swarm and the

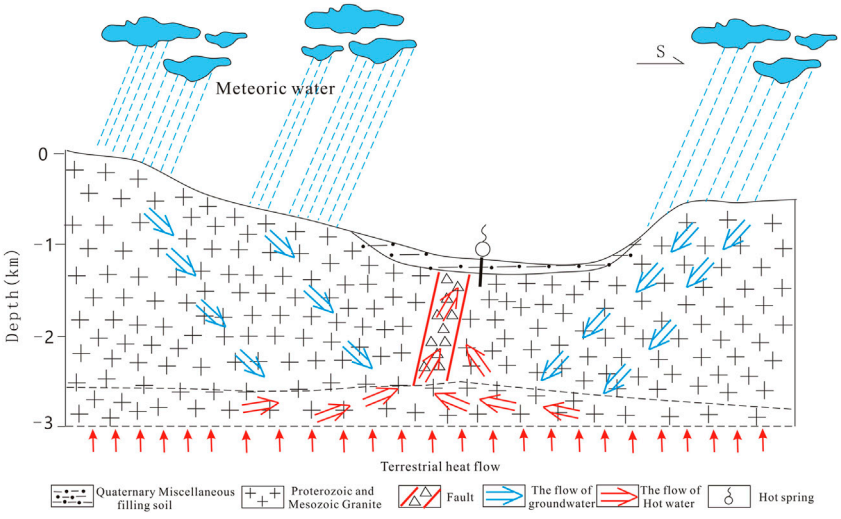

FIGURE 7
Genesis model of the Hongshuilantang Hot Spring.

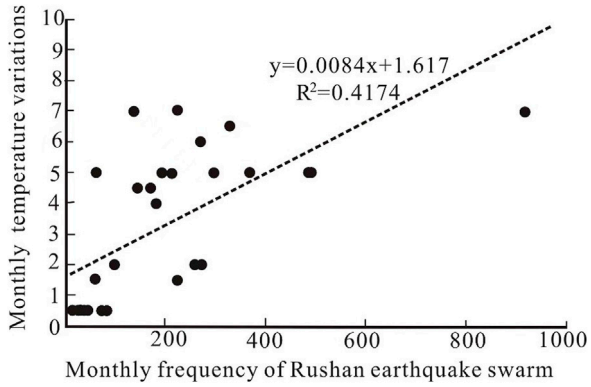

FIGURE 8
Correlation of monthly temperature variations of the Hongshuilantang Hot Spring and monthly frequencies of the Rushan earthquake swarm.

decrease in water temperature. When earthquakes of M_L 4.0 or greater magnitude were occurring in the Rushan earthquake swarm, water temperatures dropped significantly. For example, in January and April 2014, water temperatures of Hongshuilantang Hot Spring dropped by 7°C. The M_L 4.8 earthquake on 7 January 2014 and the M_L 4.6 earthquake on 4 April 2014 occurred during this period, and the highest monthly frequency of 917 earthquakes was recorded during the Rushan earthquake swarm in April 2014. The highest monthly frequency of earthquakes corresponded to the largest drop in water temperature (Figures 6, 8).

The epicenter of the Rushan earthquake swarm and the Hongshuilantang Hot Spring were located in the Jiaodong shield of the Jiaoliao fault block. According to the spatial distribution of local seismic faults, the Hongshuilantang Hot Spring and the epicenter of the Rushan earthquake swarm were both located in the Muping–Jimo fault zone (Figure 2B), suggesting a certain genesis relationship in seismic structure.

The results of the on-site investigation and verification showed no obvious changes in the surrounding observation conditions; therefore, the impact of environmental disturbances on the hot spring water temperature could be ignored. A large number of early Middle Pleistocene and pre-quaternary faults are scattered in the Jiaodong Peninsula. The Weihai *M*6.0 earthquake, which was the strongest earthquake in the history of the area, occurred in the northwest coastal part in 1948. Earthquakes in the Jiaodong Peninsula and its adjacent areas often appeared in the form of earthquake swarms, and the process of energy release was relatively slow (Zhou et al., 2002). The stress changes in the crustal medium and the water circulation in hot springs and aquifers resulted in water temperature variations due to stress increase or unloading. Thus, fluctuations of groundwater temperature could be caused by seepage from hot spring and aquifer systems (Yu and Che, 1997; Sun and Liu 2006). A study of the Xiangcheng Hot Spring also showed that stress changes could lead to connections between two adjacent hot spring aquifers, resulting in variations of water temperature (Ma, 2016).

Conclusion

1) The analysis of water quality, Na–K–Mg thermometry, and δD and $\delta^{18}O$ stable isotope levels shows that Hongshuilantang Hot Spring is not only affected by shallow meteoric water but also by deep circulating water.
2) Both the Hongshuilantang Hot Spring and the epicenter of the Rushan earthquake swarm are located in the Muping–Jimo fault zone, suggesting that they have a certain genesis relationship in seismic structure.
3) The stress increased slowly before the occurrence of the Rushan earthquake swarm, which was a continuously increasing process that changed monotonously. During this process, there were no obvious changes in water temperature caused by the Hongshuilantang Hot Spring; when the Rushan earthquake swarm occurred, the stress began to be released. When a free water surface appeared in the aquifer, the water temperatures of the hot spring decreased owing to the seepage of low-temperature underwater into the upper layer of the aquifer under the action of seismic stress unloading. After stress release, the water temperature gradually returned to normal.

Data availability statement

The original contributions presented in the study are included in the article/Supplementary Material; further inquiries can be directed to the corresponding author.

Author contributions

GD: methodology, data curation, and writing—original draft preparation. SS: methodology, data curation, supervision, conceptualization, writing—review & editing. XC: writing and reviewing. HR: methodology, data curation, validation, writing— review and editing. ZH: writing— review and editing. XZ: editing.

Funding

This study was jointly funded by the National Natural Science Foundation of China (No. 42277196), the National Natural Science Foundation of China (No. 41877299), the National Science Foundation of China (No. 42073063), the Program of Monitoring, Forecasting and Scientific Research, China Earthquake Administration (3JH-202001057), the Basic Scientific Research Program of Shandong Earthquake Agency (No. YB2220), the National Key Research and Development Program of China (No. 2019YFC1509203), and the Basic Science Research Plan of the Institute of Earthquake Science, China Earthquake Administration (No. 2020IEF0704). This work is a contribution to IGCP Project 724.

Acknowledgments

Some figures were made using Generic Mapping Tools (https://forum.genericmapping-tools.org/, last accessed March 2020) (Wessel et al., 2013).

Conflict of interest

The authors declare that the research was conducted in the absence of any commercial or financial relationships that could be construed as a potential conflict of interest.

Publisher's note

References

Chao, H., Wang, Q., and Li, J., 1997. Seismotectonic map of Shandong Province, new tectonic map of Shandong Province and instructions, China, Press, S.M, 100–132.

Che, Y., He, A., and Yu, J. (2014). Mechanisms of water-heat dynamics and earth-heat dynamics of well water temperature micro-behavior. *Acta Seismol. sin.* 36, 106–117. doi:10.3969/j.issn.0253-3782.2014.01.009

Che, Y., Yu, J., Chen, Q., Deng, Y., and Li, J. (2016). A thought on the establishment of the fault gas monitoring network-Further discussion on searching new approaches to the short/imminent earthquake prediction. *Recent Dev. World Seismol.* 12. doi:10.3969/j.issn.0235-4975.2016.12.004

Chen, L., Zheng, T., and Xu, W. (2006). A thinned lithospheric image of the Tanlu Fault Zone, eastern China: Constructed from wave equation based receiver function migration. *J. Geophys. Res.* 111, B09312. doi:10.1029/2005jb003974

Claesson, L., Skelton, A., Graham, C., Dietl, C., Mörth, M., Torssander, P., et al. (2004). Hydrogeochemical changes before and after a major earthquake. *Geol.* 32, 641–644. doi:10.1130/g20542.1

Craig, H. (1961). Isotopic variations in meteoric waters. *Science* 133, 1702–1703. doi:10.1126/science.133.3465.1702

Duan, R., Li, P., Wang, L., He, X., and Zhang, L. (2022). Hydrochemical characteristics, hydrochemical processes and recharge sources of the geothermal systems in Lanzhou City, northwestern China. *Urban Clim.* 43, 101152. doi:10.1016/j.uclim.2022.101152

Favara, R., Grassa, F., Inguaggiato, S., and Valenza, M. (2001). Hydrogeochemistry and stable isotopes of thermal springs: Earthquake-related chemical changes along belice fault (western sicily). *Appl. Geochem.* 16, 1–17. doi:10.1016/S0883-2927(00)00015-9

Gao, X., Liang, H., Wang, H., Zheng, L., Li, J., Zhao, C., et al. (2015). Origin of the mud volcano in northern Tianshan constrained by geochemical investigation. *Seismol. Geol.* 4, 1215–1224. doi:10.3969/j.issn.0253-4967.2015.04.021

Gu, Q., Ding, Z., Kang, Q., and Li, D. (2020). Group velocity tomography of Rayleigh wave in the middle-southern segment of the Tan-Lu fault zone and adjacent regions using ambient seismic noise. *Chin. J. Geophys. Chin.* 63, 1505–1522. doi:10.6038/cjg2020N0117

Igarashi, G., and Wakita, H. (1990). Groundwater radon anomalies associated with earthquakes. *Tectonophysics* 180, 237–254. doi:10.1016/0040-1951(90)90311-U

Jiang, B., Li, Z., and Yu, C. (2022). Application of geochemical temperature scale in jiyuan wulongkou geothermal area. *J. Hebei Geo Univ.* 45, 83–88. doi:10.13937/j.cnki.hbdzdxxb.2022.01.013

Jin, B., Zhang, Y., and Luan, G. (2000). Geothermal characteristics of warm spring in Jiaodong peninsula. *J. Xi'an Eng. Univ.* 1, 54–58. doi:10.3969/j.issn.1672-6561.2000.01.012

Lai, G., Jiang, C., Wang, W., Han, L., and Deng, S. (2021). Correlation between the water temperature and water level data at the Lijiang well in Yunnan, China, and its implication for local earthquake prediction. *Eur. Phys. J. Spec. Top.* 230, 275–285. doi:10.1140/epjst/e2020-000255-3

Li, Y., Zhang, M., Wang, S., Li, Z., and Wang, F. (2011). Progress of the research of stable isotope in precipitation in China:A review. *J. Glaciol. Geocryol.* 33, 624–633.

Li, B., Shi, Z., Wang, G., and Liu, C. (2019). Earthquake-related hydrochemical changes in thermal springs in the Xianshuihe Fault zone, Western China. *J. Hydrology* 579, 124175. doi:10.1016/j.jhydrol.2019.124175

Li, Y., Li, P., Cui, X., and He, S. (2021). Groundwater quality, health risk, and major influencing factors in the lower Beiluo River watershed of northwest China. *Hum. Ecol. Risk Assess. Int. J.* 27, 1987–2013. doi:10.1080/10807039.2021.1940834

Liu, Y., Ren, H., Zhang, L., Fu, H., Sun, X., He, D., et al. (2015). Undergrund fluied anomalies and the precursor mechanisms of the Ludian Ms6.5 earthquake. *Seismol. Geol.* 1, 307–318. doi:10.3969/j.issn.0253-4967.2015.01.024

Liu, H. (2021). Analysis of hydrogeological conditions in Weihai area of Shandong province. *World Non-Ferrous Met.* 567, 217–218.

Luan, G., and Li, G. (1993). The geologic geothermal background and spring-controlling structure of Jiaodong warm springs. *J. ocean Univ. Qingdao* 1, 75–82. doi:10.16441/j.cnki.hdxb.1993.01.006

Ma, Y. (2016). Earthquake-related temperature changes in two neighboring hot springs at Xiangcheng, China. *Geofluids* 16, 434–439. doi:10.1111/gfl.12161

Ma, Y., Huang, F., Xue, Y., and Wang, B. (2015). Statistical analysis of long-term observation data of water temperature in springs and wells. *Technol. Earthq. Disaster Prev.* 2, 367–377. doi:10.11899/zzfy20150217

Miyakoshi, A., Taniguchi, M., Ide, K., Kagabu, M., Hosono, T., and Shimada, J. (2020). Identification of changes in subsurface temperature and groundwater flow after the 2016 Kumamoto earthquake using long-term well temperature–depth profiles. *J. Hydrology* 582, 124530. doi:10.1016/j.jhydrol.2019.124530

Mogi, K., Mochizuki, H., and Kurokawa, Y. (1989). Temperature changes in an artesian spring at Usami in the Izu Peninsula (Japan) and their relation to earthquakes. *Tectonophysics* 159, 95–108. doi:10.1016/0040-1951(89)90172-8

Pan, S., Wang, F., Zheng, Y., Duan, Y., Liu, L., Deng, X., et al. (2015). Crustal velocity structure beneath Jiaodong Peninsula and its tectonic implications. *Chin. J. Geophys.* 9, 3251–3263. doi:10.6038/cjg20150920

Pope, E., Bird, D., and Arnórsson, S. (2014). Stable isotopes of hydrothermal minerals as tracers for geothermal fluids in Iceland. *Geothermics* 49, 99–110. doi:10.1016/j.geothermics.2013.05.005

Qu, J., Gao, S. S., Wang, C., Liu, K. H., Zhou, S., Yang, Y., et al. (2021). Crustal P-wave velocity structure and earthquake distribution in the Jiaodong Peninsula, China. *Tectonophysics* 814, 228973. doi:10.1016/j.tecto.2021.228973

Sasaki, K., Morita, J., Iwaki, C., and Ueda, A. (2021). Geochemical evaluation of geothermal resources in Toyama Prefecture, Japan, based on the chemical and isotopic characteristics of hot spring waters. *Geothermics* 93, 102071. doi:10.1016/j.geothermics.2021.102071

Shangguang, Z., Du, J., Zang, W., Wang, J., Kong, L., and Gao, S. (1998). Modern geothermal fluid geochemistry of Tanlu fault zone and Jiaoliao fault block area. *Sci. China (series D; earth Sci.* 28 (1), 23–29. doi:10.1088/0256-307X/15/11/025

Shi, M., Kang, F., Zhang, J., Gao, S., and Yu, J. (2022). Discussion on the deep heat flow diversion-acculturation between uplift and depression in different tectonic units in the Jiaodong Peninsula. *Acta Geol. Sin.* 5, 1594–1605. doi:10.19762/j.cnki.dizhixuebao.2020063

Shi, M., Zhang, J., Yin, T., Yang, N., and Jiang, H. (2019). Hydrochemistry characteristic analysis of low-medium temperature convective geothermal resources in Jiaodong Peninsula. *Acta Geol. Sin.* 1, 138–148. doi:10.19762/j.cnki.dizhixuebao.2019221

Skelton, A., Andrén, M., Kristmannsdóttir, H., Stockmann, G., Mrth, C.-M., Sveinbjrnsdóttir, r., et al. (2014). Changes in groundwater chemistry before two consecutive earthquakes in Iceland. *Nat. Geosci.* 7, 752–756. doi:10.1038/NGEO2250

Song, D. F., Chen, Y., Wang, T. G., Li, M. J., and Li, P. (2021). Organic geochemical compositions of mesoproterozoic source rocks in the yanliao rift, northern China. *Mar. Petroleum Geol.* 123, 104740–104820. doi:10.1016/j.marpetgeo.2020.104740

Su, S., Chen, Q., Zou, C., Yan, B., Du, G., and Feng, E. (2021). Hydrogeochemical characteristics and Genesis of seismic observation wells in Shandong Province, China. *Arab. J. Geosci.* 14, 2398. doi:10.1007/s12517-021-08774-w

Sun, X., and Liu, Y. (2006). Summaries of the micro temperature variations of underground water caused by loading stresses. *Recent Dev. world Seismol.* 7, 17–26.

Tian, S. (2012). *The study on the mechanism of structural geothermal fields of Weihai*. China: Jinan university.

Tian, Y. (2015). Features of hydrogen and oxygen isotopes and the make-up source for geothermal water in east Shandong geothermal area. *Geol. Sci. Technol. Inf.* 34, 182–185.

Tiwari, S., Gupta, A., and Asthana, A. (2020). Evaluating CO2 flux and recharge source in geothermal springs, garhwal himalaya, India: Stable isotope systematics and geochemical proxies. *Environ. Sci. Pollut. Res.* 27, 14818–14835. doi:10.1007/s11356-020-07922-1

Verma, A., Tiwari, S., Kumar, A., Sain, K., Rai, S., and Kumari, S. (2021). Assessment of water recharge source of geothermal systems in Garhwal Himalaya (India). *Arab. J. Geosci.* 14, 2341. doi:10.1007/s12517-021-08679-8

Wang, Z., Deng, Q., Chao, H., Du, X., Shi, R., Sun, Z., et al. (2006). Shallow depth sonic reflection profiling studies on the active Penglai Weihai fault zone offshore of the northern Shandong peninsula. *Chin. J. Of Geophys.* 4, 1092–1101. doi:10.1002/cjg2.920

Wang, Y., Ma, X. X., and Shan, W. (2011). Study on geological characteristics and origin mechanism of Hongshuilantang hot spring in Weihai city. *Land Resour. Shandong Prov.* 2, 16–19+24.

Wessel, P., Smith, W., Scharroo, R., Luis, J., and Wobbe, F. (2013). Generic mapping tools: Improved version released. *Eos Trans. AGU.* 45, 409–410. doi:10.1002/2013eo450001

Yu, J., and Che, Y. (1997). Preliminary study on hydrodynamic mechanism of microbehavior of water temperature in well. *Earthquake* 4, 389–396.

Zhang, L., Guo, L., Zhou, X., Yang, Y., Shi, D., and Liu, Y. (2021). Temporal variations in stable isotopes and synchronous earthquake-related changes in hot springs. *J. Hydrology* 599, 126316. doi:10.1016/j.jhydrol.2021.126316

Zhou, B., Ran, Y., Huan, W., and Ran, H. (2002). Late Pleistocene surface faulting and the maximum potential earthquake on the Dongshilangou segment of the Haiyang fault, Shandong province. *Seismol. Geol.* 2, 159–166. doi:10.3969/j.issn.0253-4967.2002.02

Zhu, C., Gan, W., Li, J., Jia, Y., Wang, Q., and Yin, H. (2018). Relative motion between the two blocks on either side of the Yishu fault zone after the 2011 Japan MW9.0 earthquake and its effect on seismic activity. *Chin. J. Geophys. (in Chinese)* 61, 988–999. doi:10.6038/cjg2018K0687

Zhu, G., Liu, C., Gu, C., Zhang, S., Li, Y. J., Su, N., et al. (2018). Oceanic plate subduction history in the Western pacific ocean: Constraint from late mesozoic evolution of the tan-Lu Fault Zone. *Sci. China Earth Sci.* 48, 386–405. doi:10.1007/s11430-017-9136-4

frontiers | Frontiers in Earth Science

TYPE Original Research
PUBLISHED 20 January 2023
DOI 10.3389/feart.2022.1106799

OPEN ACCESS

EDITED BY
Qingqiang Meng,
SINOPEC Petroleum Exploration and Production Research Institute, China

REVIEWED BY
Guo Xiaobo,
Xi'an Shiyou University, China
Yiming Yan,
China University of Petroleum (East China), China

*CORRESPONDENCE
Ming Cheng,
chengming@mail.iggcas.ac.cn

SPECIALTY SECTION
This article was submitted to Geochemistry, a section of the journal Frontiers in Earth Science

RECEIVED 24 November 2022
ACCEPTED 27 December 2022
PUBLISHED 20 January 2023

CITATION
Yin J, Gao C, Cheng M, Liang Q, Xue P, Hao S and Zhao Q (2023), TOC interpretation of lithofacies-based categorical regression model: A case study of the Yanchang formation shale in the Ordos basin, NW China.
Front. Earth Sci. 10:1106799.
doi: 10.3389/feart.2022.1106799

TOC interpretation of lithofacies-based categorical regression model: A case study of the Yanchang formation shale in the Ordos basin, NW China

Jintao Yin[1,2], Chao Gao[1,2], Ming Cheng[3]*, Quansheng Liang[1,2], Pei Xue[1,2], Shiyan Hao[1,2] and Qianping Zhao[1,2]

[1]Shaanxi Yanchang Petroleum (Group) Corp Ltd., Xi'an, China, [2]Shaanxi Key Laboratory of Lacustrine Shale Gas Accumulation and Exploitation, Xi'an, China, [3]Institute of Geology and Geophysics, Chinese Academy of Sciences, Beijing, China

In this paper, taking the shale of Chang 7-Chang 9 oil formation in Yanchang Formation in the southeastern Ordos Basin as an example, through the study of shale heterogeneity characteristics, starting from the preprocessing of supervision data set, a logging interpretation method of total organic carbon content (TOC) on the lithofacies-based Categorical regression model (LBCRM) is proposed. It is show that: 1) Based on core observation, and Differences of sedimentation and structure, five lithofacies developed in the Yanchang Formation: shale shale facies, siltstone/ultrafine sandstone facies, tuff facies, argillaceous shale facies with silty lamina and argillaceous shale facies with tuff lamina. 2) The strong heterogeneity of shale makes it difficult to accurately explain the TOC distribution of shale intervals in the application of model-based interpretation methods. The LBCRM interpretation method based on the understanding of shale heterogeneity can effectively reduce the influence of formation factors other than TOC on the prediction accuracy by studying the characteristics of shale heterogeneity and constructing a TOC interpretation model for each lithofacies category. At the same time, the degree of unbalanced distribution of data is reduced, so that the data mining algorithm achieves better prediction effect. 3) The interpretability of lithofacies logging ensures the wellsite application based on the classification and regression model of lithofacies. Compared with the traditional homogeneous regression model, the prediction performance has been greatly improved, TOC segment prediction is more accurate. 4) The LBCRM method based on shale heterogeneity can better understand the reasons for the deviation of the traditional model-based interpretation method. After being combined with the latter, it can make logging data provide more useful information.

KEYWORDS

ordos basin, Yan'an area, lacustrine oil shale, lithofacies classification regression, TOC interpretation model

1 Introduction

Organic matter content is an indispensable basic data for source rock evaluation, shale oil and gas reservoir evaluation and sweet spot prediction. (Curtis, 2002; Passey et al., 2010; Sondergeld et al., 2010; Alfred and Vernik, 2012; Ma, 2015; Altowairqi et al., 2015; Aldrich and seidle, 2018; Guo et al., 2021; Wei et al., 2021; Meng, 2022). Laboratory core test and analysis

technology is the most direct and accurate means to obtain the organic matter content of shale, in which total organic carbon content (TOC) is the most readily available and commonly used characterization index of organic matter content. Restricted by the lack of core data or incomplete coring in most wells, the interpretation of formation TOC with high resolution and high coverage logging data is an important means for rapid, accurate and continuous quantitative evaluation of organic matter content in shale formations (Yu et al., 2017; Wang et al., 2019; Liang et al., 2021; Chan et al., 2022; Meng et al., 2022; Zhao et al., 2022).

At present, a large number of TOC logging interpretation methods, techniques or models have been proposed. These methods can be divided into two categories: model-driven and data-driven (Huang and Williamson, 1996). Model-driven methods include formation density curve method (Schmoker, 1979; Schmoker and Hester, 1981), natural gamma intensity method (Schmoker, 1981; fertl and Chilinger, 1988), I-x method (Dellenbach et al., 1983), ΔlogR and its improved method (Passey et al., 1990; wang et al., 2016; zhao et al., 2017), CARBOLOG (Carpentier et al., 1991), etc. This type of method constructs a statistical relationship between logging response and TOC through specific assumptions (Sondergeld et al., 2010). For example, the formation density curve and the natural gamma intensity method construct the TOC logging interpretation method through the linear volume equation of the logging response (Huang and Williamson, 1996), and the ΔlogR establishes the non-linear relationship between the ΔlogR and the TOC by obtaining the superposition baseline of the porosity curve and the resistivity curve at the pure water-bearing non-hydrocarbon source rock under the premise of the known shale mature section (Passey et al., 1990; 2010).

Huang and Williamson (1996) pointed out that the model-driven method need to determine the key parameter to accurately estimate the organic matter content of the shale section. The above drawbacks restrict the application of model-driven methods in the interpretation of organic matter content and promote the development of data-driven methods (Huang and Williamson, 1996). Different from the model-driven method, the data-driven method can fully explore the statistical relationship between multi-logging response characteristics and TOC, which is more suitable for TOC interpretation of strongly heterogeneous shale (Huang and Williamson, 1996). Currently, a large number of data mining algorithms have been applied to TOC logging interpretation, including multiple linear regression, Gaussian mixture, optimization algorithm, SVM, BP neural network, deep neural network, etc., (Mendelzon and Roksoz, 1985; Huang and Williamson, 1996; Wang et al., 2014; Tan et al., 2015; Yu et al., 2017; Zhu et al., 2020; Zheng et al., 2021; Chan et al., 2022).

In the data-driven TOC interpretation technology, there are two challenges: First, the formation logging response is not only affected by TOC, but also by multi-formation factors such as particle size, mineral composition, element composition, pore development degree, pore fluid properties, etc., resulting in the logging response and organic matter content is not a simple linear relationship (Huang et al., 1996; yang et al., 2004; rezaee et al., 2007). The above characteristics have caused a prominent problem, whether the conventional logging series can provide sufficient features to make the TOC interpretation have high enough accuracy, in other words, in the formation with the same or similar logging response, whether the samples have different TOC values. Chan et al. (2020) showed that the accuracy of TOC interpretation based solely on conventional logging series may not be ideal. The TOC deep learning interpretation model constructed by adding element information to conventional logging series data is significantly better than the results of Mahmoud et al. (2017) that rely solely on conventional logging prediction models (Chan et al., 2020). It can be seen that the simple introduction of more complex machine learning algorithms cannot completely solve the accurate interpretation of TOC. It is also necessary to understand the above problems from the perspective of data characteristics, which is particularly important in shale oil and gas reservoirs with strong heterogeneity of lithology, mineral composition and elemental composition.

Another problem comes from the data mining algorithm itself. In all data-driven TOC interpretation methods, the goal is to minimize the difference between the predicted value and the true value of the expected value (such as MSE and RMSE, etc.) (Huang and Williamson, 1996; Wang et al., 2014; Tan et al., 2015; Yu et al., 2017; Zhu et al., 2020; Zheng et al., 2021; Chan et al., 2022), which is the most direct indicator of learning algorithms in model training and performance verification. However, TOC test samples are often sampled by equidistant or random methods. The strong heterogeneity of shale inevitably causes some TOC numerical interval samples to be more concentrated. The TOC data exhibit skewed distribution with a long tail (Yu et al., 2019; Wang et al., 2012), causing an imbalance in data distribution (Branco et al., 2016). The learning goal of minimizing the expected difference makes the learning algorithm pay more attention to the characteristics of high-frequency distribution samples, resulting in lower prediction accuracy for data with a small number of samples (Branco et al., 2016; 2018). Unfortunately, the TOC interval with low data density may be the focus of shale reservoir research, such as shale sections with high TOC distribution. At present, the application of learning algorithms in imbalanced data is still less involved in regression problems such as TOC logging interpretation (Branco et al., 2016; 2018).

In view of the above problems, this paper takes Yanchang Formation in Ordos Basin as the research object, and proposes a logging interpretation method of organic carbon content based on rock facies classification regression model (LBCRM) from the preprocessing of supervised data sets. This method adds an additional dimension of lithofacies to the TOC-logging response monitoring data set through the study of shale heterogeneity characteristics. The TOC interpretation sub-model based on SVM algorithm is constructed by classification, which effectively reduces the influence of formation factors other than TOC on TOC interpretation accuracy. At the same time, the degree of unbalanced data distribution is reduced, which makes the data mining algorithm achieve better prediction results. XGboost can be used to construct a high-precision rock facies logging identification method, which ensures the availability of rock facies and makes this method have practical application potential. In addition, based on the analysis of heterogeneity characteristics, the interpretation results of this method can also be combined with the traditional model-driven method to obtain more formation parameters.

2 Materials

This study is based on the Yanchang Formation shale in the southeastern Ordos Basin (Figure 1A). The shale is a Triassic

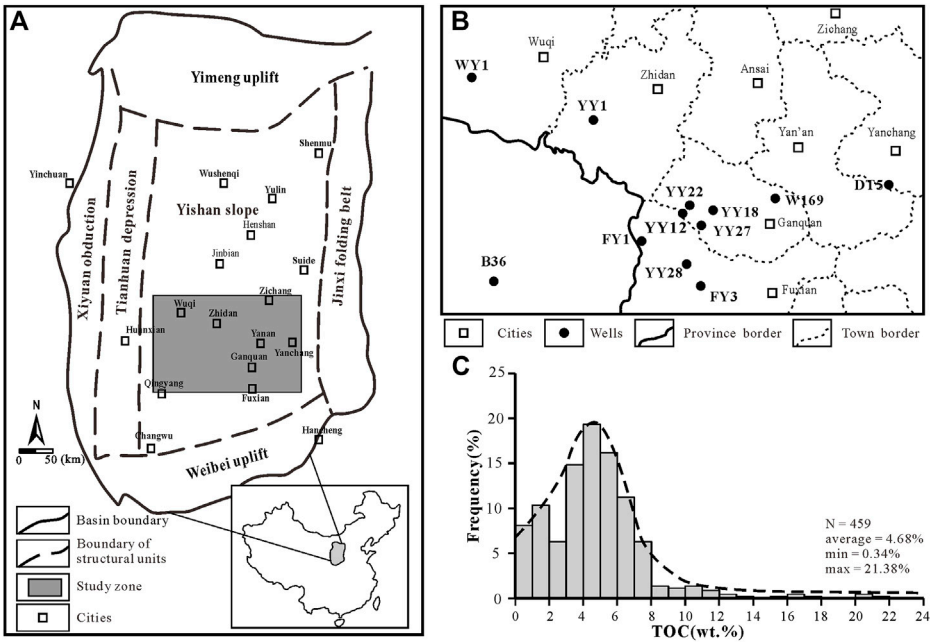

FIGURE 1
(A) Location of Ordos Basin and study area (modified by Yang et al., 2005); **(B)** Horizontal distribution of wells in the study area; **(C)** TOC frequency distribution histogram.

TABLE 1 Testing data and conventional well logs used in this study.

Well name	Testing			Gamma ray (GR)	Sonic (DT)	Resistivity (ILD,ILM, Rt)	Density (DEN)	SGR (URAN, THOR, POTA)	Neutron porosity (CNL)	Caliper (CAL)
	TOC	Mineral composition	Pyrolysis							
YY2	16	×	×	√	√	√	√	√	√	√
YY12	25	×	×	√	√	√	√	√	√	√
YY18	50	25	×	√	√	√	√	√	√	√
YY22	104	52	×	√	√	√	√	√	√	√
YY27	25	×	27	√	√	√	√	√	√	√
YY28	52	35	26	√	√	√	√	√	√	√
FY1	74	21	×	√	√	√	√	√	√	√
FY3	30	23	×	√	√	√	√	√	√	√
B36	20	×	×	√	√	√	√	√	√	√
WY1	46	13	12	√	√	√	√	√	√	√
W169	8	×	×	×	√	√	×	×	×	×
DT5	9	×	×	×	√	√	×	×	×	×

continental deposit, and the mud shale section is located in the Chang 7 ~ Chang 9 oil formation. The data come from core samples and conventional logging curves of 12 wells (Figure 1B). As shown in Table 1, based on the core description of the above 12 wells, the samples were selected for TOC, mineral composition, extraction and pyrolysis test, and the core homing work was carried out.

Among them, the TOC sample size is 459. Statistics show that the TOC distribution is 0.34 wt%~29.11 wt% (4.76% on average). From Figure 1C, it can be found that the data exhibit skewed distribution with a long tail. The high-density data distribution area is located at 3 wt% ~ 8 wt%, showing that the data has an unbalanced distribution (Buda et al., 2018; Liu et al., 2019).

In addition to the TOC test, the whole rock mineral composition and pyrolysis test were also carried out in this study. These data were used to illustrate the differences in mineral composition and oil content of different lithofacies.

Except W169 and DT5 wells which lack Density, SGR and Neutron logging series, 10 wells have complete logging series. In this study, the 10 wells were selected to construct the LBCRM method, W169 and DT5 were used for the extended application of the LBCRM method.

3 Methodology

3.1 Principle of LBCRM

In essence, data-driven TOC logging interpretation is a typical data regression problem based on learning algorithms. Suppose that a supervised data set $D_t = \{(x_i, y_i)\}_{i=1}^{n}$, where $x \in X$, $y \in Y$, is derived from the joint distribution $P_{X \times Y}$. The goal of the data-driven method is to establish a mapping relationship $f \in F: X \to Y$, such that the expected error $\varepsilon_{ex} = E_{(x,y)\sim P_{X\times Y}} L(f(x), y)$ is minimized, where $L(f(x), y)$ is the loss function, representing the difference between the predicted value $f(x)$ and the supervised target y value. In practice, the joint distribution $P_{X \times Y}$ is unknown, x and y generally take values from the supervised data set D_t, so the objective of the regression problem is to minimize $\varepsilon_{em} = E_{(x,y)\sim D_t} L(f(x), y)$. When the supervised data set is large enough, $\varepsilon = |\varepsilon_{ex} - \varepsilon_{em}|$ is small enough, so that the regression fitting relationship f has better prediction effect. For logging interpretation, x is the conventional logging response, f is the formation characteristic parameters, including mineral composition, element composition and organic matter content.

Compared with the easily available TOC data, other formation parameter data are often difficult to obtain for various reasons. Therefore, the target output in the supervised data set D_t of TOC logging interpretation is only TOC data. This requires that conventional logging responses can provide sufficient differentiated features to distinguish TOC values. A comparative study by Chan et al. (2020) and Mahmoud et al. (2017) found that prediction accuracy can be significantly improved by adding dimensional information to conventional logging responses, suggesting that conventional logging responses may not be sufficient to provide complete features for accurate interpretation of TOC.

Similar to Chan et al. (2020), the TOC interpretation model based on rock facies classification and regression improves the prediction accuracy of TOC by adding additional dimension information to logging information. Based on the study of shale heterogeneity, this method constructs a relatively homogeneous lithofacies unit and uses it as additional information to constrain TOC interpretation. The mathematical expression of the regression target of this method is to divide the D_t data set into m subsets D_t^m, and establish a function mapping relationship f_j for each subset to minimize Eq. 1:

$$\varepsilon_{em} = \sum_{j=1}^{m} \varepsilon_{em}^{j} = \sum_{j=1}^{m} E_{(x,y)\sim D_t^j} L(f(x), y), \tag{1}$$

where m is the number of types of lithofacies units,$j \in [1.2,\ldots m]$.

Figure 2 shows the basic idea of this method. Traditional data-driven TOC interpretation methods use a uniform regression model (URM) when constructing prediction models. As shown in Figure 2A, firstly, the homogeneous regression model ignores that the input data is not enough to provide enough differentiated features to describe the output target. Secondly, the data imbalance in the supervised data makes the learning algorithm have the data characteristics in the rectangular area in Figure 2B, but the fitting model in Figure 2A cannot have good prediction performance for the data outside the gray rectangular area. The classification fitting regression model shown in Figure 2C can increase the type dimension information, so that the learning algorithm can obtain a more accurate prediction model in the data within different categories. At the same time, as shown in Figure 2D, this method can also reduce the imbalance of the data, so that the learning algorithm will not only focus on the data with high frequency distribution, especially for the high density of local data distribution caused by the coincidence of different types of data.

3.2 Classification of lithofacies

At present, the classification of shale rock facies is mainly divided into two categories. One is based on the difference of sedimentary and structure on the core scale of mud shale section (Singh et al., 2008; Zhen et al., 2016; Kristen, 2015; Long et al., 2022; Zhang et al., 2022); the second is based on rock physics parameters, especially mineral composition parameters (Wang et al., 2012; Gao et al., 2018; Ou et al., 2018; Schlanser, 2015).

In this study, the rock has three corresponding characteristics. One is that the rock facies type is not easy to be too complicated for the consideration of well site application, which makes it difficult to establish a logging identification method with high prediction accuracy. The second is easy to obtain. On the one hand, it is conducive to the formation of large-scale data sets, on the other hand, the rock type classification using TOC data; The third is the thickness of rock facies should be above the vertical resolution of the logging. Taking DEN with the highest vertical resolution in conventional logging as an example, the thickness of rock facies should be at least 30 cm.

Due to the numerous petrophysical parameters affecting the logging response, a more complex classification scheme will be formed in the rock facies construction, and it is easy to fall into the rock facies classification only for TOC data with petrophysical parameters. Therefore, this study uses the difference of sedimentary and structure on the core scale as the basis for the division of rock facies. At the same time, in order to avoid the occurrence of complex lithofacies types, only the sedimentary characteristics that have obvious influence on rock physics characteristics are considered. In addition, in order to correspond to the vertical resolution of logging, the thickness of a single rock facies layer is at least 30 cm.

3.3 Machine learning method

The data mining algorithms used in this study include SVR (support vector machine) and XGboost. In addition, genetic algorithm is used to optimize the hyperparameters of the above two algorithms, and K-fold cross validation is used to improve the generalization ability of the training model.

3.3.1 SVR method

SVR has incomparable advantages in data mining of small sample data sets. Considering that there may be a small amount of data in some data sets after the construction of sub-data sets, this paper chooses SVR as the basic data mining algorithm for TOC logging interpretation. The basic concept of SVR method is to project the input data into a higher dimension by kernel function, so as to find a

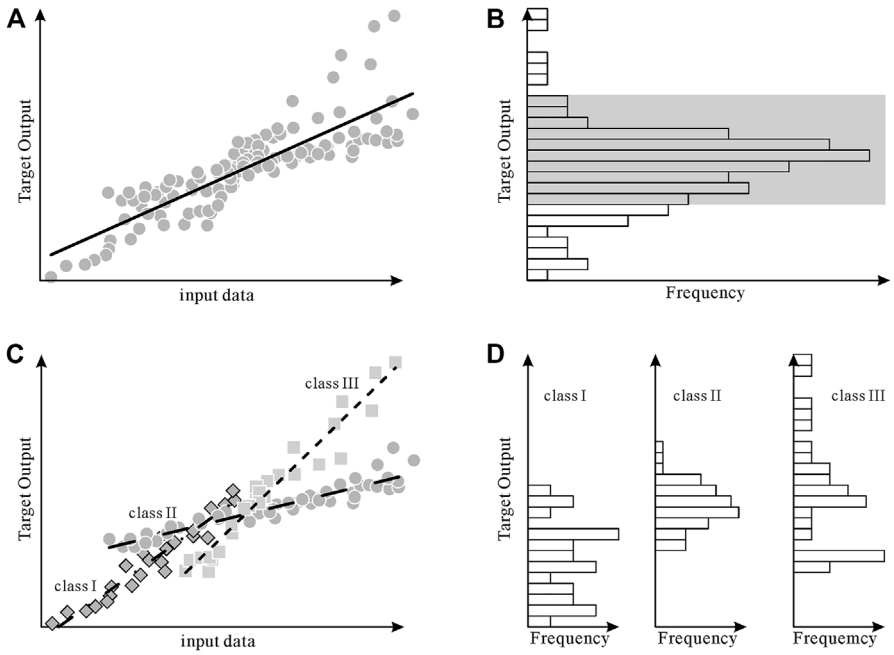

FIGURE. 2
Schematic diagram of regression prediction model based on rock facies classification **(A)** The effect of using a uniform regression fitting model in the case of incomplete input data and unbalanced supervised data; **(B)** The unbalanced distribution characteristics of the data set; **(C)** The effect of using classification fitting regression fitting model in the case of incomplete input data and unbalanced supervised data; **(D)** classification fitting regression subdataset imbalance distribution reduction.

hyperplane to establish a regression function. For a given data set $\{(x_1,y_1),\ldots..,(x_l,y_l)\}$, where $x_i \in R^n$ is the input data, $y_i \in R^1$ is the target output value, and the SVR estimation function is:

$$f(x) = w^{\mathrm{T}} \cdot \Phi(\mathrm{x}) + b, \tag{2}$$

where w and b are hyperplane parameters, $\Phi(x)$ denotes the eigenvectors after x projection. The standard form of SVR for solving hyperplane parameters is (Vapnik, 1998):

$$\min_{w,\,b,\,\xi,\,\xi^{\star}} \ \frac{1}{2}w^{T}w + C\sum_{i=1}^{l}\left(\xi_i + \xi_i^{*}\right). \tag{3a}$$

受制于.
Subject to

$$\begin{aligned} w^{T} \cdot \Phi(x_i) + b - y_i &\le \varepsilon + \xi_i, \\ y_i - w^{T} \cdot \Phi(x_i) - b &\le \epsilon + \xi_i^{*}, \\ \xi_i,\ \xi_i^{*} &\ge 0, \quad i = 1, \cdots, l, \end{aligned} \tag{3b}$$

where C is the penalty coefficient or regularization parameter, and ε, $\xi,\xi^{*} \in \mathrm{R}$ are slack variables introduced to penalize the fitting function. Eq. 1 can be transformed into a dual problem to solve, and the original problem is transformed into its corresponding Lagrangian function form, and by minimizing:

$$\begin{aligned} &\min_{\alpha,\,\alpha^{\star}} \ \frac{1}{2}\sum_{i=1}^{l}\sum_{j=1}^{l}\left(\alpha_i - \alpha_i^{*}\right)\left(\alpha_j - \alpha_j^{*}\right)K\left(x_i, x_j\right) + \varepsilon\sum_{i=1}^{l}\left(\alpha_i + \alpha_i^{*}\right) \\ &+ \sum_{i=1}^{l} y_i\left(\alpha_i - \alpha_i^{*}\right). \end{aligned} \tag{4a}$$

Subject to

$$\begin{aligned} \sum_{i=1}^{l}\left(\alpha_i - \alpha_i^{*}\right) &= 0, \\ 0 \le \alpha_i,\ \alpha_i^{*} &\le C, \quad i = 1, \cdots, l, \end{aligned} \tag{4b}$$

where $\alpha_i = (\alpha_1, \alpha_2, \ldots \alpha_l)$ is the Lagrange multiplier, and $K(x_i,x_j)$ is the kernel function. The final regression equation is:

$$f(x) = \sum_{i=1}^{n}\left(\alpha_i - \alpha_i^{*}\right)K\left(x_i, x_j\right) + b. \tag{5}$$

In this paper, polynomial kernel function, radial basis kernel function (RBF) and sigmod kernel function are selected to explain TOC respectively, so as to optimize the best kernel function type.

3.3.2 XGboost

XGboost was first proposed by Chen and Guestrin (2016). It is a machine learning algorithm that relies on the boosting principle and explores weak learners to comprehensively predict. This is mainly due to its well-known high prediction accuracy. Its basic principle is to generate a sub-classifier to fit the prediction residuals of the previous sub-classifiers, thereby continuously reducing the residuals between the true value and the predicted value, and finally integrating all sub-classifiers to give the final prediction result. The expression is:

$$\hat{y}_i = \sum_{k=1}^{K} f_k(x_i),\ f_k \in F. \tag{6}$$

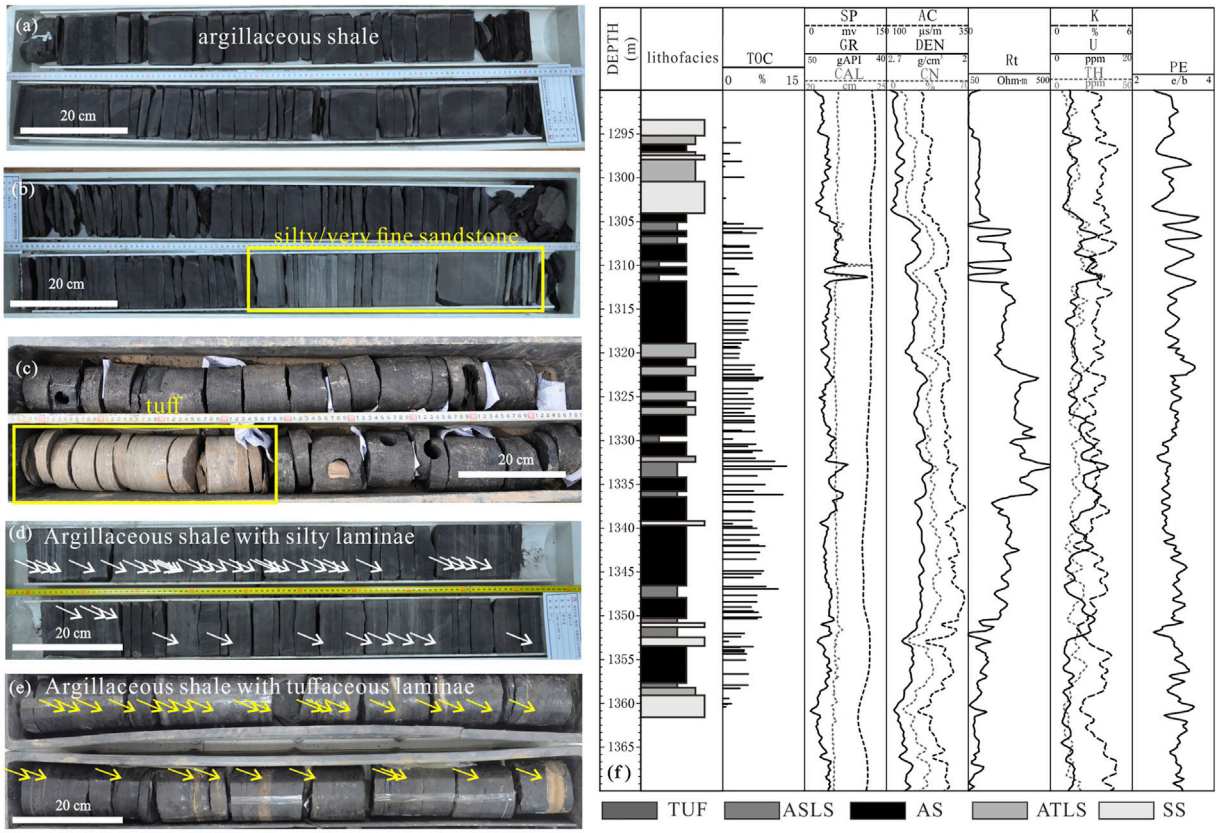

FIGURE 3
The difference of sedimentary and structure on the core scale **(A–E)**: The characteristics of different rock facies on the core **(F)** distribution and logging response of rock facies in coring section of well YY22.

Among them, $\hat{y}_i$ is the calculated predictive value of the i th sample; K denotes the number of decision trees; f_k denotes the kth submodel; x_i represents the input feature of the ith sample; F represents the set of sub-classifiers. In the Xgboost sub-classifier, the Classification and Regression Tree is usually selected. In the Xgboost algorithm, the objective function is composed of a loss function and regularization parameters. The expression is:

$$\mathrm{L}(\varphi) = \sum_i l(\hat{y}_i, y_i) + \sum_k \Omega(f_k), \text{ where } \Omega(f) = \gamma T + \frac{1}{2}\lambda\|w\|^2. \quad (7)$$

Among them, $l(\hat{y}_i, y_i)$ is the residual between the predicted value $\hat{y}_i$ and the target value y_i; f_k is the function expression of the k sub-classifier; $\Omega(f_k)$ is the penalty term of the model complexity, which can be used to smooth the final learned weights to avoid overfitting. XGboost is trained iteratively to obtain an approximation of $L(\varphi)$. Assuming that the sub-classifier trained in the t iteration is f_t, after the t iteration, the objective function can be expressed as:

$$L^t = \sum_{i=1}^{n} l(\hat{y}_i^{t-1} + f_t(x_i), y_i) + \Omega(f_k). \quad (8)$$

Equation. 8 can be further optimized using second-order approximation:

$$L^t \cong \sum_{i=1}^{n}\left[l(\hat{y}_i^{t-1}, y_i) + g_i f_t(x_i) + \frac{1}{2} h_i f_t^2(x_i)\right] + \Omega(f_k), \quad (9)$$

where, g_i and h_i are the first-order and second-order partial derivatives (gradients) of l, respectively, where $g_i = \partial_{\hat{y}^{t-1}} l(\hat{y}_i^{(t-1)}, y_i)$ 和 $h_i = \partial^2_{\hat{y}^{t-1}} l(\hat{y}_i^{(t-1)}, y_i)$. After taking them into Eq. 9 and removing the constant term, we can obtain:

$$\tilde{\mathrm{L}}^t = \sum_{i=1}^{n}\left[g_i f_t(x_i) + \frac{1}{2} h_i f_t^2(x_i)\right] + \Omega(f_t). \quad (10)$$

Define I_j={$i \mid q(x_i) = j$} as an instance set of leaf node j. Eq. 10 is rewritten by extending Ω to:

$$\begin{aligned}\tilde{\mathrm{L}}^t &= \sum_{i=1}^{n}\left[g_i f_t(x_i) + \frac{1}{2} h_i f_t^2(x_i)\right] + \gamma T + \frac{1}{2}\lambda\sum_{j=1}^{T} w_j{}^2 \\ &= \sum_{j=1}^{n}\left[\left(\sum_{i\in I_j} g_i\right) w_j + \frac{1}{2}\left(\sum_{i\in I_j} h_i + \lambda\right) w_j^2\right] + \gamma T. \end{aligned} \quad (11)$$

Therefore, the objective function is transformed into a function of the first and second partial derivatives of the loss function l, the leaf node weight, and the number of leaf nodes. In the case of fixed tree structure $q(x)$ the optimal weight w_j*of leaf node j can be calculated by the following formula:

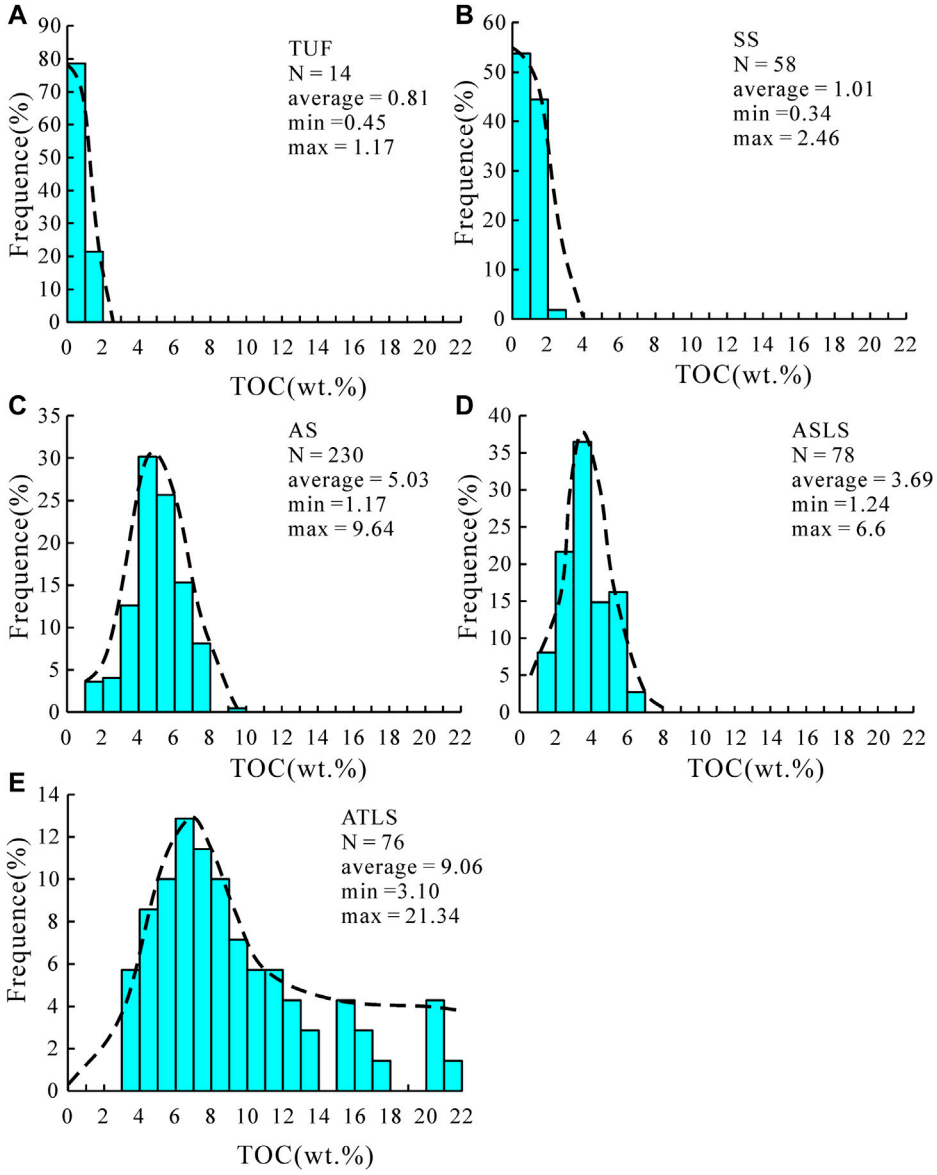

FIGURE 4
Frequency distribution histogram of TOC in TUFF **(A)**, SS **(B)**, AS **(C)**, ASLS **(D)** and ATLS **(E)**.

$$w_j^* = -\frac{\sum_{i\epsilon I_j} g_i}{\sum_{i\epsilon I_j} h_i + \lambda}. \tag{12}$$

The optimal solution formula of the objective function is as follows:

$$\tilde{L}^t(q) = -\frac{1}{2}\sum_{j=1}^{T}\frac{\sum_{i\epsilon I_j} g_i^2}{\sum_{i\epsilon I_j} h_i + \lambda} + \gamma T. \tag{13}$$

XGboost iteratively adds branches to construct sub-classifiers on the initial leaf nodes through a greedy algorithm to determine the optimal tree structure of the CART tree. Suppose there is a leaf node, I_L and I_R are instances of the left and right nodes after the node is branched. Let $I = I_L \cup I_R$, then the loss after branching is reduced to:

$$L_{split} = \frac{1}{2}\left[\frac{\sum_{i\epsilon I_L} g_i^2}{\sum_{i\epsilon I_L} h_i + \lambda} + \frac{\sum_{i\epsilon I_R} g_i^2}{\sum_{i\epsilon I_R} h_i + \lambda} - \frac{\sum_{i\epsilon I} g_i^2}{\sum_{i\epsilon I} h_i + \lambda}\right] - \gamma. \tag{14}$$

If L_{split} is greater than 0, the objective function decreases after the leaf node is split into two leaf nodes, so as to determine the node segmentation. On this basis, XGboost is optimized by feature pre-ranking, quantile approximation, and parallel lookup to quickly find the nearest split point.

3.3.3 Genetic algorithm

In the SVM and XGboost algorithm, there are a large number of hyper-parameters, which will affect the final prediction results. Therefore, it is necessary to use hyper-parameter optimization algorithm to determine which hyper-parameter system the SVM

TABLE 2 Comparision of mineral Composition and Pyrolysis parameters for different lithofacies.

Lithofacies	Type	Mineral composition				Pyrolysis parameters		
		Feldspar and quartz (%)	Clay (%)	Carbonate (%)	Pyrite (%)	S1 (mg/g)	S2 (mg/g)	S1/TOC × 100 (mg/g TOC)
TU	Average	82.26	13.12	3.76	0.86	0.32	0.96	26
	Range	73.3~87.8	8~17.5	0~9.2	0~2.5	0.31~0.32	0.84~1.07	4~48
ATSL	Average	41.57	42.67	6.18	8.88	3.75	16.88	62
	Range	24.6~63.1	22~56.5	0~17.3	2.4~24.9	0.86~6.4	4.3~48.29	24~108
AS	Average	33.74	57.02	6.78	2.48	3.65	11.10	70
	Range	17.6~48.5	45.5~75	0~18.3	0.4~7	2.3~5.54	8.24~16.32	5~109
ASLS	Average	45.66	41.33	11.22	1.79	4.75	9.67	116
	Range	27~63.8	20.5~56	2.3~36.3	0.4~6.3	1.93~6.14	4.22~15.2	75~302
SS	Average	57.17	24.74	17.22	0.86	2.15	4.20	173
	Range	13.8~82.4	8.7~37.5	3.6~50.5	0~4	0.37~6.2	0.47~15.71	69~398

and XGboost algorithm can achieve the best prediction results. This study used Genetic Algorithm to optimize hyperparameters.

Genetic algorithm was first proposed by Holland (1973). It is a parallel stochastic optimization algorithm developed from the simulation of natural genetic mechanism and biological evolution theory. The genetic algorithm starts with a set of randomly generated parameters to be optimized, which is called the initial population, where each parameter pair is called an individual. Genetic algorithm encodes each individual in series to form chromosome, and determines the fitness function according to the optimization objective to calculate the fitness of each individual. Several individuals with high fitness values are selected from the initial population, and the chromosomes encoded by these individuals are crossed and mutated to form a new generation of individual populations. Then the fitness of each individual in the new population is calculated, and the above operations are performed repeatedly until the target value or the maximum number of iterations satisfying the fitness is met. In the iterative process, the genetic algorithm can preserve the individuals with good fitness values and eliminate the individuals with poor fitness. The new population not only inherits the information of the previous generation, but also is superior to the previous generation. Through continuous iteration, the parameters can be optimized.

3.4 Evaluation metics systems

In order to evaluate the predictive performance of the model, four evaluation indicators were used in this study, including RMSE, R2, MAE, MAPE, Mlogloss and Confusion matrix. The first four indexes are used to evaluate the prediction performance of TOC, and the latter two are used to evaluate the accuracy of rock facies identification.

$$RMSE = \sqrt{\frac{1}{n}\sum_{i=1}^{n}(y_i - \hat{y}_i)^2}, \tag{15}$$

$$MAE = \frac{1}{n}\sum_{i=1}^{n}|y_i - \hat{y}_i|, \tag{16}$$

$$MAPE = \frac{1}{n}\sum_{i=1}^{n}\frac{|y_i - \hat{y}_i|}{y_i}, \tag{17}$$

Among them, y_i represents the true value of TOC, $\hat{y}_i$ is the predicted value of TOC, and n represents the number of TOC data. The lower the value of the above index represents the better performance of the prediction model.

$$mlogloss = -\frac{1}{n}\sum_{i=1}^{n}\sum_{j=1}^{m} y_{i,j}\log\left(p_{i,j}\right), \tag{18}$$

where n represents the number of samples, i is the ith sample; m represents the number of classes, j is the jth category; $y_{i,j}$ represents whether the ith sample belongs to the jth class, belongs to 1, else to 0; pi,j represents the probability that the prediction model predicts the ith sample as j.

The Confusion matrix is defined as:

$$Confusion\,matrix = \begin{Bmatrix} n_{11} & n_{12} & \cdots & n_{1m} \\ n_{21} & n_{22} & \cdots & n_{2m} \\ \vdots & \vdots & \ddots & \vdots \\ n_{m1} & n_{m2} & \cdots & n_{mm} \end{Bmatrix}. \tag{19}$$

In the formula, m is the number of categories divided, the subscript represents the label, and n_{ij} represents the number of samples whose real label is i and predicted as j. The Confusion matrix can be used to obtain the prediction accuracy, the accuracy of each category (P), and the recall rate (R). The calculation formula is as follows:

$$acc = \frac{\sum_{i=1}^{m} n_{ii}}{\sum_{i=1}^{m}\sum_{j=1}^{m} n_{ij}}, \tag{20}$$

$$P_i = \frac{n_{ii}}{\sum_{j=1}^{m} n_{ji}} \quad i \in 1, \cdots, m, \tag{21}$$

$$R_i = \frac{n_{ii}}{\sum_{j=1}^{m} n_{ij}} \quad i \in 1, \cdots, m. \tag{22}$$

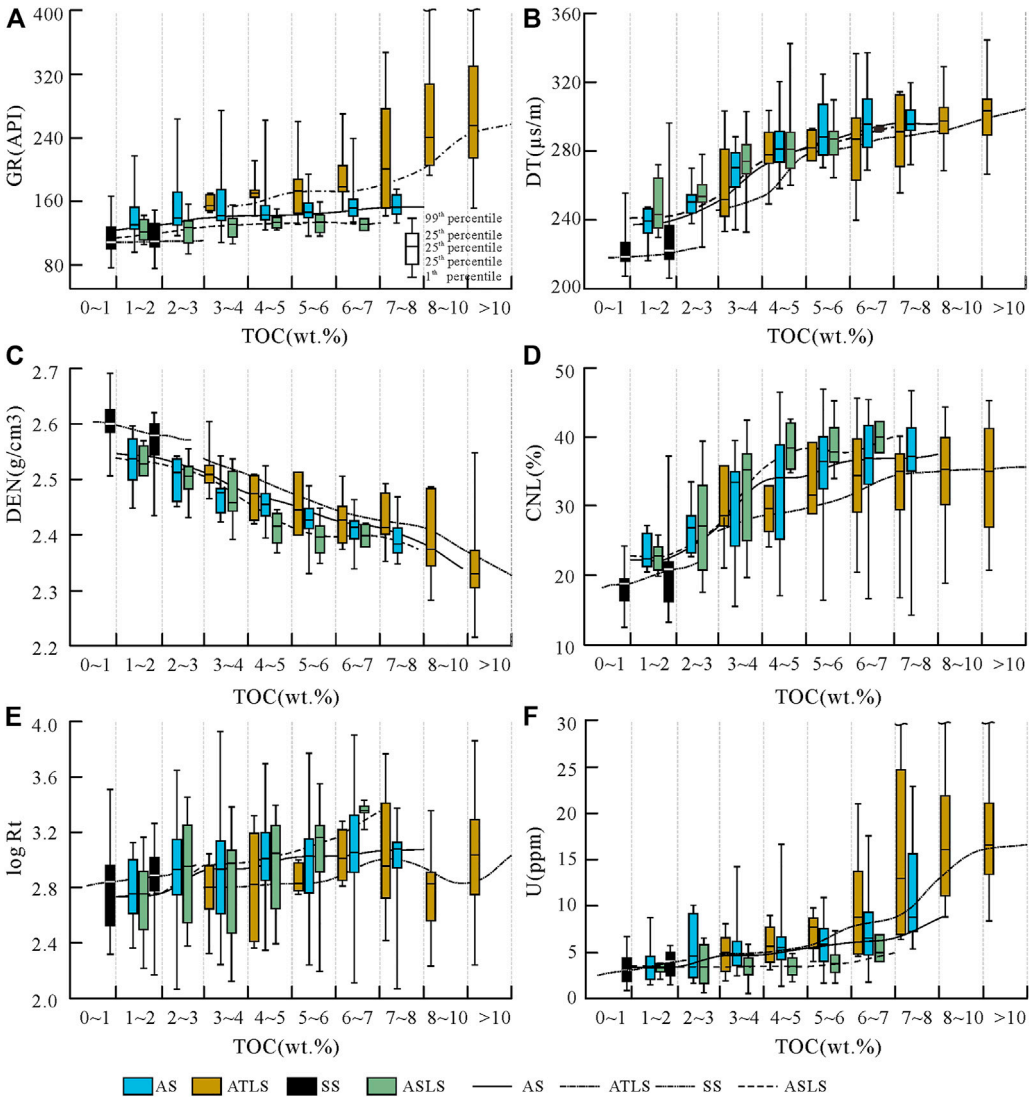

FIGURE 5
Distribution characteristics of GR **(A)**, DT **(B)**, DEN **(C)**, CNL **(D)**, logRt **(E)**, and U **(F)** in different TOC intervals of rock facies.

4 Discussion

4.1 Lithofacies and characteristics

4.1.1 Lithofacies

Based on core observation, according to the difference of sedimentary structure and structure, five lithofacies are developed in the shale of Yanchang Formation, which are argillaceous shale facies (AS), siltstone/very fine sandstone facies (SS), tuff facies (TUF), argillaceous shale facies with silty lamina (ASLS) and argillaceous shale facies with tuff lamina (ATLS). The above five rock facies are easy to identify at the core scale. AS are black, grayish black, fine particles (Figure 3A), and do not develop or develop a small amount of silty or tuffaceous layers; SS is mainly gray and grayish white, and a very small amount of grayish black argillaceous bands are developed (Figure 3B); TUF is grayish yellow, easily broken (Figure 3C), relatively homogeneous, and basically does not develop other lithologic layers; ASLS are mainly gray-black argillaceous shale, with a large number of gray-white and gray silty layers distributed inside. The thickness of these layers is generally millimeter and centimeter (Figure 3D), and the cumulative thickness of silty layer accounts for 20%–50%. The main body of ATLS is black argillaceous shale, with a large number of yellow or grayish yellow tuffaceous laminae distributed inside. The laminae thickness is generally in the millimeter and centimeter levels (Figure 3E). The cumulative thickness of the tuffaceous layer accounts for 20%–50%. Based on the above principles, a columnar distribution map of rock facies in 12 wells was drawn.

4.1.2 Distribution characteristics of TOC in lithofacies

In the TOC frequency distribution diagram of different lithofacies shown in Figure 4, there are differences in the distribution range of TOC in different lithofacies. The TOC of TUF and SS is low, mainly distributed below 2.0 wt%, (Figures 4A,B)and the TOC distribution of AS and ASLS is medium (Figures 4C,D). The average values are

TABLE 3 Optimal parameter series and cross validation root mean square error of SVM regressor obtained by genetic algorithm under different kernel function parameters.

Kernel function type	Optimize parameters	Optimize range	LBMRM								URM	
			AS		ATLS		ASLS		SS			
			Best value	CV MSE	Best value	CV MSE	Best value	CV MSE	Best value	CV MSE	Best value	CV MSE
Polynomial	E	$[2^{-10},2^{10}]$	$2^{-5.71}$	0.67	$2^{-4.67}$	2.28	$2^{-5.48}$	0.42	$2^{-3.14}$	0.18	$2^{-6.29}$	1.5
	Γ	$[2^{-10},2^{10}]$	$2^{-2.80}$		$2^{-3.41}$		$2^{-2.88}$		$2^{1.27}$		$2^{-3.48}$	
	C	$[2^{-10},2^{10}]$	$2^{4.87}$		$2^{8.39}$		$2^{5.66}$		$2^{1.10}$		10	
	D	[2,10]	2		2		2		2		2	
RBF	E	$[2^{-10},2^{10}]$	$2^{-5.79}$	0.6	$2^{-4.88}$	2.49	$2^{-7.92}$	0.43	$2^{-8.09}$	0.11	$2^{-5.35}$	1.32
	Γ	$[2^{-10},2^{10}]$	$2^{-5.21}$		$2^{-2.24}$		$2^{-1.33}$		$2^{5.53}$		$2^{2.92}$	
	C	$[2^{-10},2^{10}]$	$2^{7.08}$		$2^{5.80}$		$2^{5.38}$		$2^{-9.89}$		$2^{-1.04}$	
Sigmod	E	$[2^{-10},2^{10}]$	$2^{-5.94}$	0.62	$2^{-5.52}$	3.01	$2^{-5.36}$	0.45	$2^{-3.34}$	0.148	$2^{-6.03}$	1.57
	Γ	$[2^{-10},2^{10}]$	$2^{-6.64}$		$2^{-6.83}$		$2^{-7.58}$		$2^{0.03}$		$2^{-5.83}$	
	C	$[2^{-10},2^{10}]$	$2^{9.99}$		$2^{9.99}$		$2^{9.99}$		$2^{2.43}$		$2^{9.92}$	

5.03 wt% and 6.39 wt% The above four lithofacies have no obvious exhibit skewed distribution with a long tail, and the data have good balance. In the Yanchang Formation shale, the TOC of the ATLS is generally high, and the numerical distribution range is from 3 wt% to 22 wt% (Figure 4E). The frequency distribution guidance diagram of the lithofacies shows a weak skew distribution. Compared with Figure 1C, the proportion of data greater than 8 wt% is all increased, and the imbalance of data is weakened.

The relative proportion of different rock facies in the shale section of the Yanchang Formation is the main reason for the unbalanced distribution of TOC data in Figure 1C. In the shale interval, AS has the highest proportion of thickness, which can account for the total thickness of the shale interval. Secondly, the TOC distribution characteristics of ASLS samples are similar to those of AS, which causes the overall TOC data to be concentrated in the TOC intervals of the above two lithofacies, while in other distribution intervals, especially in the high-value TOC interval of ATLS, there are fewer samples, resulting in unbalanced distribution of data in Figure 1C. The data imbalance of TOC sub-data set of rock facies obtained by classification is reduced, which is helpful for learning algorithm to obtain more accurate prediction model.

4.1.3 Relationship between TOC and logging response in different lithofacies

As mentioned above, the relationship between formation logging response and TOC is affected by other formation parameters, including mineral composition, elemental composition, and organic matter type. Table 2 shows the differences in mineral composition and organic matter types between different rock facies.

From the perspective of mineral composition, AS has the characteristics of high clay mineral content, low felsic content and medium pyrite content. TUF and SS are characterized by low clay mineral content, low pyrite and high felsic content. The difference is that TUF has high carbonate content and SS has high carbonate content. ASLS has obvious transitional characteristics between AS and SS, that is, clay mineral content, carbonate mineral content, clay mineral content and pyrite are all at a medium level; the main characteristic of ATSL is the highest content of pyrite, which can reach 8.9% on average, and other minerals are at a medium level.

Through pyrolysis data, it can be seen that S1 and S2 are higher in the three rock phases of ATSL, AS and ASLE, with an average value of more than 3.5 mg/g and 9.5 mg/g. The S1 and S2 values of SS are lower, with an average value of 2.15 mg/g and 4.2 mg/g. The S1 and S2 values of TUF are the lowest, and S1 and S2 are below 1 mg/g. From the S1/TOC × 100 index, the SS value is the highest, reaching an average of 173 mg/g TOC, followed by ASLS (an average of 116 mg/g TOC), The average value of AS and ATSL is about 65 mg/g TOC, and TU is the lowest, only 26 mg/g TOC. S1/TOC is often used to evaluate the oil content in rocks (Jarvie, 2008). Considering that shale oil may adsorb/dissolve in kerogen, the higher S1/TOC value is generally considered to be a higher content of movable oil, that is, the higher oil content in pores (Li et al., 2015).

In addition, Qiu et al. (2014) and Akhtar et al. (2018) studied the geochemical characteristics of tuff layers in the Yanchang Formation of the Ordos Basin and found that tuff layers generally have high U and Th contents. In a comparative study, Lu (2020) and Yin et al. (2017) found that the layers of siltstone or silty lamina in Zhangjiatan shale often have low U and Th content, while argillaceous shale has relatively high U and Th content.

Figure 5 shows the logging response distribution of each rock facies in different TOC intervals, and the trend line is drawn by the connection of 50th perecentile point in each interval. Because tuff generally has the characteristics of hole enlargement (as shown in Figure 3F, YY22 well 1310 m), the logging response value has great uncertainty, so the relevant data of tuff are not drawn. It can be seen from Figure 5 that there are great differences in the logging response trend lines between different TOC intervals in different rock facies, which also shows that the differences in mineral composition, element composition and oil content of different rock facies will affect the relationship between logging response and TOC.

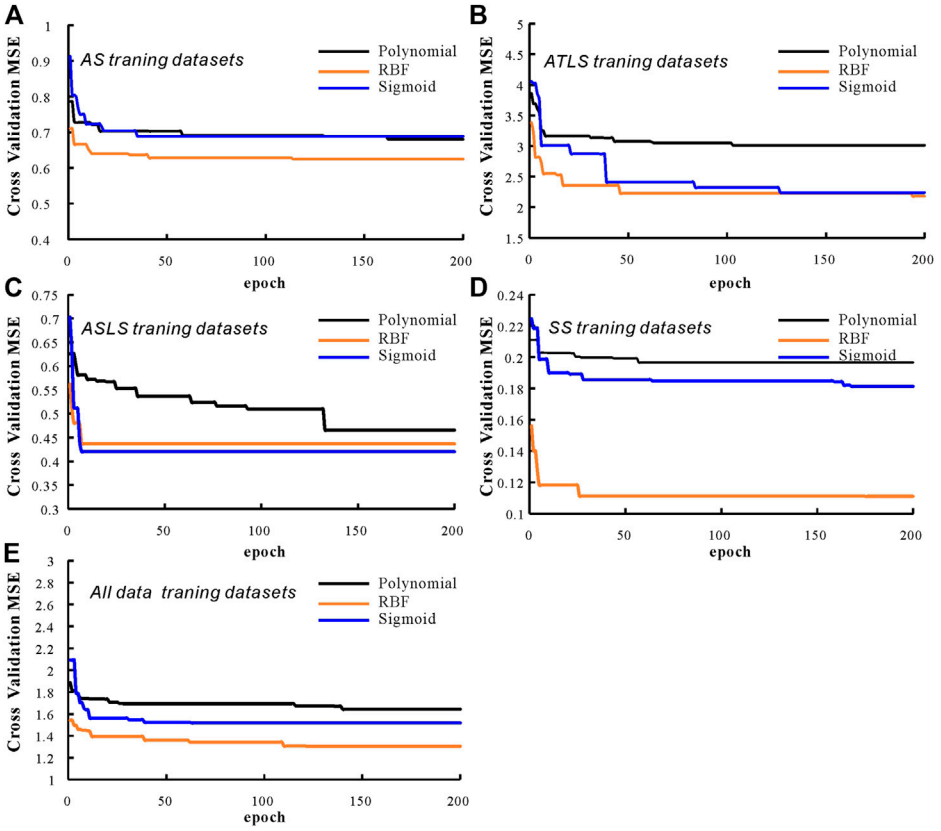

FIGURE 6
Curve of the fitness with the genetic algorithm otimization in AS training datasets **(A)**, ATLS training datasets **(B)**, ASLS training datasets **(C)**, SS training datasets **(D)** and all data training datasets **(E)**.

TABLE 4 Interpretation accuracy evaluation indexes of LBCRM and URM applied in different petrographic verification sets.

Evaluation metics	LBCRM					URM				
	AS	ATLS	ASLS	SS	All testing data	AS	ATLS	ASLS	SS	All testing data
Sample Number	43	17	15	11	86	43	17	15	11	86
MSE	0.70	2.24	0.49	0.20	0.91	1.15	11.73	0.59	1.86	3.23
RMSE	0.84	1.49	0.70	0.37	0.95	1.07	3.42	0.77	1.36	1.80
MAPE	15.76	16.37	15.20	37.84	19.56	16.32	25.14	15.90	93.23	31.65

From Figure 5, the relationship between TOC and logging response in different lithofacies can be classified into two categories:

One is that the trend lines are similar in direction but not coincident, as shown in Figures 5A–F. In Figures 5A, F, because ATLS has the highest U and Th content, it often has higher GR and U logging values under the same TOC conditions as other lithofacies. Similar SS and ASTL have lower U and Th than AS, which makes it have lower GR and U values. The difference in mineral composition may be the main reason for the inconsistency of the trend lines in Figures 5B, C. For example, the high density of pyrite and carbonate makes ASTL and SS lithofacies have higher density values under the same TOC, and similar minerals also make ASTL and SS have lower acoustic time difference. The difference in oil content caused the non-coincidence of the trend line in Figure 5D. Oil has a higher H+ content than kerogen, resulting in SS and ASLS with higher S1/TOC under the same TOC. Higher neutron porosity values, on the contrary, ASTL neutron porosity is low.

The second is the difference in the direction of the trend line, as shown in Figure 5E, the resistivity logging response distribution in different TOC intervals. The obvious feature is that the trend line of ATLS lithofacies is not obvious, and even in some TOC intervals, the resistivity decreases with the increase of TOC. The high content of pyrite in ATLS may be a key factor in this phenomenon, which also causes the resistivity of ATLS to be generally lower than that of other rock phases under the same TOC. Secondly, the low content of clay minerals with good conductivity and high oil content also lead to higher resistivity of SS and ASLS than AS.

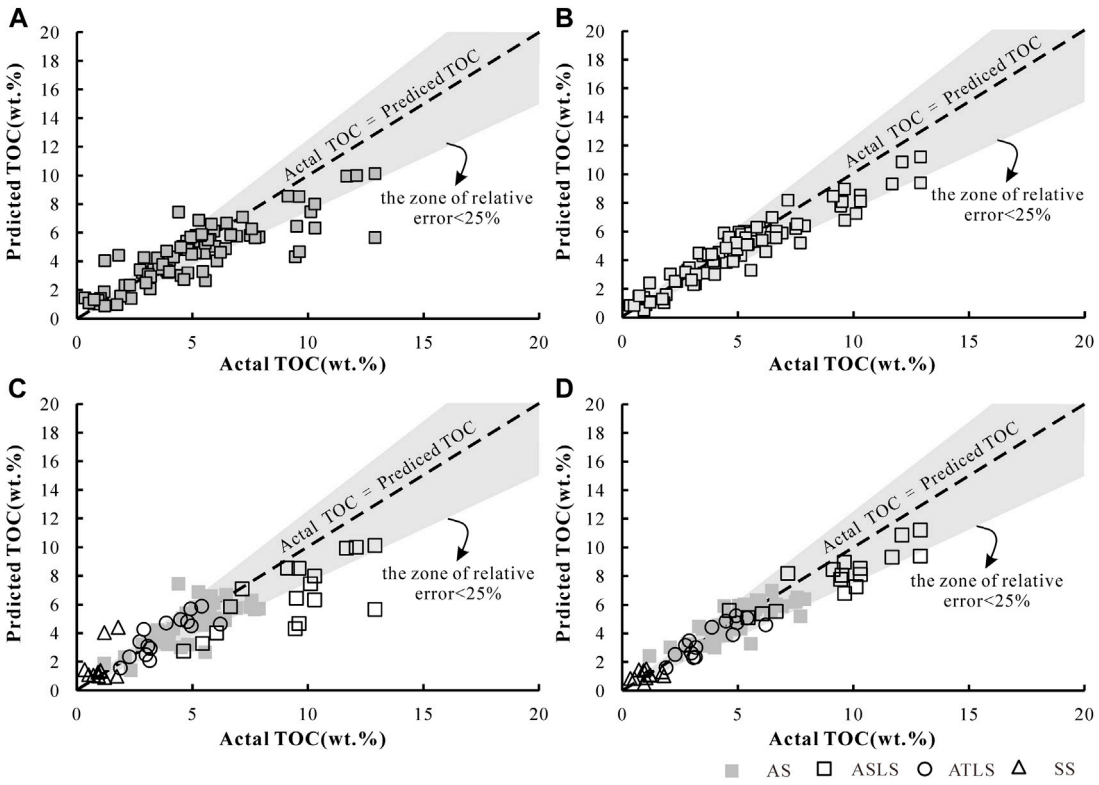

FIGURE 7
Comparison of measured and predicted TOC **(A,C)**: using uniform regression prediction model;**(B,D)**: classification regression prediction model based on rock facies. The different form of data points in Figures **(C,D)** represent lithofacies types.

It can be seen that the introduction of rock facies in the analysis of TOC and logging response relationship can better understand the relationship between TOC and different logging responses, so that the relationship is less affected by shale formation factors such as mineral composition and element composition.

4.2 TOC interpretation of LBCRM

4.2.1 Model building

In this study, four SVR models of rock facies were constructed, which were AS, SS, ATLS and ASLS. For three purposes, the prediction model of tuff facies (TUF) was not constructed: 1) the phenomenon of borehole enlargement is obvious in this lithofacies, and the quality of logging data is poor; 2) The proportion of tuff facies in the Yanchang Formation reservoir is low, and the number of TOC test samples is small. 3) The TOC content of the lithofacies is generally low and the values are concentrated (Figure 4A). Datas are derived from FY1, YY18, WY1, YY12, YY2, YY27, YY28, and B36 wells. The total number of data is 412, of which AS, SS, ATLS and ASLS are 214,55,71 and 72 respectively. The above data are randomly assigned to supervised training data sets and validation sets at a ratio of 1:4.

For the need of comparison, this study also constructed a prediction model under the uniform regression fitting mode. The same as the above data, the supervised data did not contain the relevant samples of tuff facies, and the supervised training data set and verification set were obtained from the corresponding data sets of the above four lithofacies. The supervised data include seven kinds of data such as *AC*, *DEN*, *GR*, *Rt*, *PE*, *Th/K*, *U/Th*, and TOC. The data normalization is carried out by the following formula:

$$y_i^{'} = \frac{y_{max} - y_i}{y_{max} - y_{min}}. \tag{23}$$

Among them, the logging data uses the same maximum and minimum values in the above five supervised data sets. Since the TOC of the samples in SS is much lower than that of the other rock facies, in order to ensure the final prediction accuracy, the TOC of the SS supervised data set is normalized to [0,3], and the TOC of the remaining four supervised data sets is normalized to [0,30], which is normalized to [0,30] in the uniform regression fitting model.

In this study, SVR is used as the basic algorithm, and genetic algorithm is used to optimize the hyper-parameters in SVR. The optimized parameters include kernel function type and its key parameters (Table 3). The fitness function of the genetic algorithm is the cross-validation MSE of the training data (using the K-fold cross-validation method, K = 3). The genetic algorithm uses the bidding model to select the optimal individual (the selection ratio is 0.2). After crossover and mutation operations, a new generation of population is formed. The number of populations in each generation is 150, and the number of iterations is 200. Table 3 shows the range of hyperparameter optimization.

TABLE 5 Parameter to be optimized of XGboost and its optimal value in genetic algorithm.

No.	Parameter name	Encoding type	optimal range	best value
1	Learning rate	Real number	(0.3, 0.5]	0.48
2	Max_depth	Integer	[5, 15]	11
3	Min_child_weight	Integer	[5, 10]	4
4	Gamma	Real number	[0, 0.4]	0.1
5	Sub_sample	Real number	[0.7, 1]	0.85

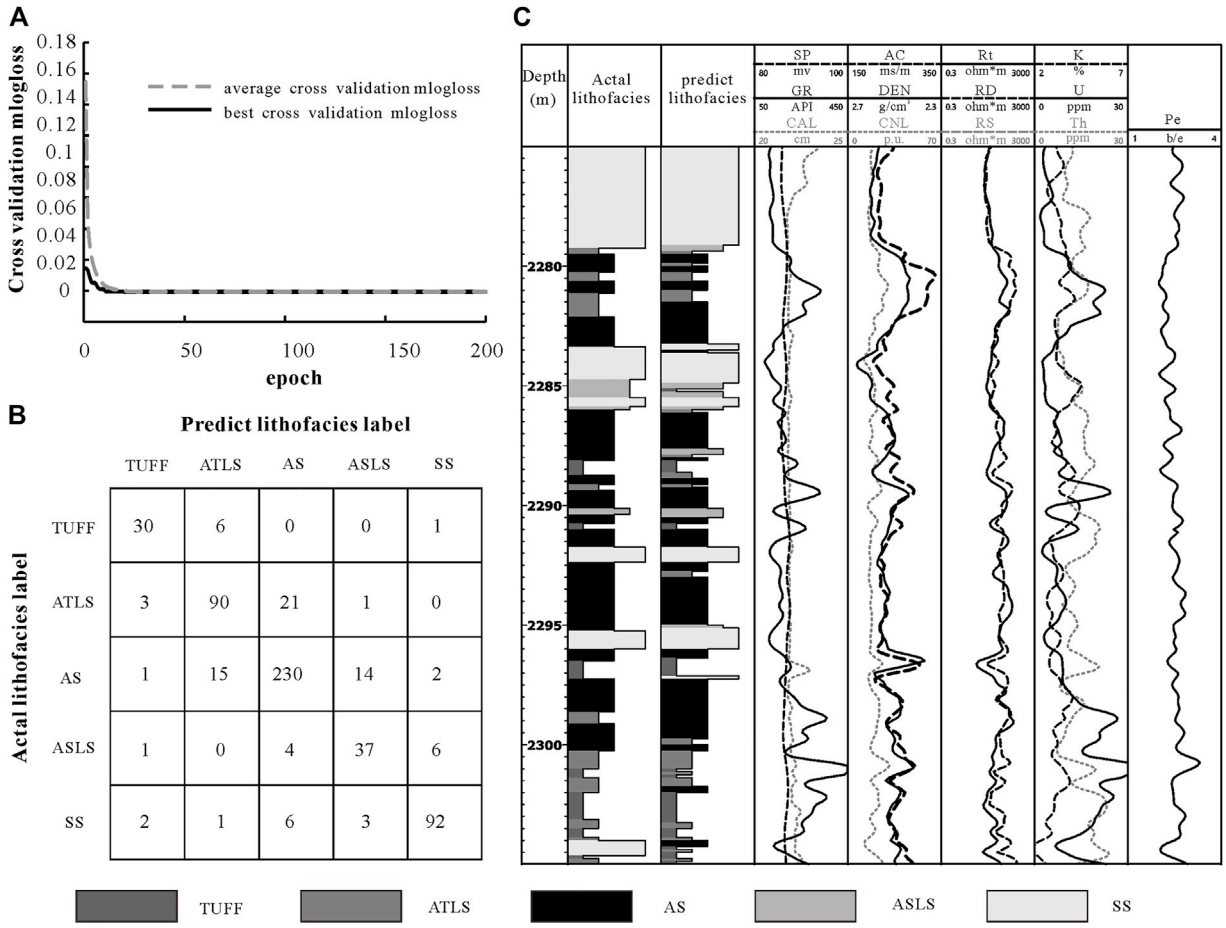

FIGURE 8
(A) The fitness change curve of genetic algorithm in XGBoost rock facies logging interpretation model optimization; **(B)** The confusion matrix of prediction results and measured results in WY1 and FY3 using XGboost rock facies logging interpretation model; **(C)** Comparison of rock facies prediction results and real results of Well WY1.

SVR and genetic algorithm are implemented based on libsvm (https://www.csie.ntu.edu.tw/~cjlin/libsvm/) and geatpy package (http://geatpy.com/index.php/quickstart/).

4.2.2 Performance of model prediction

Figure 6 shows the fitness curves of TOC interpretation model (Figures 6A–D) and homogeneous regression interpretation model (Figure 6E) based on rock facies classification and regression under genetic algorithm optimization. Table 4 lists the optimal parameters of the above optimization process and their corresponding cross validation MSE. It can be found from Figure 6 and Table 4 that the RBF kernel function obtains higher cross-validation accuracy in both interpretation models, that is, the cross-validation MSE is the smallest, which is better than the other two kernel functions. The optimal cross MSE obtained by the RBF kernel function in the homogeneous regression interpretation model is 1.3. In the TOC interpretation model based on rock facies classification regression, the optimal cross MSE in the tuffaceous/clay interbedded shale data set is

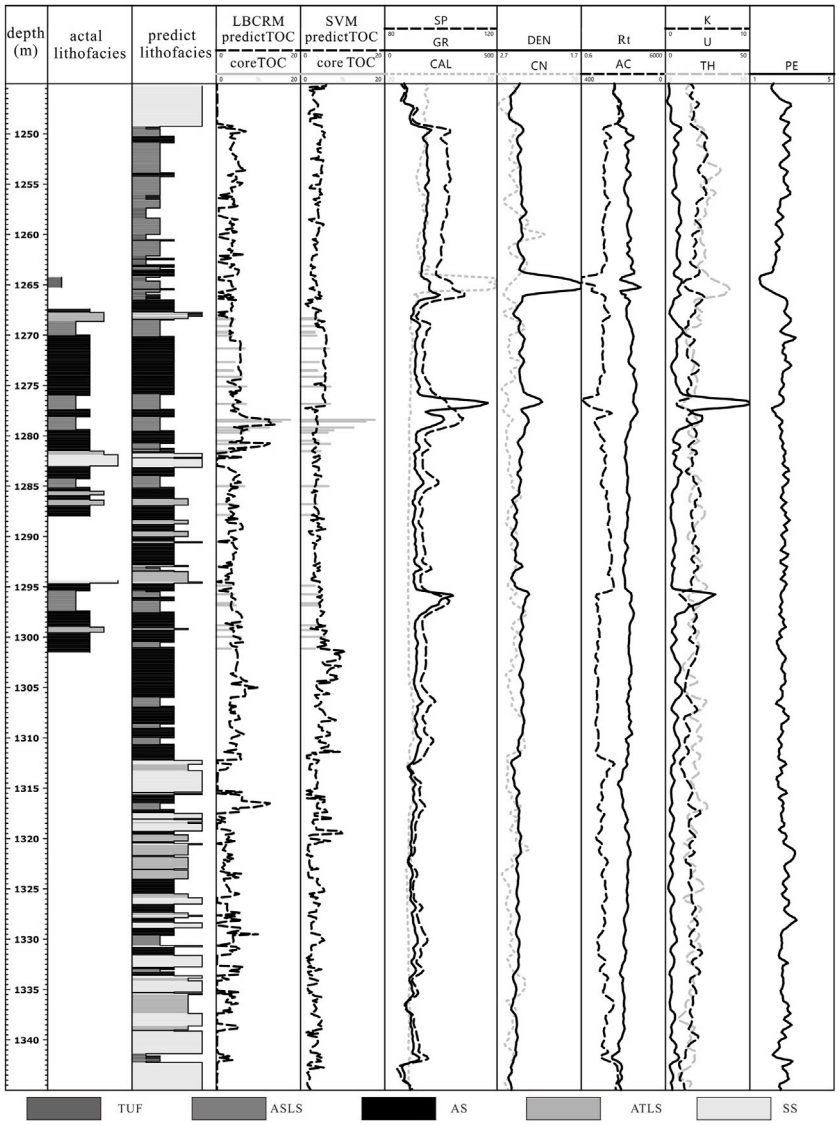

FIGURE 9
The prediction results of lithofacies and TOC in 1,250 ~ 1,340 m shale section of FY3.

TABLE 6 Evaluation metrics of XGboost classification model in validation set.

evaluation metics	Tuff	ATLS	AS	ASLS	SS
Recall	0.81	0.80	0.90	0.77	0.88
Precision	0.81	0.82	0.89	0.73	0.91

2.18, and the optimal root mean square error of other data sets is less than 0.7.

In order to better evaluate the generalization ability and prediction accuracy of the above model, the above model is applied in the corresponding validation set, and the TOC in each validation set data is predicted respectively. Figure 7 is the projection plot of the predicted TOC value and the measured TOC value of different prediction models. Figure 7A is the projection plot of the prediction results of the uniform regression interpretation model in its response data set, and Figure 7B is the projection plot of the prediction results of the classification regression interpretation model based on lithofacies in their respective validation data sets. Figure 7A shows that the overall prediction effect of the uniform regression interpretation model is poor. As shown in Table 4, MSE is 3.23, RMSE is 1.80, and MAPE is 31.65. It is worth noting that in the interval of TOC>9% in Figure 7A, the predicted value of the prediction model seriously deviates from the true value, and the relative error of the predicted value of individual data points is far more than 25%. In comparison, the classification regression interpretation model based on rock facies shown in Figure 7B has better prediction performance. The distribution of data points is closer to the baseline of real TOC equal to predicted TOC. The MSE, RMSE and MAPE in the evaluation indexes are 0.91, 0.95 and 19.56, respectively. The prediction ability is greatly improved compared with the uniform regression model.

Through the difference of prediction performance of the two interpretation models in different rock facies, the reason of poor

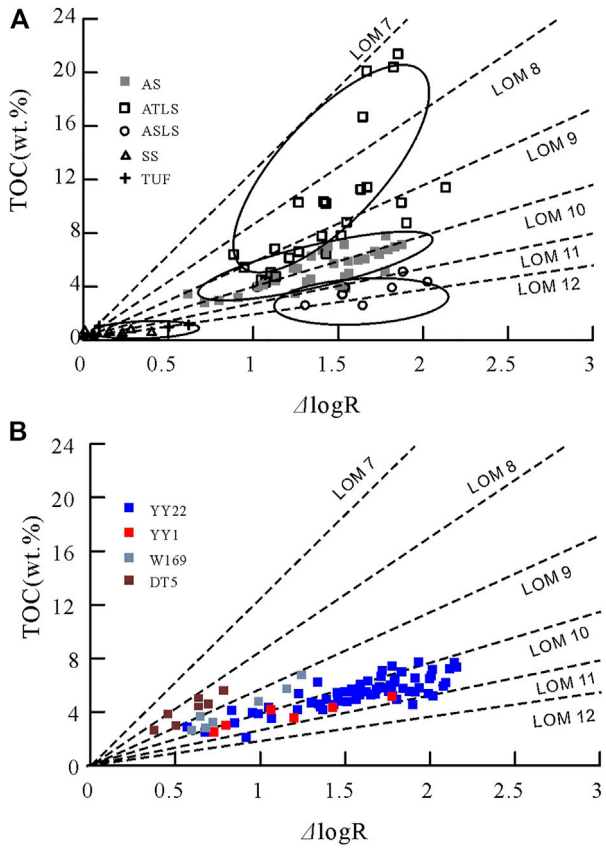

FIGURE 10
(A) The distribution characteristics of different rock facies on the ΔlgR chart; **(B)** Thermal evolution maturity prediction based on ΔlogR plot using AS ata.

TABLE 7 Comparison of Ro based on AS data and ΔlogR chart interpretation with real Ro.

Well name	*ΔlgR interpretation*		Actal R_O (%) Cai et al., 2020)
	LOM	R_O (%)	
YY2	10~11	0.82~1.05	1.10
YY22	10~11	0.82~1.05	1.05
W169	9~10	0.67~0.82	0.85
DT5	8~9	0.56~0.67	0.50

prediction performance of homogeneous prediction model can be further analyzed. Figure 7C shows the relationship between real and predicted TOC in different lithofacies under the homogeneous regression model. It can be seen from the figure that although the overall prediction performance is not good, the homogeneous regression model has higher prediction performance on AS and ASLS, and each evaluation index is at a lower level. The reason for the great decrease of prediction performance is ATLS and SS. The evaluation indexes MSE, RMSE and MAPE of ATLS prediction results are 11.73, 3.42 and 25.14 respectively. Considering the low TOC characteristics of SS, it may be more appropriate to use MAPE for evaluation, but MAPE = 93.23 is obviously beyond the acceptable range. The reason for the above characteristics can be attributed to the fact that the uniform regression model makes the learning algorithm pay more attention to the learning of data features in the high distribution density interval. The SVR algorithm learns more feature information from the 3% ~ 8% interval shown in Figure 1C for training, so that the evaluation index MSE is minimized. In this case, the prediction model will extract features from the two lithofacies of AS and ASLS. Figure 5 shows that the characteristics of TOC and logging in different lithofacies have certain differences, which results in the decline of prediction performance in ATLS and SS.

The classification regression prediction model based on lithofacies solves the problem of poor prediction performance of single prediction model in ATLS and SS, making the prediction performance close to AS and ASLS. As shown in Table 4, the prediction indexes of ATLS and SS have been greatly improved (Figure 7D). The MSE, RMSE and MAPE of ASLS are 2.24.1.49 and 16.37 respectively, and SS is 0.20,0.37 and 37.84 respectively. At the same time, the prediction performance of AS and ASLE has also been improved. For example, the MSE, RMSE and MAPE of AS are reduced to 0.70,0.84 and 15.76, and ASLS is reduced to 0.49,0.70 and 15.20, respectively.

The above prediction results show that the classification regression interpretation based on lithofacies can obtain better TOC prediction accuracy in the case of data imbalance and multi-stratigraphic factors.

4.3 TOC computation in shale interval by LBCRM

4.3.1 Model construction and performance evaluation of lithofacies test interpretation

The basis for the application of TOC interpretation model with better prediction performance is lithofacies interpretability. In this study, the lithofacies delineated in the coring section of 8 wells and their corresponding logging response values are used as supervised data sets, and the lithofacies logging recognition model is established by XGBoost algorithm.

The supervised data set includes seven kinds of logging data and lithofacies labels such as *AC*, *DEN*, *GR*, *U*, *CAL*, *Th* and *Rt*. The logging data uses the original data, and the lithofacies are coded according to TUFof 1, ATLS of 2, AS of 3, ASLS of 4, SS of 5. The XGboost algorithm is based on the XGboost package (https://github.com/d mlc/xgboost). The base model type is gbtree, the learning task is multi: softmax, and the learning objective is mlogloss. In XGboost training, K-fold cross-validation is used to obtain the cross-validation mlogloss value to determine the optimal number of iterations of the tree in XGboost, where K = 7, the maximum number is 200, and the optimal number of iterations is output after 30 iterations without performance improvement. Hyperparameters such as learning rate, max _ depth, min _ child _ weight, gamma and sub _ sample are optimized by genetic algorithm. The fitness function is set to cross mlogloss. The optimization range and coding method are shown in table 5.

Figure 8A shows the optimal and average fitness curves in the genetic algorithm optimization process, where the optimal mlogloss is 0.019, and the optimal parameters shown in Table 5 are determined. The maximum number of times obtained by using this parameter is 179. Using the prediction model obtained by this parameter training, 556 data points in the coring sections of WY1 and FY3 were identified, and the confusion matrix shown in Figure 8B was drawn (Figure 8C).

The prediction accuracy of the model in the prediction set, the prediction accuracy and recall rate of each class are calculated by the confusion matrix (Table 6). It can be seen that the accuracy and recall rate of the four rock phases of TUF, ATLS, AS and SS are greater than 0.80, and the prediction accuracy and recall rate of ASLS are low, which can still reach about 0.75. The overall prediction accuracy is 0.86, which shows that the prediction model has high prediction accuracy and lays the foundation for the application of LBCRM model in actual drilling.

4.3.2 Application for TOC content assessment

Based on lithofacies prediction model and LBCRM method, the TOC content of shale can be predicted. Firstly, the lithofacies prediction model is used to identify the lithofacies types of shale section, and the response TOC interpretation model is used to predict TOC for each lithofacies type. Figure 9 shows the lithofacies identification and TOC interpretation results of the shale depth section of 1,250 ~ 1,340 m in Well FY3. For comparison, the figure also shows the TOC calculated by a single regression model. It can be seen from Figure 9 that the TOC interpretation results obtained by the LBCRM, TOC interpretation model are closer to the measured values. Especially at 1,277 ~ 1,283 m, LBCRM successfully explained that in addition to the high TOC content in this depth section, the single regression model explained it as lower TOC.

4.4 Inspiration to model - Based interpretation

Model-based TOC interpretation is a method of TOC interpretation under appropriate assumptions and key parameters (Huang and Williamson, 1996; sondergeld et al., 2010). The strong heterogeneity of shale makes it difficult to accurately explain the TOC distribution of shale sections in the application of model-based interpretation methods. The LBCRM interpretation method based on the understanding of shale heterogeneity can better understand the model-based interpretation method and make the latter play a role in the logging interpretation of some key parameters.

Δlog*R* is the most classical and widely used model-based TOC interpretation method. Passey et al. (1990) pointed out that in immature shale, the resistivity curve is close to the base value, and Δlg*R* is mainly provided by the amplitude of acoustic time difference deviating from the base value. In mature shale, both resistivity and acoustic travel time deviate from the baseline, and Δlg*R* comes from the amplitude of the above two deviations from the base value. This also caused a statistically non-linear relationship between TOC, AC, Rt and maturity (Ro).

However, there are obvious differences in the content of conductive minerals and oil content between different rock phases, which will inevitably affect the relationship between Δlg*R*-TOC by adding additional factors beyond maturity. For example, the relationship between resistivity and TOC shown in Figure 5E, in the case of the same TOC, the ATLS has the characteristics of low resistivity and low acoustic time difference, and has the characteristics of low maturity in the Δlog*R* chart shown in Figure 10A (Passey et al., 1990). The resistivity logging values of SS and ASLS are larger due to high oil content, which makes them have high maturity characteristics in the Δlog*R* chart, and the two lithofacies often cross multiple LOM intervals; in the Δlog*R* chart, the data points from AS are often concentrated in or near a certain LOM interval. The influence of shale heterogeneity on the Δlog method has prompted a large number of scholars to propose improved models (Wang et al., 2016; zhao et al., 2017), these methods without exception hope to expand the reference range of Δlog by selecting different baselines.

This paper does not focus on improving the traditional model-based prediction method to achieve better TOC prediction performance, but according to the characteristics of AS concentrated in a certain LOM interval in Δlog*R*, the combination of LBCRM and Δlog*R* is proposed to realize the logging estimation of Ro. Through the data distribution of AS on the Δlog*R*-TOC chart of YY22, YY1, W169 and DT5 wells (the data are all derived from the shale of Chang 7) (Figure 10B), the LOM of the above 4 wells is estimated. Based on the conversion relationship between LOM and Ro by Passey (2010), the Ro distribution interval can be estimated (Table 7), Compared with the measured Ro of four wells in this area by Cai et al. (2020), the estimated value is close to the measured value, which fully shows that LBCRM can not only use logging to obtain more accurate TOC distribution in shale section, but also help geologists to explain more formation parameters after being used together with the model-based method.

5 Conclusion

1) In this study, a TOC interpretation model based on lithofacies classification regression was proposed. Through the study of shale heterogeneity characteristics, this method can effectively reduce the influence of formation factors other than TOC on prediction accuracy by constructing TOC interpretation model for each rock facies category, and reduce the degree of data imbalance distribution, so that the data mining algorithm can achieve better prediction results.
2) The interpretability of lithofacies logging ensures the wellsite application based on the regression model of lithofacies classification. Compared with the traditional homogeneous regression model, the prediction performance is greatly improved, and the prediction of high TOC and low TOC sections is more accurate.
3) The LBCRM method based on the heterogeneity of shale can better understand the reasons for the deviation of traditional model-based interpretation methods. When combined with the latter, it can make the logging data provide more useful information.

Data availability statement

The original contributions presented in the study are included in the article/Supplementary Material, further inquiries can be directed to the corresponding author.

Author contributions

JY, CG and MC conceived and designed the experiments; QL, PX and SH performed the experiments; JY and CG analyzed the data; QZ

contributed with figures l; JY, CG and MC wrote the paper. All authors read and approved the final manuscript.

Funding

This study was supported by the Major National Science and Technology Projects (No. 2017ZX05039001-005), the Research Project of YanchangOil Field Co., Ltd., 0 (No. ycsy2021jcts-B-06 and ycsy2022jcts-B-28), key R&D plan of Shaanxi Province (No. 2022GY-138,2021GY-113 and S2022-YF-YBGY-0471) and the National Natural Science Foundation of China (No. 41902136).

The authors declare that this study received funding from the Research Project of Yanchang Oil Field Co., Ltd.. The funder was not involved in the study design, collection, analysis, interpretation of data, the writing of this article or the decision to submit it for publication.

Conflict of interest

Authors TJY, CG, SQL, PX, YSH and QZ were employed by Shaanxi Yanchang Petroleum (Group) Corp.Ltd.

The remaining author declare that the research was conducted in the absence of any commercial or financial relationships that could be construed as a potential conflict of interest.

Publisher's note

References

Akhtar, S., Sahir, N., and Yang, X. Y. (2018). Genesis of tuff interval and its uranium enrichment in upper triassic of ordos Basin, NW China. *Acta Geochim.* 37, 32–46.

Aldrich, J., and Seidle, J. (2018). "Sweet spot" identifcation and optimization in unconventional reservoirs," in *AAPG datapages/search and discovery article #90323* (Salt Lake City, Utah.

Alfred, D., and Vernik, L. (2012). "A new petrophysical model for organic shales," in *SPWLA 53rd annual logging symposium* (Colombia: Cartagena).

Altowairqi, Y., Rezaee, R., Evans, B., and Urosevic, M. (2015). Shale elastic property relationships as a function of total organic carbon content using synthetic samples. *J. Pet. Sci. Eng.* 133, 392–400. doi:10.1016/j.petrol.2015.06.028

Branco, P., Torgo, L., and Ribeiro, R. P. (2018). Rebagg: Resampled BAGGing for imbalanced regression. *Proceeedings Mach. Learn. Res.* 94, 1–15.

Branco, P., Torgo, Luís, and Ribeiro, R. P. (2016). A survey of predictive modeling on imbalanced domains. *ACM Comput. Surv. (CSUR)* 49 (2), 1–50. doi:10.1145/2907070

Buda, M., Maki, A., and Mazurowski, M. A. (2018). A systematic study of the class imbalance problem in convolutional neural networks. *Neural Netw.* 106, 249–259. doi:10.1016/j.neunet.2018.07.011

Cai, Z. J., Lei, Y. H., Luo, X. R., Wang, X. Z., and Cheng, M. (2020). Characteristics and controlling factors of organic pores in the 7th member of Yanchang Formation shale in the Southeastern Ordos Basin (in Chinese). *Oil& Gas. Geol.* 41 (2), 367–379.

Carpentier, B., Huc, A. Y., and Bessereau, G. (1991). Wireline logging and source rocks estimation of organic carbon by the Carbolog method. *Log. Anal.* 32 (3), 279–297.

Chan, S. A., Hassan, A. M., Usman, M., Humphrey, J. D., Alzayer, Y., and Duque, F. (2022). Total organic carbon (TOC) quantification using artificial neural networks: Improved prediction by leveraging XRF data. *J. Pet.sci.eng.* 108, 109302. doi:10.1016/j.petrol.2021.109302

Chen, T. Q., and Guestrin, C. "XGBoost: A scalable tree boosting system," in 22nd ACM SIGKDD International Conference on Knowledge Discovery and Data Mining, New York, NY, USA, 2016, 785–794.

Chen, Y. Y., Gao, D. C., and Sun, X. N. (2020). Organic Geochemistry and Evaluation of the Shale of Yanchang Formation in Yanchang Exploration Area of Ordos Basin. *Unconv. Oil Gas* 7 (1), 32–37. doi:10.3969/j.issn.2095-8471.2020.01.007

Curtis, J. B. (2002). Fractured shale-gas systems. *Am. Assoc. Pet. Geol. Bull.* 86, 1921–1938.

Dellenbach, J., Espitalie, J., and Lebreton, F. (1983). "Source rock logging," in *Transactions of the SPWLA 8th European formation evaluation symposium* (London, UK).

Gao, F., Song, Y., Li, Z., Xiong, F., Chen, L., Zhang, Y., et al. (2018). Lithofacies and reservoir characteristics of the Lower Cretaceous continental Shahezi Shale in the Changling Fault Depression of Songliao Basin, NE China. *Mar. Petroleum Geol.* 98, 401–421. doi:10.1016/j.marpetgeo.2018.08.035

Guo, S. B., Wang, Z. L., and Ma, X. (2021). Exploration prospect of shale gas with Permian transitional facies of some key areas in China. *Pet. Geol. &Experiment* 43 (3), 377–385. doi:10.11781/sysydz202103377

Holland, J. (1973). Erratum: genetic algorithms and the optimal allocation of trials. *SIAM J. Comput.* 2 (2), 88–105. doi:10.1137/0202009

Huang, Z. H., and Williamson, M. A. (1996). Artificial neural network modelling as an aid to source rock characterization. *Mar. Petroleum Geol.* 13 (2), 277–290. doi:10.1016/0264-8172(95)00062-3

Jarvie, D. M. (2008). *Unconventional shale resource plays: Shale-gas and shale-oil opportunities*. New York, NY, USA: Fort Worth Business Press Meeting.

Li, J. J., Wang, W. M., Cao, Q., Shi, Y. L., Yan, X. T., and Tian, S. S. (2015). Impact of hydrocarbon expulsion efficiency of continental shale upon shale oil accumulations in eastern China. *Mar. Petroleum Geol.* 59, 467–479. doi:10.1016/j.marpetgeo.2014.10.002

Liang, X. W., and Li, L. (2021). Geological conditions and exploration potential for shale gas in Upper Permian Wujiaping Formation in the region of Western Hubei-eastern Chongqing[J]. *Pet. Geol. &Experiment* 43 (3), 386–394. doi:10.11781/sysydz202103386

Liu, Z., Miao, Z., Zhan, X., Wang, J., Gong, B., and Yu, S. X. (2019). *Large-scale long-tailed recognition in an open world*. louisiana, LA, USA: CVPR.

Long, H. C., and Li, S. P. (2022). The research on the heterogeneity of shale formations and its controlling factors—A case study of the second member of Funing Formation in Subei Basin[J]. *Unconv. Oil Gas* 9 (04), 78–90.

Lu, H. (2020). Master's Thesis. Beijing, China: China university of petroleum Beijing, 141.Study on tuff reservoir characteristics and formation mechanism of the Chang 7 member in the southern Ordos Basin,

Ma, Y. Z. (2015). "Unconventional resources from exploration to production," in *Unconventional oil and gas resources handbook: Evaluation and development* (Netherlands, Europe: Elsevier), 3–52.

Mahmoud, A., Elkatatny, S., Mahmoud, M., Abouelresh, M., Abdulraheem, A., and Ali, A. (2017). Determination of the total organic carbon (TOC) based on conventional well logs using artificial neural network. *Int. J. Coal Geol.* 179, 72–80. doi:10.1016/j.coal.2017.05.012

Meng, Q. Q., Li, J. Z., Liu, W. H., Fu, Q., Wang, X. F., and Wang, J. (2022). Simulation Study on the Effect of Gypsum-salt Content on Hydrocarbon Generation in Mature Stage Shale. *Special Oil Gas Reservoirs* 5, 113–118.

Meng, Q. Q. (2022). Identification method for the origin of natural hydrogen gas in geological bodies[J]. *PETROLEUM Geol. Exp.* 44 (3), 552–558. doi:10.11781/sysydz202203552

Ou, C. H., Li, C. C., Rui, Z. H., and Ma, Q. (2018). Lithofacies distribution and gas-controlling characteristics of the Wufeng–Longmaxi black shales in the southeastern region of the Sichuan Basin, China. *J. Petroleum Sci. Eng.* 165, 269–283. doi:10.1016/j.petrol.2018.02.024

Passey, Q. R., Bohacs, K., Esch, W. L., Klimentidis, R., and Sinha, S. (2010). "From oil-prone source rock to gas-producing shale reservoir-geologic and petrophysical characterization of unconventional shale gas reservoirs," in *International oil and gas conference and exhibition in China* (London, UK: Society of Petroleum Engineers).

Passey, Q. R., Creaney, S., Kulla, J. B., Moretti, F. J., and Stroud, J. D. (1990). A practical model for organic richness from porosity and resistivity logs. *AAPG Bull.* 74 (12), 1777–1794.

Qiu, X. W., Liu, C. Y., Mao, G. Z., Deng, Y., Wang, F. F., and Wang, J. Q. (2014). Late Triassic tuff intervals in the Ordos basin, Central China: Their depositional, petrographic, geochemical characteristics and regional implications. *J. Asian Earth Sci.* 80, 148–160. doi:10.1016/j.jseaes.2013.11.004

Schlanser, K. M. (2015). *Lithofacies classification in the Marcellus Shale and surrounding formations by applying Expectation Maximization to petrophysical and elastic well logs*. Laramie, WY, USA: University of Wyoming.

Schmoker, J. W. (1979). Determination of organic content of Appalachian Devonian shale from formation-density logs. *AAPG Bull.* 63 (9), 1504–1509.

Schmoker, J. W. (1981). Determination of organic matter content of Appalachian Devonian shale from gamma-ray logs. *AAPG Bull.* 65 (7), 1285–1298.

Singh, P. (2008). *Lithofacies and sequence stratigraphic framework of the barnett shale, northeastern Texas*. Ph.D. Dissertation. Norman, Oklahoma: University of Oklahoma, 81.

Sondergeld, C. H., Newsham, K. E., Comisky, J. T., Rice, M. C., and Rai, C. S. (2010). "Petrophysical considerations in evaluating and producing shale gas resources," in *SPE unconventional gas conference* (Pennsylvania, PA, USA: Society of Petroleum Engineers).

Tan, M., Song, X., Yang, X., and Wu, Q. (2015). Support-vector-regression machine technology for total organic carbon content prediction from wireline logs in organic shale: a comparative study. *J. Nat. Gas. Sci. Eng.* 26 (1), 792–802. doi:10.1016/j.jngse.2015.07.008

Vapnik, V. N. (1995). *The nature of statistical learning theory*. New York, NY, USA: Springer-Verlag, 188.

Wang, G. C., Carr, T. R., and Ju, Y. W. (2014). "Statistical reverse model to predict mineral composition and TOC content of Marcellus shale", in SPE Unconventional Resources Conference. Woodlands, TX, United States: Society of petroleum Engineers.

Wang, G. C., and Carr, T. R. (2012). Methodology of organic-rich shale lithofacies identification and prediction: A case study from Marcellus Shale in the Appalachian basin. *Comput. Geosciences* 49, 151–163. doi:10.1016/j.cageo.2012.07.011

Wang, H., Wu, W., Chen, T., Dong, X., and Wang, G. (2019). An improved neural network for TOC, S1 and S2 estimation based on conventional well logs. *J. Pet. Sci. Eng.* 176, 664–678. doi:10.1016/j.petrol.2019.01.096

Wang, P., Chen, Z., Pang, X., Hu, K., Sun, M., and Chen, X. (2016). Revised models for determining TOC in shale play: example from devonian Duvernay shale, Western Canada Sedimentary Basin. *Mar. Pet. Geol.* 70, 304–319. doi:10.1016/j.marpetgeo.2015.11.023

Wei, S. L., Huang, X. B., Li, J., Su, Y. H., and Pan, L. S. (2021). Shale gas EUR estimation based on a probability method:a case study of infill wells in Jiaoshiba shale gas field[J]. *Pet. Geol. &Experiment* 43 (1), 161–168. doi:10.11781/sysydz202101161

Yin, J. T., Yu, Y. X., Jiang, C. F., Liu, J., Zhao, Q. P., and Shi, P. (2017). Relationship between element geochemical characteristic and organic matter enrichment in Zhangjiatan Shale of Yanchang Formation,Ordos Basin. *J. China Coal Soc.* 42 (6), 1544–1556.

Yu, H., Rezaee, R., Wang, Z., Han, T., Zhang, Y., Arif, M., et al. (2017a). A new method for TOC estimation in tight shale gas reservoirs. *Int. J. Coal Geol.* 179, 269–277. doi:10.1016/j.coal.2017.06.011

Yu, Y. X., Luo, X. R., Cheng, M., Lei, Y. H., Wang, X. Z., Zhang, L. X., et al. (2017b). Study on the distribution of extractable organic matter in pores of lacustrine shale: an example of zhangjiatan shale from the upper triassic yanchang formation, ordos basin, China. *Interpretation* 5 (2), 109–126. doi:10.1190/int-2016-0124.1

Zhang, Y. Y., Zhao, D. F., Guo, Y. H., Wei, Y., Kang, W. Q., Jiao, W. W., et al. (2022). Systematic classification and characterization of small-scale sedimentary structure of the Wufeng Formation shale based on lithofacies——Influence for the evaluation of deep shale reservoirs[J]. *Unconv. Oil Gas* 9 (02), 26–33.

Zhao, D. F., Guo, Y. H., Zhu, Y. M., Zhao, S. X., Chen, Z. H., Jiao, W. W., et al. (2022). Comments on the evaluation system of accurate evaluation and selection of deep marine shale reservoirs. *Unconv. Oil Gas* 9 (02), 1–7.

Zhao, P. Q., Ma, H. L., Rasouli, V., Liu, W. H., Cai, J. C., and Huang, Z. H. (2017). An improved model for estimating the TOC in shale formations. *Mar. Pet. Geol.* 83, 174–183. doi:10.1016/j.marpetgeo.2017.03.018

Zhen, Q., Tao, Caineng Zou, Wang, Hongyan, Ji, Hongjie, and Zhou, Shixin (2016). *Lithofacies and organic geochemistry of the middle permian lucaogou Formation in the jimusar sag of the junggar basin*. NW China.

Zheng, D. Y., Wu, S. X., and Hou, M. C. (2021). Fully connected deep network: An improved method to predict TOC of shale reservoirs from well logs. *Mar. Pet. Geol.* 132, 105205. doi:10.1016/j.marpetgeo.2021.105205

Zhu, L. Q., Zhang, C., Zhang, C. M., Zhang, Z. S., Zhou, X. Q., Liu, W. N., et al. (2020). A new and reliable dual model- and data-driven TOC prediction concept: A TOC logging evaluation method using multiple overlapping methods integrated with semi-supervised deep learning. *J. Pet.sci.eng.* 188, 106944. doi:10.1016/j.petrol.2020.106944

frontiers | Frontiers in Earth Science

TYPE Original Research
PUBLISHED 25 January 2023
DOI 10.3389/feart.2022.1097806

OPEN ACCESS

EDITED BY
Qingqiang Meng,
SINOPEC Petroleum Exploration and Production Research Institute, China

REVIEWED BY
Han Chao,
Shandong University of Science and Technology, China
Wei Dang,
Xi'an Shiyou University, China

*CORRESPONDENCE
Shan Jiang,
18389360@qq.com

SPECIALTY SECTION
This article was submitted to Geochemistry, a section of the journal Frontiers in Earth Science

RECEIVED 14 November 2022
ACCEPTED 02 December 2022
PUBLISHED 25 January 2023

CITATION
Guo Q, Jiang S, Wang J, Zhou Q, Gao Y, Ye L and Yin J (2023), Prediction of hydrocarbon source rock distribution using logging curves: A case study of Es_3^2 source rock in Nanpu Sag, Huanghua depression, Bohai Bay Basin. *Front. Earth Sci.* 10:1097806. doi: 10.3389/feart.2022.1097806

Prediction of hydrocarbon source rock distribution using logging curves: A case study of Es_3^2 source rock in Nanpu Sag, Huanghua depression, Bohai Bay Basin

Qianwen Guo[1], Shan Jiang[1]*, Jianwei Wang[2], Quanzhen Zhou[1], Yongliang Gao[1,2], Lin Ye[1] and Jie Yin[1]

[1]College of Earth Sciences, Yangtze University, Wuhan, Hubei, China, [2]Jidong Oilfield Exploration and Development Research Institute, China National Petroleum, Tangshan, Hebei, China

The Es_3 is the main hydrocarbon source rock system in the Nanpu Sag. Finally, the TOC and hydrocarbon potential of each sub depression of Es_3were predicted. The study shows that the hydrocarbon source rocks of Es_3^2 and Es_3^4 sections are mainly of type II_2 and type II_1 respectively, with good organic matter type and high maturity. Biomarker compound parameters indicate that the Es_3^2 section hydrocarbon source rocks developed in a semi-saline, low to medium terrestrial source organic matter supplied reduction environment with a high algal contribution; the Es_3^4 section hydrocarbon source rocks formed in a freshwater, low terrestrial source supplied reduction environment with a medium-high algal contribution. The multiple linear regression method is more effective than the ΔlgR method in predicting hydrocarbon source rocks in the Nanpu Sag, and the prediction accuracy is higher; the correlation between TOC and $S_1 + S_2$ is the best in the model for predicting hydrocarbon potential. The TOC and hydrocarbon potential of the hydrocarbon source rocks in Es_3^1 are generally low; the high value area of TOC and hydrocarbon potential of the hydrocarbon source rocks in Es_3^2 is partly between the No. 1 tectonic zone and No. 5 tectonic zone in Linque sub depression, and the TOC and hydrocarbon potential of the hydrocarbon source rocks in Liunan sub depression are larger; the high value area of TOC and hydrocarbon potential of the hydrocarbon source rocks in Es_3^4 is mainly concentrated in Shichang sub depression.

KEYWORDS

TOC, hydrocarbon source rock evaluation, hydrocarbon generation potential, Nanpu Sag, Es_3

1 Introduction

Under the guidance of the geological theory of complex oil and gas accumulation and hydrocarbon formation (Hu, 1982; Guo, 2006; Fu et al., 2021; Liang et al., 2021; Pan et al., 2022), with the in-depth research of fine 3D seismic and comprehensive geology (Zhao and Chi, 2000; Zhou et al., 2005; Guo et al., 2021), the concepts of oil and gas-rich depressions with full-concave oil-bearing theory, oil and gas-bearing system and complex hydrocarbon generation system have been put forward successively (Magoon and Dow, 1994; Chen et al., 2000; Zhao et al., 2002; Zhao et al., 2004; Meng et al., 2008; Lin et al., 2022), which have great guiding significance for oil and gas exploration in Bohai Bay Basin. The Nanpu Sag is an important fault-type oil and gas-rich depression in the Bohai Bay Basin, mainly located in the low part of the depression and in the lithologic stratigraphic traps in the slope area (Zhao et al., 2008; Sun et al., 2015; Dang et al., 2016). Hydrocarbon source rocks are the material basis for hydrocarbon formation and determine the hydrocarbon production capacity (Cheng et al., 2021; Han et al., 2016; Kang, 2021; Meng et al., 2022). A correct understanding of hydrocarbon source rock characteristics and spreading pattern is the basis and key to hydrocarbon exploration (Huang et al., 2017).

A large number of scholars have studied hydrocarbon source rocks in major basins in China, Among them, Zou et al. (2010) simulated the maturity evolution and hydrocarbon production and discharge processes of hydrocarbon source rocks in the Bohai Bay Basin based on the sedimentary and tectonic development history of hydrocarbon source rocks combined with geochemical and thermal parameters; Lu et al. (2017) used the material balance method to quantitatively analyze hydrocarbon expulsion from source rocks in the Songliao Basin, and used the "over-pressure" module of PetroMod software to evaluate the over-pressure history of source rocks; Zhang et al. (2017) used constant water pressure and high water pressure experiments to simulate the pyrolysis of carbonaceous mudstones drilled in the Liaohe Basin, and the results showed that the number of hydrocarbon discharges had a significant contribution to the production of liquid hydrocarbons from hydrocarbon source rocks; Liu et al. (2017) established the evaluation method for hydrocarbon generating substances of marine carbonate source rocks by studying the matching relationship between the hydrocarbon source rocks in Tarim Basin and the oil and gas reservoirs in Tahe Oilfield; Pang et al. (2020) used the pyrolytic hydrocarbon generation potential index method and single-factor regression analysis to characterize the hydrocarbon generation and discharge of hydrocarbon source rocks in the Sichuan Basin and a quantitative model for the probability of reservoir formation under controlled systems; Tang et al. (2021)established evaluation criteria and hydrocarbon generation models for alkaline lacustrine hydrocarbon source rocks in the Mahu Depression of the Dzungar Basin. (Song et al., 2021).quantified the potential of different resource types in the Tsaidam Basin based on the geochemical and petrological characteristics of hydrocarbon source rocks combined with the buoyancy-driven hydrocarbon formation depth (BHAD) and the lower limit of movable resource abundance.

In recent years, some scholars have evaluated hydrocarbon source rocks in the Nanpu Sag, mainly including hydrocarbon source rock development sections, geochemistry and hydrocarbon production and discharge characteristics. (Guo et al., 2013). used a basin and hydrocarbon-bearing system modelling approach to study the hydrocarbon transport history of the Nanpu Sag, suggesting that hydrocarbon source rocks are mainly developed in Ed_3 of the Dongying Formation, Es_1 and Es_3 of the Shahejie Formation; Gang et al. (2021) conducted rock pyrolysis, gas chromatography-mass spectrometry, elemental geochemistry organic and inorganic analyses on several samples showing that the Es_3 section has higher organic carbon content than the Ed_3 and Es_1 sections, and the hydrocarbon source rocks have the highest hydrocarbon generation potential, with the Ed_3 and Es_1 section hydrocarbon source rocks being of type II_1-II_2, and the Es_3 section hydrocarbon source rocks being dominated by type II_2-III chevrons. (Pei et al., 2016). studied the genesis of oil reservoirs in four tectonic zones in the Nanpu Sag, pointing out that the hydrocarbon source rocks in the Ed_3 and Es_1 sections were deposited in a freshwater anoxic environment, and the hydrocarbon source rocks in the Es_3 section were deposited in a high salinity, anoxic interval, with a large contribution from terrestrial organic matter (TOM); Wei and Sun. (2017) concluded that the thickest effective hydrocarbon source rocks in the Ed_3 section are located in the Linque and Liunan sub depressions based on hydrocarbon source rock evaluation characteristic parameters and the oil source comparison method, and that the Caofeidian sub depression has greater exploration potential. (Wang et al., 2021). and (Zhu et al., 2013) considered the initial hydrogen index and conversion ratio during hydrocarbon source rock evolution based on the measured rock-eval pyrolysis data, which more realistically reflected the hydrocarbon generation and discharge history of hydrocarbon source rocks. For the study of the hydrocarbon source rocks in the Es_3sub-section of the Nanpu Sag, (Zuo et al., 2010), concluded that two hydrocarbon source foci developed early in the Es_3^2 of the Bohai Bay Basin, and that the Nanpu Sag was one of the main hydrocarbon source foci that evolved with geological evolution; Zhu et al. (2013) concluded that Es_3^4 is a high quality hydrocarbon source rock with an effective hydrocarbon source rock thickness of approximately 250 m through detailed comparative analysis of oil shale and crude oil biomarkers and isotopic signatures.

Although the evaluation of the key hydrocarbon source rock formations in the Nanpu Sag is based on certain research, the sub-sections of Es_3 with hydrocarbon generation potential are

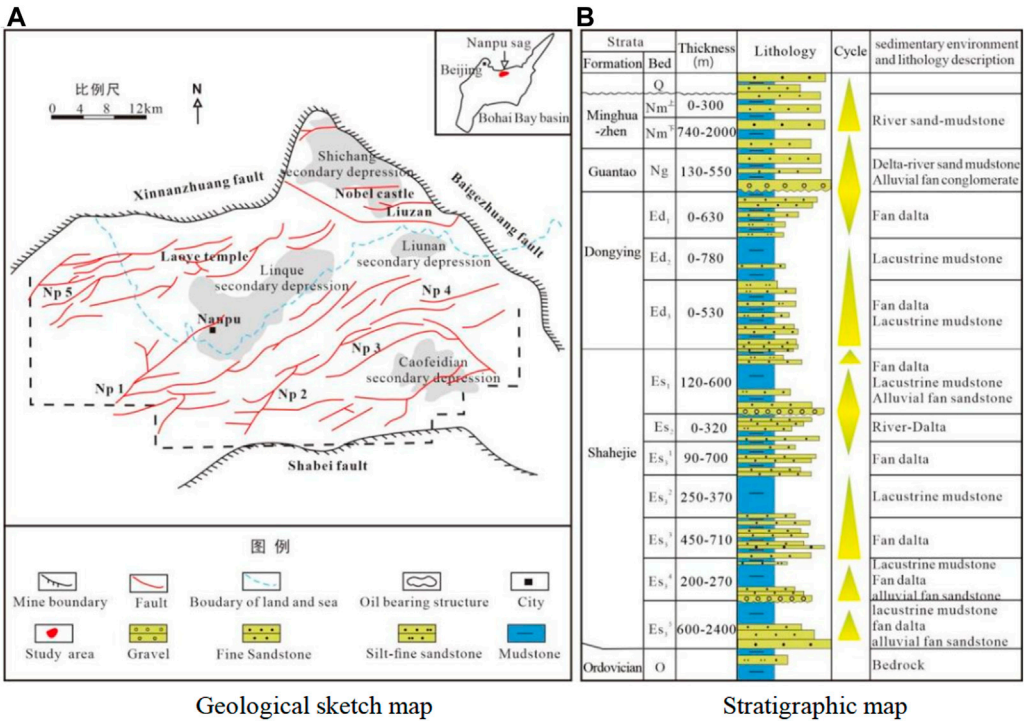

FIGURE 1
Structural and comprehensive geological histogram of the study area. **(A)** Geological sketch map **(B)** Stratigraphic map.

not studied in detail enough, resulting in a lack of clarity on the genesis type and resource potential of the tight oil system, which limits the further exploration of tight oil, therefore, the comprehensive evaluation system of hydrocarbon source rocks in each sub-section Es_3 of needs to be improved. In this paper, the hydrocarbon source rocks in the Es_3 section of the Nanpu Sag were evaluated and studied through a large number of sample analysis and testing experiments; a quantitative TOC prediction model for the Es_3 section was established based on the logging curves using the improved ΔlgR method and multiple linear regression method, and the key wells were selected to compare the predicted and measured TOC values. It also establishes a model for predicting the hydrocarbon generation potential of the Es_3 section hydrocarbon source rocks; finally, the organic carbon and hydrocarbon generation potential of each sub-section of Es_3 in the study area are predicted. It has important theoretical and application values for the evaluation of hydrocarbon resources and the next exploration direction in the Nanpu Sag.

2 Geological overview

The Nanpu Sag is located in the northeastern part of the Huanghua depression in the Bohai Bay basin. It has a tectonic pattern of northern fault and southern superstructure developed through the application of block faulting in the Middle and Cenozoic eras on the base of the North China Platform, covering an area of about 1930 km^2 (Li et al., 2010; Xu et al., 2010). The depression is mainly developed on the Southwest Zhuang, Baige Zhuang and Shabei boundary faults (Wang et al., 2020), and can be divided into four hydrocarbon bearing depressions, namely the Caofeidian sub depression, the Linque sub depression, the Liunan sub depression and the Shichang sub depression, and eight major tectonic zones, namely the Nanpu1-5, Laoyemiao, Gaoshangpu and Liuzan. The Caofeidian sub depression is located in the southern part of the Nanpu3 structure, the Linque sub depression is located in the southern part of the Laoyemiao structure, the Liunan sub depression is in the central part of the Nanpu4 and Liuzan structures, and the Shichang sub depression is located in the northern part of the Gaoshangpu structure (Cheng et al., 2022). The Nanpu Sag is characterized by a complex fracture system consisting of fractures of different levels and different time periods, and the fractures and their subdivisions form a complex fracture system (Figure 1A). The sedimentary rocks of the Nanpu Sag are up to 8000 m thick and consist of the Shahejie Formation (Es) and Dongying Formation (Ed) of the Palaeocene and the Minghuazhen Formation (Nm) and Tantao Formation (Ng) of the

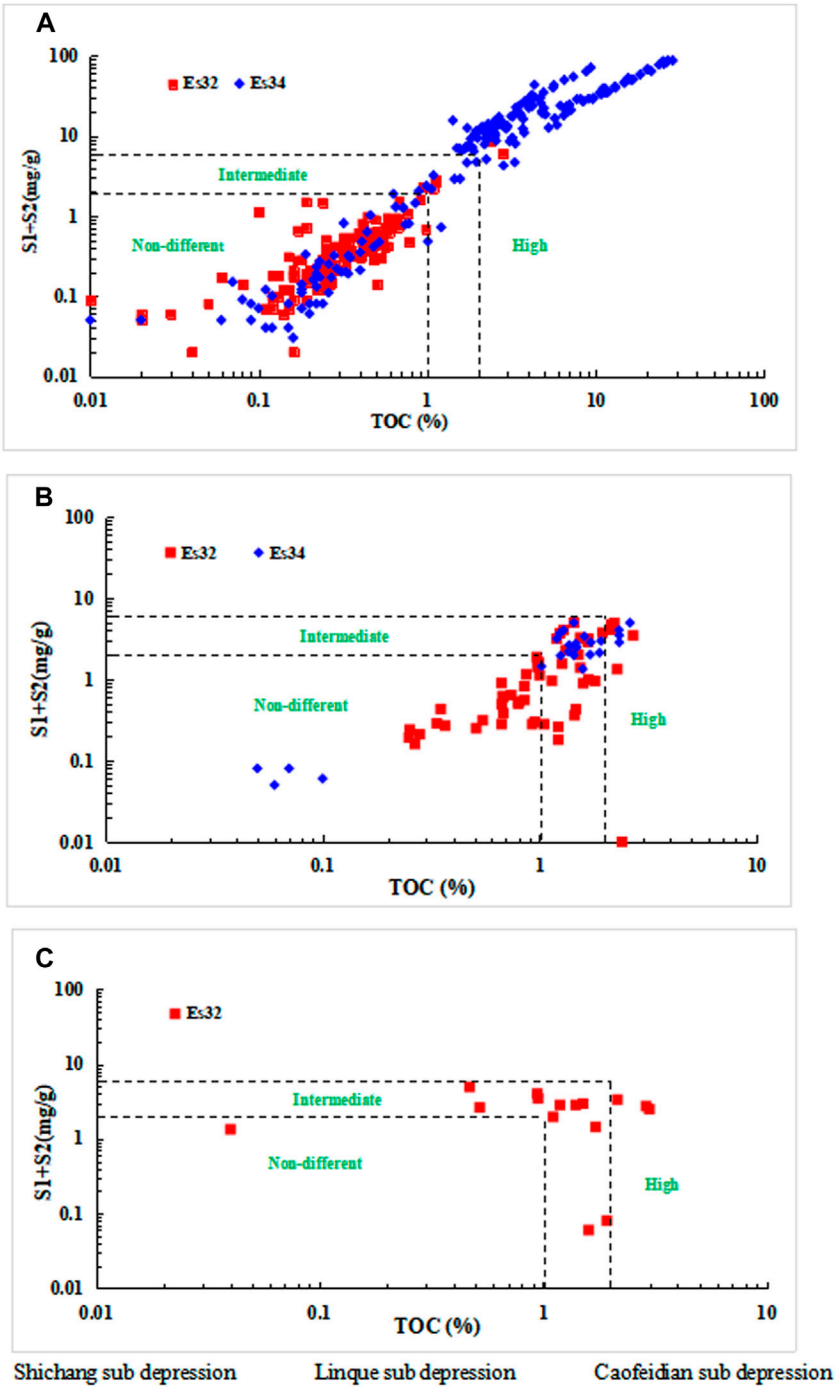

FIGURE 2
Statistical distribution map of organic matter abundance of Es_3 source rocks in different sub depressions of Nanpu Sag. **(A)** Shichang sub depression. **(B)** Linque sub depression. **(C)** Caofeidian sub depression.

Neoproterozoic (Chen et al., 2020). The Shahejie Formation stratigraphy can be divided into Es_1, Es_2, and Es_3. Among them, the Es_3 section is a shallow lake-deep lake, fan delta and alluvial fan deposition, which shows a complete secondary cycle of coarse lower, medium and fine upper, with a total thickness of 600–2000 m and an overall upward thinning. It is divided into five sub-sections (Es_3^5, Es_3^4, Es_3^3, Es_3^2, and Es_3^1) based on lithology from the bottom up (Figure 1B).

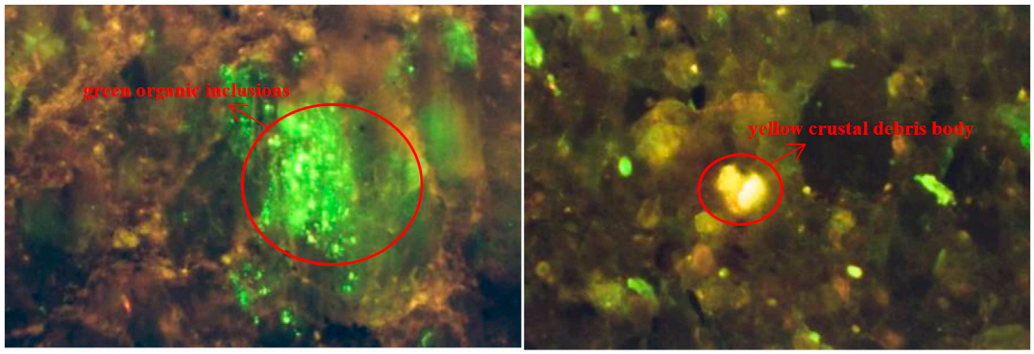

FIGURE 3
Group of maceral photographs of Es_3 source rocks in Nanpu Sag. **(A)** Nanpu280, Es_3^2, 4011.87 m green organic inclusions. **(B)** Liu15, Es_3^4, 4520.12 m yellow crustal debris body.

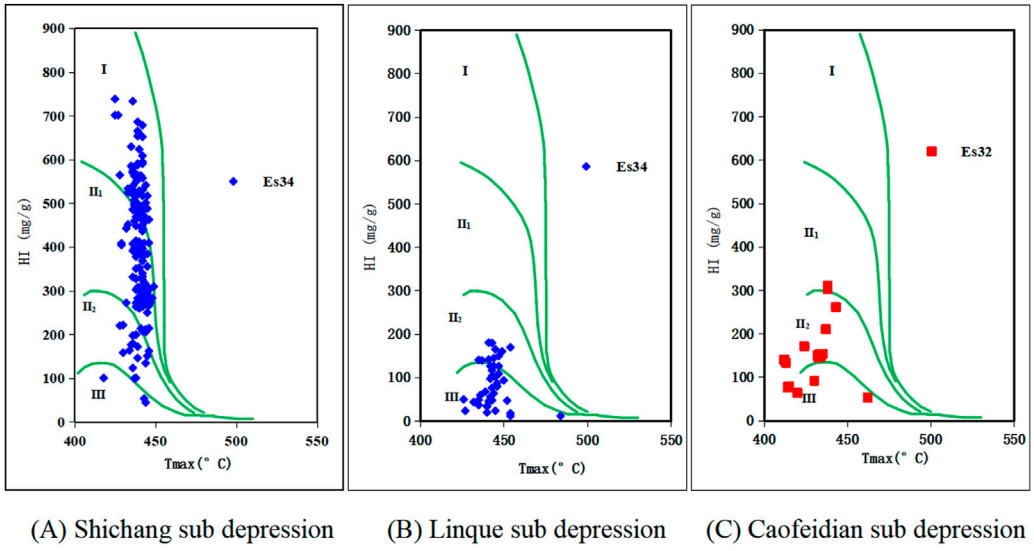

FIGURE 4
Classification of organic matter types of Es_3 source rocks in different sub depressions of Nanpu Sag. **(A)** Shichang sub depression. **(B)** Linque sub depression. **(C)** Caofeidian sub depression.

3 Hydrocarbon source rock evaluation

Three sets of hydrocarbon source rocks, Es_3^1, Es_3^2, and Es_3^4, are developed in the Es_3 section of the Nanpu Sag, of which Es_3^2 and Es_3^4 are the main hydrocarbon source rocks. This study focuses on the evaluation of the effective hydrocarbon source rocks in the Es_3^2 and Es_3^4 sections of the Shichang, Linque and Caofeidian sub depressions.

3.1 Organic matter abundance

Organic matter abundance refers to the enrichment of organic matter per unit mass of rock. Indicators that effectively reflect the organic matter abundance of hydrocarbon source rocks include organic carbon (TOC), hydrocarbon generating potential (S1+S2), chloroform bitumen "A" and total hydrocarbon (HC), *etc.* (Bojang and Xiongqi, 2014). According to the organic matter abundance

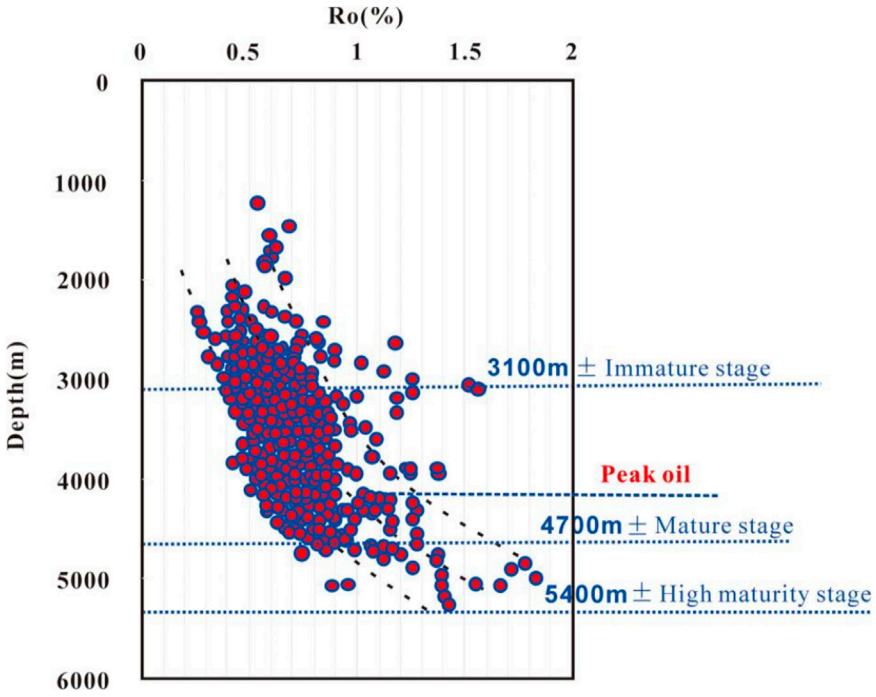

FIGURE 5
Relationship between R_o and depth of source rocks in Nanpu Sag.

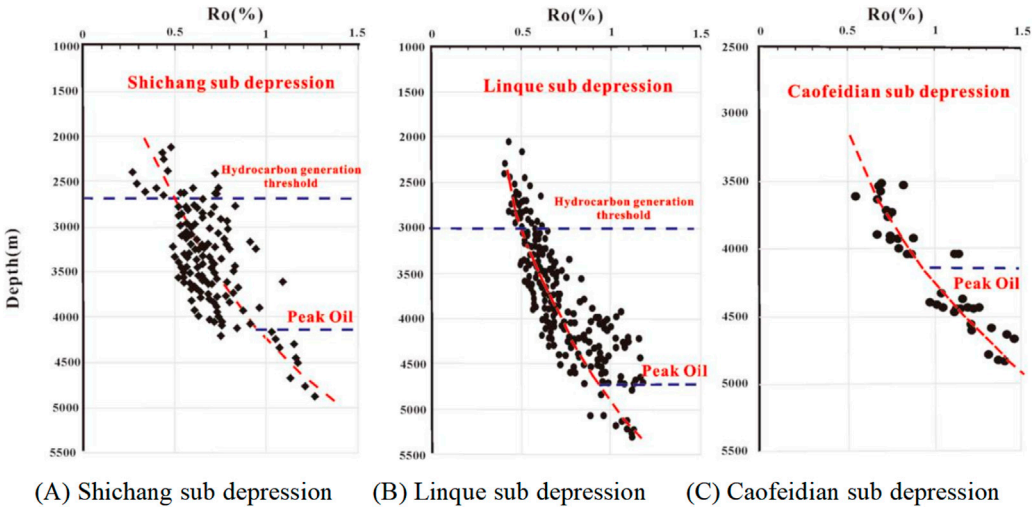

FIGURE 6
Relationship between R_o and depth of Es_3 source rocks in different sub-depressions of Nanpu Sag. **(A)** Shichang sub depression. **(B)** Linque sub depression. **(C)** Caofeidian sub depression.

distribution map, the organic carbon content of Es_3^2 is 0.12%–2.82%, with an average value of 0.41%; the hydrocarbon potential value is 0.10–9.21 mg/g, with an average value of 0.67 mg/g; the hydrocarbon source rock abundance of Es_3^2 is a poor hydrocarbon source rock, not the main hydrocarbon source rock section in Shichang sub depression. The organic carbon content of Es_3^4 is 0.21%–35.18%, with an average value of 4.13%. The organic carbon content of Es_3^4 ranges from 0.21% to 35.18%,

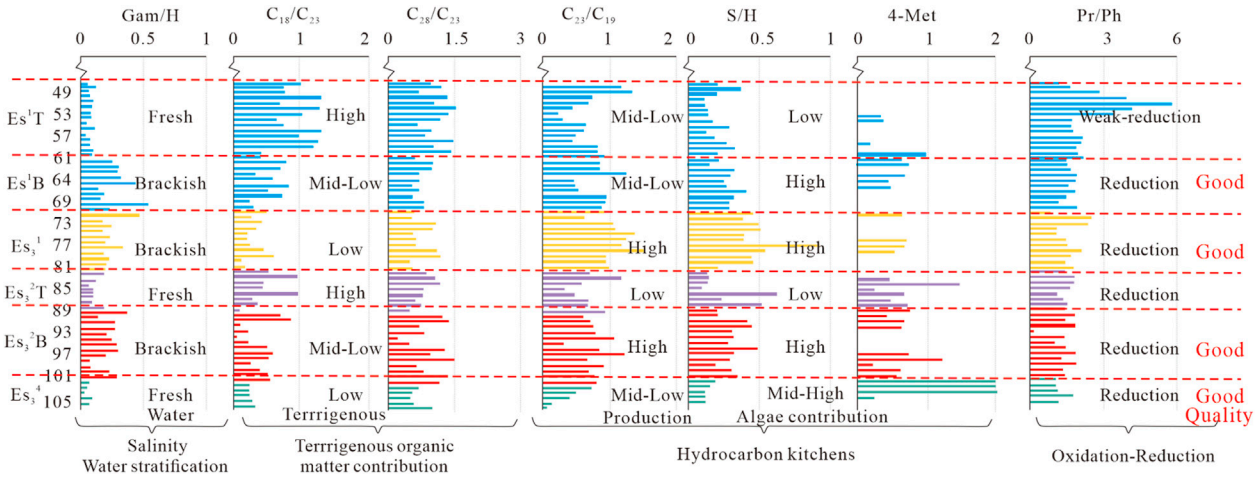

FIGURE 7
Characteristics of organic geochemical parameters of Es_3 source rocks of Nanpu Sag.

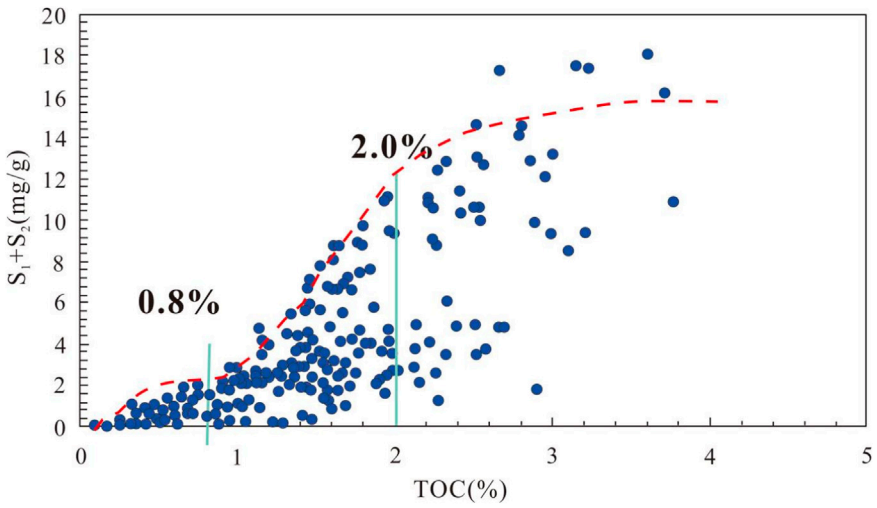

FIGURE 8
Relationship between S_1 + S_2 and TOC of Es_3 source rocks in Nanpu Sag.

with an average value of 4.13%; the hydrocarbon potential values are distributed from 0.20 to 105.1 mg/g, with an average value of 15.81 mg/g; Es_3^4 is the main hydrocarbon source rock section in Shichang sub depression (Figure 2A). The organic carbon content of section Es_3^2 in Linque Sub-pavement ranges from 0.25% to 2.71%, with a mean value of 1.16%; the hydrocarbon potential values are distributed from 0.18 to 4.97 mg/g, with a mean value of 1.46 mg/g. The organic carbon content of section Es_3^2 in Caofeidian sub depression ranges from 0.47% to 2.99%, with a mean value of 1.43%; the hydrocarbon potential values range from 0.56 to 9.92 mg/g, with a mean value of 3.46 mg/g; Es_3^2 section hydrocarbon source rocks are the main hydrocarbon source rock section of Linque and Caofeidian sub depression (Figures 2B,C).

3.2 Organic matter types

The organic matter type is one of the main indicators for classifying organic phases and evaluating the hydrocarbon generation potential of organic matter (Lu et al.,2012). The data collected show the following characteristics of the organic

TABLE 1 Identification criteria of Es_3 source rocks in Nanpu Sag.

Sub depression	Layer	Effective hydrocarbon source rock			High quality hydrocarbon source rocks		
		TOC (%)	S1+S2 (mg/g)	Ro (%)	TOC (%)	S1+S2 (mg/g)	Ro (%)
Shichang	Es_3	>.8	>2	>0.5	>2.0	>6	>.7
Linque		>.8	>2	>0.5	>2.0	>6	>.7
Caofeidian		>.8	>2	>0.5	>2.0	>6	>.7

microfraction: the specular group is generally low in content, grey in oil-immersion reflected light, and the specular bodies do not fluoresce; the inert group is slight in content, with grey-white filamentous bodies predominating in oil-immersion reflected light; the crustacean group has mainly laminar algal bodies, microsporidia yellow (Figure 3A), fluorescent microsporidia, mostly occurring as flat rings and worms, a few greenish-yellow fluorescent, striped thin-walled keratophores; mineral asphalt matrixmostly disperse, crustacean; very few fluorescent bodies with strong green fluorescence (Figure 3B). In this study, the main method of pyrolysis analysis was used to classify the organic matter types of hydrocarbon source rocks in the Nanpu Sag. The hydrogen index HI of hydrocarbon source rock pyrolysis can classify the type of organic matter. The temperature Tmax corresponding to the appearance of the P_2 peak during pyrolysis can determine the maturity of organic matter, and the organic matter type of hydrocarbon source rock can be judged by making an intersection diagram between the hydrogen index and Tmax. The rock pyrolysis analysis shows that the best organic matter type is found in the Es_3^4 section of the Shichang sub depression (Figures 4A,B), dominated by type I~II_2, with the least terrestrial supply; the hydrocarbon source rocks in the Linque and Caofeidian sub depression Es_3^2 sections have more contribution from higher plants (Figure 4C), and the organic matter type is dominated by type II_2~III mixed cheese roots.

3.3 Organic matter maturity

The abundance of organic matter determines the amount of hydrocarbon producing material base of the hydrocarbon source rock, the type of organic matter determines the hydrocarbon producing potential of the hydrocarbon source rock, and the ability to produce oil or gas is closely related to the degree of thermal evolution of the organic matter (Xia et al., 2019). The Specular body reflectance (Ro) is currently the most common method for determining the maturity of organic matter. According to the measured data (Figure 5), the Specular body reflectance (Ro) of hydrocarbon source rocks in the Nanpu Sag is mainly distributed in the range of 0.25%–1.75%. Ro is distributed in the depth range of 2000–5500 m, and the relationship with depth is not very clear, even the shallow part is higher than the deep part of Ro. This is mainly due to the influence of the igneous rocks prevalent in the Nanpu Sag. Leaving aside the anomalies influenced by igneous rocks, the conventional peak oil generation should correspond to a depth of roughly 4200 m, with the angry phase being deeper. According to the trend of Ro, the immature stage is not indicated, and the boundary between the low and mature stages is roughly around 3100 m depth.

The reflectance data of the specular bodies were analyzed by different sub depression sub-tectonic zones, in different tectonic zones of the Nanpu Sag, there are some differences in the rate of increase of Ro with increasing depth of the strata. The hydrocarbon source rocks in the Es_3^4 section of the Shichang sub depression are all in the mature stage, with a hydrocarbon generation limit of about 2700 m and a peak oil generation at about 4200 m (Figure 6A). The hydrocarbon source rocks in the Es_3^2 section of the Linque sub depression are in the mature stage, with a hydrocarbon generation limit of about 3000 m and a peak oil generation at about 4700 m (Figure 6B). The hydrocarbon source rocks of section Es_3^2 in Caofeidian sub depression have entered the mature stage, with hydrocarbon generation threshold less than 3500 m and oil generation peak at 4200 m (Figure 6C).

3.4 Biomarker characteristics

Biomarker compounds are derived from organisms that have lived (especially lipid-like compounds) and are complex molecular fossils. The parameters basilane/phytane (Pr/Ph), sterane/hoxane (S/H), C_{19} tricyclic terpene/C_{23} tricyclic terpene (C_{19}/C_{23}TT), C_{20} tricyclic terpene/C_{23} tricyclic terpene (C_{20}/C_{23}TT), C_{27}/C_{29} rule sterane parameters, gammacerane index (gammacerane/αβ-C_{30}holo) and 4-methyl sterane (4MSI) were selected as the seven parameters are used to distinguish the organic geochemical characteristics of the hydrocarbon source rocks in each sub-section of theEs_3. The study shows (Figure 7) that there are significant differences between the Es_3^2 and Es_3^4 sections mainly in terms of water properties and biogenic composition. The mean Pr/Ph value of the hydrocarbon source rocks in the Es_3^2 section is 1.8, the weakly reduced water environment, the mean Gam/H index is 0.22, the mean C_{27}/C_{29} sterane value is 0.85, the mean C_{19}/C_{23} and C_{20}/C_{23} tricyclic terpene parameters are 0.39 and 0.93 respectively; the mean S/H value is 0.31. The developmental environment is generally a reduced environment with semi-saline, low to medium terrestrial organic

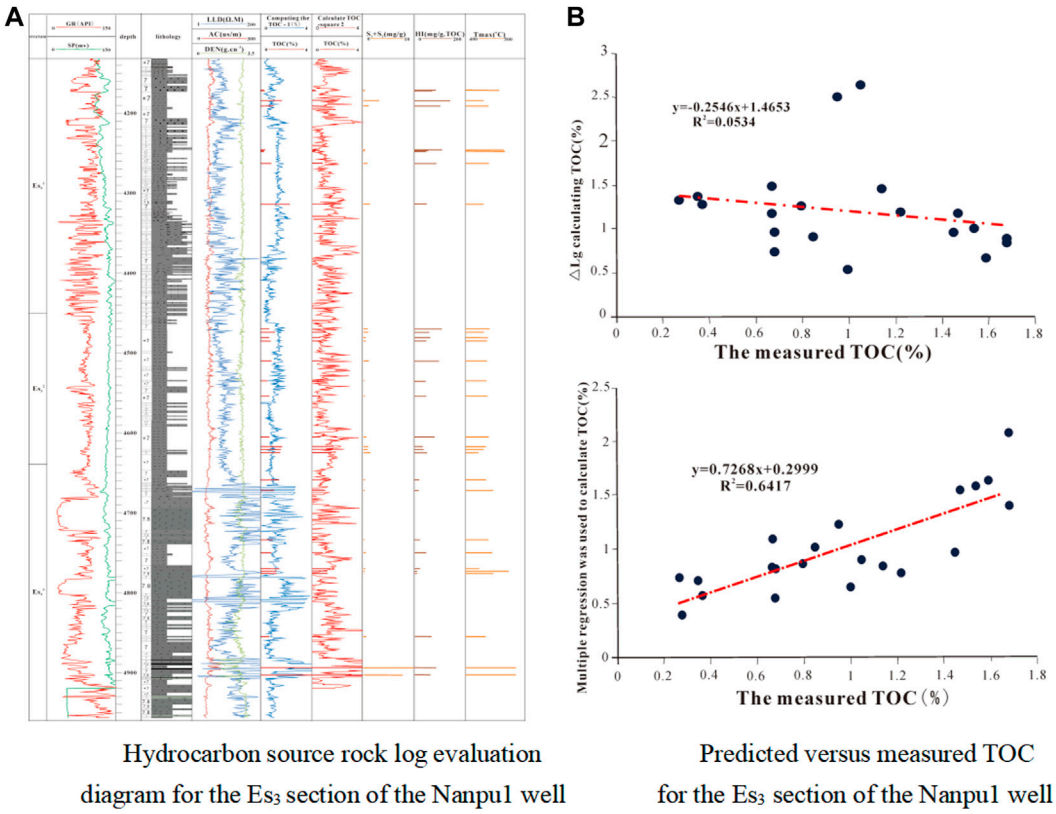

FIGURE 9
The diagram of logging evaluation and relationship between prediction and measured of Es_3 source rock in well Nanpu1. **(A)** Hydrocarbon source rock log evaluation diagram for the Es_3 section of the Nanpu1 well. **(B)** Predicted versus measured TOC for the Es_3 section of the Nanpu1 well.

matter supply and a large contribution from algae. Es_3^4 section hydrocarbon rock Pr/Ph mean 1.2, weak reduction-reduction water environment, Gam/H index mean 0.05, C_{27}/C_{29} sterane mean 0.43, C_{19}/C_{23} and C_{20}/C_{23} tricyclic terpene parameter means 0.23 and 0.56 respectively; S/H mean 0.13. Although organic matter productivity was not prominent, the contribution of methanogens was evident and generally formed in a freshwater, low terrestrial supply reduction environment with a medium-high algal contribution.

4 Hydrocarbon generation potential prediction model

4.1 Effective hydrocarbon source rock identification

The identification of effective hydrocarbon source rocks is mainly evaluated in terms of organic matter abundance, organic matter type and maturity of hydrocarbon source rocks, which require the three conditions of being rich in organic matter, having reached maturity stage and being able to discharge hydrocarbons effectively at the same time (Hou et al.,2015). The inflection point where the hydrocarbon production potential (S_1 + S_2) changes with the abundance of hydrocarbon source rocks will produce obvious inflection points (Figure 8). The inflection point where the hydrocarbon production potential increases significantly is usually taken as the discriminatory limit for effective hydrocarbon source rocks, while the inflection point where the hydrocarbon production potential no longer increases significantly is taken as the discriminatory limit for high-quality hydrocarbon source rocks. The parameters for identifying hydrocarbon source rocks in the Es_3 section were determined by subdividing the Nanpu Sag, and the criteria for identifying hydrocarbon source rocks in the study area were established (Table 1). The lower limit of hydrocarbon source rock abundance in the Es_3 section is TOC >0.8%, and the lower limit of high quality hydrocarbon source rock abundance is TOC >2.0%.

4.2 TOC prediction model

The main methods for quantitative evaluation of hydrocarbon source rocks based on logging data are ΔlgR method, multiple linear regression method and CNN neural

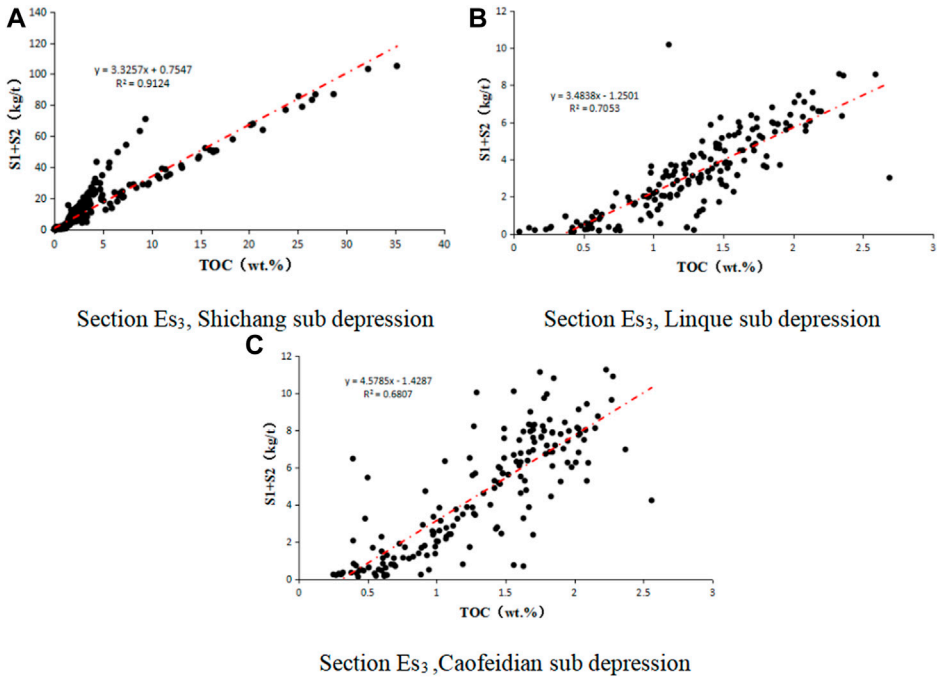

FIGURE 10
Cross plot of measured TOC and S_1+S_2 of Es_3 source rocks in different sub depressions of Nanpu Sag. **(A)** Section Es_3, Shichang sub depression. **(B)** Section Es_3, Linque sub depression. **(C)** Section Es_3 , Caofeidian sub depression.

network method, *etc.* Although the CNN neural network method has greater advantages in solving non-linear complex problems, it is difficult to express them in expressions. Currently, multiple linear regression and ΔlgR methods are widely used in the quantitative prediction and evaluation of hydrocarbon source rocks.

1) ΔlgR

The ΔlgR method was originally proposed by Passey et al. Based on the theory of qualitative identification of hydrocarbon source rocks by natural gamma curves, two curves of sonic time difference and resistivity are applied, and when the rocks are fine-grained and non-hydrocarbon source rocks, these two logging curves overlap together to show the baseline, and the difference in magnitude between the two curves is the ΔlgR value. The model can effectively eliminate the porosity on the logging response value of organic carbon content The effect of Eq:

$$\Delta \log R = \log\left(R/R_b\right) + x \times \left(\Delta t - \Delta t_b\right)$$

The ΔlgR method was used to predict the TOC content of hydrocarbon source rocks using the equation.

$$TOC = \left(\Delta \log R\right) \times 10^{2.297 - 0.1688Ro}$$

To avoid the uncertainty that arises when manually superimposing the acoustic and resistivity curves, the ΔlgR equation is deformed as follows.

$$TOC = a \times \lg R + b \times \Delta t + c$$

where R is the resistivity, R baseline is the resistivity of the non-hydrocarbon source rock section, Δt is the acoustic time difference, Δt baseline is the acoustic time difference of the non-hydrocarbon source rock section, x is the coefficient, R_o is the organic matter maturity index, and the values of a, b and c can be obtained by analysis of samples from the study area and fitting with least squares.

Considering that the lithological combination and maturity of hydrocarbon source rocks under different sedimentary phase zones in different areas of the Nanpu Sag may cause differences in logging response, in order to improve the TOC logging prediction model in the study area, the actual hydrocarbon source rock sample points and logging parameters were counted in the Linque sub depression, Caofeidian sub depression and Shichang sub depression respectively, and regression analysis was carried out according to the above equation to obtain the TOC prediction models for different sub depressions Es_3 sections in turn, although there are some differences in the prediction models in different areas, the

TABLE 2 Prediction model of hydrocarbon generation potential of Es_3 source rocks of Nanpu Sag.

Sub depression	Layer	S1+S2 quantitative forecasting model	Correlation coefficient
Shichang	Es_3	S1+S2=3.3257*TOC+0.7547	0.912
Linque		S1+S2=3.4828*TOC-1.2501	0.705
Caofeidian		S1+S2=4.5785*TOC-1.4287	0.681

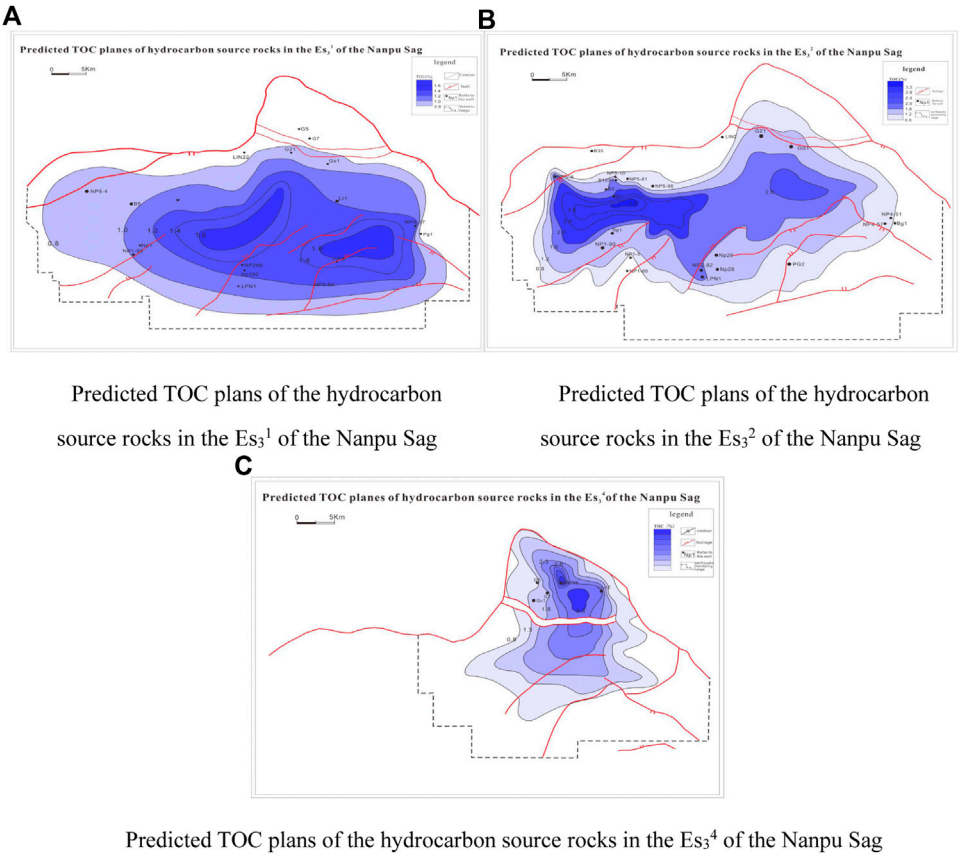

FIGURE 11
TOC planimetry of Es_3 source rocks in different sub depressions of Nanpu Sag. **(A)** TOC planimetry of the hydrocarbon source rocks in the Es_3^1 sub depression. **(B)** TOC planimetry of the hydrocarbon source rocks in the Es_3^2 sub depression. **(C)** TOC planimetry of the hydrocarbon source rocks in the Es_3^4 sub depression.

correlation coefficient of the ΔlgR method TOC prediction model for the Nanpu Sag is generally around 0.65.

2) Multiple linear regression

Multiple linear regression is to take hydrocarbon source rock TOC as the dependent variable and multiple logging parameters that correlate well with TOC as independent variables to establish multiple regression equations, and determine the best TOC quantitative prediction model through multiple regression analysis. The hydrocarbon source rocks in the Es_3 section of the Nanpu Sag are characterized by high natural gamma, high acoustic time difference, high resistivity and low density in the logging curve response. The high gamma of hydrocarbon source rocks is due to the small particle size and large specific surface area of hydrocarbon source rocks, which adsorb more radioactive element uranium; the high resistivity is due to the presence of organic matter with poor electrical conductivity in high quality hydrocarbon source rocks, resulting in a large resistivity; the high acoustic time difference value between

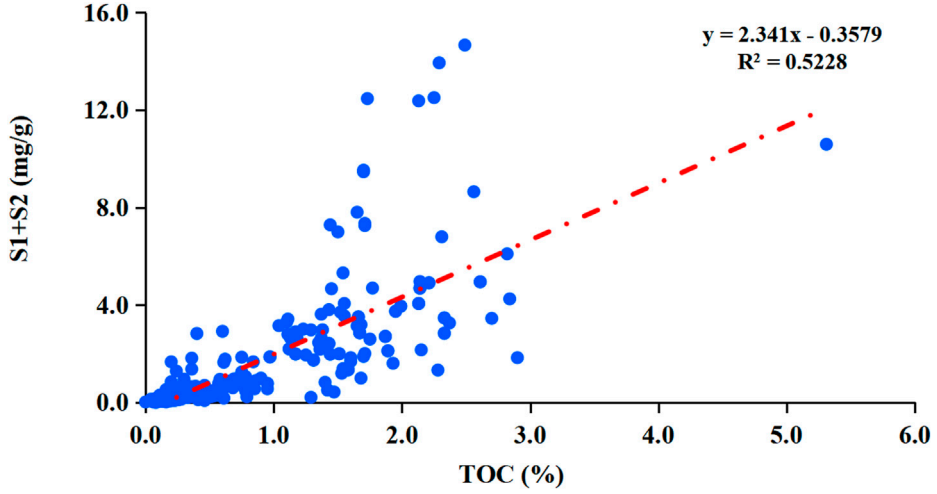

FIGURE 12
Linear diagram of TOC and S_1 + S_2 of Es_3 source rocks of Nanpu Sag.

organic matter and oil and gas in hydrocarbon source rocks is larger than the rock skeleton will cause the increase of acoustic time difference (AC) in the formation; the density of organic matter in hydrocarbon source rocks (1.1–1.4 g/cm ^{3}) is much lower than that of quartz and clay, so the density logging values (DEN) show low values. Based on the measured TOC of hydrocarbon source rocks in the Nanpu Sag and the five logging parameters, GR, AC, RT, DEN, and SP, using data analysis tools, a multiple regression model was constructed.

$$TOC = a \times GR + b \times AC + c \times RT + d \times DEN + e \times SP + f$$

Where: a, b, c, d and e are constants; f is the random error.

To improve the accuracy of the prediction formulae, the measured TOC data and corresponding logging parameters in the study area were statistically grouped separately according to different blocks.

To verify the accuracy of the two methods, a single well with more geochemical analysis data was selected to compare the predicted TOC values with the measured TOC values. The Nanpu1 well is located near the SW1 tectonic zone in the Linque sub depression. The well has more organic carbon analysis data in the Es_3 section and the logging data is of good quality. The organic carbon logging response model (Figure 9A) shows that the measured organic carbon distribution in the Es_3^1 and Es_3^2 sections of the Nanpu1 well ranges from 0.35% to 1.68%, with an average value of 0.97%. The interpretation of the logs showed that the correlation coefficient between TOC and measured TOC calculated by the ΔlgR model was 0.23, while the correlation coefficient between TOC and measured TOC calculated by the multiple linear regression model was 0.801. It can be seen visually (Figure 9B) that the comparison between the predicted TOC and measured TOC by the multiple linear regression method also revealed a better agreement between the two, indicating that the multiple linear regression The comparison between the TOC predicted by the multiple linear regression method and the measured TOC also reveals a better agreement between the two, indicating that the multiple linear regression method is better than the ΔlgR method in predicting the hydrocarbon source rocks in the Es_3 section of the Nangpu1 well in the Linque sub depression, with a higher prediction accuracy.

4.3 Hydrocarbon generation potential prediction model

In this study, the total organic carbon content (TOC) and rock pyrolysis hydrocarbon potential (S_1+S_2) of the measured hydrocarbon source rock samples from the Es_3 section of Shichang, Linque and Caofeidian sub depression were calculated and correlation analysis was performed to predict the hydrocarbon potential of the Es_3 hydrocarbon source rock.

As can be seen from the rendezvous plot (Figure 10), the measured geochemical parameters TOC of Es_3 hydrocarbon source rock samples in the study area show a good positive correlation with S1 + S2, with the best correlation between TOC and S1 + S2 in the Shichang sub depression and the next best correlation in the Linque sub depression. The correlation coefficients are 0.912, 0.705, and 0.681 for Shichang.

Linque and Caofeidian respectively. The multiple regression method of logging parameters can predict the TOC of hydrocarbon source rocks in the study area more accurately, so the predicted TOC can be used to predict the hydrocarbon generation potential again, and the model for predicting the hydrocarbon generation potential is as follows.

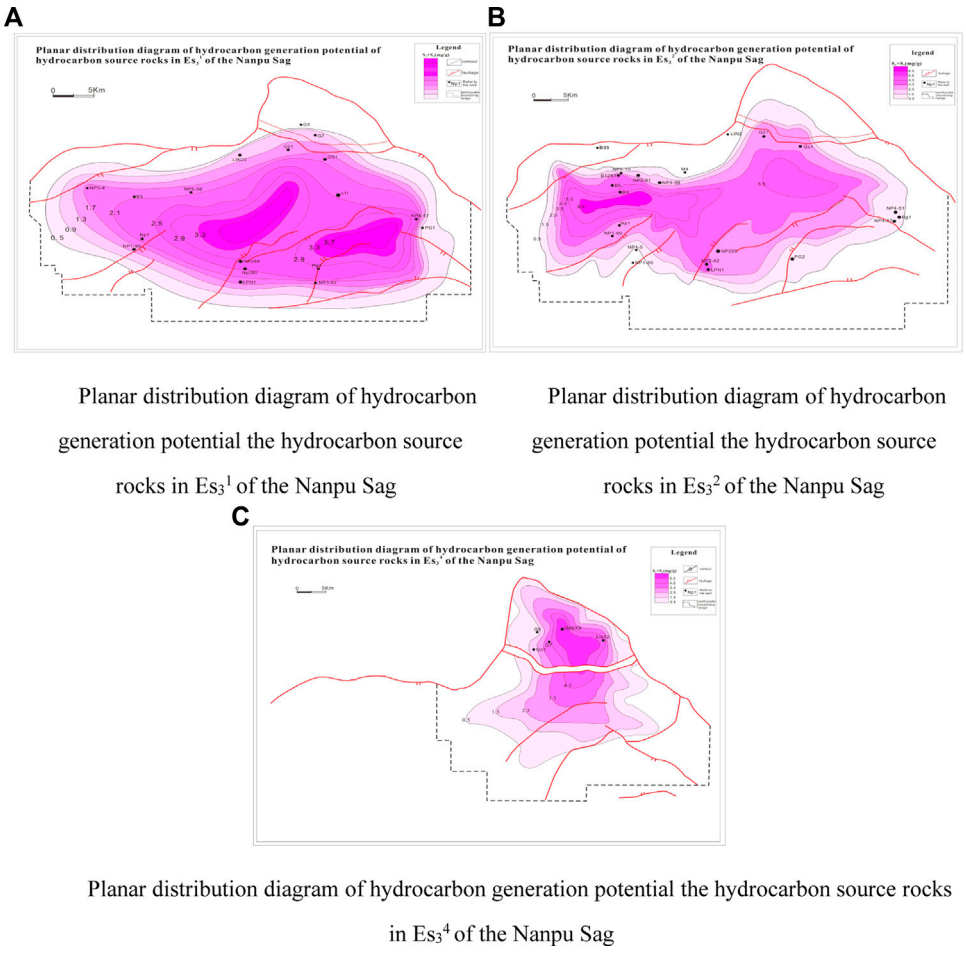

Planar distribution diagram of hydrocarbon generation potential the hydrocarbon source rocks in Es_3^1 of the Nanpu Sag

Planar distribution diagram of hydrocarbon generation potential the hydrocarbon source rocks in Es_3^2 of the Nanpu Sag

Planar distribution diagram of hydrocarbon generation potential the hydrocarbon source rocks in Es_3^4 of the Nanpu Sag

FIGURE 13
Plane prediction map hydrocarbon generation potential of Es_3 source rocks of Nanpu Sag. **(A)** Plan view of the hydrocarbon potential of the Es_3^1 sub-section. **(B)** Plan view of the hydrocarbon potential of the Es_3^2 sub-section. **(C)** Plan view of the hydrocarbon potential of the Es_3^4 sub-section.

$$S_1 + S_2 = a \times TOC + b$$

Where: a is a constant; b is a random error. a and b values can be obtained by analysing samples from the study area with a linear fit, and the final model for predicting the hydrocarbon generating potential of the Es_3 section of the Nanpu Sag is obtained (Table 2).

5 Predicted planar distribution of hydrocarbon source rocks

5.1 Predicted organic carbon planes

The prediction of total organic carbon in hydrocarbon source rocks in the study area is mainly based on the method of point-controlled pits and pits-controlled surface. Firstly, the predicted wells controlling each sub depression were selected and the median of the predicted TOC curve of a single well was calculated as the TOC value of that well. The trend of TOC between wells is combined with the trend of TOC between wells to control the internal spreading of each tectonic zone and sub depression. Finally, the TOC of each tectonic zone and sub depression is linked with the sedimentary phase spread to produce a TOC contour map for that section of the formation.

TOC values for hydrocarbon source rocks in the Es_3^1 section are generally not high, with predicted TOC greater than 2.0% area, and only relatively high areas exist in the Linque sub depression and Caofeidian sub depressions, with overall TOC between 1.4% and 1.6% (Figure 11A). The TOC in the No. 5 tectonic zone ranges from 0.8% to 1.0%; in the slope area between No. 1 and No. 3 tectonic zone, the TOC ranges from 0.8% to 1.2%, gradually decreasing from the Linque sub depression to the slope; the TOC in the Liunan sub

depression is around 1.0%; and the TOC in the Shichang sub depression is generally low, basically not reaching the lower limit of 0.8% effective hydrocarbon source rock.

The high value hydrocarbon source rocks of Es_3^2 section are mainly concentrated between the No. 5 and No. 1 tectonic zones in the Linque sub depression and the Liunan sub depression (Figure 11B). The high TOC values in the Linque sub depression trend nearly east-west, with TOC ranging from 2.0% to 3.2%; the Linque sub depression TOC ranging from 1.6% to 2.0%; the Shichang sub depression TOC values ranging from 0.8% to 1.2%; and the Caofeidian sub depression TOC values ranging from 0.8% to 1.2%.

The area of high TOC values for hydrocarbon source rocks in the Es_3^4 section is mainly concentrated in the Shichang sub depression (Figure 11C), with average values ranging from 1.3% to 4.3%, with the highest TOC of 35% in well G66x9; the overall TOC is slightly lower in the Linque sub depression area, ranging from 1.3% to 2.0%.

5.2 Hydrocarbon potential plane projection

The regression of the single well measured and predicted TOC against the single well $S_1 + S_2$ was used to establish the hydrocarbon source rock relationship for the Es_3 section (Figure 12). The linear relationship was combined with the TOC prediction results to predict the hydrocarbon potential of each layer and then combined with the single well control to obtain a hydrocarbon potential plan.

The hydrocarbon source rocks in the Es_3^1 section have relatively low hydrocarbon generation potential, with $S_1 + S_2$ at a maximum of 4.0 mg/g, mainly concentrated in the Linque sub depression and Caofeidian sub depression (Figure 13A). The north-west oriented hydrocarbon source rocks are relatively high between the No. 2 and No. 3 structures in the Linque sub depression, with $S_1 + S_2$ at 3.0–4.0 mg/g; the $S_1 + S_2$ in the Caofeidian sub depression is 3.0–4.0 mg/g, and the high value area is obviously controlled by faults and spreads in an east-west direction; the $S_1 + S_2$ in the No. 5 tectonic zone is between 0.5 and 2.5 mg/g, and the hydrocarbon generation potential has a trend of low in the west and high in the east; the $S_1 + S_2$ in the Liunan sub depression is 0.5–2.5 mg/g, and the $S_1 + S_2$ in the Liunan sub depression is 0.5–2.5 mg/g. $S_1 + S_2$ is between 0.5 and 2.5 mg/g, and the hydrocarbon potential gradually decreases from southwest to northeast.

Es_3^2 section hydrocarbon source rocks $S_1 + S_2$ reach 3.5 mg/g in the vicinity of Linque sub depression, Liunan sub depression and No. 2 tectonic zone (Figure 13B). Among them, the east-west trending high hydrocarbon potential zone is developed between the No. 5 tectonic zone and No. 1 tectonic zone in Linque sub depression, with $S_1 + S_2$ between 5.5 and 6.5 mg/g; $S_1 + S_2$ in Liunan sub depression is between 5.5 and 6.0 mg/g; Caofeidian sub depression has low hydrocarbon potential, with S_1+S_2 between 1.5 and 3.5 mg/g.

The high hydrocarbon potential of the Es_3^4 section is mainly concentrated in the Shichang sub depression, with $S_1 + S_2$ ranging from 5.5 to 6.0 mg/g in the central sub depression area, including up to 36.0 mg/g in well G66x9 $S_1 + S_2$. The hydrocarbon potential decreases to the south, with $S_1 + S_2$ ranging from 2.5 to 4.5 mg/g in the Liunan sub depression area (Figure 13C).

6 Conclusion

1) The lower limit of hydrocarbon source rock abundance in the Es_3 section is TOC >0.8%; the lower limit of high quality hydrocarbon source rock abundance is TOC >2.0%; by establishing a quantitative TOC prediction model and selecting a single well with more geochemical analysis data to compare the predicted TOC with the measured TOC values, it is found that the multiple linear regression method is more effective than the ΔlgR method in predicting hydrocarbon source rocks in the Nanpu Sag. The results show that the multiple linear regression method is more effective and more accurate than the ΔlgR method in predicting hydrocarbon source rocks in the Nanpu Depression.
2) Total organic carbon content (TOC) and rock pyrolysis hydrocarbon potential ($S_1 + S_2$) were calculated for the core samples from Shichang, Linque and Caofeidian sub depressions, respectively, and correlation analysis was performed to establish a hydrocarbon potential prediction model. The best correlation between TOC and $S_1 + S_2$ was found in Shichang sub depression, and the second best correlation was found in Linque sub depression.
3) The TOC values and hydrocarbon potential of the hydrocarbon source rocks in section Es_3^1 are generally low, mainly concentrated in the Linque and Caofeidian sub depressions; the high TOC values and hydrocarbon potential of the hydrocarbon source rocks in section Es_3^2 are partly between the No. 5 and No. 1 tectonic zones in the Linque sub depression, and the TOC values and hydrocarbon potential of the Liunan sub depression as a whole are high; the high TOC values and hydrocarbon potential of the hydrocarbon source rocks in section Es_3^4 are mainly concentrated in the Shichang sub depression. The Es_3 section hydrocarbon source rocks have high TOC values and hydrocarbon potential mainly in the Shichang sub depression.

Data availability statement

The original contributions presented in the study are included in the article/Supplementary Material, further inquiries can be directed to the corresponding author.

Author contributions

QG: Methodology and validation; SJ: Supervision, review and editing; QZ: Methodology and software; YG: Sample collection and experimentation; JW: Sample analysis and validation; LY: Graphical collation and software; JY: Experimentation.

Acknowledgments

Thank you to the reviewers HC and WD for their constructive comments on this paper.

Conflict of interest

The authors declare that the research was conducted in the absence of any commercial or financial relationships that could be construed as a potential conflict of interest.

Publisher's note

All claims expressed in this article are solely those of the authors and do not necessarily represent those of their affiliated organizations, or those of the publisher, the editors and the reviewers. Any product that may be evaluated in this article, or claim that may be made by its manufacturer, is not guaranteed or endorsed by the publisher.

References

Bojang, F., and Xiongqi, P. (2014). Hydrocarbon expulsion quantity of source rock, Nanpu sag, Bohai Bay Basin, China. *Petroleum Sci. Technol.* 32, 1690–1696. doi:10.1080/10916466.2011.572109

Chen, J. Y., Xiong, S. Q., and Bi, Y. P. (2000). Characteristics of hydrocarbon-bearing systems in fractured basins. *J. Petroleum* 2, 36–41+3.

Chen, X., Jiang, F. J., and Zhao, Z. X. (2020). Hydrocarbon discharge characteristics of hydrocarbon source rocks in the east third section of the Dongying Formation, Nanpu Sag, Bohai Bay Basin. *Sci. Technol. Eng.* 20, 5566–5574.

Cheng, D. H., Jiao, X. R., and Wang, J. W. (2022). Huang Hua was trapped in the southern castle, the ancient near the sand section of the shale oil reservoir characteristics and oil and gas significance. *Rocky Reserv.* 34, 70–81.

Cheng, D. S., Dou, L. R., and Wang, J. C. (2021). Evaluation of hydrocarbon source rocks and oil source analysis in the Doseo Basin, Chad. *J. Geol.* 95, 413–3425.

Dang, W., Zhang, J. C., Tang, X., Chen, Q., Han, S., Li, Z., et al. (2016). Shale gas potential of Lower Permian marine-continental transitional black shales in the Southern North China Basin, central China: Characterization of organic geochemistry. *J. Nat. Gas Sci. Eng.* 28, 639–650. doi:10.1016/j.jngse.2015.12.035

Fu, X. D., Zhang, T. F., and Wu, J. P. (2021). Characteristics and main controlling factors of tight oil reservoirs in Cretaceous Tengger Formation, A'nan Sag. *Erlian Basin Petroleum Geol. Exp.* 43 (1), 64–76. doi:10.11781/sysydz202101064

Gang, W. Z., Guo, Y., Gao, G., Yang, S., Jiang, C., Chen, G., et al. (2021). An integrated organic-inorganic geochemical characterization of Paleogene sediments in No.1 Structural Belt of the Nanpu Sag, Bohai Bay Basin, eastern China: implications for the origin of organic matter. *Geochem. Explor. Environ. Anal.* 21. doi:10.1144/geochem2019-060

Guo, S. B. (2006). Stratigraphic model of stratigraphic sequence in terrestrial fault basins. *Petroleum Explor. Dev.* 5, 548–552.

Guo, Y. C., Pang, X. Q., Dong, Y. X., Jiang, Z., Chen, D., and Jiang, F. (2013). Hydrocarbon generation and migration in the Nanpu Sag, Bohai Bay Basin, eastern China: Insight from basin and petroleum system modeling. *J. Asian Earth Sci.* 77, 140–150. doi:10.1016/j.jseaes.2013.08.033

Guo, Y. L., Liu, C. R., and Li, H. M. (2021). Effective techniques for seismic description of reservoirs in jiyang depression, Bohai Bay Basin. *Petroleum Geol. Exp.* 43, 121–127.

Han, S. B. A., Zhang, J. C., Yang, C., Bai, S., Huang, L., Dang, W., et al. (2016). Well log evaluation of shale gas reservoirs and preservation conditions of Lower Cambrian shale succession inCengong Block of southeast Sichuan basin, south China. *J. Nat. Gas Sci. Eng.* 33, 337–346. doi:10.1016/j.jngse.2016.05.019

Hou, Z. P., Pang, X. Q., Ouyang, X. C., Zhang, B., Shen, W., Guo, F., et al. (2015). Upper limit of maturity for hydrocarbon generation in carbonate source rocks in the Tarim Basin Platform, China. *Arab. J. Geosci.* 8, 2497–2514. doi:10.1007/s12517-014-1408-9

Hu, C. Y. (1982). Oil-bearing zones control the distribution of oil and gas fields-an effective theory for regional exploration in the terrestrial basins of eastern China. *J. Petroleum* 2, 9–13.

Huang, W. B., Hersi, O. S., Lu, S. F., and Deng, S. (2017). Quantitative modelling of hydrocarbon expulsion and quality grading of tight oil lacustrine source rocks: Case study of Qingshankou 1 member, central depression, Southern Songliao Basin, China. *Mar. Petroleum Geol.* 84, 34–48. doi:10.1016/j.marpetgeo.2017.03.021

Kang, H. Q. (2021). Controlling factors of hydrocarbon source rock development in the Madingo Formation of the Lower Congo Basin and its control on hydrocarbon formation. *China Offshore Oil Gas* 33, 11–24.

Li, H. Y., Jiang, Z. X., and Dong, Y. X. (2010). Formation conditions and model of ancient submerged mountains in the Nanpu No.2 formation, Jidong Oilfield. *Fract. block oil gas field* 17, 678–681.

Liang, X., Wu, L. L., and Li, Y. D. (2021). Oil source correlation and its relationship with deeply buried hydrocarbon accumulation in Tianjingshan Paleo-uplift area, northern segment of Western Sichuan Depression. *Petroleum Geol. Exp.* 43, 96–111.

Lin, T., Tan, C., and Wang, T. S. (2022). Differential hydrocarbon accumulation and its influence on the formation of gas reservoirs in the Longwangmiao Formation, central Sichuan Basin. *Petroleum Explor. Dev.* 44, 655–665.

Liu, W. H., Borjigin, T., Wang, X. F., Li, M., Hu, G., Wang, J., et al. (2017). New knowledge of hydrocarbon generating theory of organic matter in Chinese marine carbonates. *Petroleum Explor. Dev.* 44, 159–169. doi:10.1016/s1876-3804(17)30020-4

Lu, S. F., Chen, F. W., Li, J. J., Wang, W., Li, H., Cao, R., et al. (2012). Identification of the lower limit of high-quality source rocks and its relation to hydrocarbon accumulation-Taking the Beier Sag in the Hailaer Basin as an example. *Pet. Sci.* 9, 10–17. doi:10.1007/s12182-012-0176-y

Lu, S. F., Huang, W. B., Li, W. H., Xue, H., Xiao, D., Li, J., et al. (2017). Lower limits and grading evaluation criteria of tight oil source rocks of southern Songliao Basin, NE China. *Petroleum Explor. Dev.* 44, 505–512. doi:10.1016/s1876-3804(17)30058-7

Magoon, L. B., and Dow, W. G. (1994). *The petroleum system-from source to trap*. Oklahoma, United States: AAPG, 1–30.

Meng, Q. Q., Li, J. Z., and Liu, W. H. (2022). Simulation experiments on the effect of anthophyllite content on hydrocarbon production in mature stage shales. *Spec. Reserv.* 29, 113–118.

Meng, Q. Q., Qin, J. Z., and Liu, W. B. (2008). Experimental study on the hydrocarbon production characteristics of multicellular macrobenthic algae. *J. Petroleum* 6, 822–826.

Pan, W. L., Peng, J. N., and Zhai, C. B. (2022). Residual strata and hydrocarbon accumulation model of marine sediments in Subei Basin. *Petroleum Geol. Exp.* 44, 231–240.

Pang, X. Q., Zhang, T. Y., Ma, X. H., Zheng, D., Wang, W., Wang, X., et al. (2020). Hydrocarbon generation and expulsion features of the Upper Triassic Xujiahe Formation source rocks and their controlling effects on hydrocarbon accumulation in the Sichuan Basin, Central China. *Geol. J.* 55, 4977–4996. doi:10.1002/gj.3653

Pei, L. X., Gang, W. Z., Gao, G., Dong, Y., and Huang, Z. (2016). Petroleum origin and accumulation in the rift basin: A case study from the Nanpu sag, Bohai Bay Basin, China. *Arab. J. Geosci.* 9, 185. doi:10.1007/s12517-015-2248-y

Song, Y. C., Wang, E. Z., Peng, Y. T., Xing, H., Wu, K., Zheng, Y., et al. (2021). Conventional and unconventional hydrocar-bon resource potential evaluation of source rocks and reservoirs: A case study of the upper xiaganchaigou formation,

western qaidam basin, northwest China. *Nat. Resour. Res.* 30, 4355–4377. doi:10.1007/s11053-021-09953-y

Sun, B., Tang, D., and Li, X. M. (2015). Hydrocarbon generation evolution and hydrocarbon origin of hydrocarbon source rocks in the Nanbu Depression, Bohai Bay Basin. *Sci. Technol. Eng.* 15, 67–73+126.

Tang, Y., He, W. H., Bai, Y. B., Zhang, X., Zhao, J., Yang, S., et al. (2021). Source rock evaluation and hydrocarbon generation model of a permian alkaline lakes-A case study of the fengcheng formation in the Mahu sag, junggar basin. *MINERALS* 11, 644. doi:10.3390/min11060644

Wang, E. Z., Feng, Y., Liu, G. Y., Chen, S., Wu, Z., and Li, C. (2021). Hydrocarbon source potential evaluation insight into source rocks-A case study of the first member of the Paleogene Shahejie Formati-on, Nanpu Sag, NE China. *Energy Rep.* 7, 32–42. doi:10.1016/j.egyr.2020.11.099

Wang, E. Z., Liu, G. Y., Pang, X. Q., Zhao, Z., Feng, Y., Wu, Z., et al. (2020). An improved hydrocarbon generation potential method for quantifying hydrocarbon generation and expulsion characteristics with application example of Paleogene Shahejie Formation, Nanpu Sag, Bohai Bay Basin. *Mar. Petroleum Geol.* 112, 104106. doi:10.1016/j.marpetgeo.2019.104106

Wei, X., and Sun, Y. S. (2017). Evaluation of hydrocarbon source rocks in the Dongying Formation of the Nanbu Depression and contribution of oil sources. *Daqing Petroleum Geol. Dev.* 36, 25–32.

Xia, L. W., Cao, J., Wang, M., Mi, J. L., and Wang, T. T. (2019). A review of carbonates as hydrocarbon source rocks:basic geochemistry and oil-gas generation. *Pet. Sci.* 16, 713–728. doi:10.1007/s12182-019-0343-5

Xu, D. Y., Zhou, J. Y., and Wang, H. (2010). Significance of reservoir formation indication of the hydrochemical characteristics of the Dongying Formation in the Nanpu sag, Bohai Bay Basin. *Pet. Exp. Geol.* 32, 285–289.

Zhang, Z. N., Wu, Y. D., Sun, L. N., Li, Y., Fu, D., Su, L., et al. (2017). The changes of hydrocarbon generation and potential in source rocks under semi-closed conditions with 50–840 bar water pressure. *Petroleum Sci. Technol.* 35, 1487–1494. doi:10.1080/10916466.2017.1347678

Zhao, W. Z., and Chi, Y. L. (2000). Regional distribution of hydrocarbon-bearing formations in the Bohai Bay Basin and the main controlling factors. *J. Petroleum* 01, 10–15+3.

Zhao, W. Z., Zou, C., and Wang, Z. C. (2004). The theory of full oil content in oil-rich depressions-implications and significance. *Petroleum Explor. Dev.* 2, 5–13.

Zhao, Y. D., Liu, L. F., and Zhang, Z. H. (2008). Distribution and hydrocarbon generation characteristics of hydrocarbon source rocks in the Paleozoic stratigraphic framework of the Nanbu Depression. *J. Sedimentology* 26, 1077–1085.

Zhou, H. M., Dong, Y. X., and Liu, Y. H. (2005). *Theory and practice of oil and gas exploration in fractured basins: The case of nanbu depression in Bohai Bay Basin*. Beijing: China University of Petroleum Press.

Zhu, G. Y., Wang, Z. J., and Su, J. (2013). Geochemical characteristics of high-quality hydrocarbon source rocks in the Nanpu sag of the Bohai Bay Basin, China. *Oil Shale* 30, 117–135. doi:10.3176/oil.2013.2.03

Zuo, Y. H., Qiu, N. S., and Pang, X. Q. (2010). Hydrocarbon kitchen evolution of E(2)s(3) source rock of the Bohai Offshore area, North China. *Chin. J. Geophys. Chin. Ed.* 53, 2415–2426. doi:10.1002/cjg2.1551

frontiers | Frontiers in Earth Science

TYPE Original Research
PUBLISHED 08 February 2023
DOI 10.3389/feart.2023.1139981

OPEN ACCESS

EDITED BY
Qingqiang Meng,
SINOPEC Petroleum Exploration and Production Research Institute, China

REVIEWED BY
Chuanqi Tao,
Liaoning Shihua University, China
Xiangdong Gao,
East China University of Technology, China

*CORRESPONDENCE
Pei Xue,
gwl330@163.com

SPECIALTY SECTION
This article was submitted to Geochemistry, a section of the journal Frontiers in Earth Science

RECEIVED 08 January 2023
ACCEPTED 25 January 2023
PUBLISHED 08 February 2023

CITATION
Xue P, Liang Q, Gao C, Yin J, Hao S and Zhao Q (2023), Thermodynamic analysis of the difference in adsorption characteristics of CH_4 and CO_2 on continental shale. *Front. Earth Sci.* 11:1139981. doi: 10.3389/feart.2023.1139981

Thermodynamic analysis of the difference in adsorption characteristics of CH_4 and CO_2 on continental shale

Pei Xue*, Quansheng Liang, Chao Gao, Jintao Yin, Shiyan Hao and Qianping Zhao

Research Institute, Shaanxi Yanchang Petroleum (Group) Co., Ltd., Xi'an, Shaanxi, China

In order to explain the difference in adsorption characteristics of CH_4 and CO_2 on continental shale from the perspective of thermodynamics, the isothermal adsorption experiments of CH_4 and CO_2 adsorbed by shale in Yanchang Formation in Ordos Basin were carried out, and the excess adsorption capacity was corrected to absolute adsorption capacity. Then the Clausius-Clapeyron equation was used to analyze the isosteric heat of adsorption of CH_4 and CO_2 on shale. The results show that, for calculating the absolute adsorption capacity, Ozawa empirical formula or Van der Waals approximation method should be used to calculate the adsorption phase density. The absolute adsorption capacity should be selected as the basic data for calculating the isosteric heat of adsorption. The reason is that the excess isosteric heat of adsorption has a negative value in the low adsorption capacity stage, which is contradictory to the fact that the adsorption process is exothermic, and is significantly higher than the absolute isosteric heat of adsorption. There is a good linear positive correlation between the isosteric heat of adsorption and the adsorption amount of CH_4 and CO_2 adsorbed by continental shale, and the isosteric heat of adsorption of CH_4 is greater than that of CO_2. The absolute initial isosteric heat of adsorption of CH_4 and CO_2 adsorbed by shale is 52.04 kJ/mol and 27.71 kJ/mol, indicating that the adsorption force of CH_4 on Yanchang Formation shale is stronger than that of CO_2.

KEYWORDS

continental shale, isothermal adsorption, excess adsorption capacity, absolute adsorption capacity, isosteric heat of adsorption

1 Introduction

In recent years, with the increasing exploration and development of shale gas resources, shale gas has become an important support for the continuous growth of global natural gas production, shale gas production exceeds 8,000 × 10^8 m^3 in 2021, accounting for 20% of total natural gas production (Zou et al., 2022). Shale gas mainly exists in free and adsorbed states on the surface of shale pores, clay mineral particles and organic matter pores (Xia et al., 2015; Zhou S. et al., 2016). Adsorption gas accounted for 20%–85% of the total gas (Curtis, 2002; Zhang et al., 2004). Study on the adsorption characteristics and mechanism of shale is an important part of theoretical research on shale gas exploration and development, which is of great significance to the evaluation of shale gas resources and the development programs compilation (Jia et al., 2012; Zou et al., 2012; Meng et al., 2021; Han et al., 2022).

Adsorption characteristics of shale are affected by many factors such as adsorbate type, shale material composition and pore structure, temperature and pressure conditions of the

system (GASPARIK et al., 2014; M. E.Curtis, 2010). In terms of adsorbate types, many scholars have used physical simulation (Zhu et al., 2016; Yang et al., 2017; Zhang et al., 2019) or molecular simulation methods (Li et al., 2014; Hongguan and June 2016; Sui and Yao, 2016; Wang et al., 2017) to study the differences in the adsorption characteristics of CH_4 and CO_2 on shale (Zhu et al., 2016; Yang et al., 2017; Zhang et al., 2019) and its material composition (kerogen (Hongguan and June 2016), clay minerals (Li et al., 2014; Sui and Yao, 2016; Wang et al., 2017), etc.). The results show that for the same shale, under the same temperature and pressure conditions, the adsorption capacity of CO_2 on shale, kerogen and clay minerals is greater than that of CH_4. The adsorption capacity ratio of shale to CO_2 and CH_4 can reach more than 1.5 (Zhu et al., 2016; Yang et al., 2017), and some samples even reach about 5 times (Zhang et al., 2019). Shale has an obvious competitive adsorption advantage for CO_2 (Wang et al., 2016; Liang and Li, 2021), which is the fundamental reason that supercritical CO_2 can be used to enhance shale gas exploitation (Liang and Li, 2021; Lu et al., 2021). Although some studies have revealed the differences of adsorption characteristics of CO_2 and CH_4 on shale, the reasons for the differences are still lack of theoretical analysis. The adsorption system is accompanied by changes of thermodynamic energy during the adsorption process, that is reflected in the form of adsorption heat. The adsorption heat reflects the strength of the interaction between the adsorbent and the adsorbate, and the heterogeneity of the adsorbent surface. Therefore, studying the thermodynamic characteristics of shale adsorption process can further clarify the adsorption mechanism.

There are some understandings on the adsorption thermodynamic characteristics of marine shale and coal. Some scholars have studied the thermodynamic characteristics of CH_4 adsorption on Longmaxi shale (GUO et al., 2013), Niutitang shale (YANG et al., 2014) in Sichuan Basin and Carboniferous shale (LI et al., 2016) in Qaidam Basin. The results show that there is a linear correlation between the adsorption heat and the adsorption capacity of CH_4 adsorbed on shale, but the positive and negative correlations are different. NODZENSKI. (1998); KIM et al. (2011) analyzed the thermodynamic difference of adsorption of CO_2 and CH_4 on coal rock, indicating that the heat of adsorption of CO_2 on coal is greater than that of CH_4, revealing the essence of competitive adsorption of CO_2 and CH_4 on the surface of coal from thermodynamic perspective. Because the adsorption characteristics of different adsorption systems are obviously different, the existing research results are difficult to accurately reflect the adsorption mechanism of continental shale. At the same time, the existing research results use the excess adsorption capacity to analyze the thermodynamic characteristics. But the excess adsorption capacity cannot represent the actual adsorption capacity of the adsorbent. Therefore, the isosteric heat of adsorption calculated by using the excess adsorption capacity cannot reflect the thermodynamic characteristics of the adsorption process.

In this paper, the isothermal adsorption experiments of CH_4 and CO_2 adsorbed by the continental shale in Ordos Basin at 30°C, 45°C and 60°C were carried out. The difference between the excess and the absolute adsorption capacity was studied. The isosteric heat of adsorption of CH_4 and CO_2 adsorbed by continental shale was analyzed to explain the competitive adsorption mechanism. The research results are of great significance to improve the analysis method of adsorption thermodynamics and further clarify the competitive adsorption mechanism of CH_4 and CO_2 in continental shale.

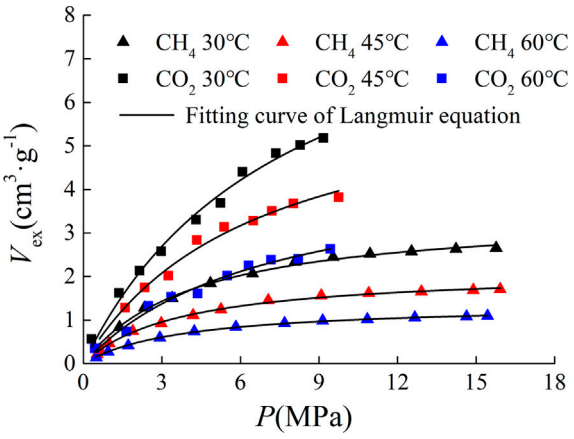

FIGURE 1
The sorption isotherm of shale of Yanchang Formation.

2 Expeiment

2.1 Experimental samples

During the Chang7 period, the sedimentary center of Ordos basin is located in the central and southern part of the basin, mainly developing semi-deep and deep lake sedimentary microfacies. The thickness of the dark shale (Zhangjiatan shale) of the Chang7 strata formed by deposition is between 400 and 500 m, of which the thickness of the single layer is up to 30 m, and the thickness of the Chang7 shale in Ganquan area is between 45 and 60 m.

The experimental samples are form Well CY1 in Xiasiwan Town, Ganquan Area, Ordos Basin. The sampling horizon is the Upper Triassic Yanchang Formation. The samples are gray-black shale, with a specific surface area of 3.54 m^2/g, TOC of 4.31%, organic matter type of II_1, Ro of 0.91%, quartz content of 14.4%, feldspar content of 10.5%, clay mineral content of 53.7%, and a small amount of pyrite and carbonate.

Due to the low evolution degree of organic matter in Yanchang Formation shale, a large number of liquid hydrocarbons formed during the thermal evolution process occupy the micropores in the shale, and methane is easily soluble in liquid hydrocarbons. Therefore, in order to eliminate the influence of liquid hydrocarbons on the adsorption of CO_2 and CH_4 on samples, and truly reflect the thermodynamic characteristics of the adsorption process, organic matter solvent extraction is required for the shale sample. Experimental samples from the same core sample, through organic matter solvent extraction, vacuum drying, crushing, screening, made into a particle size of about 0.2 mm broken samples, and according to the experimental requirements are divided into three, and sealed spare.

2.2 Experimental method

The instrument used in this experiment is FY-KT1000 isothermal adsorption instrument. The experimental method refers to the relevant provisions of GB/T 19,560–2008 “high pressure isothermal adsorption test method of coal. “ According to the temperature and pressure conditions of the sampled formation, the experimental temperatures were set to 30°C, 45°C, and 60°C, respectively. The

TABLE 1 The fitting parameters of Langmuir equation.

T/°c	CH_4		CO_2	
	V_{Lex}/(cm³/g)	P_{Lex}/MPa	V_{Lex}/(cm³/g)	P_{Lex}/MPa
30	3.45	4.23	9.67	7.79
45	2.14	3.71	6.66	6.61
60	1.38	3.81	4.60	7.05

The subscript ex represents the excess adsorption, distinguished from the absolute adsorption subscript ab below.

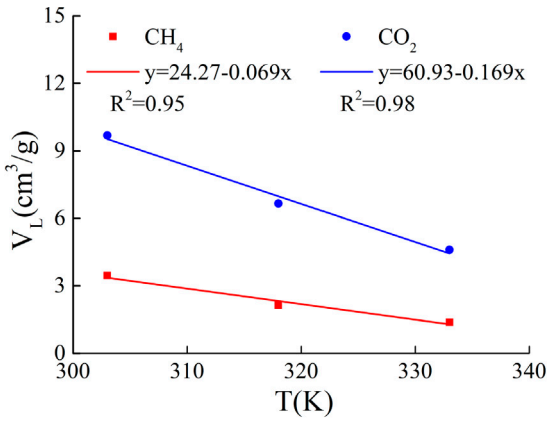

FIGURE 2
The relationship of Langmuir volume and temperature.

initial pressure of the experiment was 0.5 MPa, and the upper limit of pressure was 16 MPa. A total of 10–11 pressure points were measured at different temperatures. The test gradually increased from the initial pressure to the upper limit of pressure, and the equilibrium time at each equilibrium pressure point was not less than 12 h. The experimental gases are CH_4 and CO_2 with a purity of 99.99%.

3 Result and discussion

3.1 Adsorption properties of samples

The experimental samples are from the same core with the same sample preparation method and sample specification. The difference of experimental results is mainly due to the difference of experimental temperature and pressure conditions and adsorbate types. The experimental results are shown in Figure 1.

It can be seen from Figure 1 that under the same temperature and pressure conditions, the adsorption capacity of CO_2 is greater than that of CH_4. With the increase of temperature, the adsorption capacity of shale decreases. The isothermal adsorption curve was fitted by Langmuir equation, which can be expressed as

$$V = \frac{V_L P}{P + P_L} \quad (1)$$

Where V is isothermal adsorption capacity, g/cm³. V_L is Langmuir volume, cm³/g. P_L is Langmuir pressure, Pa. P is pressure, Pa. The fitting results of Langmuir equation are shown in Table 1. The fitting results show that the Langmuir volume (V_L) gradually decreases with the increase of temperature, and the relationship between Langmuir pressure (P_L) and temperature is not obvious. Langmuir equation is widely used in the isothermal adsorption curve fitting of coalbed methane and shale gas. It assumes that there is no interaction between adsorbate molecules, and the surface of the adsorbent is homogeneous. It is suitable for describing the monolayer adsorption process on a uniform solid surface, and has high fitting accuracy in the low gas pressure (≤ 15 MPa) stage.

The Langmuir volume and temperature were fitted by linear function, and the fitting results are shown in Figure 2. There is a good negative linear correlation between Langmuir volume and temperature, and the Langmuir volume of CO_2 adsorbed by shale is more sensitive to temperature than that of CH_4. And the study shows that the Langmuir volume of shale is positively correlated with porosity, organic matter abundance, organic matter maturity and clay mineral content, and negatively correlated with average pore size.

Since the critical temperature of CH_4 and CO_2 is −82.6°C and 31°C, and the critical pressure is 4.64 MPa and 7.4 MPa, respectively, when the experimental temperature and pressure conditions exceed the critical point, the adsorption of gas in shale belong to supercritical adsorption. The isothermal adsorption curve under supercritical state will have a maximum value, but there is no maximum value in the experimental results. Liu Shengxin et al. (LIU et al., 2015) determined the isothermal adsorption curve of CO_2 on the Carboniferous shale in the Qaidam Basin. The maximum value appeared near the temperature of 45°C and the gas pressure of 7.5 MPa, but the isothermal adsorption curve of CH_4 in the same shale sample did not appear. It can be seen that the appearance of the maximum value is related to the gas type. Zhou et al. (2000) believed that the appearance of the maximum value required the high experimental pressure and large specific surface area.

3.2 Adsorption phase density

Adsorbed phase density is the key parameter to calculate the absolute adsorption capacity by using excess adsorption capacity. The density of adsorbed phase is often calculated by theoretical estimation and equation fitting, which cannot be measured directly under supercritical conditions. The commonly used calculation methods of adsorbed phase density (see Table 2) mainly include the adsorption phase density constant approximation method (MURATA et al., 2001; NIKOLAEV and DUBININ, 1958; MENON, 1968; FINDENEGG and Loring, 1984; MEHTA and DANNER, 1985), empirical formula method (OZAWA et al., 1976) and excess adsorption capacity curve fitting method (Ross and Bustin, 2007; Clarkson and Haghshenas, 2013; Zhou S. W. et al., 2016). The density of the adsorption phase has a great influence on the correction

TABLE 2 The calculation method of adsorbed phase density.

Estimation method		Calculation formula	References	Remark
constant approximation method	Van der Waals constant approximation	$\rho_a = \rho_{van} = \frac{MRT_c}{8p_c}$	NIKOLAEV and DUBININ (1958)	ρ_a is adsorption phase density,g/cm^3. M is gas molecular mass,g/mol. R isuniversal gas constant, J/(mol•K). T_c is critical temperature, K. p_c is critical pressure, Pa. ρ_{lp} is normal boiling point density, g/cm^3. ρ_c iscritical density, g/cm^3.ρ_b is boiling point density, g/cm^3. T_b is boiling point temperature, K. *n*ex is excess adsorption amount, mmol/g; $n_{ab,L}$ is the Langmuir volume of absolute adsorption amount, mmol/g. $p_{ab,L}$ is the Lamguir pressure of excess adsorption amount,Pa
	Boiling Point Liquid Density Approximation	$\rho_a = \rho_{lp}$	MENON (1968), FINDENEGG and Loring (1984)	
	Critical density approximation	$\rho_a = \rho_c$	MEHTA and DANNER (1985)	
Ozawa empirical formula		$\rho_a = \rho_b \exp[-0.002\,5 \times (T - T_b)]$	OZAWA et al. (1976)	
excess adsorption capacity curve fitting method	Langmuir equation fitting	$nex = \frac{n_{ab,L}\,p}{p_{ab,L}+p}\left(1 - \frac{\rho g}{\rho_a}\right)$	Ross and Bustin (2007)	
	L-F equation fitting	$n_{ex} = \frac{n_{ab,L}\,(bp)^m}{1+(bp)^m}\left(1 - \frac{\rho g}{\rho_a}\right)$	Zhou S. et al. (2016)	
	Linear Fitting of Descending Curve	$n_{ex} = a + b\rho_g$	Clarkson and Haghshenas (2013)	

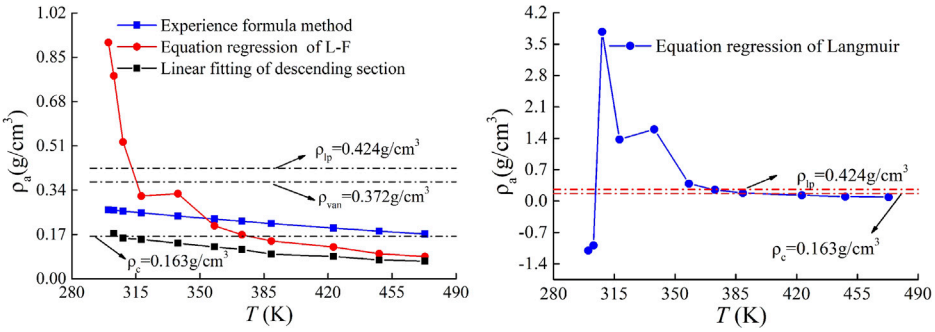

FIGURE 3
Adsorbed density curve from different calculation methods.

results of the absolute adsorption amount. The smaller the density of the adsorption phase is, the greater the absolute adsorption amount is. Therefore, considering the accuracy of the absolute adsorption amount correction results, it is necessary to screen the calculation method of adsorption phase density.

Under supercritical conditions, the adsorbed molecules lose the average moving energy due to the action of adsorption potential, but still have high rotational and vibrational energy. Therefore, the density of adsorbed phase under supercritical conditions is obviously higher than the critical density, and slightly lower than the density of boiling point liquid at atmospheric pressure (Hu et al., 2002). Theoretically, the curve of absolute adsorption capacity is monotonic, and there is no maximum value (Kondo et al., 2005). Therefore, the rationality of different adsorption phase density estimation methods in Table 2 can be verified from the perspectives of adsorption phase density range and absolute adsorption capacity monotonicity. Figure 3 is the relationship curve between CH_4 adsorption phase density and temperature obtained by different adsorption phase density calculation methods.

In order to verify the rationality of the adsorbed phase density in a large temperature and pressure range, the excess adsorption data are derived from Reference (RexerBenhamAplin and Thomas, 2013). The temperature range of the data is 26.85°C–199.85°C, and the pressure range is 0.08–14 MPa.

It can be seen from Figure 3 that in the temperature range of 26.85°C–199.85°C, the liquid density at the normal pressure boiling point of CH_4 is approximately 0.424 g/cm^3, and the critical density is approximately 0.163 g/cm^3.

Therefore, the adsorption phase density of CH_4 should be in the range of 0.163 g/cm^3–0.424 g/cm^3. The approximate value of Van der Waals with 0.372 g/cm^3, and the density of adsorption phase of CH_4 obtained by Ozawa empirical formula method with 0.265–0.172 g/cm^3 are reasonable.

There are only two data points in the descending section of the excess adsorption curve under the temperature of 26.85°C, and the data points are too few to carry out linear fitting. Therefore, for the excess adsorption capacity curve in the temperature range of 29.85–199.85°C, the linear fitting method of the downward section is used to calculate the adsorption phase density. The results show that the adsorption phase density is in the range of 0.17434–0.06772 g/cm^3. With the increase of temperature, the adsorption phase density gradually decreases, and the adsorption phase density is only in a reasonable range at 29.85 °C. The rest are lower than the critical density value of 0.163 g/cm^3.

The adsorption phase density obtained by the regression method of the L-F equation is between 0.9066 and 0.0807 g/cm^3, and the

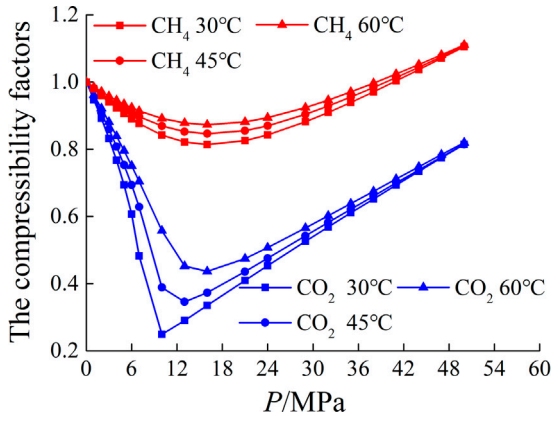

FIGURE 4
The compressibility factor of CH_4 and CO_2.

calculation results are in a reasonable range only in the temperature range of 44.85–115.85°C. The density of the adsorbed phase obtained by the Langmuir equation regression method is only in a reasonable range at a temperature of 84.85°–115.85°C. At a temperature of 26.85°C and 29.85°C, the calculation results have negative values and that is meaningless. In the temperature range of 26.85–199.85°C, only the adsorption phase density obtained by Ozawa empirical formula and van der Waals approximation is in the reasonable range of CH_4 adsorption phase density. In this paper, the Ozawa empirical formula is used to calculate the absolute adsorption capacity.

3.3 Excess and absolute adsorption capacity

Since the influence of the adsorbed phase volume is neglected in the data processing of the isothermal adsorption experiment, the experimental results represent the adsorption amount corresponding to the remaining part of the actual adsorbed gas density minus the gas phase density, which is called the excess adsorption amount. The actual adsorption amount is the absolute adsorption amount, and the absolute adsorption amount is greater than the excess. At present, the correction formula proposed by MOFFAT and WEALE. (1955) is used to realize the conversion from excess adsorption to absolute adsorption. The formula is expressed as

$$V_{ab} = \frac{V_{ex}}{1 - \frac{\rho_g}{\rho_a}} \tag{2}$$

Where V_{ab} is sbsolute adsorption amount, g/cm^3. V_{ex} 为is excess adsorption amount, g/cm^3. ρ_g is gas phase density under equilibrium adsorption conditions, g/cm^3. ρ_a is adsorption phase density, g/cm^3.

Due to the large variation of the compression factors of CH_4 and CO_2 under the experimental temperature and pressure conditions (as shown in Figure 4), if the ideal gas state equation is used to calculate the gas phase density, it will cause large errors. Therefore, the real gas state equation is used to calculate the gas phase density. The gas phase density can be expressed as

$$\rho_g = \frac{MP}{ZRT} \tag{3}$$

Where M is molar mass, g/mol. Z is real gas compression factor, which is calculated by Peng-Robinson equation. R is universal gas constant, 8.314 J/(K×mol). T is absolute temperature, K.

The phase change and density curve of CH_4 and CO_2 under the experimental temperature and pressure conditions are shown in Figure 5. For CH_4, there is a phase change from gas phase to supercritical state under experimental conditions. For CO_2, the experimental temperature 30°C is lower than its critical temperature (31°C), at which CO_2 changes from gas phase to liquid phase. At the temperature of 45°C and 60°C, CO_2 changes from gas phase to supercritical state, during the phase change of CO_2, the density increases greatly.

Based on the results of isothermal adsorption experiments, the excess adsorption capacity was converted to absolute adsorption capacity by using Formula (2) combined with the calculation method of gas phase density and adsorbed phase density. The absolute adsorption capacity and its fitting curve are shown in Figure 6.

The absolute adsorption capacity is greater than the excess, and the difference between them is affected by the temperature, pressure and gas type. In the low pressure range of 0 MPa–4 MPa, the difference between them is small, and the difference increases with the increase of pressure. Under low temperature, the difference is larger than that under high temperature. The difference between the absolute and excess adsorption capacity of CO_2 on shale is greater than that of CH_4 under the same temperature and pressure.

The absolute adsorption curve was fitted by Langmuir Eq. 1 and Freundlich equation. The Freundlich equation can be expressed as

$$V = kP^{1/n} \tag{4}$$

Where k and n are fitting constants. Fitting results and fitting parameters are shown in Figure 6 and Table 3. The fitting results show that above the critical temperature, the fitting effect of Langmuir equation on the absolute adsorption curve is better than that of Freundlich equation. For the adsorption of CO_2 below the critical temperature, due to the phase transition of CO_2 from gas phase to liquid phase, the fitting parameters of Langmuir volume and Langmuir pressure are obviously not of practical significance, and the fitting degree of Freundlich equation is higher.

Langmuir and Freundlich equations reflect the different energy relationships in the adsorption process. The Langmuir equation represents that the adsorption heat does not change with the adsorption amount, and the adsorbate is less sensitive to the heterogeneity of the adsorbent surface. The Freundlich equation represents that the adsorption heat and adsorption amount satisfy the logarithmic correlation. The adsorbate is sensitive to the inhomogeneity of the adsorbent surface, and preferentially adsorbed at the highly active site.

3.4Isosteric heat of adsorption of CH_4 and CO_2 on shales

The isosteric heat of adsorption refers to the enthalpy change when a mol of gas is adsorbed when the temperature, pressure and surface area of the adsorbent are constant. That is, when the adsorption amount is constant, the heat released during the adsorbent adsorbs infinitely small amount of gas molecules. The heat is the instantaneous value of enthalpy change during adsorption process. The isosteric heat of adsorption can indirectly reflect the adsorption force of the adsorption system and the inhomogeneity of the adsorbent surface. Isosteric heat of adsorption is usually calculated by the Clausius-Clapeyron equation (RAMIREZ-

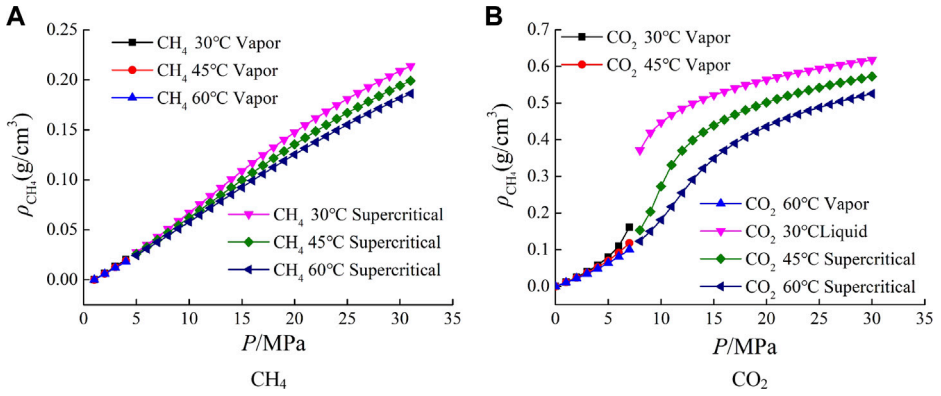

FIGURE 5
The phase change and density curve of CH_4 and CO_2.

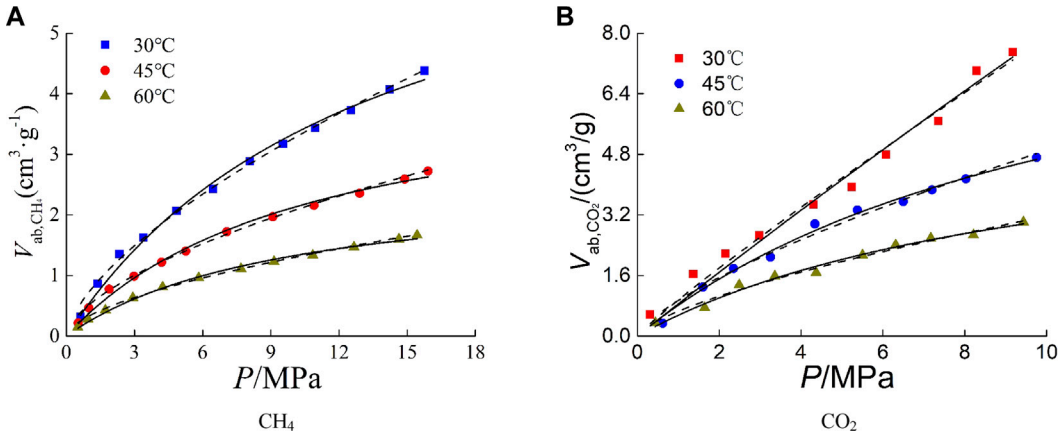

FIGURE 6
The absolute adsorption isotherm of shale of Yanchang Formation.

TABLE 3 The fitting parameters of Langmuir and Frenudlich equations.

Fitting equation		CH_4			CO_2		
Langmuir equation	T/°C	V_{Lab}/(cm³/g)	p_{Lab}/MPa	R^2	V_{Lab}/(cm³/g)	p_{Lab}/MPa	R^2
	30	7.88	13.61	0.9933	123.97	145.15	0.9791
	45	4.39	10.71	0.9934	10.17	11.50	0.9920
	60	2.63	9.88	0.9944	6.19	12.28	0.9853
Freundlich equation	T/°C	k	n	R^2	k	n	R^2
	30	0.73	1.54	0.9933	0.95	1.09	0.9812
	45	0.52	1.66	0.9905	0.94	1.39	0.9843
	60	0.33	1.69	0.9898	0.66	1.46	0.9843

PASTOR and BULNES, 2000) with isothermal adsorption capacity. The equation can be expressed as

$$\frac{1}{P}\frac{dP}{dT} = \frac{q_{st}}{RT^2} \quad (5)$$

Where q_{st} is isosteric heat of adsorption, J/mol. By deforming and integrating both side of Eq. 5 can be expressed as

$$\ln p = -\frac{q_{st}}{RT} + C_2 \quad (6)$$

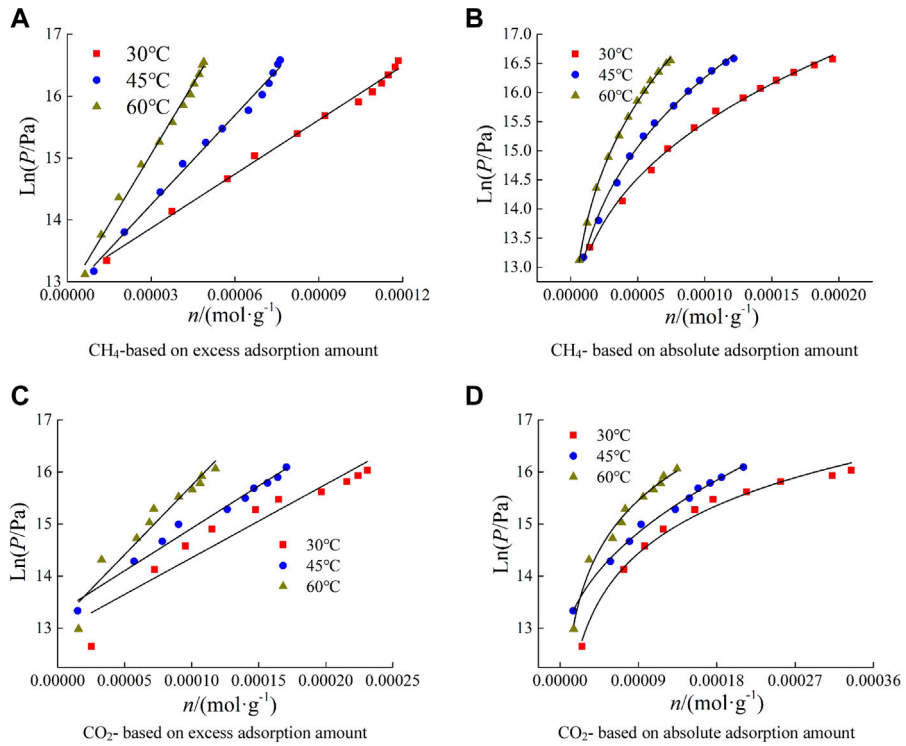

FIGURE 7
The fitting curve of ln*p*-*n*under different types of adsorption capacity.

where C_2 is integration constant. Eq. 6 shows that 1/T and lnp have a linear relationship, and the isosteric heat of adsorption q_{st} corresponding to the adsorption capacity n can be obtained from the slope. Assuming the slope is A, the isosteric adsorption heat is

$$q_{st} = -RA \tag{7}$$

For the convenience of subsequent description, the isosteric heat of adsorption obtained based on excess adsorption capacity is referred to as the excess isosteric heat of adsorption, and based on absolute adsorption capacity is referred to as the absolute isosteric heat of adsorption. Relative to the initial isosteric heat of adsorption, respectively referred to as excess initial isosteric heat of adsorption and absolute initial isosteric equal heat of adsorption.

Linear function Eq. 8 and power function Eq. 9 were used to fit the pressure logarithm-adsorption amount (lnp-n) data based on excess and absolute adsorption amount, respectively.

$$\ln p = a_1 + b_1 n_{ex} \tag{8}$$

$$\ln p = a_2 + b_2 n_{ab}{}^{c} \tag{9}$$

where a_1, b_1, a_2, b_2 and c are fitting function parameters. n_{ex} is excess adsorption amount, mol/g. n_{ab} is absolute adsorption amount, mol/g. The fitting results of lnp-n are shown in Figure 7. The results showed that the lnp-n data based on excess adsorption conformed to linear function fitting, and the lnp-n data based on absolute adsorption conformed to power function fitting.

Using Eq.8–9, ln*p* under several adsorption capacities is calculated, and the data of lnP-T^{-1} is linearly fitted. The fitting function is

$$\ln p = AT^{-1} + B \tag{10}$$

where A and B are fitting parameter。 The fitting curves of lnP-T^{-1} based on different types of adsorption amounts are shown in Figure 8. The fitting results show that the lnp-T^{-1} data are linear, and linear function fitting correlation coefficient of lnp-T^{-1} based on absolute adsorption capacity is above 0.98.

The isosteric heat of adsorption was calculated according to Eq. 7 combined with the slope of lnp-T^{-1} fitting function. The excess and absolute isosteric heat of adsorption curves of CH_4 and CO_2 adsorbed by Yanchang Formation shale are shown in Figure 9. The isosteric heat of adsorption of CH_4 is greater than that of CO_2. The excess isosteric heat of adsorption is obviously greater than the absolute, and as the adsorption amount increases, the difference between them gradually increases. Considering that the absolute adsorption capacity represents the actual adsorption capacity in the adsorption process, it can be considered that the excess isosteric heat of adsorption can not truly reflect the thermodynamic characteristics of the adsorption system. If the excess eat of adsorption is used as the characterization parameter of thermodynamic characteristics, the results of thermodynamic analysis will be higher. Therefore, the absolute adsorption capacity should be used as the basic data for thermodynamic analysis.

The linear function is used to fit the isosteric heat of and adsorption capacity. The linear fitting equation is expressed as,

$$q_{st} = a_3 + b_3 n \tag{11}$$

Where a_3, b_3 is fitting constant. a_3 is intial isosteric heat of adsorption,J/mol. b_3 is change rate of isosteric heat of adsorption, J/mol. The linear fitting parameters of isosteric heat and adsorption capacity are shown in Figure 9 and Table 4.

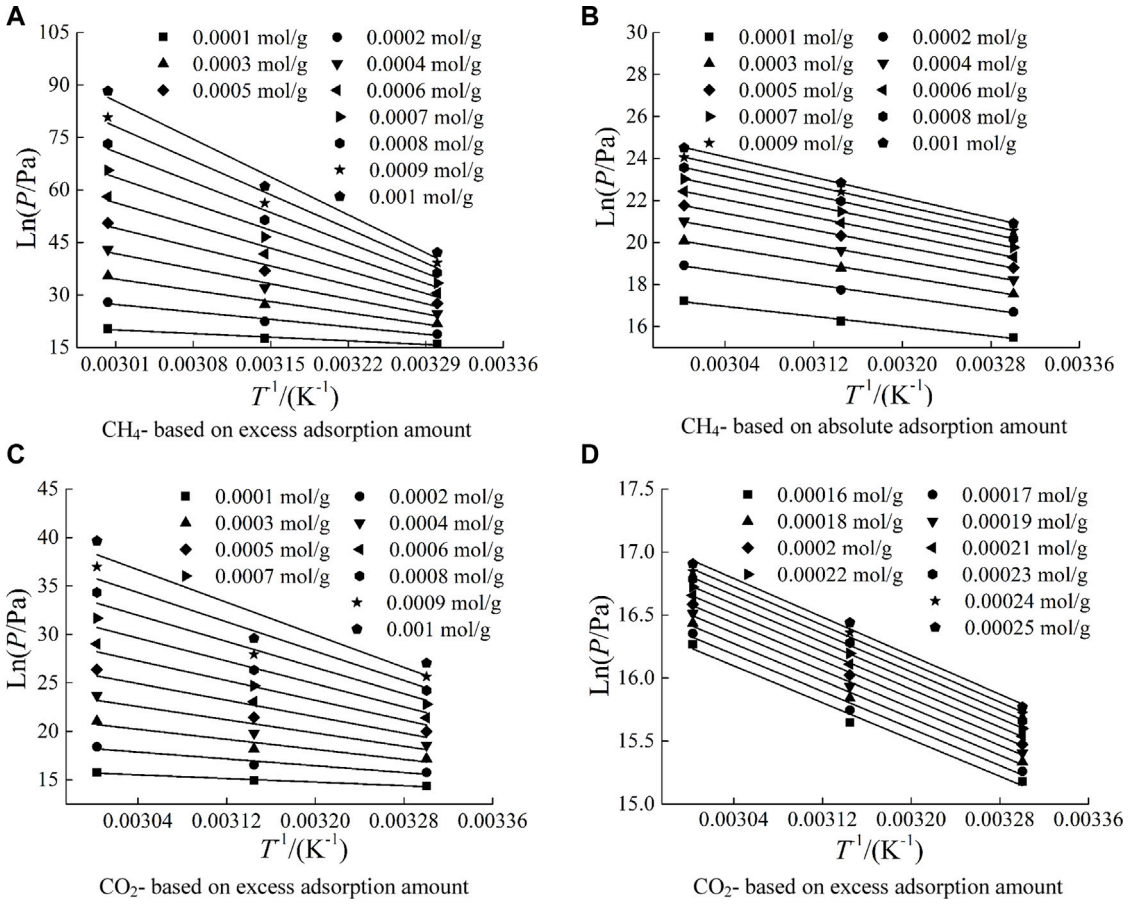

FIGURE 8
The fitting curve of lnp-T^{-1}under different types of adsorption capacity.

For the adsorption of CH_4 on shale, the excess initial adsorption heat is less than zero, which is inconsistent with the fact that the adsorption process is exothermic. Therefore, from the point of view of the rationality of the initial isosteric heat of adsorption, the use of excess adsorption capacity as the basic data of adsorption thermodynamic analysis will cause a negative value of isosteric heat of adsorption in the low adsorption capacity stage, which is contradictory to the exothermic phenomenon of adsorption process. This also shows that the adsorption thermodynamic analysis should be based on the absolute adsorption capacity.

And the calculation results of isosteric heat show that there is a linear positive correlation between the isosteric heat of adsorption and the adsorption amount of CH_4 and CO_2 adsorbed by shale. There are three kinds of change rules between isosteric heat and adsorption capacity, that is, isosteric heat is constant, with the increase of adsorption capacity increases, it decreases with the increase of adsorption amount. The variation law is affected by the heterogeneity of adsorbent surface and the interaction force between adsorbate molecules. The surface heterogeneity of the adsorbent determines that the adsorbate molecules are preferentially adsorbed at high active sites and then gradually adsorbed at relatively weak active sites, which results in the decrease of adsorption heat with the increase of adsorption amount. The interaction force between adsorbate molecules increases with the increase of adsorption amount, which leads to the increase of adsorption heat (RUTHVEN, 1984). It can be seen that the isosteric heat of adsorption of CH_4 and CO_2 adsorbed by Yanchang Formation shale is greatly affected by the interaction between gas molecules.

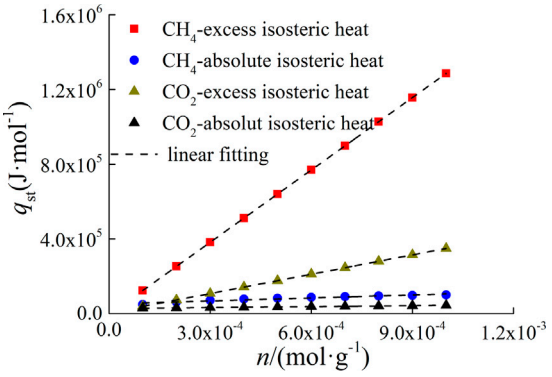

FIGURE 9
The isosteric heat of adsoptionunder different types of adsorption capacity.

Under the same adsorption system, the initial isosteric heat of adsorption reflects the molecular force between the adsorbent and the adsorbate. The larger the initial isosteric heat, the greater the force of the adsorbent surface to the gas molecules (NODZENSKI, 1998). It can be seen from Table 4 that when n = 0, the absolute initial isosteric heats of CH_4 and CO_2 adsorbed by shale are 52.04 kJ/mol and 27.71 kJ/mol, respectively, indicating that the

TABLE 4 The linear fitting parameters of isosteric heat and adsorption capacity.

Gas type	Data type	a_3	b_3	R^2
CH_4	based on excess adsorption amount	−5,514.42	1.29 × 109	0.999 9
	based on absolute adsorption amount	52,047.82	5.36 × 107	0.999 9
CO_2	based on excess adsorption amount	4,160.16	3.45 × 108	0.999 9
	based on absolute adsorption amount	27,713.76	1.66 × 107	0.999 9

adsorption force of CH_4 on Yanchang Formation shale is stronger than that of CO_2, but this cannot be used to demonstrate the feasibility of replacing CH_4 with CO_2 in engineering practice. The reason is that the adsorption of CH_4 and CO_2 by shale in this experiment is carried out independently, while the replacement process in the actual reservoir is carried out on the basis of CH_4 molecules adsorbed on the surface of shale. CH_4 desorption and CO_2 adsorption are carried out at the same time. There is an interaction between CH_4 and CO_2 molecules, which is reflected in the interaction between desorption heat and adsorption heat.

4 Conclusion

Based on the isothermal adsorption experimental data of CH_4 and CO_2 adsorbed by continental shale in Ordos Basin, the difference between excess adsorption capacity and absolute adsorption capacity was analyzed. Then, the Clausius-Clapeyron equation was used to study the thermodynamic characteristics of continental shale adsorption based on different types of adsorption capacity, and the reasons for the difference in adsorption performance of CO_2 and CH_4 by shale were revealed from the thermodynamic point of view.

(1) The absolute adsorption capacity is greater than the excess, the difference between them is affected by temperature, pressure and gas type. The difference decreases with increasing temperature, and increases with increasing pressure, and when the adsorption gas is CO_2, the difference between them is larger than CH_4.
(2) In the temperature range of 26.85–199.85°C, the adsorption phase density obtained by Ozawa empirical formula and Van der Waals approximation is in the reasonable range of CH_4 adsorption phase density.
(3) The thermodynamic analysis of the adsorption process should use the absolute adsorption capacity as the basic analysis data. The reason is that the excess isosteric heat of adsorption has a negative value in the low adsorption capacity stage, which is contradictory to the fact that the adsorption is exothermic. And the excess isosteric heat is significantly higher than the absolute isosteric heat.
(4) There is a good linear positive correlation between the isosteric heat of adsorption and the adsorption amount of CH_4 and CO_2 adsorbed by continental shale in Ordos Basin, and the isosteric heat of CH_4 is greater than that of CO_2. The absolute initial isosteric heat of adsorption of CH_4 and CO_2 adsorbed by shale is 52.04 kJ/mol and 27.71 kJ/mol, indicating that the adsorption force of CH_4 on Yanchang Formation shale is stronger than that of CO_2.

Data availability statement

The original contributions presented in the study are included in the article/supplementary material, further inquiries can be directed to the corresponding author.

Author contributions

PX is responsible for writing the article. QL and CG are responsible for carrying out isothermal adsorption experiments. JY, SH, and QZ are responsible for drawing.

Conflict of interest

Authors PX, QL, CG, JY, SH, and QZ were employed by the company Shaanxi Yanchang Petroleum (Group) Co, Ltd.

Publisher's note

References

Clarkson, C. R., and Haghshenas, B. (2013). "Modeling of supercritical fluid ad-sorption on organic-rich shales and coal," in SPE Unconventional Resources Conference-USA, The Woodlands Texas, USA, 10-12 April 2013. doi:10.2118/164532-MS

Curtis, J. B. (2002). Fractured shale-gas systems. *AAPG Bull.* 86, 1921–1938. doi:10.1306/61EEDDBE-173E-11D7-8645000102C1865D

Findenegg, G. H., and Loring, R. (1984). Fluid adsorption up to the critical point. Experimental study of a wetting fluid/solid interface. *J. Chem. Phys.* 81 (7), 3270–3276. doi:10.1063/1.448036

Gasparik, M., Bertier, P., Gensterblum, Y., Ghanizadeh, A., Krooss, B. M., and Littke, R. (2014). Geological controls on the methane storage capacity in organic-rich shales. *Int. J. Coal Geol.* 123 (2), 34–51. doi:10.1016/j.coal.2013.06.010

Guo, W., Xiong, W., Gao, S., Hu, Z., Liu, H., Yu, R., et al. (2013). Impact of temperature on the isothermal adsorption/desorption characteristics of shale gas. *Petroleum Explor. Dev.* 40 (4), 481–485. doi:10.1016/S1876-3804(13)60066-X

Han, S., Tang, Z., Wang, C., Horsfield, B., Wang, T., and Mahlstedt, N. (2022). Hydrogen-rich gas discovery in continental scientific drilling project of songliao basin,

northeast China: New insights into deep Earth exploration. *Sci. Bull.* 67 (10), 1003–1006. doi:10.1016/j.scib.2022.02.008

Hongguan, S., and Jun, Y. (2016). Molecular simulation of CO2/CH4 competitive adsorption in kerogen. *J. China Univ. Petroleum* 40 (2), 147–154. doi:10.3969/j.issn.1673-5005.2016.02.019

Hu, T., Ma, Z., and Yao, H. (2002). Study on high pressure adsorption isotherms of supercritical methane. *Nat. Gas Chem. industry(C1 Chem. Chem. Eng.* 27 (2), 36–40. doi:10.3969/j.issn.1001-9219.2002.02.010

Jia, C., Zheng, M., and Zhang, Y. (2012). Unconventional hydrocarbon resources in China and the prospect of exploration and development. *Petroleum Explor. Dev.* 39 (2), 139–146. doi:10.1016/s1876-3804(12)60026-3

Kim, H. J., Yao, S., He, J., Lee, H. H., and Lee, C. H. (2011). Adsorption characteristics of CO_2 and CH_4 on dry and wet coal from subcritical to supercritical conditions. *Chem. Eng. J.* 171 (1), 45–53. doi:10.1016/j.cej.2011.03.035

Kondo, S., Ishikawa, Y., and Abe, I. (2005). *Adsorption science*. Beijing: Chemical Industry Publishing House.

Li, W., Fang, X., Li, B., and Zeng, F. (2014). Molecular simulaton of the sorption of methane and carbon dioxide in the montmorillonite. *J. Northeast Petroleum Univ.* 38 (3), 25–30. doi:10.3969/j.issn.2095-4107.2014.03.004

Li, X., Cao, F., Yue, G., Li, Y., and Yu, Q. (2016). The experimental study of adsorption characterisitic of Carboniferous shale in Eastern Qaidam. *Earth Sci. Front.* 23 (5), 95–102. doi:10.13745/j.esf.2016.05.010

Liang, X., and Li, L. (2021). Geological conditions and exploration potential for shale gas in upper permian wujiaping Formation in the region of Western hubei-eastern chongqing. *Petroleum Geol. Exp.* 43 (3), 386–394. doi:10.11781/sysydz202103386

Liu, S., Zhong, J., Ma, Y., Yin, C., Liu, C., Li, Z., et al. (2015). Super-critical isothermal adsorption of gas in shale. *Coal Geol. Explor.* 43 (3), 45–50. doi:10.3969/j.issn.1001-1986.2015.03.009

Lu, Y., Zhou, J., Xian, X., Tang, J., Zhou, L., Jiang, Y., et al. (2021). Research progress and prospect of the integrated supercritical CO_2 enhanced shale gas recovery and geological sequestration. *Nat. Gas. Ind.* 41 (6), 60–73. doi:10.3787/j.issn.1000-0976.2021.06.007

M. E. Curtis (2010). "Structural characterization of gas shales on the micro and nano-scales," in SPE Unconventional Gas Conference, Calgary, Alberta, Canada, October 19–21, 2010.

Mehta, S. D., and Danner, R. P. (1985). An improved potential theory method for predicting gas-mixture adsorption equilibria. *Industiral Eng. Chem. Fundam.* 24 (3), 325–330. doi:10.1021/i100019a008

Meng, Q., Jin, Z., Sun, D., et al. (2021). Geological background and exploration prospects for the occurrence of high-content thydrogen. *Petroleum Geol. Exp.* 43 (2), 208–216. doi:10.11781/sysydz202102208

Menon, P. G. (1968). Adsorption at high pressures. *Chem. Rev.* 68 (3), 277–294. doi:10.1021/cr60253a002

Moffat, D. H., and Weale, K. E. (1955). Sorption by coal of methane at high pressure. *Fuel* 43, 449.

Murata, K., El-Merraoui, M., and Kaneko, K. (2001). A new determination method of absolute adsorption isotherm of supercritical gases under high pressure with a special relevance to density-functional theory study. *J. Chem. Phys.* 114 (9), 4196–4205. doi:10.1063/1.1344926

Nikolaev, K. M., and Dubinin, M. M. (1958). Concerning adsorptional properties of carbon adsorbents3:A study of adsorption isotherm s of gases and vapors on active carbons over a wide interval of temperatures,including the critical region. *Bull. Acad. Sci. USSR Div. Chem. Sci.* 7 (10), 1124–1133. doi:10.1007/bf00914939

Nodzenski, A. (1998). Sorption and desorption of gases (CH_4,CO_2) on hard coal and active carbon at elevated pressures. *Fuel* 7 (11), 1243–1246. doi:10.1016/s0016-2361(98)00022-2

Ozawa, S., Kusumi, S., and Ogino, Y. (1976). Physical adsorption of gases at high pressure. IV. An improvement of the Dubinin—astakhov adsorption equation. *J. Colloid Interface Sci.* 56 (1), 83–91. doi:10.1016/0021-9797(76)90149-1

Ramirez-Pastor, A. J., and Bulnes, F. (2000). Differential heat of adsorption in the presence of an order–disorder phase transition. *Phys. A* 283 (1-2), 198–203. doi:10.1016/s0378-4371(00)00152-7

RexerBenhamAplin, T. F. T. M. J. A. C., and Thomas, K. M. (2013). Methane adsorption on shale under simulated geological temperature and pressure conditions. *Energy & Fuels* 27 (6), 3099–3109. doi:10.1021/ef400381v

Ross, D. J. K., and Bustin, R. M. (2007). Impact of mass balance calculations on adsorption capacities in microporous shale gas reservoirs. *Fuel* 86 (17/18), 2696–2706. doi:10.1016/j.fuel.2007.02.036

Ruthven, D. M. (1984). *Principle of adsorption and adsorption process*. New York: John Wiley & Sons, 62–84.

Sui, H., and Yao, J. (2016). Molecular simulation of CH_4/CO_2 adsorption in clay minerals. *J. Northeast Petroleum Univ.* 40 (2), 90–98.

Wang, Q., Li, C., Pan, S., and Jiang, J. (2017). A molecular simulation study on the adsorption of CH_4 and CO_2 on the mineral substances in oil shale. *J. Fuel Chem. Technol.* 45 (11), 1310–1316. doi:10.3969/j.issn.0253-2409.2017.11.005

Wang, X., Zhai, Z., Xu, J., Wu, S., Li, J., Sun, L., et al. (2016). Molecular simulation of CO_2/CH_4 competitive adsorption in organic matter pores in shale under certain geological conditions. *Petroleum Explor. Dev.* 43 (5), 841–848. doi:10.1016/s1876-3804(16)30100-8

Xia, Y., Jin, Y., Cheng, M., and Cheng, K. (2015). Gas flow in shale reservoirs. *Chin. Sci. Bull.* 60, 2259–2271. doi:10.1360/n972014-01175

Yang, F., Ning, Z., Wang, Q., Liu, H., and Kong, D. (2014). Thermodynamic analysis of methane adsorption on gas shale. *J. Central South Univ. Sci. Technol.* 45 (8), 2871–2877. doi:10.1117/12.536380

Yang, F., Yue, C., Li, S., Ma, Y., Xu, X., et al. (2017). Adsorption characteristics of CH_4 and CO_2 on silurian shale in Sichuan Basin. *J. Chem. Industry Eng.* 68 (10), 3851–3859. doi:10.11949/j.issn.0438-1157.20170488

Zhang, C., Zhou, S., Jing, L., Cheng, K., Sun, Z., Li, P., et al. (2019). Adsorption characteristics of CH_4 and CO_2 on shale and its application to binary mixture adsorption under high-pressure conditions: A case study of the Longmaxi Formation shale in jiaoshiba area of Sichuan Basin. *Geochimica* 48 (6), 580–589. doi:10.19700/j.0379-1726.2019.06.006

Zhang, J., Jin, Z., and Yuan, M. (2004). Reservoiring mechanism of shale gas and its distribution. *Nat. Gas. Ind.* 24 (7), 15–18.

Zhou, L., Ming, L., and Zhou, Y. (2000). Adsorption measurement and theoretical analysis of supercritical methane on high surface area activated carbon. *Sci. China* 30 (1), 49–56.

Zhou, S. W., Yan, G., Xue, H. Q., Guo, W., and Li, X. (2016). 2D and 3D nanopore characterization of gas shale in Longmaxi formation based on FIB-SEM. *Mar. Pet. Geol.* 73, 174–180. doi:10.1016/j.marpetgeo.2016.02.033

Zhou, S., Wang, H., Xue, H., Guo, W., and Lu, B. (2016). Difference between excess and absolute adsorption capacity of shale and a new shale gas reserve calculation method. *Nat. Gas. Ind.* 36 (1), 12–20. doi:10.3787/j.issn.1000-0976.2016.11.002

Zhu, Y., Song, X., Guo, Y., Xu, F., Sun, N., and Wei, W. (2016). High-pressure adsorption characteristics and controlling factor of CH_4 and CO_2 on shales from Longmaxi Formation, Chongqing, SichuanBasin. *Nat. Gas. Geosci.* 27 (10), 1942–1952. doi:10.11764/j.issn.1672-1926.2016.10.1942

Zou, C., Yang, Z., Tao, S., Li, W., Wu, S., Hou, L., et al. (2012). Nano-hydrocarbon and the accumulation in coexisting source and reservoir. *Petroleum Explor. Dev.* 39 (1), 15–32. doi:10.1016/s1876-3804(12)60011-1

Zou, C., Zhao, Q., Wang, H., Xiong, W., Dong, D., Yu, R., et al. (2022). The main characteristics of marine shale gas and the theory & technology of exploration and development in China. *Nat. Gas. Ind.* 42 (8), 1–13. doi:10.3787/j.issn.1000-0976.2022.08.001

frontiers | Frontiers in Earth Science

TYPE Original Research
PUBLISHED 23 February 2023
DOI 10.3389/feart.2023.1131539

OPEN ACCESS

EDITED BY
Qingqiang Meng,
SINOPEC Petroleum Exploration and Production Research Institute, China

REVIEWED BY
Haijian Lu,
Chinese Academy of Geological Sciences (CAGS), China
Shengfa Liu,
Ministry of Natural Resources, China

*CORRESPONDENCE
Bin Zhai,
zhai686@126.com

SPECIALTY SECTION
This article was submitted to Geochemistry, a section of the journal Frontiers in Earth Science

RECEIVED 25 December 2022
ACCEPTED 08 February 2023
PUBLISHED 23 February 2023

CITATION
Du G, Zhai B, Su S, Sui L, Chang X, Ren H, Sun M and Wang L (2023), Hydrogeochemical characteristics and the genesis of the No. Lu 32 well in the Jiaodong Peninsula, China.
Front. Earth Sci. 11:1131539.
doi: 10.3389/feart.2023.1131539

Hydrogeochemical characteristics and the genesis of the No. Lu 32 well in the Jiaodong Peninsula, China

Guilin Du[1,2], Bin Zhai[3,4]*, Shujuan Su[5], Lailun Sui[6], Xiangchun Chang[1], Hongwei Ren[7], Maiyu Sun[8] and Lili Wang[9]

[1]College of Earth Science and Engineering, Shandong University of Science and Technology, Qingdao, China, [2]Weihai Earthquake Monitoring Center, Weihai, China, [3]Laboratory for Marine Mineral Resources, Qingdao National Laboratory for Marine Science and Technology, Qingdao, China, [4]The Key Laboratory of Gas Hydrate, Ministry of Natural Resources, Qingdao Institute of Marine Geology, Qingdao, China, [5]Yantai Earthquake Monitoring Center Station, Shandong Earthquake Agency, Yantai, China, [6]The No. 6 Geological Brigade of Shandong Geological and Mineral Exploration and Development Bureau, Weihai, China, [7]National Institute of Natural Hazards, Ministry of Emergency Management of China, Beijing, China, [8]Weihai Emergency Rescue Command and Protection Center, Weihai, China, [9]CNPC EastChina Design Institute Co., Ltd., Qingdao, China

The No. Lu 32 well is a seismic observation well situated on the easternmost tip of the Penglai–Weihai fault zone in the Jiaodong Peninsula. It is necessary to reveal the genetic mechanism of the water in this well for earthquake forecasting along the Penglai–Weihai fault zone. Water samples were collected from the No. Lu 32 well, neighboring wells, and seawater to measure the hydrochemical composition and main hydrogen and oxygen isotopic compositions. The water type of the No. Lu 32 well is Cl–Na, which may be due to the influence of seawater intrusion. Hydrogen and oxygen isotopes indicate that the No. Lu 32 well and adjacent wells are mainly influenced by meteoric water, that the high salinity in the water is mainly from the mixing of modern seawater, and that the proportion of seawater there is approximately 5%. Observation of water temperature data in the No. Lu 32 well over several years shows regular annual variations. This comprehensive study shows that the well is greatly affected by seawater backflow infiltration and shallow water. The results of this paper provide an important reference for exploring the hydrogeochemical characteristics and genesis of wells in other coastal zones.

KEYWORDS

No. Lu 32 well, hydrochemistry, genesis, seawater mixing, water temperature

1 Introduction

Geochemical methods have been widely used in studies of groundwater genesis and characteristics (Lai et al., 2021; Song et al., 2021; Su et al., 2021). The main research direction of geochemical methods for earthquake observations is focused on soil gas measurements near seismically active fault zones, ion concentrations in observation wells, and hydrogen and oxygen isotope compositions from water (Gao et al., 2015; Tiwari et al., 2020; Zhang et al., 2021). The most important hydrochemical method is related to water chemistry and hydrogen and oxygen isotope composition analysis (Pope et al., 2014; Sasaki et al., 2021), which are used for analyzing ions in groundwater and verifying groundwater anomalies (Liu et al., 2015).

The groundwater temperatures and levels in seismic observation wells are important tools in earthquake forecasting (Lai et al., 2016; Lai et al., 2021). Groundwater temperatures have both

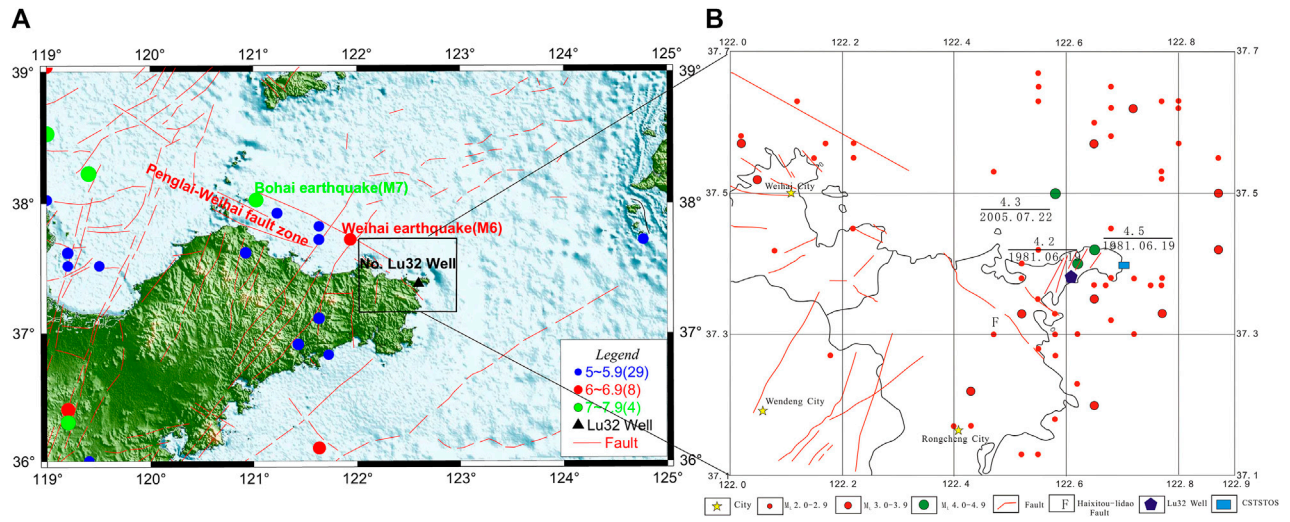

FIGURE 1
Seismotectonic settings of the No. Lu 32 well in the Jiaodong Peninsula, China. **(A)** Geological setting; **(B)** regional location [CSTSTOS is the Chengshantou seawater temperature observation station, and fault information and earthquake information are revised from (Chao et al., 1997)].

normal and abnormal changes. Previous studies have suggested that some strong earthquakes may cause abnormal variations in water levels and water temperatures, which are called the "coseismic" effects of water temperature (Ma et al., 2015). However, not all abnormalities are caused by earthquakes (Liu et al., 2015). Therefore, it is important to conduct a quantitative analysis when water temperature data exhibit abnormal variations, to quickly determine the cause of abnormal changes and to verify whether the changes are precursor abnormalities related to an earthquake or disturbances in earthquake monitoring and forecasting (Liu et al., 2015; Ma, 2016; Miyakoshi et al., 2020).

In this study, we take the No. Lu 32 well in the Jiaodong Peninsula as an example and use geochemical methods to constrain the causes of abnormal fluctuations in the groundwater temperature during an earthquake. Since this observation well is located on the easternmost tip of the Penglai–Weihai fault zone, its tectonic location has special significance for earthquake monitoring and forecasting. In this paper, we combine the regional geological and hydrogeological conditions and test the water chemistry and hydrogen–oxygen isotope compositions of the No. Lu 32 well and neighboring wells to comprehensively analyze the characteristics of the observation well, which will help to finally constrain the cause of abnormal groundwater temperatures during the earthquake process. At the same time, this analysis has some implications for groundwater temperatures in observation wells affected by seawater.

2 Geological settings

As the collision edge zone between the North China and Yangtze blocks, the Jiaodong Peninsula is characterized by a complicated crustal structure (Zhao et al., 2010; 2013; Gu et al., 2020; Qu et al., 2021). A great number of frequent moderate–strong earthquakes have occurred along the active fault zone in the Jiaodong Peninsula Penglai–Weihai fault zone, such as the Weihai M6.0 and Bohai M7.0 (Pan et al., 2015; Qu et al., 2021).

The No. Lu 32 well is located near the eastern side of the Haixitou–Lidao Fault, which is a fracture developed on land at the easternmost tip of the Penglai–Weihai fault zone (Figures 1, 2). The Yantai–Weihai section in the eastern part of the Penglai–Weihai fault zone is a Middle Pleistocene active tectonic section, and no Late Pleistocene stratigraphic discontinuity has been found there until now. The Penglai–Weihai fault zone has controlled the occurrence of historical earthquakes; the 1548 M7.0 earthquake occurred in the western part of the fault zone, and the 1948 M 6.0 earthquake occurred in its eastern part (Wang et al., 2006; Pan et al., 2015; Gu et al., 2020). The Haixitou–Lidao Fault is 27 km long, with a strike of 300°–320° and a tendency to the northeast. The middle of the fault has gentle dips of 50°–60°, while the northwest and southeast sections have larger dips of 75°–85°. The whole fault zone forms a gentle wave shape. The fault appears as a transitional zone of different colors from satellite images, with light gray–white areas on the northeast side and green, brown, and pink areas on the southwest side. The topography and landforms have obvious tonal contrasts along the fault, which indicates the controlling role of the fault on the landform. The fault experienced different activities from the Early to Middle Pleistocene, but these movements have ceased since the Late Pleistocene. According to its tectonic rock characteristics, overlying geological ages, and geomorphological features, the northwest section of the fault (Haixitou–Wangguanzhuang section) has manifested older activity, implying that it was active in the pre-Quaternary, while the southeast section (Chegu–Lidao section) was active in the Middle Pleistocene.

3 Data and methods

3.1 Hydrochemical characteristics and δD and $\delta^{18}O$ stable isotopes

To analyze the genesis of water temperature variations, water samples from the No. Lu 32 well were collected from March 2016 to April 2018. Chemical ion concentrations and δD and $\delta^{18}O$ stable isotope compositions

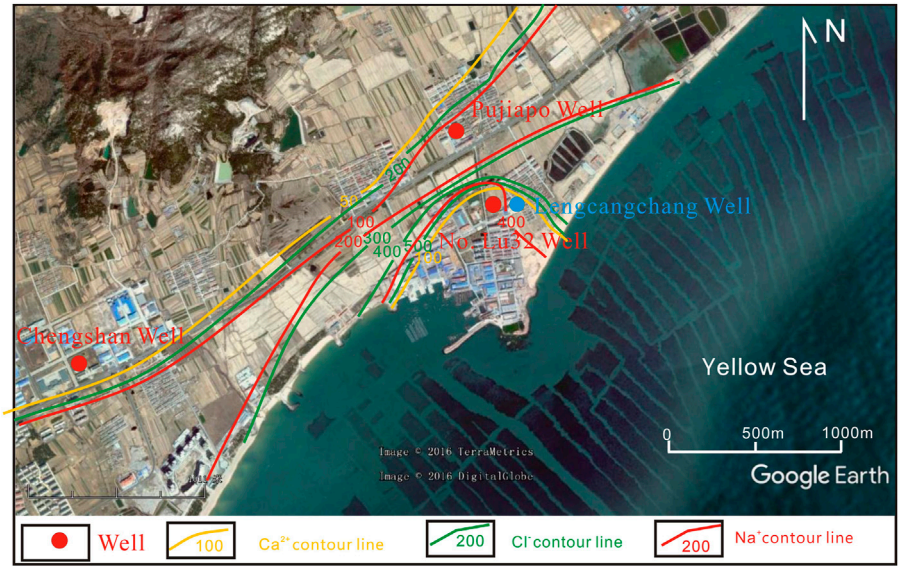

FIGURE 2
Location and distribution of the ion contours of the No. Lu 32 well and surrounding wells (sampling period: April 2017).

in water samples were measured. To analyze the spatial distribution characteristics of water chemistry, the ion contents and hydrogen and oxygen isotope compositions of the Lengcangchang, Pujiapo, and Chengshan wells in the vicinity were collected and tested in April 2017 (Figure 2). The Lengcangchang well is located approximately 50 m from the No. Lu 32 well, the Pujiapo well is approximately 600 m from it, and the Chengshan well is approximately 3.5 km from the No. Lu 32 well (Figure 2). The ion concentrations and δD and $\delta^{18}O$ stable isotope compositions were measured at the Key Laboratory of Crustal Dynamics, National Institute of Natural Hazards, Ministry of Emergency Management of China. Volumetric analysis methods and CIC-200 ion chromatograph were used for hydrochemistry analysis. δD and $\delta^{18}O$ stable isotopes were measured using a type of LGR 912-0008 Hydrogen-Oxygen Stable Isotope Analyzer.

3.2 Water temperature for long-term observations

The No. Lu 32 well is 94 m deep, and the observed aquifer is fracture water in granite. Digital underground water temperature and water level observations have been implemented since September 2007. The No. Lu 32 well uses an SZW-1A digital thermometer for geothermal observation, with a probe depth of 89 m, and an LN-3A digital water level meter for digital water level observations was used in the well with a probe depth of 7.1 m.

4 Results

The hydrochemical characteristics and δD and $\delta^{18}O$ stable isotope compositions are shown in Table 1. The ion contents and hydrogen and oxygen isotope compositions of the wells and seawater were collected in April 2017 and tested once, while the waters from No. Lu 32 well were collected five times from March 2016 to April 2018. It can be seen from Table 1 that the ion contents of seawater were higher than those of the wells.

4.1 Chemical type of the No. Lu 32 well water

Piper diagrams were drawn according to the Ca^{2+}, Mg^{2+}, and Na^{+}–K^{+} concentrations and relative Cl^{-}, SO_4^{2-}, and HCO_3^{-}contents (Figure 3), which can directly indicate the general chemical characteristics of the samples and water types. The intersection point obtained from the upper diamond represents the milliequivalent contents of anions and cations in the waters, the triangle in the lower left corner represents the milliequivalent contents of cations, and the triangle in the lower right corner represents the milliequivalent contents of anions. Figure 3 shows that the Na^{+}, K^{+}, and Cl^{-} milliequivalent concentrations were relatively high, and the water chemistry type of the No. Lu 32 well was the Cl–Na type, indicating intermediate mineralization water of mixed origin and that the water may be related to seawater.

4.2 Water–rock reaction processes

The Na–K–Mg ternary diagram is mainly used to analyze the water–rock equilibrium state in groundwater (Su et al., 2021). According to the analysis of the Na–K–Mg ternary diagram, seawater is located near the mineral equilibrium line, and the Na–K–Mg water–rock interaction reaches the ionic equilibrium state (Figure 4). In contrast, the data of the No. Lu 32 well and nearby wells were basically distributed near the Mg end, which indicated unsaturated water, the water–rock interaction had not yet reached the ionic equilibrium state, and the water–rock interaction was still ongoing, indicating that the No. Lu 32 well possessed the characteristics of shallow water (Figure 4).

TABLE 1 Hydrochemical characteristics of the No. Lu 32 well and seawater in the Jiaodong Peninsula.

No.	Name	K^+ (mgL^{-1})	Na^+ (mgL^{-1})	Ca2+ (mgL^{-1})	Mg^{2+} (mgL^{-1})	F^- (mgL^{-1})	Cl^- (mgL^{-1})	SO_4^{2-} (mgL^{-1})	NO^{3-} (mgL^{-1})	HCO_3^- (mgL^{-1})	δD (‰)	δ^2O (‰)	Data
1	Lu32 well	54.91	288.91	28.95	54.32	1.96	531.29	162.17	94.65	N.D.	−51.48	−7.43	Mar 2016
2		50.04	299.28	111.36	21.52	0.84	578.98	133.19	71.80	154.08	−71.94	−10.43	Jun 2016
3		28.363	304.290	111.288	25.259	1.217	517.105	132.502	73.006	N.D.	−67.11	−9.33	Dec 2016
4		15.262	498.236	125.576	10.632	0.779	866.124	123.319	54.530	361.769	−54.95	−7.32	Apr 2017
5		33.92	480.07	131.69	27.23	0.92	926.13	109.87	47.66	227.98	−39.50	−4.90	Apr 2018
6	Seawater	442.72	9818.6	343.56	1241.94	3.06	17543.14	2411.94	82.52	158.156	−5.097	−0.538	Aug 2017
7	Lengcangchang well	2.010	323.774	141.328	19.768	0.375	715.009	152.728	65.583	244.312	−41.73	−5.94	Apr 2017
8	Chengshan well	5.385	67.521	26.392	4.708	0.331	131.082	31.669	6.033	155.044	−53.00	−7.615	Apr 2017
9	Pujiapo well	7.837	132.828	75.356	9.436	0.389	242.024	64.062	219.51	79.8712	−50.35	−7.06	Apr 2017

10.3389/feart.2023.1131539

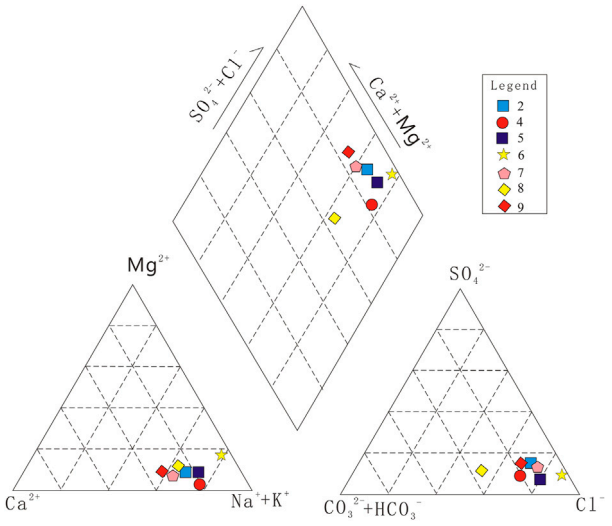

FIGURE 3
Piper diagram of the No. Lu 32 well.

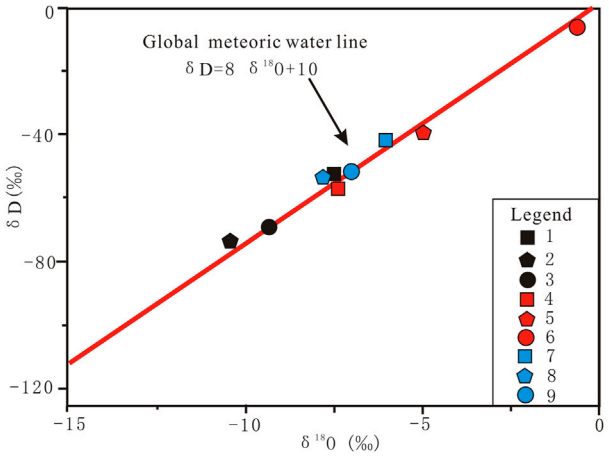

FIGURE 5
Relationships between the δD and $\delta^{18}O$ values of the No. Lu 32 well and the Global Meteoric Water Line (GMWL) [the number in the figure corresponds to that in Table 2, and the GMWL is from (Craig, 1961)].

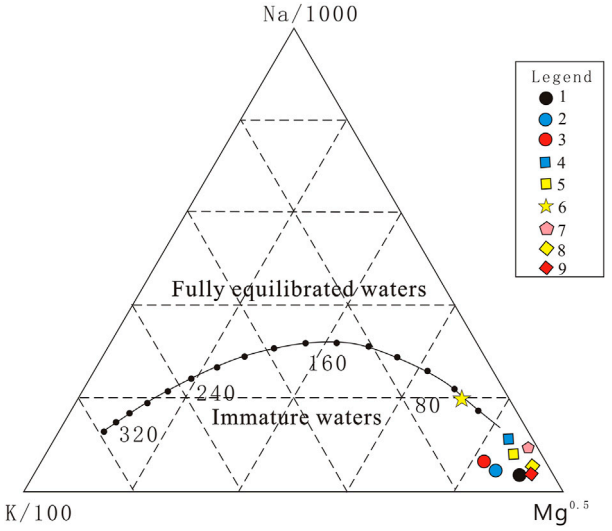

FIGURE 4
Na–K–Mg diagram of the No. Lu 32 well (the number in the figure corresponds to that in Table 1).

4.3 δD and $\delta^{18}O$ stable isotope characteristics

The isotope analysis method has been widely used in environmental hydrogeological research. The analysis of hydrogen and oxygen isotopes is an effective method for constraining the origin of groundwater (Tiwari et al., 2020; Sasaki et al., 2021; Duan et al., 2022). The Global Meteoric Water Line is the red line in Figure 5 (Craig, 1961; Li et al., 2011). The hydrogen and oxygen stable isotopes of nine samples were distributed near this line, and it is inferred that the study well and adjacent wells were influenced by meteoric water.

4.4 Annual variations in water temperature

The water temperature of the No. Lu 32 well has shown several fluctuations since January 2014, with a maximum variation of approximately 0.10°C.The water temperature exhibits a certain annual variation, and its variations from 2018 were used as an example. As shown in Figure 6, the water temperature in the observation well fluctuated several times between October and May of the following year, and the characteristics of the changes varied from year to year.

5 Discussion

Fluid geochemistry, such as the determination of hydrogeochemical characteristics and measurement of stable hydrogen and oxygen isotopes, is a promising and important method for determining the genesis of groundwater (Su et al., 2021; Du et al., 2023). Based on previous geological data of water chemistry and hydrogen–oxygen isotope compositions, water chemistry data were first used to analyze the water type and water–rock interactions of the No. Lu 32 well; the relationship between the No. Lu 32 well and meteoric water was then analyzed based on the hydrogen–oxygen isotope compositions.

5.1 Spatial distribution of ion contents in the No. Lu 32 well and neighboring wells

Coastal zones are the most sensitive regions on Earth, and have multiple groundwater quality types, such as fresh, brackish, and saline

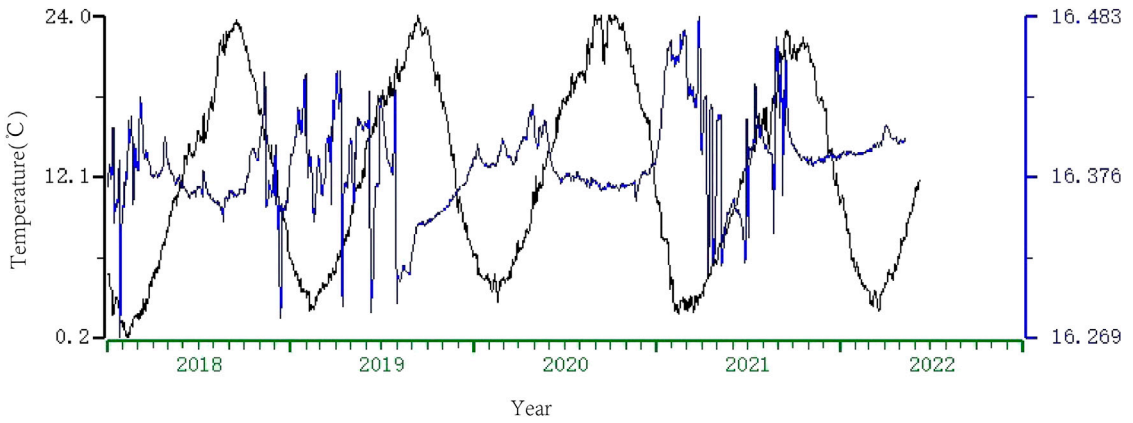

FIGURE 6
Comparison of temperature between CSTSTOS and the No. Lu 32 well from January 2018 to May 2022. The black line is the seawater temperature of CSTSTOS, and the blue line is the groundwater temperature of the No. Lu 32 well.

TABLE 2 Seawater and groundwater mixing at different ratios.

Name		K^+ (mgL^{-1})	Na^+ (mgL^{-1})	Ca^{2+} (mgL^{-1})	Mg^{2+} (mgL^{-1})	F^- (mgL^{-1})	Cl^- (mgL^{-1})	SO_4^{2-} (mgL^{-1})	NO^{3-} (mgL^{-1})	HCO_3^- (mgL^{-1})
Seawater		442.72	9818.6	343.56	1241.94	3.06	17543.14	2411.94	82.52	158.156
Pujiapo well		7.837	132.828	75.356	9.436	0.389	242.024	64.062	219.51	79.8712
Seawater mixing ratio	5%	29.58	617.11	88.76	71.06	0.52	1107.08	181.45	212.66	83.78
	10%	51.32	1101.4	102.17	132.68	0.65	1972.13	298.84	205.81	87.69
Average value of the No. Lu 32 well		36.49	374.157	101.77	27.79	1.143	683.92	132.21	68.329	247.94

water (Sun et al., 2023). The results of the water chemistry analysis in April 2017 showed the contours of Na^+, Ca^{2+}, and Cl^- in the No. Lu 32, Chengshan, and Pujiapo wells (Figure 2). At the same time, with increasing distance from the sea, the ion content of seawater exhibited a decreasing trend from the No. Lu 32, Lengcangchang, and Chengshan wells to the Pujiapo well, suggesting that their sources may be seawater infiltration. This spatial distribution characteristic of the water chemistry compositions is consistent with previous research results in other coastal zones (Liu et al., 2017; Sun et al., 2023).

5.2 Seawater mixing effect

From the water chemistry data, we found that the No. Lu 32 well received a small amount of seawater recharge, and the mixing ratio of seawater was calculated using the water chemistry ratio method (Jaime, 1990; Wang, 2018) by the following equation:

$$M = x^*F + (1 - x)^*S \quad (1)$$

where x is the proportion of groundwater in the mixing water, F is the content of a certain ion in groundwater, (1−x) is the proportion of seawater in the mixing water, S is the content of a certain ion in seawater, the ion content in seawater is referred to as the global average ion contents (Wang, 2018), and M is the content of a certain ion in the mixing water. The calculation results are shown in Table 2. The mixing ratio of the No. Lu 32 well was approximately 5%.

5.3 Annual variations between well and seawater temperatures

To analyze the possible effects of seawater temperature changes on groundwater temperature in the No. Lu 32 well, we collected the ocean forecast values of the surface water temperatures in the neighboring area, Port West, which is next to a farming area (Figure 2); the temperature comparison chart is shown in Figure 6.

There is a clear seasonal variation in the seawater temperature in the western Yellow Sea region (Hou et al., 2010), with an increasing trend in April and the highest annual surface water temperature from June to August; the highest values in 20 m and 30 m of seawater start in August–October (Quan et al., 2013), which is also similar to the time when the water temperature in the No. Lu 32 well exhibits an increasing trend (Figure 6). As the coastal area of the Jiaodong Peninsula has experienced severe seawater backflow in recent years, we cannot eliminate the possibility that seawater backflow and other factors influence the water temperature in the observation well.

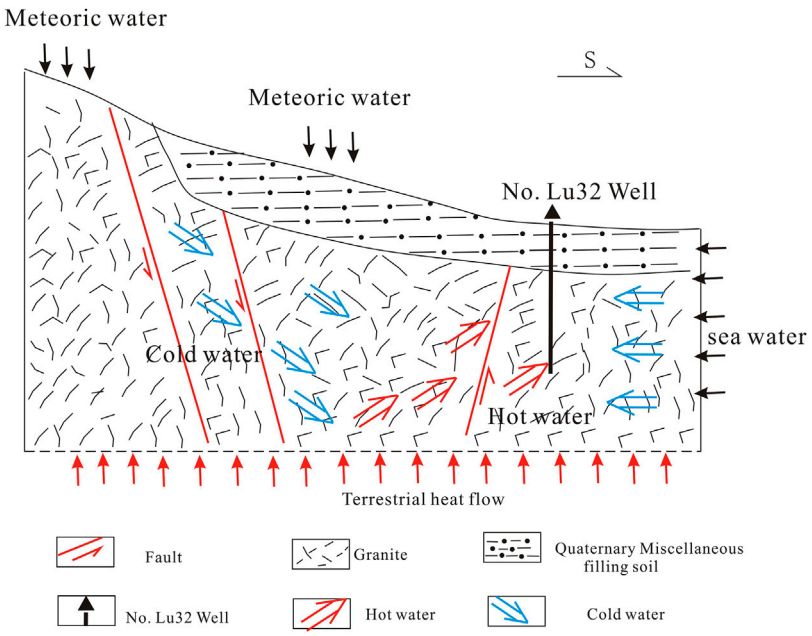

FIGURE 7
Genetic model of the No. Lu 32 well.

5.4 Genetic model

Through analyzing hydrochemical characteristics and hydrogen and oxygen isotope characteristics, combined with geochemical and geological survey results, the genesis of groundwater can be comprehensively inferred, providing a scientific basis for the analysis of water temperature change characteristics (Sui et al., 2020; Du et al., 2023). The Na^+, K^+, and Cl^- concentrations were relatively high, which may be related to the influence of seawater, while the hydrogen and oxygen isotopes showed that meteoric water may be the source of the No. Lu 32 well. Based on the surrounding geological features, as well as the groundwater and seawater, the groundwater genetic model of the No. Lu 32 well was established (Figure 7). Figure 7 shows that the water level is influenced by meteoric water, while the water temperature changes produce a certain annual pattern of variation due to the influence of seawater. Our research conclusion is similar to the groundwater study in the adjacent area of the Huanghai Sea (Gao et al., 2016; Sun et al., 2023).

6 Conclusion

The water chemistry type of the No. Lu 32 well is Cl–Na, which indicates intermediate mineralization water with a mixed origin. The Na–K–Mg ternary diagram analysis reveals that the water is unsaturated, the water–rock interaction state has not yet reached ionic equilibrium, and the water–rock interaction is still ongoing, indicating that the No. Lu 32 well exhibits the characteristics of shallow water. The hydrogen and oxygen isotope distributions are near the meteoric water line, and it is presumed that the No. Lu 32 well and the neighboring wells are influenced by meteoric water. Since the water temperature of the No. Lu 32 well has some quasi-synchronous and morphological similarity with seawater temperature, the results of the water chemistry and isotope analysis of this well also indicate that the groundwater is influenced by seawater. A comprehensive analysis suggests that the No. Lu 32 well is affected by various factors, including seawater backflow infiltration and shallow water.

Data availability statement

The original contributions presented in the study are included in the article/Supplementary Material; further inquiries can be directed to the corresponding author.

Author contributions

GD: methodology, data curation, and writing—original draft preparation. SS: writing—review and editing. BZ: methodology, conceptualization, and writing—review and editing. LS: writing—review and editing. XC: writing—review. HR: methodology, data curation, and validation. MS: editing. LW: editing.

Funding

This study was financially supported by the Laoshan Laboratory (Nos LSKJ202203504 and LSKJ202204201), the Monitoring, Prediction and Research-combined Project of the China Earthquake Administration (No. SJH202302059), the National Key Research and Development Program of China

(No. 2019YFC1509203), and the Marine Geological Survey Program of the China Geological Survey (DD20221707).

Acknowledgments

Some figures were made using the Generic Mapping Tools (https://forum.generic-mapping-tools.org/, last accessed March 2020) (Wessel et al., 2013).

Conflict of interest

Author LW was employed by CNPC East China Design Institute Co., Ltd.

The remaining authors declare that the research was conducted in the absence of any commercial or financial relationships that could be construed as a potential conflict of interest.

Publisher's note

All claims expressed in this article are solely those of the authors and do not necessarily represent those of their affiliated organizations, or those of the publisher, the editors, and the reviewers. Any product that may be evaluated in this article, or claim that may be made by its manufacturer, is not guaranteed or endorsed by the publisher.

References

Chao, H., Wang, Q., and Li, J. (1997). *Seismotectonic map of Shandong Province, new tectonic map of Shandong Province and instructions* (China: S.M. Press), 100–132.

Craig, H. (1961). Isotopic variations in meteoric waters. *Isotopic Var. Meteoric Waters* Scinece 133, 1702–1703. doi:10.1126/science.133.3465.1702

Du, G., Su, S., Chang, X., Ren, H., Huo, Z., and Zhang, X. (2023). Hydrogeochemical characteristics and Genesis of Hongshuilantang Hot Spring and its water temperature anomalies during the Rushan earthquake swarm in Eastern China. *Front. Earth Sci.* 10, 1088240. doi:10.3389/feart.2022.1088240

Duan, R., Li, P. Y., Wang, L., He, X., and Zhang, L. (2022). Hydrochemical characteristics, hydrochemical processes and recharge sources of the geothermal systems in Lanzhou City, northwestern China. *Urban Clim.* 43, 101152–152. doi:10.1016/j.uclim.2022.101152

Gao, X., Liang, H., Wang, H., Zheng, L., Li, J., Zhao, C., et al. (2015). Origin of the mud volcano in northern Tianshan constrained by geochemical investigation. *Seismol. Geol.* 4 (37), 1215–1224. doi:10.3969/j.issn.0253-4967.2015.04.021

Gao, M., Hou, G., and Guo, F. (2016). Conceptual model of underground brine formation in the silty coast of laizhou bay, bohai sea, China. *J. Coast. Res.* 74, 157–165. doi:10.2112/si74-015.1

Gu, Q., Ding, Z., Kang, Q., and Li, D. (2020). Group velocity tomography of Rayleigh wave in the middle-southern segment of the Tan-Lu fault zone and adjacent regions using ambient seismic noise. *Chin. J. Geophys. Chin.* 63 (4), 1505–1522. doi:10.6038/cjg2020N0117

Hou, C., Guo, P., and Zhou, L. (2010). The mechanism analysis of water temperature difference between Shidao, Xiaomaidao,and Haiyang. *Trans. Oceanol. Limnol.* 2, 6–10. doi:10.13984/j.cnki.cn37-1141.2010.02.006

Jaime, J. (1990). Groundwater problems in coastal areas: E. Custodio (with the collaboration of G.A. Bruggeman and others) UNESCO, 1987, ISBN: 92-3-102415-9. *Adv. Water Resour.* 154. doi:10.1016/0309-1708(90)90010-2

Lai, G., Jiang, C., Han, L., Sheng, S., and Ma, Y. (2016). Co-seismic water level changes in response to multiple large earthquakes at the LGH well in Sichuan, China. *Tectonophysics* 679, 211–217. doi:10.1016/j.tecto.2016.04.047

Lai, G., Jiang, C., Wang, W., Han, L., and Deng, S. (2021). Correlation between the water temperature and water level data at the Lijiang well in Yunnan, China, and its implication for local earthquake prediction. *Eur. Phys. J. Special Top.* 230 (1), 275–285. doi:10.1140/epjst/e2020-000255-3

Li, Y., Zhang, M., Wang, S., Li, Z., and Wang, F. (2011). Progress of the research of stable isotope in precipitation in China:A review. *J. Glaciol. Geocryol.* 33 (3), 624–633.

Liu, Y., Ren, H., Zhang, L., Fu, H., Sun, X., He, D., et al. (2015). Undergrund fluied anomalies and the precursor mechanisms of the Ludian Ms6.5 earthquake. *Seismol. Geol.* 1 (337), 307–318. doi:10.3969/j.issn.0253-4967.2015.01.024

Liu, S., Tang, Z., Gao, M., and Hou, G. (2017). Evolutionary process of saline-water intrusion in holocene and late Pleistocene groundwater in southern laizhou bay. *Sci. Total Environ.* 607–608 (0048-9697), 586–599. doi:10.1016/j.scitotenv.2017.06.262

Ma, Y. (2016). Earthquake-related temperature changes in two neighboring hot springs at Xiangcheng, China. *Geofluids* 16 (3), 434–439. doi:10.1111/gfl.12161

Ma, Y., Huang, F., Xue, Y., and Wang, B. (2015). Statistical analysis of long-term observation data of water temperature in springs and wells. *Technol. Earthq. Disaster Prev.* 2 (10), 367–377. doi:10.11899/zzfy20150217

Miyakoshi, A., Taniguchi, M., Ide, K., Kagabu, M., Hosono, T., and Shimada, J. (2020). Identification of changes in subsurface temperature and groundwater flow after the 2016 Kumamoto earthquake using long-term well temperature–depth profiles. *J. Hydrology* 582, 124530. doi:10.1016/j.jhydrol.2019.124530

Pan, S., Wang, F., Zheng, Y., Duan, Y., Liu, L., Deng, X., et al. (2015). Crustal velocity structure beneath Jiaodong Peninsula and its tectonic implications. *Chin. J. Geophys.* 9, 3251–3263. doi:10.6038/cjg20150920

Pope, E., Bird, D., and Arnórsson, S. (2014). Stable isotopes of hydrothermal minerals as tracers for geothermal fluids in Iceland. *Geothermics* 49, 99–110. doi:10.1016/j.geothermics.2013.05.005

Qu, J., Gao, S., Wang, C., Liu, K., Zhou, S., Yang, Y., et al. (2021). Crustal P-wave velocity structure and earthquake distribution in the Jiaodong Peninsula, China. *Tectonophysics* 814, 228973. doi:10.1016/j.tecto.2021.228973

Quan, Q., Mao, X., Yang, X., Hu, Y., Zhang, H., and Jiang, W. (2013). Seasonal variations of several main water masses in the southern Yellow Sea and East China Sea in 2011. *J. Ocean Univ. China* 12 (4), 524–536. doi:10.1007/s11802-013-2198-5

Sasaki, K., Morita, J., Iwaki, C., and Ueda, A. (2021). Geochemical evaluation of geothermal resources in Toyama Prefecture, Japan, based on the chemical and isotopic characteristics of hot spring waters. *Geothermics* 93, 102071. doi:10.1016/j.geothermics.2021.102071

Song, D., Chen, Y., Wang, T., Li, M., and Li, P. (2021). Organic geochemical compositions of mesoproterozoic source rocks in the yanliao rift, northern China. *Mar. Petroleum Geol.* 123, 104740–104820. doi:10.1016/j.marpetgeo.2020.104740

Su, S., Chen, Q., Zou, C., Yan, B., Du, G., and Feng, E. (2021). Hydrogeochemical characteristics and Genesis of seismic observation wells in Shandong Province, China. *Arabian J. Geosciences* 14 (22), 2398. doi:10.1007/s12517-021-08774-w

Sui, L., Du, G., and Chen, Q. (2020). Formation mode of wenquantang hot spring in weihai city. *Shandong Land Resour.* 36, 40–45. doi:10.12128/j.issn.16726979.2020.10.007

Sun, Q., Gao, M., Wen, Z., Hou, G., Dang, X., Liu, S., et al. (2023). Hydrochemical evolution processes of multiple-water quality interfaces (fresh/saline water, saline water/brine) on muddy coast under pumping conditions. *Sci. Total Environ.* 857 (1), 159297. doi:10.1016/j.scitotenv.2022.159297

Tiwari, S., Gupta, A., and Asthana, A. (2020). Evaluating CO2 flux and recharge source in geothermal springs, garhwal himalaya, India: Stable isotope systematics and geochemical proxies. *Environ. Sci. Pollut. Res.* 27 (13), 14818–14835. doi:10.1007/s11356-020-07922-1

Wang, X. (2018). *A study of the charateristics and genesis of the hot springs in the western Shandong Peninsula*. Master. Beijing: China University of Geosciences.

Wang, Z., Deng, Q., Chao, H., Du, X., Shi, R., Sun, Z., et al. (2006). Shallow depth sonic reflection profiling studies on the active Penglai Weihai fault zone offshore of the northern Shandong peninsula. *Chin. J. Geophys.* 4 (49), 1092–1101. doi:10.1002/cjg2.920

Wessel, P., Smith, W., Scharroo, R., Luis, J., and Wobbe, F. (2013). Generic mapping tools: Improved version released. *Eos,Transactions Am. Geophys. Union* 45 (94), 409–410. doi:10.1002/2013eo450001

Zhang, L., Guo, L., Zhou, X., Yang, Y., Shi, D., and Liu, Y. (2021). Temporal variations in stable isotopes and synchronous earthquake-related changes in hot springs. *J. Hydrology* 599, 126316. doi:10.1016/j.jhydrol.2021.126316

Zhao, L., Xie, X., Wang, W., Zhang, J., and Yao, Z. (2010). SeismicLg-waveQtomography in and around northeast China. *J. Geophys. Res.* 115 (B8), B08307. doi:10.1029/2009jb007157

Zhao, L., Xie, X., Wang, W., Zhang, J., and Yao, Z. (2013). Crustal lg attenuation within the North China craton and its surrounding regions. *Geophys. J. Int.* 195 (1), 513–531. doi:10.1093/gji/ggt235

frontiers | Frontiers in Earth Science

TYPE Original Research
PUBLISHED 09 March 2023
DOI 10.3389/feart.2023.1132820

OPEN ACCESS

EDITED BY
Qingqiang Meng,
SINOPEC Petroleum Exploration and Production Research Institute, China

REVIEWED BY
Jiachun Li,
Peking University, China
Yin Liu,
China University of Petroleum, Huadong, China

*CORRESPONDENCE
Lijun Song,
8210954@qq.com
Yonghe Sun,
29595342@qq.com

SPECIALTY SECTION
This article was submitted to Geochemistry, a section of the journal Frontiers in Earth Science

RECEIVED 28 December 2022
ACCEPTED 16 February 2023
PUBLISHED 09 March 2023

CITATION
Song L, Ruan Y, Sun Y, Xie F, Li J and Yuan Y (2023), Dynamic background on formation, evolution, and later reformation of the Late Paleozoic–Early Mesozoic Basin in Songliao and its significance for hydrocarbon exploration. *Front. Earth Sci.* 11:1132820. doi: 10.3389/feart.2023.1132820

Dynamic background on formation, evolution, and later reformation of the Late Paleozoic–Early Mesozoic Basin in Songliao and its significance for hydrocarbon exploration

Lijun Song[1]*, Yongqi Ruan[1], Yonghe Sun[2]*, Fenquan Xie[3], Junlong Li[1] and Yulong Yuan[1]

[1]Xi'an Shiyou University, Xi'an, Shaanxi, China, [2]Chongqing University of Science and Technology, Chongqing, China, [3]Northeast Petroleum University, Daqing, Heilongjiang, China

Located on the Songnen block of the Northeast Asia block group, the Songliao Basin is sandwiched by three major plates in Siberia, North China, and the Pacific Ocean. The recognition of the basin's properties and the dynamic processes of formation, evolution, and late reformation of the Late Paleozoic–Early Mesozoic Basin (LP-EMB), which has suffered from intense multi-stage, and various types of late reformation, are always controversial. On the basis of previous research on the regional tectonic geological background, combined with petrochemical and chronological data from core samples and seismic data, the attributes, evolution process, and late reformation of the LP-EMB and its dynamic environments have been deeply analyzed. Since the Late Paleozoic, it has successively experienced the development of Late Hercynian to Early–Middle Indosinian rifts and subsequent multi-stage superimposed transformation stages, which can be divided into the near-north-trending thrust reformation in the Late Indosinian, the near-west-trending thrust reformation in the Early Yanshanian, the differential extensional reformation in the early Late Yanshanian, the strike-slip shearing and deep burial reformation in the middle Late Yanshanian, and the strike-slip compression fold transformation in the late Late Yanshanian to the early Himalayan. The formation of the LP-EMB was mainly controlled by back-arc extension caused by the subduction and retreat of the paleo-Pacific Plate and partly by the closure of the Paleo-Asian Ocean between the North China Plate and the Northeast Asia micro-block group. The later reformation stages were closely related to the collision extrusion, strike-slip activity, and deep mantle activity caused by either the relative convergence movement between Songnen and other micro-blocks in the Northeast China micro-block group or by the remote collision effect of the Northeast China micro-block group and the surrounding plates. The inner fault zone (body), which was formed by multi-phase fault cutting, and the top weathering and denudation unconformity surface, are potential sites of hydrocarbon accumulation, from which natural gas has been transported along the fault and fracture belt into the weathering crust and the inner fracture zone in the Upper Paleozoic–Lower Mesozoic (UP-LM). This study significantly expands our knowledge of the tectonic evolution and gas exploration of the Songliao Basin.

KEYWORDS

Songliao Late Paleozoic–Early Mesozoic basin, formation and evolution, late reformation, dynamic mechanism, hydrocarbon prospects

1 Introduction

The Songliao Basin, on the Songnen block in the middle of the Northeast Asia block group, is surrounded by the Siberia, North China, and Western Pacific plates (Figure 1). The pre-Paleozoic folded-crystalline basement of the basin was formed by the multi-phase collage of intra-ocean island arcs, or micro-block, which was rifted from the Siberian Plate or the subducting island arc in the Paleo–Asian Ocean through three collages: 1) the collage of early Caledonian combined with the Erguna and Xing'an blocks along the Xigutu suture zone in the early Early Paleozoic, 2) the collage of late Caledonian combined with the Songnen and Jiamusi–Xingkai blocks along the Mudanjiang suture in the pre-Devonian, and 3) the collage of late Hercynian combined with the Songnen and Erguna–Xing'an blocks along the Nenjiang suture in the late Early Carboniferous to early Late Carboniferous (Liu et al., 2019).

The present Songliao Basin is mainly composed of the middle to lower parts of the Lower Cretaceous rifted strata, the upper part of the Lower Cretaceous to Upper Cretaceous depression strata and the Cenozoic depression strata (Figure 2). Among them, the Lower Cretaceous rifted strata are composed of the Huoshiling Formation (K_1h), the Shahezi Formation (K_1sh), the Yingcheng Formation (K_1y), and the Denglouku Formation (K_1d), which were unconformably covered by the Lower Cretaceous Quantou Formation (K_1q), the Upper Cretaceous Qingshankou Formation (K_2q), the Yaojia Formation (K_2y), the Nenjiang Formation (K_2n) and the Sifangtai Formation (K_{2s}). The Mingshui Formation (K_2m) and the Cenozoic depression strata, composed of Paleogene, Neogene and Quaternary, are unconformably overlaid on the underlying strata (Figure 2) (Di, 2013; Du, 2017).

Between the Cretaceous strata and the basement, it is a set of Upper Paleozoic–Lower Mesozoic (UP-LM) sedimentary strata of the Songliao Basin (Figures 2, 3). The precise age (Huang et al., 2019), lithological composition (Chen, 2016; Guo et al., 2019; Zhang et al., 2020), structural characteristics (Zhang, 2006; Wang, 2016; Du, 2017), evolution process (Liu et al., 2003; Zhang et al., 2006), reservoir characteristics (Chen, 2016; Du, 2017; Guo et al., 2019), and hydrocarbon accumulation laws (Du, 2017; Zhang et al., 2019) have been discussed in previous studies. It has been shown that the rock series, composed of metamorphic sandstone, marble, slate, and phyllite, have developed multiple sets of thrust faults in different directions among them, through long-term weathering and denudation, thermal metamorphism, dynamic metamorphism, and other late transformations since the Late Paleozoic (Wu et al., 2000; Chen, 2016). There remain differing opinions on the formation age, formation evolution, and later transformation of this set of rock series due to the lack of a systematic understanding of the process and its dynamic environment, which restricts in-depth promotion of petroleum exploration and development.

In analyses of the formation time of the LP-EMB and its basin properties, formation, evolution and reformation processes, the dynamic environment and hydrocarbon accumulation conditions are of greatly significant in enriching the theoretical understanding and improving the scientific guidance of petroleum exploration. They can also be used as references for petroleum exploration in other Upper Paleozoic basins and superimposed reformation basins in China (Guo et al., 2021; Fang et al., 2021; Niu et al., 2021).

2 Materials and methods

The data involved in this study include 2D/3D seismic data, well loggings, and borehole core analysis test data such as geochemical, chronological, and thin-section identification data. In addition, numerous previous research results have been collected and used in this study, especially recent regional geological survey results (Zhou et al., 2018; Liu et al., 2019; Wang et al., 2021), oil field deep drilling data (Du, 2017; Guo et al., 2019; Hou et al., 2018; Huang et al., 2019a; Huang et al., 2019b) and regional geological background research results (Maruyama and Seno, 1986; Maruyama, 1997; Han et al., 2015).

To understand the basin properties, the processes of formation, evolution and late reformation and the hydrocarbon conditions of the LP-EMB, we comprehensively interpreted seismic data, analyzed structural evolution based on the equilibrium profiles of L1 and L2, analyzed the dynamic process of basin formation, evolution and late reformation and combined these with previous research results.

To highlight the accuracy and rationality of the understandings, we integrate the data from different sources and scales into the same figures to emphasize the coupling relationship between the basin's evolution and late reformation, as well as its deep and regional structures. Therefore, a comprehensive analysis was generally used in this study.

3 Formation and evolution

3.1 Deposition age

Drilling on the paleo-central uplift of the Songliao Basin has revealed that the UPLM lithology is complex, composed of sedimentary rocks, metamorphic rocks and syntectonic magmatic rocks. It is mainly composed of volcanic rocks or volcaniclastic rocks, as evidenced by the deposition of rhyolite and andesite revealed in the cores of wells Ss 10, Fs 3, Xs 17, Xushen 33, and Ss 201, and the location of volcanic rock areas in an A-K original rock lithology discrimination map of schist samples from wells Lt 1 and Lt X3 (Figure 1).

It was mainly composed of volcaniclastic rocks (Figures 4A, B) from the Permian to the middle Triassic, developed in the strongly volcanic activity of the late period of the Late Hercynian to the middle Indosinian period, as evidenced by the range of chronological data (from 308 to 245Ma, peak at 270 Ma) from volcanic rock samples of wells Lt 1, Ss 10, Ws 2, Ss 201, Fs 10, Lt X3, and Zs 3; the two Permian volcanic events erupted at 282.5 ± 2.8 Ma and 255.4 ± 2.6 Ma, as evident from andesite samples from well Ss 10 (Huang et al., 2019). In addition, volcanic rocks (264 ± 3Ma, 287 ± 5Ma, 274 ± 3Ma, Ding et al., 2007), intrusive rocks

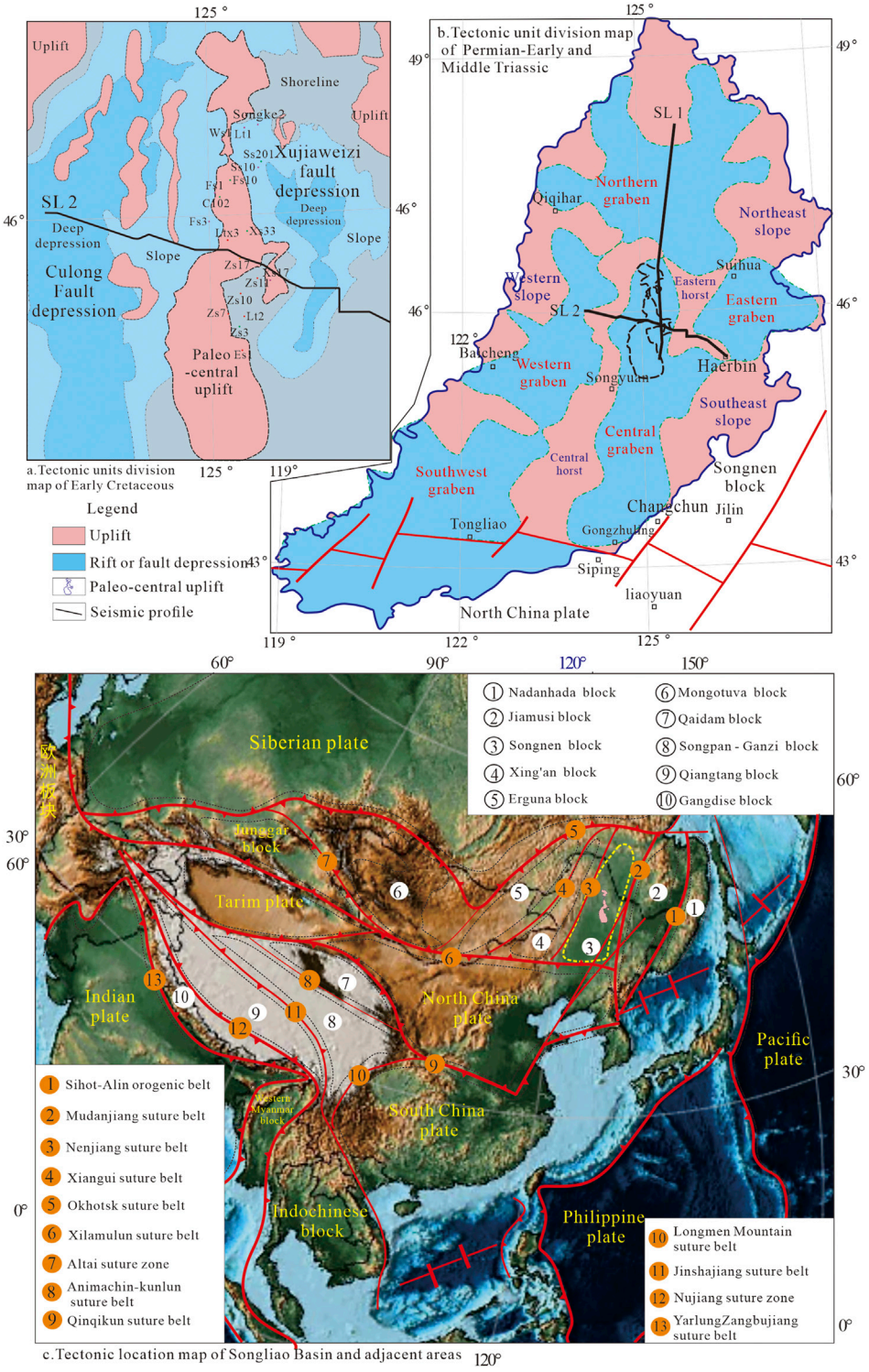

FIGURE 1
Structural characteristics and tectonic setting of Songliao Basin. Paleogeographic maps modified from Scotese (2016).

(305 ± 2Ma), granodiorite (well DuI-4, Wu et al., 2011), and quartz diorite (236 ± 3Ma, well T6- 1, Gao et al., 2007) have also been found in the periphery of the paleocentral uplift of the Songliao Basin.

The Nenjiang Ocean, between the Songnen and Erguna–Xing'an blocks, was closed in the late Early Carboniferous and the early Late Carboniferous (Liu et al., 2019). In the western margin of the Songliao Basin, Permian in outcrops is unconformable over

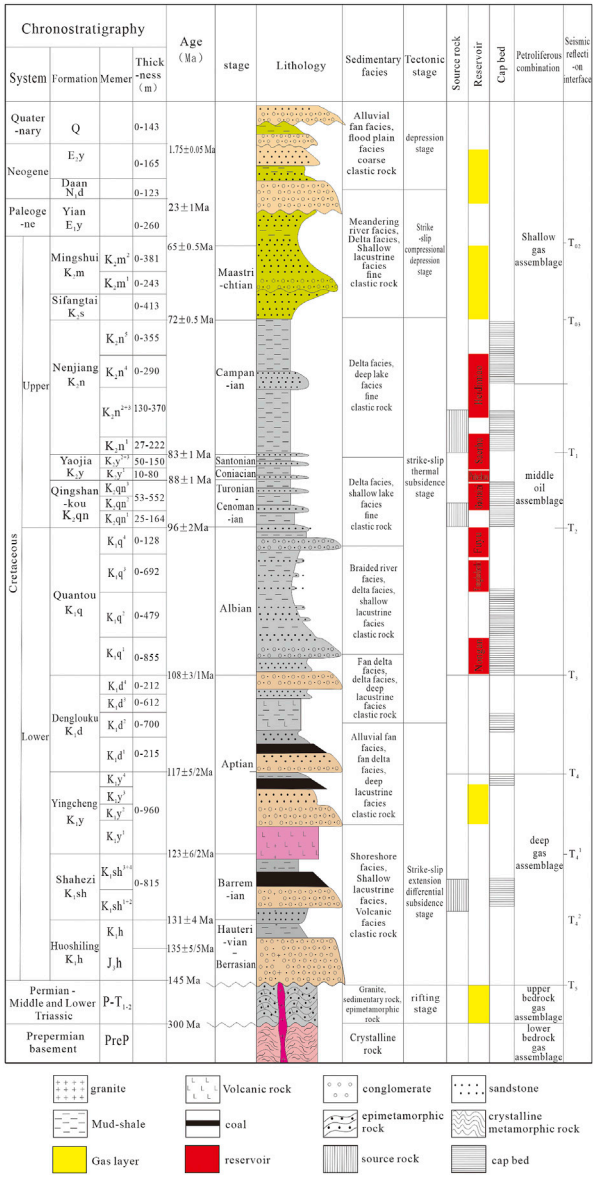

FIGURE 2
Synthetical histogram of strata in Songliao Basin.

Carboniferous (Li, 2019). Therefore, the set of rock series should be reasonably assumed to have been deposited during the Late Paleozoic to Early Mesozoic.

3.2 Basin properties, formation, and evolution

3.2.1 Back-arc extensional rifting stage

The distribution of UPLM volcanic-bearing clastic rocks is controlled by normal faults, mainly in the nearly north–south rift trough (Figures 3, 5A, 6A). A discriminant map of the geochemical tectonic environment of TiO_2-(Fe_2O_3+MgO) and Al_2O_3/SiO_2-(Fe_2O_3+MgO) (Bhatia, 1983) shows the characteristics of the continental region and rift environment, which are similar to the East African Rift (Huntsman-Mapila et al., 2009) (Figures 4C, D). It indicates that the Mudanjiang Ocean was reopened on the east side of the Songnen block in the Permian, as evidenced by the intrusion age (251 ± 1 Ma) of metamorphic gabbro samples and the eruption age (252 ± 1 Ma) of metamorphic pillow-like basalt samples, with the characteristics of paleo-oceanic crust fragments, in the Mudanjiang ophiolite melangite belt in Pingan Village, Yilan County (Liu et al., 2019). The paleo-Pacific Ocean crust on the east side of the Jiamusi Block began to subduct during the late Carboniferous, as evidenced by the Zhenzishan Formation deposited in the continental margin sedimentary environment in the Upper Carboniferous (Liu et al., 2019). In addition, the Songnen block drifted rapidly from west to east during the Late Paleozoic (Scotese, 2016).

The aforementioned evidence indicates that the Mudanjiang Ocean was reopened under a back-arc extension background caused by the rapid subduction and retraction of the Paleo-Pacific plate. Therefore, the Songnen block and its adjacent areas were also rifting under the back-arc extension background starting in the late Hercynian and possibly lasting until the middle Indosinian (Figure 6A).

3.2.2 Collision rift stage

The Xilamulun suture zone began to close in the late Permian to Early–Middle Triassic (Wang et al., 2016) and began to provide provenance for the Linxi Formation in the Linxi area, as evidenced by the Permian pillow lava in the ophiolite (~260 Ma, Miao et al., 2007); the Permian Radiolaria in the semi-deep-sea or deep-sea siliceous rocks of the ophiolite belt in Linxi County (Wang and Fan, 1997); the syn-collision granite in Dayushan, Jilin Province (248 Ma, Sun et al., 2004); and the Early Mesozoic detrital zircon composition in the Linxi Formation sandstones in eastern Inner Mongolia (238 Ma, Han et al., 2015; 249~233 Ma, Wang et al., 2021).

The aforementioned evidence reveals that the east–west crustal extension rifting events in the Songnen block and the surrounding areas may have been partly influenced by the collision of the North China Plate and the Northeast Asia block group (Figures 5B, 6B) and was in a collisional rifting stage in the Early and Middle Triassic.

3.2.3 Tectonic evolution

Under the back-arc east–west direction extension caused by the subduction of the Paleo-Pacific plate, the crust was extending east to west; rifts were developing in the Northeast Asia block group in the Permian and were filled with volcaniclastics from 308 Ma to 245 Ma (peak at 270Ma) (Figures 2, 4–6).

From the end of the Late Permian to the Early-to-Middle Triassic, the Songliao Basin entered the stage of collision rift caused by north–south extrusion as the North China Plate collided with the Northeast Asia block group. The Middle Triassic andesite (242.6 ± 0.77 Ma, Hou et al., 2018) drilled from the core of well Songke II also supports the volcanic rift events in this period.

4 Late basin reformations

Since the late Triassic, the LP-EMB has experienced complex late tectonic evolution, in which different interwoven properties and

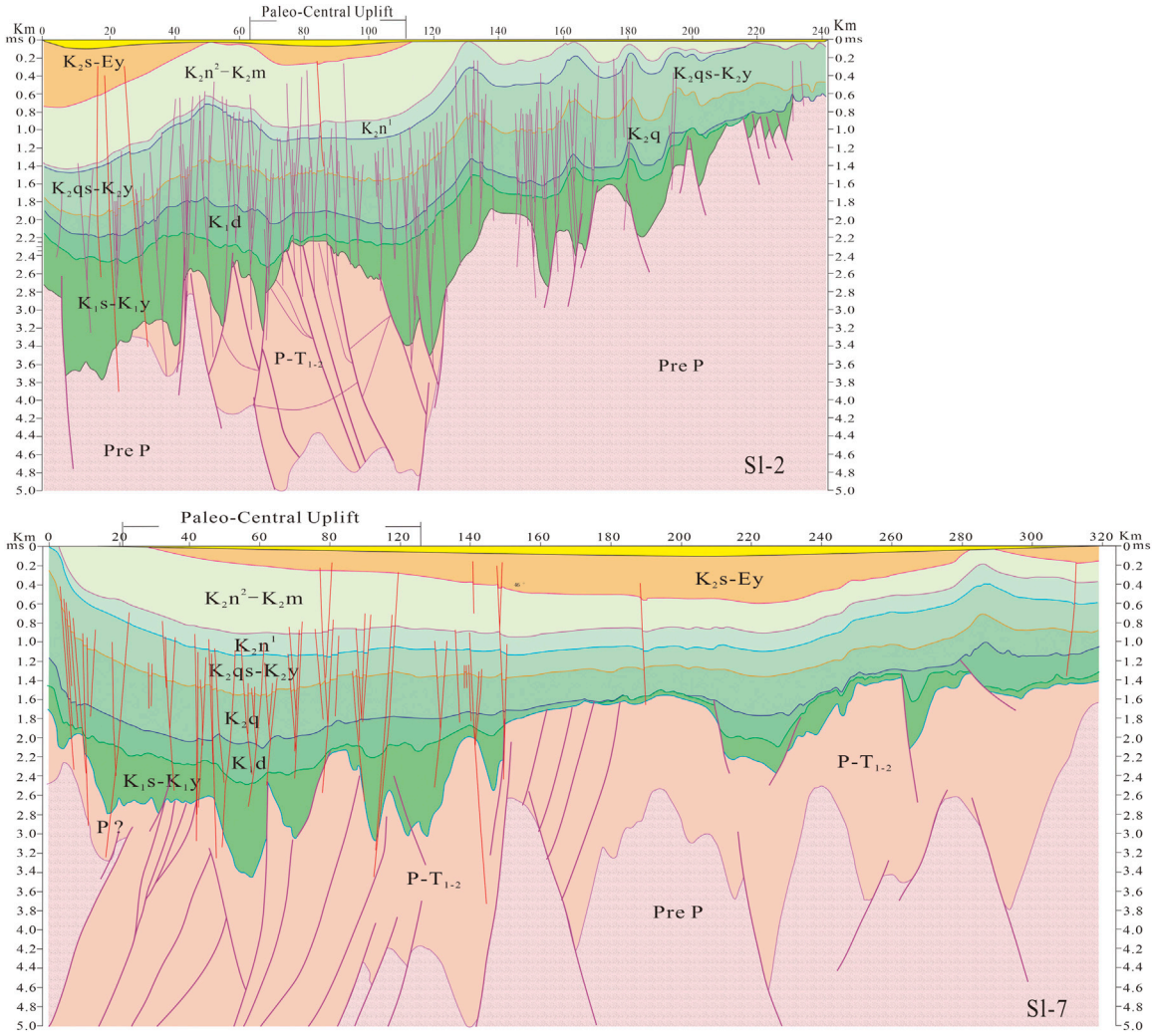

FIGURE 3
Structural profile of SL-1 and SL-2 in Songliao Basin (locations of the section are shown in Figure 1).

occurrence faults developed in the UP-LM (Figures 3, 5, 6). Among these, the inner east–west thrust faults and the near north–south thrust faults successively developed, followed by the negative flower strike-slip faults developed and controlled by the former and lower fault.

4.1 Extrusion thrust reformation

4.1.1 North–south-directed thrust transformation in the late Indosinian

South-dipping thrust faults developed in the UP-LM (Figure 3). In the Late Triassic, the southern margin of the Songnen block was strongly squeezed by the south–north-directed continental collision of the North China Plate and the Northeast Asian block group, as proved by evidence such as the metamorphic events of the Changchun–Panshi–Huadian–Kaishantun metamorphic complex in the eastern section of the Xilamulun suture zone (230 Ma, Zhou et al., 2019), the presence of Late Triassic granite intrusion in the central Jilin Province (216 ± 3 Ma, Sun et al., 2005) and the distribution of the Indosinian S-type granitic zone in the northern margin of the North China Plate (Xie, 2016).

The aforementioned evidence indicates that in the Late Indosinian, under the tectonic background of north–south-directed continent-continental compressional collision caused by the closure of the paleo-Asian Ocean along the Xilamulun suture (Figure 6B), the UP-LM experienced extrusion and thrust transformation from south to north, with the development of south-dipping imbrachial fan-type thrust faults (Figures 3, 5B) and magmatic intrusion in the late Triassic, such as the late Indosinian granite from wells Zs 11 (214 Ma) and Zs 10 (224 Ma).

4.1.2 East–west-directed thrust transformation in the early Yanshanian

East-dipping thrust faults developed in the UP-LM (Figure 3) and indicate that the collision between the Jiamusi and Songnen blocks occurred in the early Yanshanian, as evidenced by the formation of ophiolite melange in the

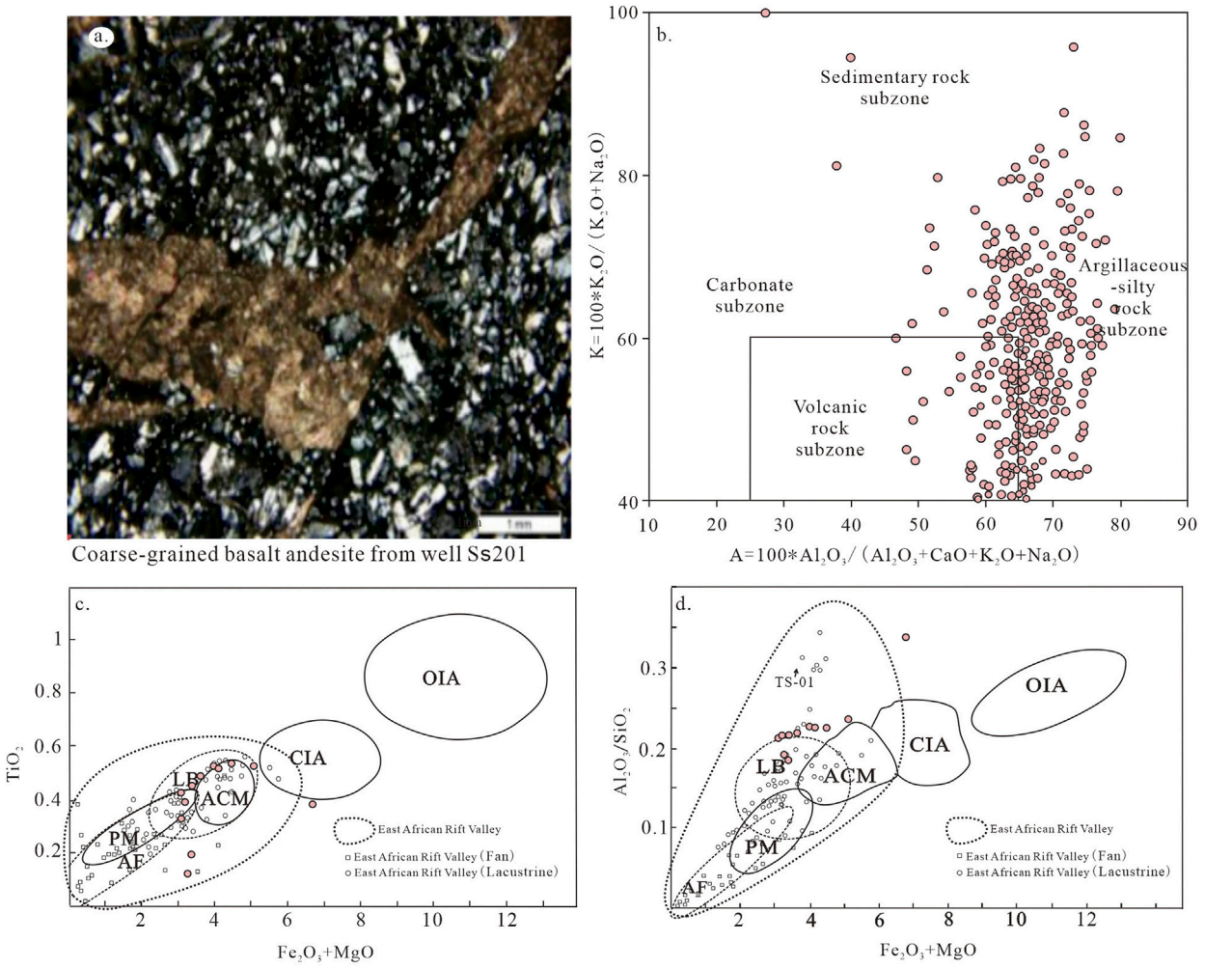

AF:Fan of intracontinental rift (Huntsman-Mapila,et al. , 2015); OIA:Oceanic island arc (Bhatia,1983); CIA : Continental island arc(Bhatia,1983);
LB:Lacustrine of intracontinental rift(Huntsman-Mapila, et al. , 2015); ACM:Active continental margin(Bhatia,1983); PM:Passive continental margin(Bhatia,1983)

FIGURE 4
Lithologic photos and discrimination map of volcanic rocks in Songliao Basin.

Heilongjiang Group between the Jiamusi and Songnen blocks in the early Jurassic (Wu et al., 2007); the metamorphic age of its internal structural melange was from 165 to 180 Ma in the Jurassic (Wu et al., 2004).

Numerous Jurassic granites intruded into the central Jilin Province and the Zhangguangcai rise (Sun et al., 2005; Wu et al., 2007) and the Jurassic granites (192–168 Ma, Zhang et al., 2004) in Yanbian County, on the eastern margin of the Songnen block, should be considered the result of this subduction collision.

The aforementioned evidence indicates that in the Early-to-Middle Jurassic, under the tectonic background of the compressional collision between the Jiamusi and Songnen blocks along the Mudanjiang suture (Figure 6C), east-dipping thrust-napper structures were developed in the UP-LM due to the intense east–west-directed tectonic compression (Figures 3, 5B). At the same time, the early Yanshanian granitic magmas intruded into the UP-LM, resulting in the hydrothermal transformation of these rift systems. Therefore, wells such as Zs 3 (170 Ma), Zs 7 (170 Ma), C403 (172 Ma), and Fs 901 (180 Ma) were drilled into early Yanshanian granite.

4.2 Difference in burial transformation

The Northeast Asia block group migrated northward (Hou et al., 2009) from the Early Cretaceous Huoshiling period through the Denglouku period (Lin et al., 2003), and multiple rifts (such as the Xujiaweizi and Gulong fault depressions) experienced multiphase rifting under the influence of right-handed strike-slip extension in Northeast Asia (Lin et al., 2003). Meanwhile, the Nujiang Ocean between the Gangdise and Qiangtang blocks was closed (Scotese, 2016).

These findings indicate that the influence of right-lateral strike-slip extension led to the closure of Nujiang Ocean, the extension of the near-SN fault formed in the former stage, and subsequently, the

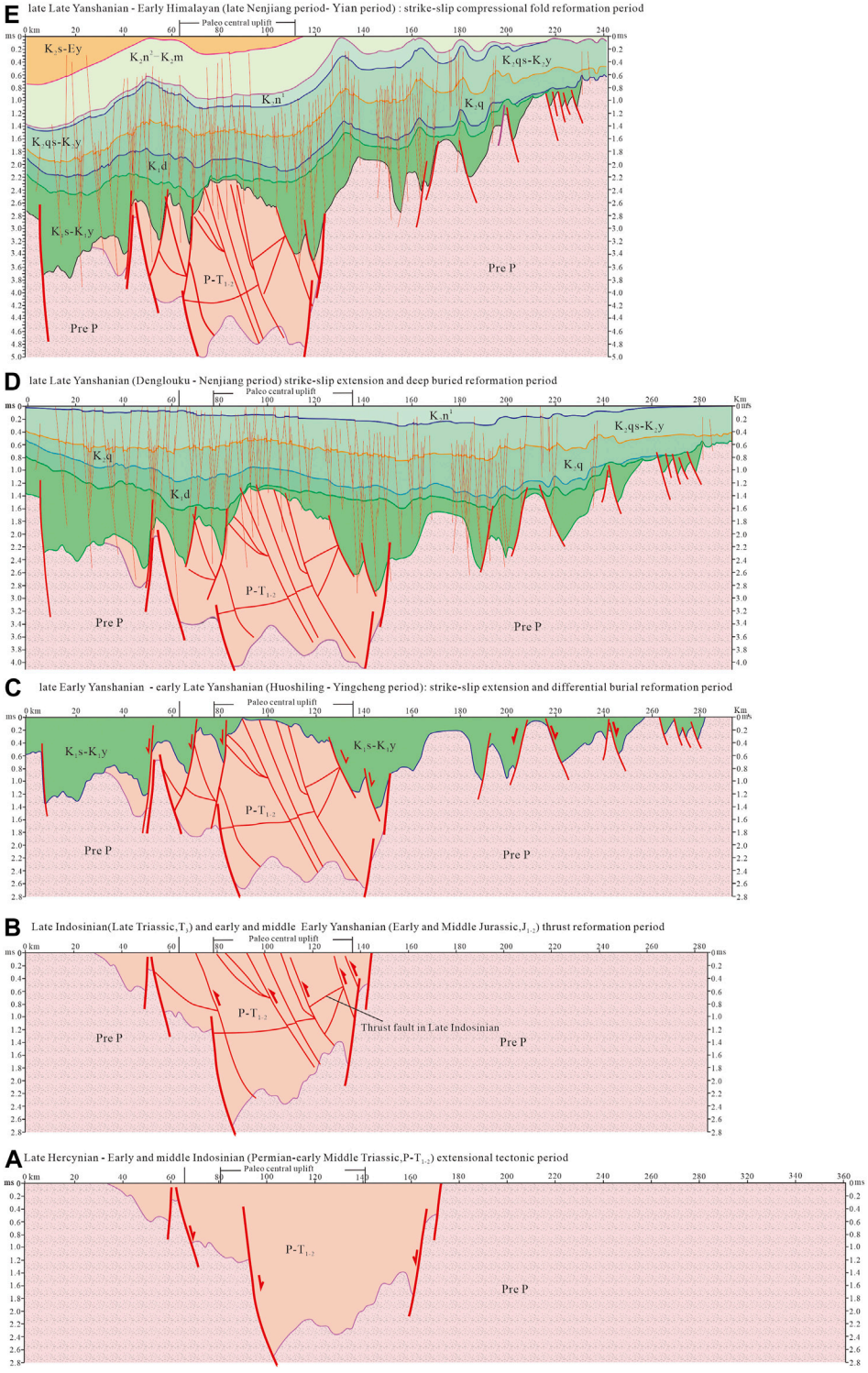

FIGURE 5
Structural evolution of east–west section of SL2 in Songliao Basin (location of the section is shown in Figure 1).

UP-LM undergoing differential rise or burial transformation. With the rapid subsidence of the Xujiaweizi and Gulong fault depressions, the paleocentral uplift in the Songliao Basin rose rapidly (Figures 3, 5C, 6D), accompanied by mantle upwelling and volcanic eruption.

Intermediate acid rhyolite volcanic rocks (108–116 Ma, peak 111–113 Ma) in the Xujiaweizi fault depression recorded the dextral strike-slip extensional rifting event (Zhang, 2007).

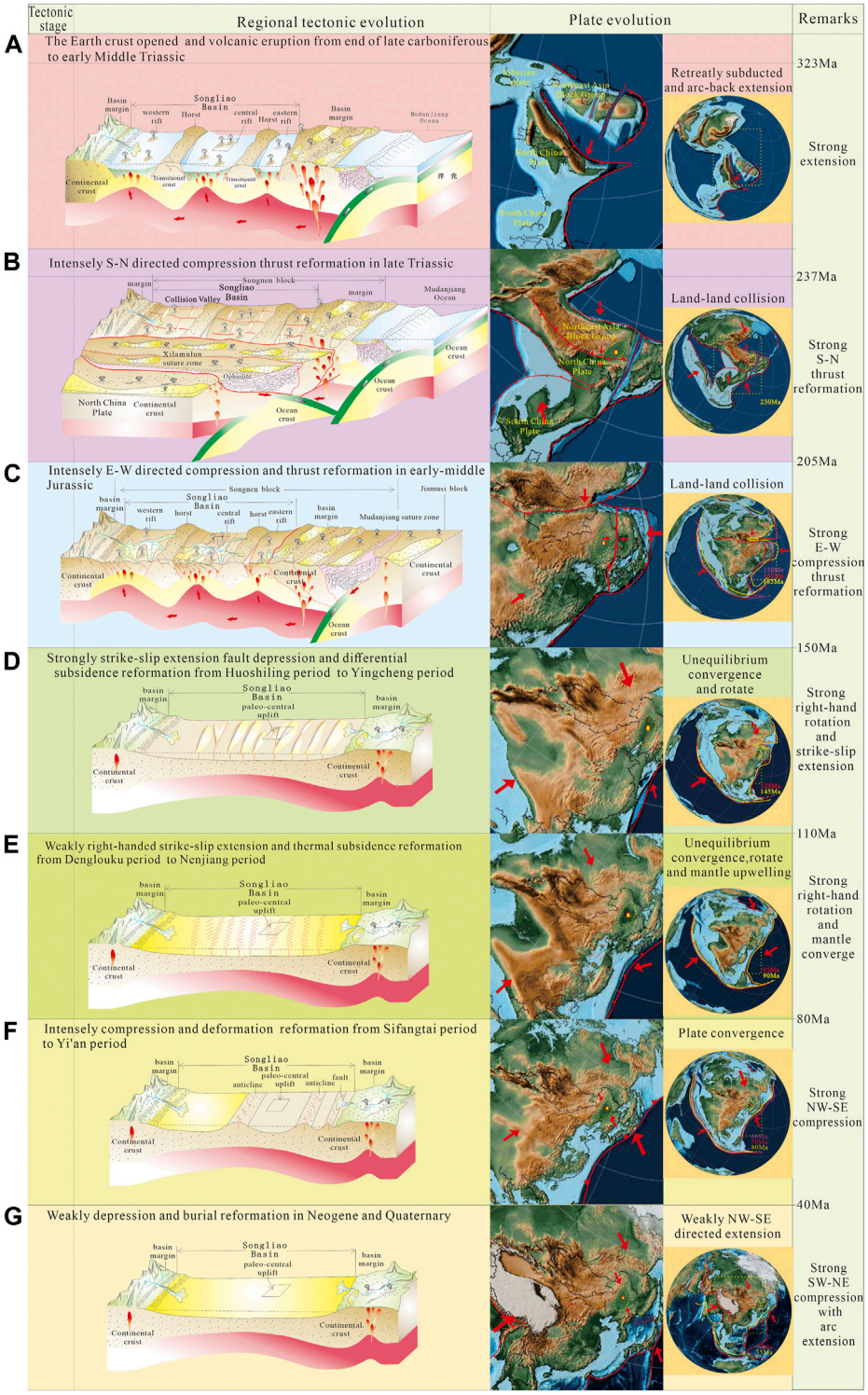

FIGURE 6
Schematic diagram of dynamic background of formation, evolution, and later transformation of Songliao Basin. Paleogeographic maps modified from Scotese (2016).

4.3 Shear-deep burial transformation

The time between the Early Cretaceous Qingshankou period and the Nenjiang Period was characterized by plastic crustal thinning, volcanic eruption, intense thermal subsidence, and the extensive development of a small, negative flower-like normal fault system in Songliao Basin (Figures 3, 5D). At the same time, it was occurred the closure of the Nujiang Ocean, the closure of the

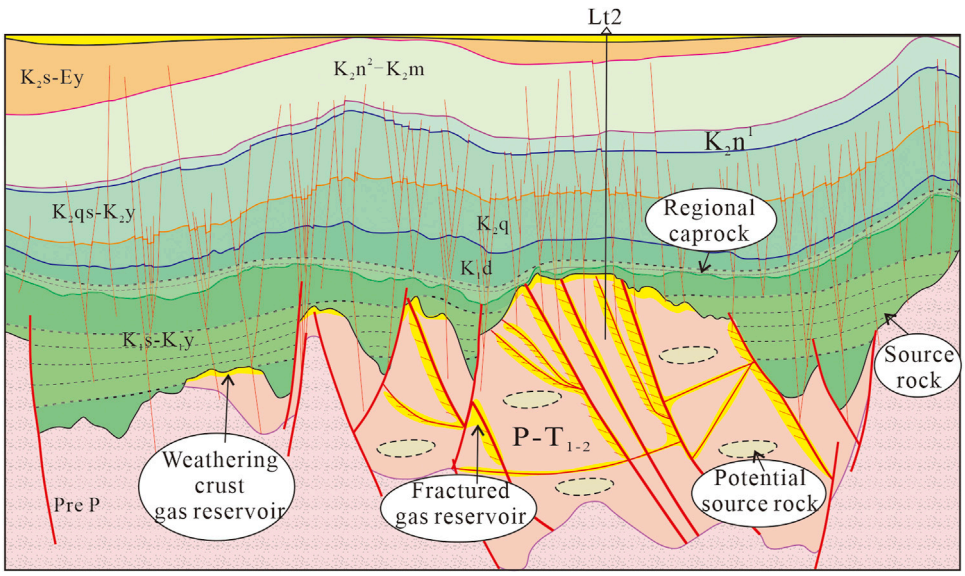

FIGURE 7
Natural gas accumulation model diagram.

Mongolian–Okhotsk Sea, the southwest-directed subduction of the Plaeo-pacific Plate (Izanagi plate) (Figure 6, Maruyama, 1997; Maruyama, 1997), and the clockwise rotation of the Northeast Asia block group, which drifted rapidly to the south (Hou et al., 2009).

The aforementioned evidence indicates that strong subsidence with right-lateral strike-slip shearing, under the tectonic background of dextral strike-slip and mantle convergence upwelling, caused the closure of the Nujiang Ocean, the closure of the Mongolian–Okhotsk Sea and the southwest-directed subduction of the Plaeo-pacific Plate(Izanagi plate) (Figure 6E).

As a result, the UP-LM was covered by the super-thick strata of the second member the Denglouku Formation and it's overlying layer and suffered a certain dextral strike-slip shear transformation (Figures 3, 5). The volcanic rocks of the Nenjiang Formation in well Songke 2 (83.35 ± 0.11 Ma, 83.498 ± 0.052 Ma, Hou et al., 2018) recorded this tectonic-thermal event.

4.4 Strong squeeze reformation

From the late Nenjiang Period to the Mingshui period of the Late Cretaceous, the depositional center of the lake basin moved westward and gradually shrank (Song, 2010). Finally, a series of NE-trending folds and NW-trending small normal fault systems was formed, including the Daqing placanticline (Huang et al., 2019).

In the meantime, the Siberia plate was drifting southward and colliding with the Northeast Asia block group, and the Mongolia–Okhotsk sea trough was eventually closed (Scotese, 2016), while the Pacific-Izanagi plate was subducting nearly westward and retreating south-eastward (Scotese, 2016) (Figure 6F).

The aforementioned evidence indicates strong sinistral strike-slip shear-extrusion from the end of the Yanshanian to the Early Himalayan (Figures 3, 5E), caused by NWW-SEE-directed compressional convergence between the Siberia plate and the Northeast China block group along the Mongolia–Okhotsk suture.

The aforementioned evidence demonstrates that, under the tectonic background of NWW-SEE-directed sinistral compression mainly driven by the Siberia plate drifting southward and colliding with the Northeast Asia block group, the UP-LM was transformed by shear-extrusion from the end of the Yanshanian through the early Himalayan, and a series of NNE-trending folds was formed in the overlying strata (Figures 3, 5). Afterward, the Songliao Basin was formed, and only a molasse formation with a thickness of less than 150 m was deposited on the underlying eroded unconformity in the Late Himalayan (Figure 3).

5 Significance of petroleum exploration

Potential source rocks were developed in the Upper Paleozoic to Early Mesozoic rifted strata, with TOCs ranging from 0.017% to 0.198% (Zhang et al., 2019). In addition, dark argillaceous source rocks of the Shahezi Formation were widely distributed across the Early Cretaceous fault depression (Pei, 2008). The methane gas reservoir in the UP-LM is mainly from the Shahezi Formation (94.71%) (Zhang et al., 2008), whose carbon isotope distribution of methane in natural gas (−31‰~−23.9‰) is essentially consistent with that in the dark mudstone adsorption gas of the Shahezi Formation (−30.2‰~−24.8‰) (Li et al., 2006; Wang et al., 2014).

The UP-LM was affected by multi-stage thrust and multi-stage shear, so that the dense fractures developed along the fracture plane formed the inner fracture zone or fracture body. The oil and gas generated in potential hydrocarbon source rocks in the UP-LM and in the source rock of the Shahezi Formation migrated along the inside fracture and fracture belt into the top-weathering crust trap and the inside fracture zone, or fracture belt trap, to form gas reservoirs under the mudstone seal of the second segment of the

Lower Cretaceous Denglouku Formation (Figure 7). The gas measurement results of multiple internal fracture sections in wells Lt 1, Lt 2, and Ch102 are good, which fully proves that the internal fracture gas reservoir has important exploration potential.

6 Conclusion

The formation, evolution, and late transformation processes of the UP-LM and its petroleum accumulation are discussed. The complex splice process between the Songnen block and other blocks or plates resulted in multi-period magmatic activity and superimposed transformation of metamorphic deformation in the UP-LM of the Songliao Basin.

The rifts developed in the Songliao Basin from the Permian through the Middle Triassic are filled with pyroclastic rock series. Therein, the back-arc extension rifts developed in the Late Hercynian belong to the west-dipping subduction and retreat of the Paleo-Pacific plate along the Siholt–Arin suture belt; subsequently, the rifts continued to develop in the Early and Middle Indosinian causedby the north–south- directed convergence collage of the North China Plate and the Northeast Asia block group along the Xilamulun suture zone. Since then, the UP-LM has experienced multiple intense transformations: the late Indosinian north–south-directed compressional thrust transformation causing the closure of the Paleo-Asian Ocean; the Early Yanshanian east–west-directed compressive thrust transformation caused by the closure of Mudanjiang Ocean; the shear differential burial transformation in the early Late Yanshanian and, subsequently, the shear-deep burial transformation in the late Late Yanshanian causing the closure of the Nujiang Ocean between the Gangdise and Qiangtang blocks; and the compression-shear transformation primarily originating from the closure of the Sea of Okhotsk from the end of the Yanshanian through the Early Himalayan.

The multiple groups of faults and fractures developed in the UP-LM through multi-stage thrust and shear transformation. The natural gas migrated from the inner stratum and source rock of the Shahezi Formation along the unconformity plane and fault plane to the top-weathering crust gas reservoirs and internal fracture gas reservoirs. The weathering crust reservoir and inner fracture reservoir at the intersection of multiple fault groups are favorable targets for petroleum accumulation.

Data availability statement

The original contributions presented in the study are included in the article/Supplementary Material; further inquiries can be directed to the corresponding authors.

Author contributions

LS, YS, and FX wrote the paper, YR completed the paper map, and JL and YY collected and collated paper data.

Funding

This study was supported by the Natural Science Foundation of China (No. 41102072) and the China Geological Survey Project (No. DD20160227).

Conflict of interest

The authors declare that the research was conducted in the absence of any commercial or financial relationships that could be construed as a potential conflict of interest.

Publisher's note

References

Bhatia, M. R. (1983). Plate tectonics and geochemical composition of sandstones. *J. Geol.* 91 (6), 611–627. doi:10.1086/628815

Chen, J. (2016). *The study of bedrock characteristics and advantages of reservoir of central paleouplift in northern Songliao Basin*. Thesis. China: A Dissertation Submitted to China University of Geosciences for Master Degree.

Di, J. X. (2013). Characteristics analysisof Paleocentral Uplift belt of North Songliao baisn natural gas reservior. *Inner Mongolia petrochemical Industry* (2), 151–152

Ding, R. X., Shu, P., Ji, X. Y., Qu, Y. M., Cheng, R. H., and Zhang, B. (2007). SHRIMP zircon U-Pb age and geological meaning of reservoir volcanic rocks in Qingshen gas fifield of the Songliao basin, NE China. *J. Jilin Univ. (Earth Sci.)* 37, 525–530. doi:10.13278/j.cnki.jjuese.2007.03.017

Du, J. (2017). Analysis of natural gas accumulation conditions and exploration perspective in the central paleo-uplift belt (north), Songliao Basin. *China Pet. Explor.* 22 (5), 1–14. doi:10.3969/j.issn.1672-7703.2017.05.001

Fang, C., Liang, Y., and Yan, X. (2021). Guiding and method for division of petroleum exploration play in superimposed reformation basin. *Petroleum Geol. Exp.* 43 (6), 1078–1088. doi:10.11781/sysydz2021061078

Gao, F. H., Xu, W. L., Yang, D. B., Pei, F. P., Liu, X. M., and Hu, Z. C. (2007). LA-ICP-MS zircon U-Pb dating from granitoids in southern basement of Songliao basin: Constraints on ages of the basin basement. *Sci. China (D)* 50, 995–1004. doi:10.1007/s11430-007-0019-7

Guo, J., Shan, X., and Hao, G. (2019). Identification of basement lithology in central uplift zone of Songliao Basin by Fisher discriminant analysis. *J. Heilongjiang Univ. Sci. &Technology* 29 (1), 60–65. doi:10.3969/j.issn.2095-7262.2019.01.011

Guo, S., Wang, Z., and Ma, X. (2021). Exploration prospect of shale gas with Permian transitional facies of some key areas in China. *Petroleum Geol. Exp.* 43 (3), 377–385. doi:10.11781/sysydz202103377

Han, J., Zhou, J., Wang, B., and Cao, J. (2015). The final collision of the CAOB: Constraint from the zircon U-Pb dating of the Linxi Formation,Inner Mongolia. *Geosci. Front.* 6 (2), 211–225. doi:10.1016/j.gsf.2014.06.003

Hou, H., Wang, C., Zhang, J., Ma, F., Fu, W., Wang, P., et al. (2018). Deep continental scientific drilling engineering in Songliao Basin: Resource discovery and progress in Earth science research. *Geol. China* 45 (4), 641–657. doi:10.31035/cg2018036

Hou, Q., Feng, Z., and Feng, Z. (2009). *Continental petroleum geology in Songliao basi*. Beijing: Petroleum Industry Press, 70.

Huang, L., Tong, H., Yang, D., Fan, J., and Huang, H. (2019b). A new model for the formation and evolution of middle-shallow faults in the Daqing placanticline,Songliao Basin. *Acta Geol. Sin.* 93 (3), 597–605. doi:10.19762/j.cnki.dizhixuebao.2019040

Huang, Q., Zhu, G., Wang, H., and Cheng, H. (2019a). Zircon U-Pb age of the basement rocks and its geological significances in paleo- central uplift belt of Songliao Basin. *Petroleum Geol. Oilfield Dev. Daqing* 38 (3), 1–7. doi:10.19597/J.ISSN.1000-3754.201811055

Huntsman-Mapila, P., Tiercelin, J. J., Benoit, M., Ringrose, S., Diskin, S., and CottenHémond, J. C. (2009). Sediment geochemistry and tectonic setting: Application of discrimination diagrams to early stages of intracontinental rift evolution, with examples from the okavango and southern tanganyika rift basins. *J. Afr. Earth Sci.* 53 (12), 33–44. doi:10.1016/j.jafrearsci.2008.07.005

Li, J., Liu, W., and Song, L. (2006). A study of hydrocarbon generation conditions of deep source rocks in Xujiaweizi fault depression of the Songliao Basin. *Nat. Gas. Ind.* 26 (6), 21–24.

Li, J. Y. (2006). Permian geodynamic setting of northeast China and adjacent regions: Closure of the paleo-Asian ocean and subduction of the paleo-Pacific plate. *J. Asian Earth Sci.* 26 (3-4), 207–224. doi:10.1016/j.jseaes.2005.09.001

Lin, W., Chen, Y., Faure, M., and Wang, Q. C. (2003). Tectonic implications of new late cretaceous paleomagnetic constraints from eastern liaoning peninsula, NE China. *J. Geophys. Research-Solid Earth* 108 (B6), 1–17. doi:10.1029/2002jb002169

Liu, X., Meng, L., Huang, C., and Zhao, C. (2003). GIS-based reconstruction of basin paleotectonics: An example from paleo-central uplift belt, northern Songliao Basin. *Earth Science— J. China Univ. Geosciences* 28 (3), 346–350.

Liu, Y. J., Feng, Z. Q., Jiang, L. W., Jin, W., Li, W. M., Guan, Q. B., et al. (2019). Ophiolite in the eastern central asian orogenic belt,NE China. *Acta Petrol. Sin.* 35 (10), 3017–3047. doi:10.18654/1000-0569/2019.10.05

Maruyama, S. (1997). Pacific-type orogeny revisited: Miyashiro-type orogeny proposed. *Isl. Arc* 6, 91–120. doi:10.1111/j.1440-1738.1997.tb00042.x

Maruyama, S., and Seno, T. (1986). Orogeny and relative plate motions: Example of the Japanese islands. *Tectonophysics* 127, 305–329. doi:10.1016/0040-1951(86)90067-3

Miao, L. C., Liu, D. Y., Zhang, F. Q., Fan, W. M., Shi, Y. R., and Xie, H. Q. (2007). Zircon shrimp U-Pb ages of the "xinghuadukou group" in hanjiayuanzi and xinlin areas and the "zhalantun Group"in inner Mongolia, da hinggan mountains. *Chin. Sci. Bull.* 52 (8), 1112–1124. doi:10.1007/s11434-007-0131-2

Niu, C., Wang, F., He, J., and Tang, G. (2021). Accumulation factor matching and model of Bozhong 19-6 buried hill gas reservoir, Bohai Sea area. *Petroleum Geol. Exp.* 43 (2), 259–267. doi:10.11781/sysydz202102259

Pei, M. (2008). Study on sequence stratigraphy of deep order of paleo-central uplift belt. Thesis. Daqing: A Dissertation submitted to Daqing Pettoleum Institute For the Academic Degree of Master of Science.

Scotese, C. R. (2016). Paleomap PaleoAtlas for GPlates and the PaleoData plotter program, paleomap Project. Avaliable At: http://www.earthbyte.org/paleomappaleoatlas-for-gplates/.

Song, Y. (2010). The post-rift tectonic inversion of Songliao Basin,NE China and its dynamic background. Thesis. Wuhan: A Dissertation Submitted to China University of Geosciences for the Doctor Degree of Philosophy.

Sun, D., Wu, F., Gao, S., and Lu, X. (2005). Confirmation of two episodes of A-type granite emplacement during late triassic and early jurassic in the central Jilin Province, and their constraints on the structural pattern of eastern jilin-heilongjiang area, China. *Earth Sci. Front.* 12 (2), 263–275.

Sun, D., Wu, F., Zhang, Y., and Gao, S. (2004). The final closing time of the west Lamulun River -Changchun -Yanji plate suture zone Evidence from the Day ushan granitic pluton, Jilin Province. *J. Jilin Univ. Earth Sci. Ed.* 34 (2), 174–181.

Wang, D., Li, S., Zhou, X., Liu, W., Lin, Y., Zeng, Q., et al. (2016). Shrimp U-Pb dating of detrital zircon from the upper permian Linxi Formation in eastern inner Mongolia,and its geological significance. *Geol. Rev.* 62 (4), 1021–1040. doi:10.16509/j.georeview.2016.04.018

Wang, J. (2016). *Study on the basement structure characteristics of the paleo-central uplift belt*. Thesis. Daqing: A Dissertation submitted to Daqing Pettoleum Institute For the Academic Degree of Master of Science.

Wang, M., Sun, Y., Wang, W., Wang, Y., and Shi, L. (2014). Gas generation characteristics and resource potential of the deep source rock in Xujiaweizi fault depression, northern Songliao Basin. *Nat. Gas. Geosci.* 25 (7), 1011–1018. doi:10.11764/j.issn.1672-1926.2014.07.1011

Wang, X., Ren, Y. S., Zhang, Y., and Zhao, D. S. (2021). Sedimentary response to the non-synchronous closure of paleo-Asian ocean: Evidence from U-Pb ages and Hf isotopic compositions of detrital zircons from the Linxi Formation, NE China. *Int. Geol. Rev.* 63 (2), 144–160. doi:10.1080/00206814.2019.1706650

Wang, Y., and Fan, Z. (1997). Discovery of permian radiolarians in ophiolite belt on northern side of xarmoron river, neimonggol and its geological significance. *Acta Palaeontol. Sin.* 36 (1), 5869.

Wu, F. Y., Sun, D. Y., Ge, W. C., Zhang, Y. B., Grant, M. L., Wilde, S. A., et al. (2011). Geochronology of the Phanerozoic granitoids in northeastern China. *J. Asian Earth Sci.* 41 (1), 1–30. doi:10.1016/j.jseaes.2010.11.014

Wu, F. Y., Sun, D. Y., Jahn, B. M., and Wilde, S. A. (2004). A Jurassic garnet-bearing granitic pluton from NE China showing tetrad REE patterns. *J. Asian Earth Sci.* 23, 731–744. doi:10.1016/s1367-9120(03)00149-4

Wu, F. Y., Sun, D. Y., Li, H. M., and Wang, X. (2000). Zircon U-Pb ages of the basement rocks beneath the Songliao Basin, NE China. *Chin. Sci. Bull.* 45 (16), 1514–1518. doi:10.1007/bf02898900

Wu, F. Y., Yang, J. H., Lo, C. H., Wilde, S. A., Sun, D. Y., and Jahn, B. M. (2007). The Heilongjiang group: A jurassic accretionary complex in the Jiamusi massif at the Western pacific margin of northeastern China. *Isl. Arc* 16 (1), 156–172. doi:10.1111/j.1440-1738.2007.00564.x

Xie, K. (2016). Petrogenesis of early late jurassic rhyolite from zhirui basin in southern great xing'an range: Constraints from chronology and geochemistry. Thesis. Nanchang: Dissertation for master's degree of East China University of technology.

Zhang, F., Chen, H., Dong, C., Yu, X., Xiao, J., Pang, Y., et al. (2008). Evidence for the existence of precambrian basement under the northern Songliao basin. *Geol. China* 35 (3), 421–428.

Zhang, F. (2007). Early cretaceous volcanic event in the northern Songliao Basin and its geodynamics. Thesis. Hangzhou: A Dissertation submitted to Zhejiang University for the Academic Degree of Doctor of Science.

Zhang, F., Ran, Q., Wu, Y., and Ren, Z. (2019). Geochemical characteristics and reservoir forming conditions of the natural gas in the paleo central uplift zone in the northern Songliao Basin. *Nat. Gas. Geosci.* 30 (1), 126–132. doi:10.11764/j.issn.1672-1926.2018.10.002

Zhang, M., Zhang, Y., and Nian, X. (2006). Deep-seated structural characteristic and evolution of paleo-central uplift belt in northern Songliao basin. *J. Daqing Petroleum Inst.* 30 (5), 107–110.

Zhang, Y. B., Wu, F., Wilde, S. A., Zhai, M., Lu, X., and Sun, D. (2004). Zircon U-Pb ages and tectonic implications of 'early paleozoic' granitoids at yanbian, Jilin Province, northeast China. *Isl. Arc* 13 (4), 484–505. doi:10.1111/j.1440-1738.2004.00442.x

Zhang, Y., Luo, G., and Li, Y. (2020). Identification method of basement lithology in the central paleo-uplift belt(north) of Songliao basin. *Mud Logging Eng.* 31 (1), 120–124. doi:10.3969/j.issn.1672-9803.2020.01.022

Zhang, Y. (2006). Structural research and basement lithology prediction of the paleo-central uplift belt in northern Songliao basin. Thesis. Daqing: A Dissertation submitted to Daqing Pettoleum Institute for the Academic Degree of Master of Science.

Zhou, J. B., Wilde, S. A., Zhao, G. C., and Han, J. (2018). Nature and assembly of microcontinental blocks within the Paleo-Asian Ocean. *Earth-Science Rev.* 186, 76–93. doi:10.1016/j.earscirev.2017.01.012

frontiers | Frontiers in Earth Science

TYPE Original Research
PUBLISHED 10 March 2023
DOI 10.3389/feart.2023.1142141

OPEN ACCESS

EDITED BY
Qingqiang Meng,
SINOPEC Petroleum Exploration and Production Research Institute, China

REVIEWED BY
Changyu Fan,
Northwest University, China
Yinghai Guo,
China University of Mining and Technology, China

*CORRESPONDENCE
Hui Zhang,
zhanghui01_cq@petrochina.com.cn
Jie Hui,
1229348618@qq.com

SPECIALTY SECTION
This article was submitted to Geochemistry, a section of the journal Frontiers in Earth Science

RECEIVED 11 January 2023
ACCEPTED 22 February 2023
PUBLISHED 10 March 2023

CITATION
Zhao W-B, Zhang H, Shi Y-H, Fu X-X, Hui J and Jing X-Y (2023), Geological characteristics and exploration potential of the coal measure gas from Shan 2 of the Shanxi formation in the eastern Ordos Basin.
Front. Earth Sci. 11:1142141.
doi: 10.3389/feart.2023.1142141

Geological characteristics and exploration potential of the coal measure gas from Shan 2 of the Shanxi formation in the eastern Ordos Basin

Wei-Bo Zhao[1,2], Hui Zhang[1,2]*, Yun-He Shi[1,2], Xun-Xun Fu[1,2], Jie Hui[1,2]* and Xue-Yuan Jing[1,2]

[1]National Engineering Laboratory for Exploration and Development of Low Permeability Oil and Gas Fields, Xi'an, Shaanxi, China, [2]Research Institute of Exploration and Development of PetroChina Changqing Oilfield Company, Xi'an, Shaanxi, China

"Coal measure gas," excluding tight (low-permeability) sandstone gas, refers in this study to the self-sourcing unconventional natural gas stored in coal, shale, and fine siltstone. It is characterized by various types of occurrences and reservoirs, a distinct cyclic succession of coal measure strata, widely distributed mosaic hydrocarbon accumulations, three types of coal measure gas accumulations, and configurations of vertically multiple-stacked gas-bearing reservoirs. Coal measure gas from Shan 2 can be divided—according to the grain size of sandstone, configurations of sandstone–coal–mudstone association, thickness, and layers—into four types: thick massive sandstone–coal–mudstone (type I), fine siltstone–coal–mudstone (type II), thin sandstone–mudstone–sandstone (type III), and coal–mudstone (type IV). Comprehensive evaluation suggests that the coal measure gas in the Suide-Mizhi area of the southern Ordos Basin presents an important and favorable accumulation option, characterized by coalbed methane, shale gas, and tight gas stored in sandstone–mudstone–coal strata. Therefore, it is essential to conduct full future assessments for the coal beds, shale, and tight gas controlling exploration for the "vertical gas-bearing zone" by three-dimensional exploration.

KEYWORDS

Ordos Basin, Upper Paleozoic, Shan 2, coal measure gas, exploration potential

1 Introduction

The vision for a "beautiful China" and energy-structure adjustment have significantly increased the need for natural gas consumption, which relies on imported gas to satisfy energy demands. In 2019, China's domestic annual gas production was 1777×10^8 m^3 against gas imports of 1322×10^8 m^3, with dependence on external gas rising to 43.1%. Domestic annual gas production is expected to reach 3200×10^8 m^3 by 2030, with natural gas consumption at 5500×10^8 m^3 offset by a dependence on external gas of 64% (Zou et al., 2018; Zou et al., 2019). The increasing demand for energy and the limited amount of gas produced in China makes the exploration and exploitation of coal measure gas imperative because it could be a larger contributor to annual gas production.

Exploration for coal measure gas dates back to the 1940s in the Eames River Basin, to the west of the Weser River in the northwestern basin of Germany (Shi et al., 1985). The Groningen coal measure gas field was first discovered in the northeastern West Holland Basin, with reserves of over one trillion cubic meters; gas fields relating to coal measures with high reserves had been since found in many coal-bearing basins of Asia, Europe, Oceania, and the Americas. Coal measure gas exploration in China began in the 1970s and was first systematically reviewed by Dai (1979)—a milestone in the domestic theoretical framework of coal measure gas. By 2016, 39 coal measure gas fields were discovered, accounting for 66% of large gas fields in China. By 1978, coal measure gas accounted for 9% of total reserves and 2.5% of the annual production of natural gas in China, with these figures rising to 58.7% and 61.5% in 2017, with total reserves and annual production of 92,538.51 $\times$ 10^8 m^3 and 902.14 $\times$ 10^8 m^3, respectively. China's coal measure gas production is expected to exceed 1000 $\times$ 10^8 m^3 in 2030 (Dai et al., 2014; Zou et al., 2019). The exploration and exploitation of coal measure gas promotes the energy security, social stability, and natural gas industry development of China.

The Upper Paleozoic coal measure strata of the Ordos Basin in Western China mainly occur in the Benxi Formation, Taiyuan Formation, and Shan 2 of the Shanxi Formation. The coal beds are interbedded with dark mudstone and tight sandstone, showing highly active gas logging. Coal measure gas resources in the Ordos Basin are estimated to be around 20 trillion square meters (Fu et al., 2016), showing huge exploration potential and becoming a new natural gas exploration frontier. Research and testing for the Upper Paleozoic coal measure gas in the Ordos Basin has been conducted in recent years by the Changqing Oilfield Company. The results show that the Ordos gas content is about 0.2–1.0 m^3/t for shale, 0.1–0.5 m^3/t for fine siltstone, and 6–10 m^3/t for coal rocks. The vertical well of the Shanxi Formation has achieved gas production of 6366–6728 m^3/d, and the horizontal well of Shan 2 has achieved gas production of 14126 m^3/d, confirming that coal measure strata generally contain gas and have great exploration potential.

The objective of this article is to provide a comprehensive overview of the theoretical framework and exploration achievements for Upper Paleozoic coal measure gas in the Ordos Basin by discussing the definition, types, and geological characteristics of Shan 2 (Permian). By unifying several aspects of coal measure gas, this article evaluates these favorable accumulations and helps open up new exploration and exploitation for Shan 2, promoting the large-scale exploration and exploitation of coal measure gas in China's marine continental alteration facies.

2 Characteristics of Upper Paleozoic coal measure gas in the Ordos Basin

2.1 Geological setting

The Ordos Basin spans the five provinces of Shaanxi, Gansu, Ningxia, Inner Mongolia, and Shanxi and is a large multiple cyclic superimposed cratonic basin with general subsidence, depression migration, and simple structure. It is divided into six tectonic units: the western thrust belt, Tianhuan depression, Yishan slope, western Shanxi flexural fold belt, Yimeng uplift, and Weibei uplift (Figure 1). Its proven gas reserves are prominently distributed in the Yishan slope. The study area is the eastern Ordos Basin, developing the Upper Carboniferous Benxi Formation with barrier island-tidal flat-lagoon facies, Lower Permian Taiyuan Formation with braided stream-delta-lagoon-tidal flat-barrier island-shallow marine shelf carbonate deposits, and the Shanxi Formation with delta-tidal depositional facies. The Shanxi Formation has more stable, continuous, and thicker shale layers than the Benxi and Taiyuan formations, which is a favorable stratum for coal measure gas exploration. Shan 2 of the Shanxi Formation has high organic matter abundance and strong hydrocarbon generation ability, which is the target stratum of coal measure gas exploration in this study.

2.2 Definition of coal measure gas

"Coal measure gas," also termed "coal-derived gas," refers to natural gas related to coal measures. As defined by Dai (1982), coal-derived gas was generated by humic organic matter in the coal formation process. With the development of exploration and exploitation, many researchers are trying to give different definitions from the viewpoint of accumulation dynamics. However, due to the multiple storage spaces of natural gas in coal measures and varying perspectives studied by different researchers, the problem of defining coal measure gas has led to misconceptions that have, in some cases, impeded exploration efforts. Wang et al. (2014) proposed that coal measure gas was sourced from organic matter contained in coal measures during the processes of biochemistry, physical chemistry, and coalification from the perspectives of geology and deposit economy, including shale gas in coal measure shale, coalbed methane in coal beds, tight (low-permeability) gas in coal measure sandstone, and gas hydrates. Jiang et al. (2015) took Taohua mudstone as the boundary, defining the Upper Paleozoic Benxi Formation, Taiyuan Formation, Shanxi Formation, and lower Shihezi Formation coal-bearing strata in the Ordos Basin as coal measures, and the gas in them as coal measure gas. Ouyang et al. (2018) suggested that coal measure gas referred to coalbed methane from coal beds and gas from adjacent tight sandstone reservoirs; this was an economic definition. More recently, the term "coal measure gas" has been defined as stranded coalbed methane and shale gas from coal measure source rocks, such as coal and carbonaceous and dark shales, and accumulated as self-sourcing or outside-sourcing reservoirs; it can be subdivided into unconventional continuous "coalbed methane," "shale gas," "tight gas," and conventional "trapped accumulations" (Zou et al., 2019). Three large coal-measure tight sandstone gas fields (Daniudi, Yulin, and Zizhou) were discovered in the eastern Ordos Basin, with proven geological reserves of over 1000$\times$$10^8$ m^3. The reservoir rocks of the main reserves of Shan 2 are composed of medium-coarse to coarse quartz sandstone and lithic sandstone (Zhao et al., 2013), with pore throat structure of mainly intergranular pores and medium-coarse throats (>0.2 μm) in the Yulin gas fields, and residual intergranular pores and thin throats in the Zizhou gas fields (Lan et al., 2007; Wang et al., 2015). However, comprehensive gas

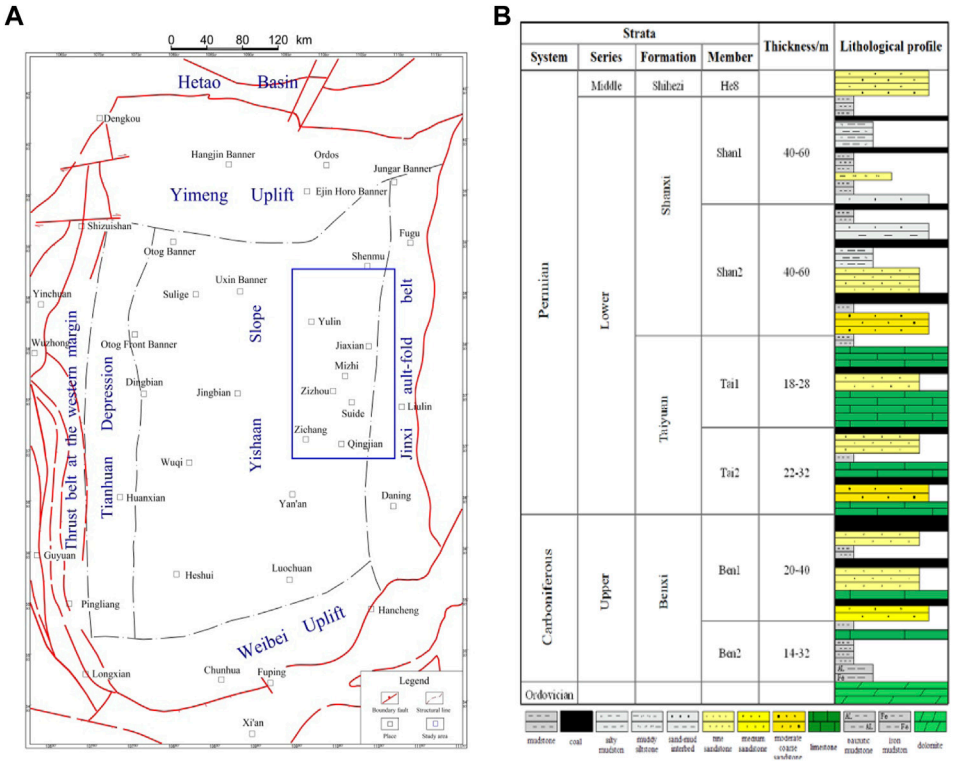

FIGURE 1
Tectonic unit division **(A)** and stratigraphic column **(B)** of the Carboniferous–Lower Permian in the Ordos Basin.

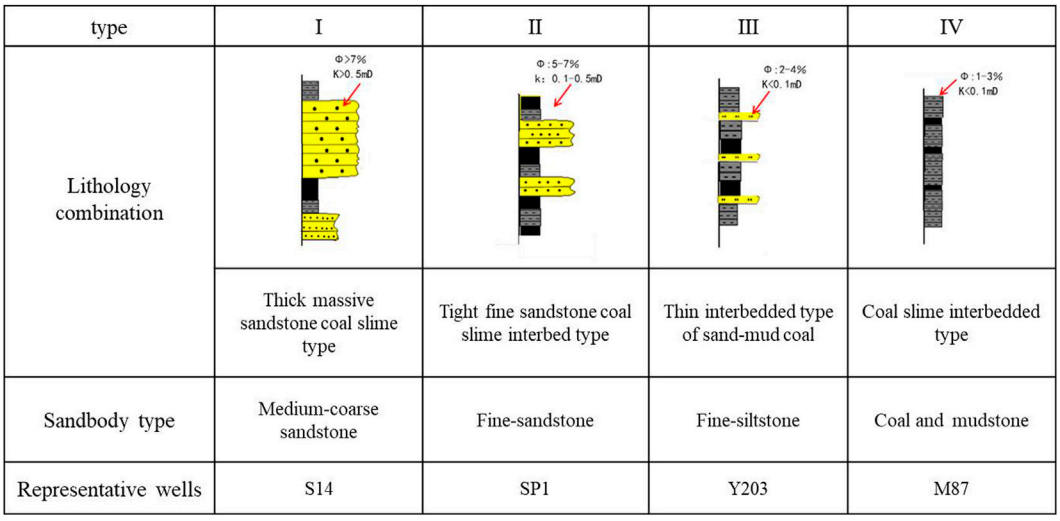

FIGURE 2
Classification of Shan 2 coal measure gas in the Ordos basin.

potential evaluation is needed for the siltstone interbedded with thin mudstone in the eastern Ordos Basin, characterized by and interbedded fractures under argon ion light-field emission electron microscopy and nano-sized pores and throats. The coal measure gas in this paper, excluding the coal measure tight sandstone gas in current exploration and exploitation, specifically refers to the unconventional self-sourcing natural gas stored in coal beds, shale, and fine siltstone.

2.3 Shan 2 coal measure gas types in Ordos basin

Coal measure gas is mainly stored in coal seams and the sand-mudstone partings that can be evaluated and extracted together, which can vertically expand exploration and exploitation space and increase resource abundance. Varying assemblages of coal seams and sand-mudstones lead to different coal measure gas reservoir types and mining strategies. In the context of the configurations between coal beds and adjacent sandstones defined by Ouyang et al. (2018), there are four combination relationships of coal measure gas: multi-layer coal and sandstones (type I), multi-layer coal and less layer or no sandstones (type II), monolayer/less layer coal and multi-layer sandstones (type III), as well as monolayer/less layer or no coal and less layer or no sandstones (type IV). In this article, four types of coal measure gas (Figure 2) are identified according to sandstone grain size, configurations of sandstone-coal-mudstone, thickness, and seams. Type I has already been economically exploited, while the remaining types are prioritized currently.

Type I is thick massive sandstone-coal-mudstone characterized by developed thick massive sandstone bodies that are coarse quartz sandstone and lithic quartz sandstone, which have good physical properties, porosity of more than 7%, permeability of more than 0.5 °mD. Hydrocarbon gas generated from coal beds, the mainly gas source rocks, is directly stored in the neighboring sandstones, forming the source-reservoir interactive coal measure gas accumulations in a combination with favorable regional seal rocks.

Type II is interbedded fine siltstone-coal-mudstone characterized by multiple assemblages of interactive, vertically cyclic superposition sandstone and coal beds, reflecting cyclical coal-forming environments (cyclothems). The sandstone is fine lithic quartz sandstone and lithic sandstone with tight structure, with porosity of 5%-7% and permeability of 0.1-0.5°mD. Coal beds can be considered as both source rocks and reservoirs, hydrocarbon gas from which is stored in the nearby sandstone, forming the combination of tight sandstone gas and coalbed methane accumulations with favorable regional seal rocks.

Type III is interbedded thin sandstone-mudstone-coal. It is marked by developed coal beds and undeveloped sandstones, indicative of a marsh depositional environment. Such type has developed mudstone and lack of terrigenous clasts, which are favorable factors equipped with regional cap rocks resulting in coalbed methane and shale gases accumulations.

Type IV is interbedded coal-mudstone, implying a deep-water sedimentary environment. It is marked by thick mudstones, thin coal beds, and undeveloped sandstone bodies, with a favorable sealing condition, supporting the formation of single coalbed methane and shale gas accumulations.

3 Geological characteristics of coal measure gas

Coal measure is a set of co-genetic coal beds or coal line-bearing sedimentary deposits formed by marine continental alteration or continental settings, occurring in residual basins with different structural properties. Coal measure gas is focused on both the genetic correlations of various reservoirs and the differences between various types of reservoirs and accumulations that result from the geological factors of coal measure gas.

3.1 Diversities of storage and reservoir

Coal measure gas occurs in three states: coal methane as absorbed gas, coal measure tight sandstone gas as free gas, and shale gas as mixed state. The abundance of organic matter gradually increases from inorganic reservoirs (sandstones) through mixed reservoirs (shale) to organic reservoirs (coal beds), forming the reservoir lithological sequence without boundary; this is the fundamental reason for the state diversities of coal measure gas that account for different mechanisms and exploitation strategies. There are many types of coal measure source rocks, such as coal beds, carbonaceous mudstone, and dark mudstone, with high accumulative thickness, high gas-generating intensity, and sufficient gas source, resulting in abundant coal measure gas resources. Three layers of coal seams at a depth of 1000–2000 m with 100 m intervals were distributed in the Fenghe Basin of Wyoming, United States, the coalbed methane and sandstone gas of which were exploited at different pressures, with coal bed–sandstones tens to hundreds of meters thick exploited simultaneously. Here, 20 vertical wells had a daily gas production of thousands of cubic meters, with a peak of 20×10^4 m^3. In 2001–2002, a pilot test of coalbed methane and tight sandstone gas co-production was conducted in the Baihe uplift of the Pitsens Basin, United States. Coal beds were at depths of 1560–2561 m, and 65 wells targeting deep coalbed methane and tight sandstone gas were exploited simultaneously. The test showed that average daily gas production was about 1.09×10^4 m^3, with a peak of 1.44×10^4 m^3—60% of which was generated from coal beds (Fu et al., 2016). In 2017, a breakthrough was made in the vertical well exploitation test of coalbed methane in the daily gas production of Yangmeican 1 well, Guizhou Province, China, with target layers of coal beds, carbonaceous mudstone, and tight sandstone reaching 4656 m^3 and were maintained above 3600 m^3/d for 50 days—the highest record for vertical well gas production in southwest China. The resource abundance of Yangmeishu syncline coal measure gas where the well is located 4.79×10^8 m^3/km^2 is six times higher than that of pure coalbed methane. The modeling experiment shows that the exhaustion of coal rocks is very efficient compared with marine source rocks, reaching 75% at the maximum vitrinite reflectance of 1.0% and 90% at 5.5%. This indicates that the natural gas generated from coal is mainly injected into other reservoirs and is the major source of coal measure gas and adjacent non-coal measure gas accumulations.

3.2 Distinct cyclicity of coal measures' depositional sequence

Coal measures are deposited in continental and continental and marine alteration settings, the lithology and thickness of which are

controlled by geological processes; they are characterized as thin layers and various lithologies, interbedded sandstone–mudstone–coal beds, and highly cyclicity. Such cyclicity results in both variations of coal measure gas reservoirs—leading to diversities of occurrence state—and different associations of source–reservoir–cap with various structures, moderate thickness, and multiple internal sealings that are vertically controlled by stratigraphic sequence. This results in the vertical development of several fluid pressure systems and complex gas–water correlations in the coal measure. Different fluid pressure systems in coal measures are close to each other, having a fragile dynamic energy balance and being vulnerable to disturbance by exploitation. Various correlations of associations of source–reservoir–cap lead to the same layers (such as coal beds and shale) having the functions of source rocks, reservoirs, and cap, and to the gas having the nature of self-sourcing reservoirs and outside-sourcing reservoirs—the depositional factor for the varieties of coal measure gas. The variable source–reservoir–cap combination leads to the same rock layer (such as coal seam or shale rock) having the functions of source rock, reservoir, and cap rock, resulting in natural gas in the same combination having both the characteristics of self-generation and self-storage; it is the sedimentary control factor of the types of diversity of coal measure gas reservoirs. The vertical combination of coal rock and sandstone determines the migration and accumulation mode of coal measure strata, including *in situ* accumulation with "source–reservoir contact" and long-distance accumulation controlled by reservoir and migration channels. The variations in reservoirs of coal measures lead to distinct differences in the mechanical properties of lithology reservoirs, which encourages effective and uniform exploitation, technical innovation, and reservoir reconstruction. The Surat Basin in Australia has recently been the most successful coal measure gas development basin in the world, with average gas production per well of 2.83–5.66×10^4 m^3/d with a peak of 56×10^4 m^3/d. The depositional cyclicity of the Middle Jurassic Wallon sub-group coal measure is noticeable, developing fining-upward fluvial deposition, strata thickness of 305–365 m, more than 100 coal-bearing layers (average 40 layers), and over 70% of single-layer coal beds with thicknesses of less than 1.0 m. It is inferred that thin coal beds are frequently interbedded with sandstone, carbonaceous mudstone, and mudstone, thus improving the permeability of coal-bearing layers with 5–5000 mD, designing vertical well and open hole completion technology through the whole coal measures can realize the efficient mining of coal measures gas. to effectively achieve commingling production. The varying thickness ratios of coal beds and sandstone imply that the dominant thin coal layers lead to much more frequent interbedding, thus favoring the preservation of coal measure gas, dehydration of coal beds, and coalbed methane desorption.

3.3 Characteristics of widely distributed and mosaic hydrocarbon accumulation

Coal measure is formed in a diversity of depositional settings, including alluvial fans, river–lakes, deltas, and lagoon-tidal flats. Weak hydrodynamic deposition dominated by shallow marine carbonate rocks and lagoon-tidal flat and lake mudstones occurs widely in high-stand system tracts. Strong hydrodynamic deposition dominating alluvial fan, river, and delta sandstones occurs in low-stand system tracts, while sandstone has good lateral continuity in the direction of the palaeocurrent but poor continuity in the vertical and oblique palaeocurrent direction, showing quasi-strata and lenticular shapes in the profile. The transformation stages of the two-system domains are more conducive to the wide development of weak hydrodynamic peat bogs, forming large-scale comparable main coal beds. These geometric characteristics display widely distributed mud-coated sand, mud-coated coal, mudstone, and coal beds, with three-dimensional distribution patterns of single sandstone in the mosaic of coal measure that produce mudstone and coal beds in the sediment facies change. Coal measure source rocks are superimposed with gas reservoirs, proximal source accumulations, interbedding, or even the same layers of source rocks and reservoirs, which are the contributing privileges for accumulations. In addition, the source rocks, coal reservoirs, and shale reservoirs in coal measures are distributed widely, while the sandstone reservoirs have limited distribution, but the wall rocks have strong ability in sandstone reservoirs. Such factors are of crucial importance for coal measure strata accumulation, such that gas accumulations that dominantly occur in coal measures are characterized by coal measure source rocks with small-scale segmentation and many low abundance gas fields. Furthermore, the distribution and abundance of natural gas are controlled by zones with good physical properties of heterogeneous contiguous sandstone, which is the basic geological factor as coal measure gas is a dominantly lithological gas reservoir.

3.4 Characteristics of three coal gas accumulation patterns

The reason why coal measure sandstone densifies is that sediments are enriched in plastic components, organic matter, and organic acids that lead to the accumulation process of "first densification and then charging" of coal measure sandstone. Current research and geological knowledge suggest that coal measure sandstone contains a certain amount of carbonaceous material, and organic detrital variations also affect sandstone gas accumulations. Sedimentation is the basic factor of reservoir densification controlling the original porosity features. The tight sandstone reservoir depositional settings show some common features: slow sedimentary rate, weak and steady hydrodynamic conditions, dominantly coastal zone facies relating to delta deposition, distinct sandy mudstone interbedded with coal beds, a high content of primary clay interstitial material, and lithic fragments and feldspars which easily diagenetically transform and that are not conducive to primary pore preservation. Upper Paleozoic coal measure sandstone in the northeast margin of Ordos Basin is dominated by quartz and lithic sandstones, with lithic content of 5%–50% and feldspar content of less than 25%; and the clay minerals are a significant cement and are mainly illite, kaolinite, and chlorite, with content of 5%–15% up to 35%. Considering the extent of diagenetic influence, the tight sandstone reservoirs can be divided into three types: compaction, cementation, and other origins. Mechanical compaction is the most important factor in the early diagenetic stage of induced sandstone

densification, contributing to porosity decrease in the whole diagenetic process. The organic origin of sandstone densification has attracted much research attention in recent years. Large amounts of organic acids produced by the hydrocarbon generation process of coal measure source rocks enter the adjacent sandstone, and the acid diagenetic fluid environment leads to a lack of carbonate mineral cementation, which mainly forms the secondary increase of quartz particle silica precipitation, the loss of primary pores, and the densification of sandstone. In the late diagenetic stage, organic acid setting leads to distinct silica and kaolinite cementation under relatively high formation temperature and pressure, and the increase of PH values of formation fluids leads to the formation of late carbonate cementation, the further loss of residual pores, and sandstone densification. The volume of CO_2 produced in the organic matter generation process of coal measure gas can reach 50%–70% of that of hydrocarbon gas, which is much higher than the current CO_2 content of coal measure gas (<5%); large amounts of missing gaseous CO_2 are deposited in the reservoir pores in the form of solid carbonate, and carbonate cement of 0.32 m^3 can be formed by the complete conversion of 1 m^3 CO_2 under ideal conditions. The dynamic process of hydrocarbon gas and CO_2 of coal is not synchronous, and two periods of CO_2-concentrated generation exist in weak and high-mature diagenetic processes, which differ from multiple large-scale hydrocarbon gas generation. The gas generation behavior of coal measure source rocks leads the sandstone reservoir to experience serious densification in the early diagenetic stage and the coal measure strata having a pattern of "first densification and then accumulation." The depositional site of coal measure sandstone is adjacent to that of enriched organic materials, and the early-formed organic-rich sediments are scoured by syndiagenesis or pene-contemporaneous channel, forming the preserved organic detritals mixed in the sandy sediments. Therefore, the most important lithological feature of coal measure sandstone is that it has a relatively high content of organic detritals. The gas-bearing tight sandstone of coal measures contains many coal cuttings or carbonaceous mudstone particles, the majority of which can account for 30%–40% of the view area, and the minority of which is more than 5%—generally between 10% and 20%. The organic detritals obviously affect the physical properties of sandstone. On the one hand, organic detrital increases the pore surface area of the sandstone reservoir, and the pore surface area increases 600 times when 1 m^3 coal breaks into organic detritals with a diameter of 1 mm. On the other hand, the organic detrital contents and the porosity and permeability of sandstone increase. It is thus inferred that coal measure sandstone gas has the accumulation characteristics of partially self-sourcing reservoirs and has a gas production mode and pumping and producing system that differs from those of conventional sandstone reservoirs. In addition, organic detritals improve, to some extent, the physical properties of tight sandstone reservoirs, and so the related exploitation, reconstruction, and gas-producing methods must be adjusted.

Coal measure gas has complicated source–reservoir relationships, and specific carrier systems reallocate the natural gas generated by source rocks, which is crucially important to co-accumulation for coal measure gas. Tight sandstone has no privilege of migration pathways and mainly migrates diffusely. Crevasse splay sandstone has a "chimney" effect on the hydrocarbon expulsion and subsequent migration to the sandstone reservoir. Natural gas in coal measure lacks large-scale lateral migration conditions, but migration in the form of episodic inrush flow driven by abnormal pressure shows vertical and short distance rapid accumulation. The coal measure free gas in the Qinshui Basin migrates in two ways: 1) a macroscopic transport system, including fault, unconformity surface, and collapse column; and 2) a micro-transport system, including micro-pores and micro-cracks of coal beds and roof sandstone. In the Zhengzhuang–Fanzhuang region, the system is micro-transport that is composed of fault, extensive coal beds "layered evaporative" plane hydrocarbon expulsion, and collapse column, which forms three coal measure gas accumulation patterns of primary, adjusted, and reformed type. A similar material modeling experiment shows that the efficiency, rate, and gas saturation of natural gas is controlled by sandstone permeability contrast. The greater the permeability heterogeneity, the greater the effective accumulation potential of coal measure strata. The distributive channel and other sandstone with good physical properties are confined by sandstone or mudstone with poor physical properties, which is conducive to the effective accumulation and preservation of natural gas. The macroscopic occurrence of a coal measure displays a huge "box," such as the large Daniudi tight gas field in the northern Ordos Basin, which is sealed by both regional cap physical properties and abnormal pressure. The industrial gas reservoir is strictly confined in the box, superimposed with multiple large lithological traps, and consists of a "near source box type" accumulation pattern. Such a pattern has dominant source-controlling, reservoir-controlling, high-pressure sealing, and near-source accumulation geological configuration characteristics. The structure is not the reservoir-controlling factor. The breakthrough of coal measure gas exploitation in the Hangjinqi area on the northern margin of the Ordos Basin is a typical case of such accumulation. By analyzing the configuration relationship between the enrichment of coal measure gas and the sealed layer, the adjustment of the later structure, and formation occurrence, it is evident that coalbed methane is apt to accumulate in the regional mudstone cap and floor layers, and areas where it has little tectonic uplift, with smooth and equilibrium state formation occurring after the accumulation stage. We developed a concept of a closed system containing not only enriched coalbed methane but also other types of coal measure gas.

3.5 Multiple vertical gas-bearing combination features

The frequent interbedding of different lithologies in a coal measure inevitably leads to the repeated occurrence of water and gas-blocking layers or inner sealing layers in a longitudinal direction, which then forms an independent gas-bearing system in different layers of a coal measure. A superimposed gas-bearing system is defined as two or more independent gas-bearing systems overlapping each other vertically in the same coal measure. The common phenomenon that different coal measure layers in the same well have a different fluid pressure coefficient is actually the concrete manifestation of the superimposed gas-bearing system. The

TABLE 1 Evaluation parameter table of the favorable zone of coalbed methane in eastern Ordos.

Type	Thickness(m)	Gas-bearing content (m^3/t)	Coal bed depth (m)
I	Single layer >3 m	>6	1800–2250
	Accumulation ≥10 m		
II	Single layer >3 m	>6	<1800 or >2250
	Accumulation 3–10 m		

difference between reservoir physics and the fluid energy of a superposition gas-bearing system is that the coal measure gas co-production process shows inter-system interference and complicated geological conditions, thus constraining the full release of coal measure gas productivity.

The sequence stratigraphic framework is the physical basis for the formation of a superimposed gas-bearing system. The lack of hydrodynamic connection between a coal measure and adjacent water-bearing layers constitutes the hydrogeological basis of the system. The superimposed gas-bearing system is the product of sediment-hydrogeology-structure conditions that control the system. A superimposed gas-bearing system is controlled by depositional setting and the related sequence stratigraphic structure. Coal measures with fluvial-delta-lacustrine facies vertically display a "unified gas-bearing system," while coal measures with "delta-tidal flat-lagoon" facies can form "superimposed gas-bearing systems"; the sequence stratigraphic structure controlling the gas bearing and physical properties of the coal measure reservoir. Low permeability strata deposited near the maximum flood surface and associated with marine mudstone have a partition barrier effect on the vertical flow of coalbed methane, which is considered the fundamental geological reason for the formation of superimposed gas-bearing systems. Such low-permeability rocks are defined as a "key layer," which gradually develops from the delta plain facies to the delta front facies, leading to the vertical structure and superposition of the gas-bearing system becoming more complex and evident.

4 The exploration potential of coal measure gas

Coalbed methane, shale gas, and fine sandstone gas reservoirs have different controlling factors for accumulation, which determine how different favorable gas zones have different controlling factors. Therefore, it is essential to consider different parameters to select favorable zones.

4.1 Coalbed methane favorable zone

The most direct and crucial parameters for target selection and evaluation of coalbed methane are thickness, gas-bearing contents, resource abundance, adsorption saturation, permeability, and coal-bed depth (Wang et al., 2006; Tian et al., 2010); these are important to the recoverability and economy of coalbed methane. The coalbed methane of Shan 2 has high thermal maturity with R_o generally higher than 1.6%, which is in a high coal rank. The cumulative thickness of coal beds is 6–10 m, with a high range of 7 m^3/t–20 m^3/t gas content. The coalbed methane abundance in the Daning-Jixian region adjacent to the study area is 2.85 × 10^8 m^3/km^2, and the adsorption saturation of coalbed methane wells with daily gas production of more than 1000 m^3 is greater than 50% (Tian et al., 2010). The coal beds in the currently exploited coalbed methane blocks are mainly buried at a shallow depth of 1300 m, while the coal bed of Shan 2 in the study area has a high depth of 1900–2400 m and low permeability of almost lower than 0.5 mD, which is medium-to low-permeability coal. The practice of coalbed methane exploration and development shows that the single coalbed layer is more than 3 m thick, and the coalbed methane reservoir has good resource potential when the accumulative thickness is over 10 m and commercial development value when the coalbed methane has content of over 6 m^3/t and daily gas production of over 1000 m^3. Research shows that, worldwide, coalbed methane resources are dominantly distributed in coal beds with depths of 1500 m (Kuuskraa and Wyman, 1993). A new round of coalbed methane resource evaluation in China suggests that the coalbed methane resource is 30×10^{12} m^3 at a depth of 1500–3000 m, accounting for 54.5% of the total resource, with abundant deep coalbed methane resource (Li et al., 2016). As a consequence, according to the criteria of thickness, gas-bearing concentration, resource abundance, and adsorption saturation of high-rank coalbed methane proposed by Wang et al. (2006), we determined the evaluation parameter of the favorable zone (Table 1) and selected the favorable coalbed methane zones of Shan 2 (Figure 5). We thus show that the favorable zones of coalbed methane are distributed in the Yulin-Suide region, and the thick coal beds distribute zonally in a N–S trend. Although coal is developed in the south and east of the region, the single layer has a negligible thickness and thus little exploration and development potential as coalbed methane. In addition, in the current economic and technical conditions, it is economically difficult to separately exploit coalbed methane because of its high burial depth, high drilling cost, and low permeability.

4.2 Favorable zones of shale gas

The critical parameters for shale gas zone evolution include organic content, maturity, thickness, gas-bearing content, physics, and brittle mineral content (Li et al., 2011; Wang et al., 2013). The shale of the Shan 2 study area has a wide range of TOC of 0.08%–37.11% (average 2.0%), while the Shanxi Formation has Ro ranging 1.45%–2.37% (average 1.89%), suggesting that the organic maturity

TABLE 2 Evaluation parameter table of the favorable zone of shale gas in eastern Ordos.

Type	TOC (%)	Thickness (m)	Porosity (%)	Permeability (mD)	Brittle mineral content (%)	Gas-bearing content (m^3/t)
I	>2	Shan 2 >30 and accumulation of Shan 22 and Shan 23 >15	>2	>0.00001	>40	>2
II		Shan 2>30				

TABLE 3 Evaluation parameter table of the favorable zone of fine siltstone gas in eastern Ordos.

Parameter	Reservoir thickness (m)	Porosity (%)	Permeability (mD)	Gas saturation (%)
Value	≥1	≥3.5	≥0.1	≥55

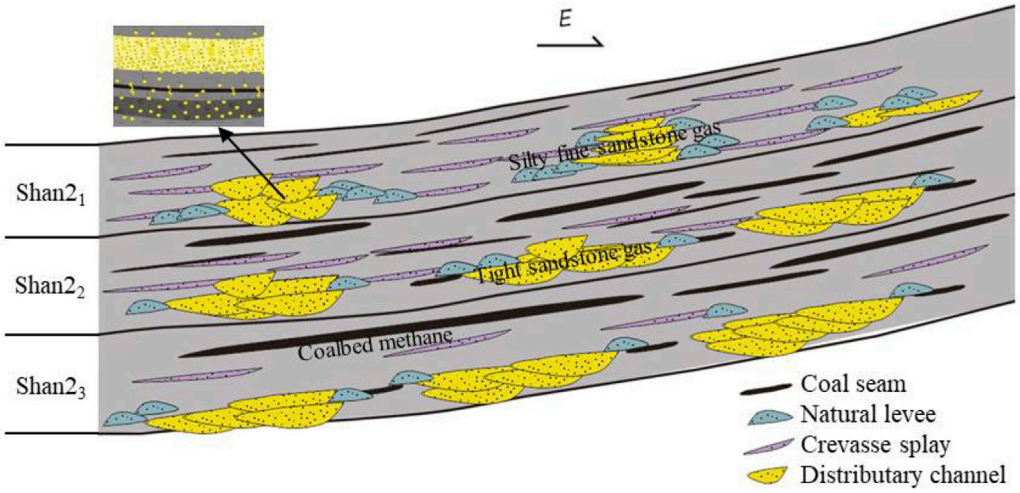

FIGURE 3
Accumulation pattern of sandstone–mudstone–coal associations in coal-bearing strata.

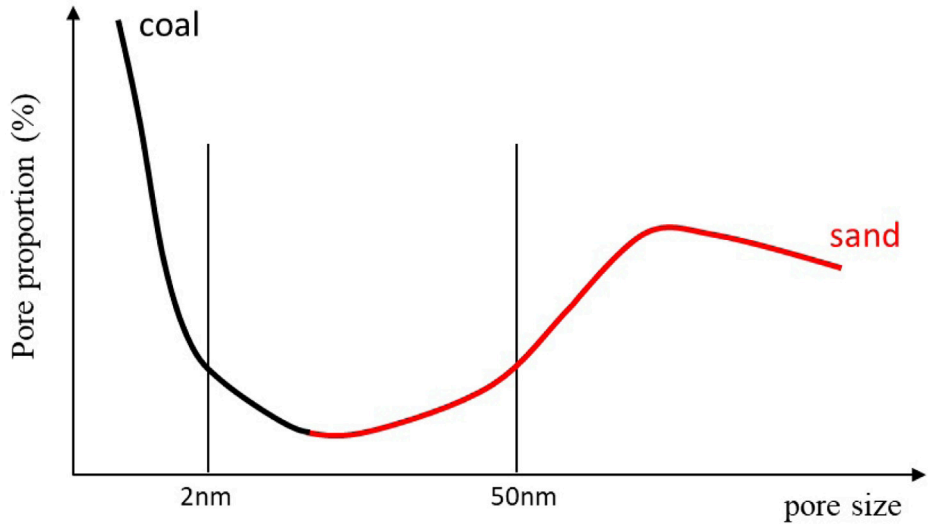

FIGURE 4
V-type curve of pore distribution for sandstone–coal association in Ordos Basin.

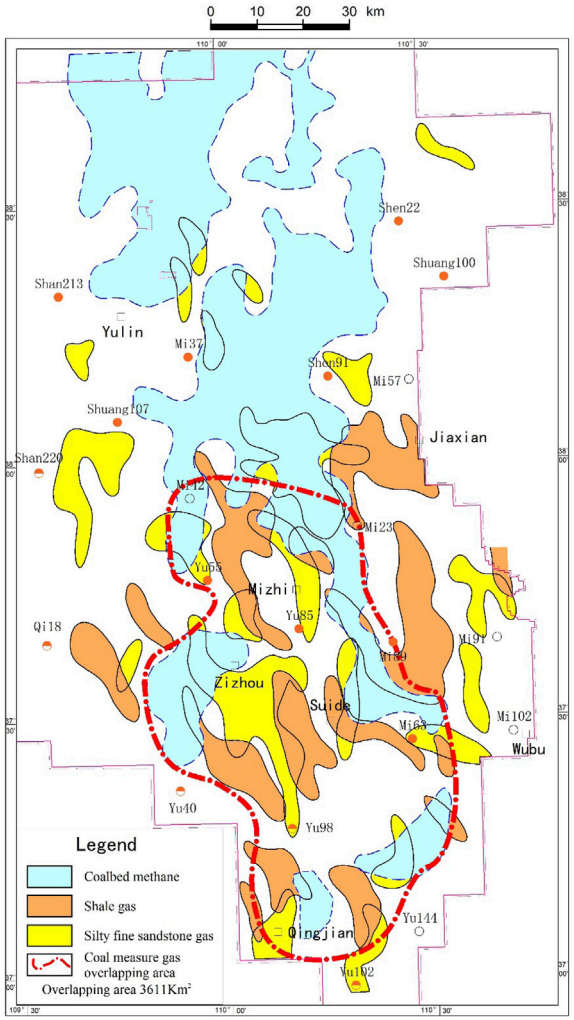

FIGURE 5
Favorable zone of coal measure gas distribution of Shan 2 in eastern Ordos Basin.

of the target shale layer in the high maturity stage is higher than the lowest standard (Ro = 1.1%) of commercial exploitation of shale gas, which is beneficial to the formation of shale gas accumulation. The thickness of a single layer of shale gas reservoir is generally less than 10 m, but its cumulative thickness is generally greater than 30 m; therefore, the shale gas of Shan 2 has exploitation potential. The field test showed that the shale has low gas content, varying 0.19 m^3/t–2.16 m^3/t (average 0.64 m^3/t), and the adsorption experiment implies that the Shanxi Formation shale has a high absorbed gas content of 0.56 m^3/t–15.28 m^3/t (average 3.28 m^3/t). This demonstrates that the Shanxi Formation has a high potential for absorbed gas content. The Shan 2 shale has a permeability of 0.0019 mD–0.317 mD (average 0.0415 mD)—higher than that of commercial shale gas reservoirs with lowest values of 0.00001 mD—and has low porosity ranging 0.2%–4.7% (average 1.7%)—lower than that of commercial shale gas reservoir with lowest values of 2%. Brittle minerals include quartz, feldspar, and carbonates (calcite, siderite, and ferridolomite,) and pyrite with contents of 10%–71% (average 49.9%), while the clay minerals have relatively high contents of 29%–90% (50.1%), which has an adverse impact on reservoir fracturing.

Considering the commercial exploitation quantitative technical indicators of shale gas in the current technical conditions, we determined the evaluation parameter of the favorable zone (Table 2), and the favorable zone distribution of Shan 2 shale gas (Figure 5) is in the south of the Jiaxian region.

4.3 Favorable zone of fine siltstone gas

Shan 2 fine siltstone is tight and so has worse properties than those of medium-coarse sandstones, but has similar key factors of accumulation, which determine that the key parameters of the favorable area are reservoir thickness, physical properties, and gas content. The thickness of the Shan 2 siltstone reservoir is controlled by depositional micro-facies types, including a delta plain distributary channel flanking zone, delta front underwater distributary channel flanking zone, mouth bar far end, and shore shallow lake bar. There are limited studies on the lowest thickness of sandstone gas, gas testing, and core physical property analysis, considering the possible co-production of such sandstone and other reservoirs; we define the lower range of sandstone thickness as 1 m. Because the good reservoir physical properties of Shan 2 fine siltstone are lithic quartz sandstone, we determine for physical criteria that porosity is greater than 3.5%, permeability is more than 0.1 mD, and the lower limit of gas saturation is 55%, based on the previous studies (Table 3). Therefore, this study selects the favorable zone of Shan 2 siltstone gas reservoir that is zonally distributed in the southern Jiaxian region of N–S trending, with a small single layer thickness and distribution area.

4.4 Favorable zone of coal measure gas

The coupling accumulation of coal measure gas is facilitated by the high content of organic matter in coal-bearing rock series, the strong cycle, the overlapping of reservoir space, and the difference in the development of reservoir pore structure. In the Shanxi formation of the Ordos Basin, the transitional phase of marine and continental coal measure source rocks are mainly gas generation, and this formation features thin interbedded development with fine sand. Therefore, its hydrocarbon expulsion efficiency is high, organic matter nanopores are not developed, and the gas from the coal seam and coal measure shale rock, as the source rock, can accumulate and form tight coal measure sandstone gas in the adjacent coal measure sandstone layer. In the formation of vertical three-dimensional gas geological characteristics, each reservoir space overlap formed a natural cap conducive to the preservation of coal measures gas (Figure 3).

Due to the low content of brittle minerals in mudstone and coal seam are difficult to reform in the coal measures of the Shan 2 member, it is difficult to reform. Given the low gas content of fine silty sand rock, it is difficult to industrially develop a single type of coalbed methane, mud shale gas, and tight sandstone gas in coal measures. Therefore, considering coal measure gas as a whole and simultaneously using a single well to conduct integrated exploration

and development of coalbed methane gas, mud shale gas, and tight sandstone gas would not only reduce the exploration and development cost of unconventional natural gas but also improve the use efficiency and profit of a gas well, as well as production life. The combination of sand and coal in the study area forms a V-shaped curve (Figure 4) with both free gas and adsorbed gas, which can accommodate both large and micro-pores, thus achieving high production by fracturing horizontal or highly deviated wells. According to the comprehensive evaluation, sand and peat interbedding developed in the south; through the superposition of coalbed methane, shale gas, and tight gas favorable areas, it is believed that there is a favorable area of coal measure gas accumulation in the Suide-Mizhi area in the south (Figure 5), with an area of 3,265.4 km^2 and predicted resources of 322.821 billion square meters.

5 Conclusion

"Coal measure gas," excluding tight sandstone gas, refers in this study to self-sourcing unconventional natural gas stored by coal, shale, and fine siltstone, characterized by various reservoir and accumulation modes, distinct cyclical coal measure sedimentary sequences, widely distributed and mosaic hydrocarbon accumulation, the three coal gas accumulations, and multiple configurations of vertical gas-bearing reservoirs. Based on the grain-size distribution of sandstone, configurations of sandstone-coal-mudstone association, and strata thickness and layers, coal measure gas from Shan 2 can be divided into four types: thick massive sandstone-coal-mudstone (type I), fine siltstone-coal-mudstone (type II), thin sandstone-mudstone-sandstone (type III), and coal-mudstone (type IV). Type I has already been economically exploited, while the remaining types are currently prioritized.

The favorable coalbed methane area is mainly distributed in the Yulin-Suide area, and the thick coal seam is zonally distributed from south to north. The favorable area of mountain shale gas is distributed in the south of Jiashan County. The favorable areas of silty sand gas reservoir are mainly distributed in the south of Jiaxian. The comprehensive evaluation has shown that sand and peat interbedding developed in the south, and favorable areas of coalbed methane, shale gas, and tight gas are superimposed in the Suide-Mizhi area in the south. The comprehensive evaluation of coal seam, shale, and tight gas should be strengthened in exploration, and three-dimensional exploration should be conducted based on the vertical gas bearing zone.

Data availability statement

The datasets presented in this study can be found in online repositories. The names of the repository/repositories and accession number(s) can be found in the article/supplementary material.

Author contributions

W-BZ wrote the full text, HZ and Y-HS were responsible for the relevant experimental operation and appropriate relevant data, X-XF and JH drew the figure, and X-YJ completed the statistical data.

Funding

This research was supported by "Research on strategy and evaluation technology of new area and new strata and new field of coal-bed methane" (Grant No. 2021DJ2303) and "Study on sweet spots evaluation and yield-increasing mechanism of Upper Paleozoic coal-bed methane in central and eastern Ordos Basin" (Grant No. 2022D-JB01).

Conflict of interest

Authors W-BZ, HZ, Y-HS, X-XF, JH, and X-YJ were employed by the Research Institute of Exploration and Development of PetroChina Changqing Oilfield Company.

Publisher's note

References

Dai, J. X. (1982). Definition and classification of coal-derived gas. *Geol. Rev.* 28 (4), 370–372.

Dai, J. X. (1979). Natural gas and oil formation in coalification processes. *Petroleum Exploitation Dev.* 6 (3), 10–17.

Dai, J. X., Ni, Y. Y., Huang, S. P., Liao, F. R., Yu, C., Gong, D. Y., et al. (2014). Significant function of coal-derived gas study for natural gas industry development in China. *Nat. Gas. Geosci.* 25 (1), 1–22. doi:10.11764/j.issn.1672-1926.2014.01.0001

Fu, X. H., Deleqiati, J., Zhu, Y. M., Shen, J., and Li, G. (2016). Resources characteristics and separated reservoirs' drainage of unconventional gas in coal measures. *Earth Sci. Front.* 23 (3), 36–40. doi:10.13745/j.esf.2016.03.005

Jiang, T., Liu, Z. Y., Wang, T., and Song, H. Z. (2015). Discussion on upper paleozoic coal measures gas reservoiring mechanism in northeastern Ordos Basin. *Coal Geol. China* 27 (7), 43–47. doi:10.3969/j.issn.1674-1803.2015.07.10

Kuuskraa, V. A., and Wyman, R. E. (1993). Deep coal seams: An overlooked source for long-term natural gas supplies. Gas technology symposium. *Soc. Petroleum Eng.* 26196, 587–596.

Lan, C. L., He, S. L., Men, C. Q., Zhang, J. F., and Lan, Y. F. (2007). A study of deliverability variations in low-pressure, low-permeability reservoirs: Paleozoic reservoir in Ordos basin. *Nat. Gas. Ind.* 27 (12), 99–101.

Li, X. Z., Wang, Y. H., Jiang, Z. C., Chen, Z. L., Wang, L. Z., and Wu, Q. (2016). Progress and study on exploration and production for deep coalbed methane. *J. China Coal Soc.* 41 (1), 24–31. doi:10.13225/j.cnki.jccs.2015.9003

Li, Y. J., Liu, H., Liu, J. X., Cao, L. C., and Jia, X. C. (2011). Geological regional selection and an evaluation method of resource potential of shale gas. *J. Southwest Petroleum Univ.* 33 (2), 28–34. doi:10.3863/j.issn.1674-5086.2011.02.004

Ouyang, Y. L., Tian, W. G., Sun, B., Wang, B., Qi, L., Sun, Q. P., et al. (2018). Characteristics of coal measure gas accumulation and such gas exploration strategies in China. *Nat. Gas. Ind.* 38 (3), 15–23. doi:10.3787/j.issn.1000-0976.2018.03.002

Shi, X. Z., Dai, J. X., Wang, Z. M., Zhu, J. W., and Liu, J. Q. (1985). A study of carbon isotope of coal-formed gas in FRG and its inspiration to us. *Nat. Gas. Ind.* 5 (2), 1–9.

Tian, W. G., Li, W. Z., and Sun, B. (2010). "Preliminary study on the evaluation parameter standards of Chinese coal-bed gas constituency," in *Theory and technology of coalbed methane exploration and development*. Editors F. J. Sun, S. L. Feng, Q. B. Zhao, B. A. Xian, W. Z. Li, and J. P. Ye (Beijing: Petroleum Industry Press), 25–31.

Wang, R. G., Li, W. H., Liao, Y. Y., Feng, Y. J., Guo, Y. Q., Ma, Y., et al. (2015). Study on the characteristics of the upper paleozoic Shanxi and xiashihezi formation in Zizhou gas field, Ordos basin. *Chin. J. Geol.* 50 (1), 249–261. doi:10.3969/j.issn.0563-5020.2015.01.16

Wang, S. Q., Wang, S. Y., Man, L., Dong, D. Z., and Wang, Y. M. (2013). Appraisal method and key parameters for screening shale gas play. *J. Chengdu Univ. Technol.* 40 (6), 609–620. doi:10.3969/j.issn.1671-9727.2013.06.01

Wang, T., Wang, Q. W., and Fu, X. H. (2014). The significance and the systematic research of the unconventional gas in coal measures. *Coal Geol. Explor.* 42 (1), 24–27. doi:10.3969/j.issn.1001-1986.2014.01.005

Wang, Y. B., Tian, W. G., and Li, W. Z. (2006). Criteria for the evaluation of coalbed methane area selection in China. *Geol. Bull. China* 25 (9-10), 1104–1107.

Zhao, D. F., Zhao, J. Z., and Chen, Y. (2013). An analysis on the characteristics of the Shan 2 formation gas pools in Yulin-Zizhou area of Ordos basin. *Nat. Gas. Geosci.* 24 (2), 320–328.

Zou, C. N., Yang, Z., He, D. B., Wei, Y. S., Li, J., Jia, A., et al. (2018). Theory, technology and prospects of conventional and unconventional natural gas. *Petroleum Exploitation Dev.* 45 (4), 604–618. doi:10.1016/s1876-3804(18)30066-1

Zou, C. N., Yang, Z., Huang, S. P., Ma, F., Sun, Q. P., Li, F. H., et al. (2019). Resource types, formation, distribution and prospects of coal-measure gas. *Petroleum Exploitation Dev.* 46 (3), 451–462. doi:10.1016/s1876-3804(19)60026-1

frontiers | Frontiers in Earth Science

TYPE Review
PUBLISHED 17 May 2023
DOI 10.3389/feart.2023.1176051

OPEN ACCESS

EDITED BY
Yi-Xiang Chen,
University of Science and Technology of China, China

REVIEWED BY
Silvia Massaro,
Università degli Studi Aldo Moro, Italy
Fabio Dioguardi,
University of Bari Aldo Moro, Italy

*CORRESPONDENCE
Marco Neri,
marco.neri@ingv.it

RECEIVED 28 February 2023
ACCEPTED 09 May 2023
PUBLISHED 17 May 2023

CITATION
Giammanco S, Bonfanti P and Neri M (2023), Radon on Mt. Etna (Italy): a useful tracer of geodynamic processes and a potential health hazard to populations. *Front. Earth Sci.* 11:1176051. doi: 10.3389/feart.2023.1176051

Radon on Mt. Etna (Italy): a useful tracer of geodynamic processes and a potential health hazard to populations

Salvatore Giammanco, Pietro Bonfanti and Marco Neri*

Etna Observatory, National Institute of Geophysics and Volcanology, Catania, Italy

Radon gas and its radioactive daughters have been extensively studied on Mt. Etna, both in local volcanic rocks and in all types of fluid emissions from the volcano (crater gases, fumaroles, mofettes, soil gases, groundwaters). The first measurements date back to 1976 and were carried out both in local volcanic rocks and in the crater plume. Since then, fifty-four scientific articles have been published. The largest majority of them (more than 50%) correlated radon emissions with volcanic activity and/or magma dynamics inside Mt. Etna. Many others were focused on possible correlations between time variations of in-soil radon and tectonic activity. The concentration of radionuclides in Etna volcanic rocks was measured on several occasions in order to set background values of radon parents and to study the dynamics of Etna magmas. Some articles analyzed the concentrations of radon in Etna groundwaters and their temporal changes in relation to volcanic activity. Only a few studies focused on methodological aspects of radon measurements in the laboratory. Finally, in recent years, geoscientists began to analyze the possible negative effects on human health from high concentrations of indoor radon in houses near active faults. The overall results show that, in most cases, it is possible to understand the endogenous mechanisms that cause changes in soil radon release from rocks and its migration to the surface. Several physical models were produced to explain how those changes were correlated with Etna's volcanic activity, making them potential precursors, especially in the cases of eruptive paroxysms. More complex is the analysis of radon changes in relation to tectonic activity. Indeed, if measurements of radon in soil is now considered a robust methodology for identifying buried faults, radon time variations are not always clearly correlated with seismic activity. This difficulty is likely due to the complex interplay between tectonic stress, magma migration/eruption and gas release through faults. In any case, the potential high hazard for human health due to high concentrations of indoor radon in houses close to faults seems to be a well-established fact, which requires particular attention both from the scientific community and the public health authorities.

KEYWORDS

radon, Mt. Etna, volcano monitoring, human health, soil gas, indoor pollution, magmatic degassing, faults

1 Introduction

Radon gas has attracted the attention of geoscientists at least in the past 50 years, because of its great potential as tracer of many geodynamic processes such as volcanic eruptions and earthquakes, due to its physical properties (chemical inertness, high density, relatively short half-life, widespread distribution). More recently, it also came under the spotlight because of its severe impact on human health, due to its radioactivity and its capability to diffuse and accumulate in the atmosphere inside buildings.

On Mt. Etna volcano studies on radon and, more generally, on natural radioactive isotopes started in the mid-1970s (Capaldi et al., 1976; Lambert et al., 1976). However, it was only in the last 20 years that radon was extensively and deeply studied in terms of its sources, sinks and mode of transport to the surface. Until today, a remarkable number of data were produced from very different types of samples (rocks, groundwaters, crater gases, fumarole gases, soil gases, air; Figure 1) that have shed more light both on the benefits of using radon gas to understand how this volcano works and on its high potential risk for human health.

The World Health Organization (WHO), through the International Agency for Research on Cancer (IARC), has classified radon in Group 1 of carcinogenic substances, which includes substances for which there is sufficient evidence of carcinogenicity on the basis of human epidemiology studies. In particular, exposure to radon indoor increases the risk of contracting lung cancer. Other possible health effects of radon exposure have been studied, such as an increased risk of leukemia, but to date there are no certain conclusions other than the increased risk of lung cancer. The extent of the risk depends both on the concentration of radon to which people are exposed and on how long the exposure lasts. The risk of lung cancer was found to increase by 8.4% per 100 Bq m^{-3} increase in measured radon (Darby et al., 2005). Given equal conditions of radon exposure, smokers are more at risk (about 25 times more) than non-smokers due to the synergistic effect between radon and cigarette smoke (Darby et al., 2005). In Italy, the Istituto Superiore di Sanità has estimated that about 10% of the 31,000 cases of lung cancer recorded every year is attributable to radon.

This work is intended not only to give the state of the art in the research on radon on Mt. Etna, with categorized lists of all papers published on this subject and a brief description of the main results obtained, but also to provide a comprehensive model of what we have understood about this volcano and its environment based on the radon and radio-isotopes data collected so far and to figure out what possible developments (both scientific and technical) can take place in the near future.

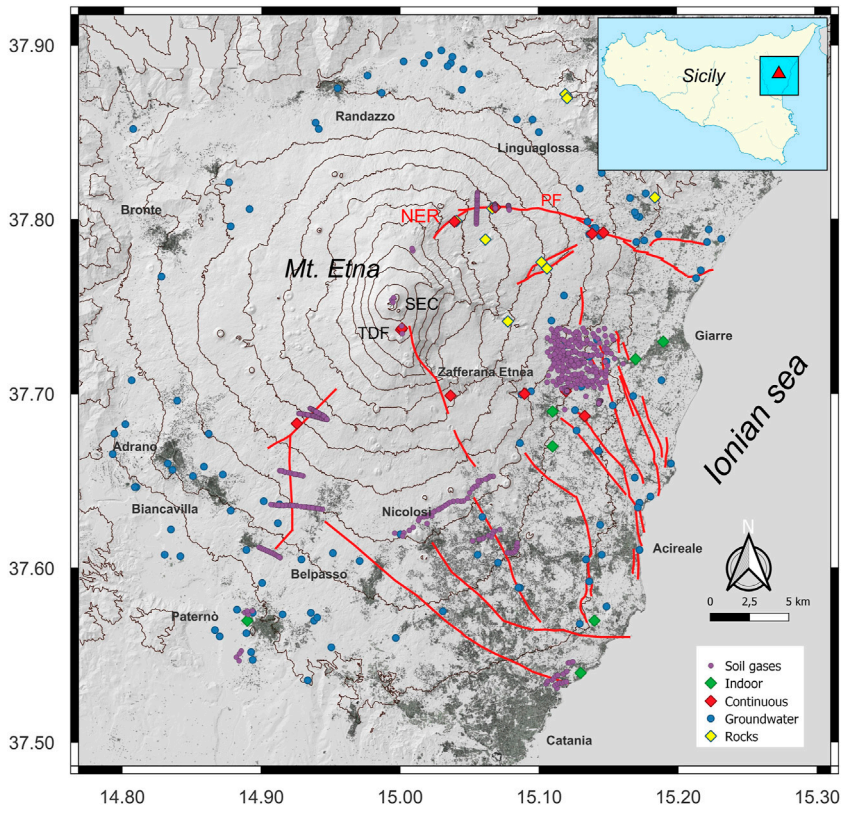

FIGURE 1
Sketch map of the Mt. Etna area, showing the different types of radon measurements carried out so far (see the legend). The red lines show the major tectonic faults on the Volcano. The main towns are also indicated with their names. TDF = Torre del Filosofo; NER = North-East Rift; PF = Pernicana Fault. Elevation contour lines every 250 m.

2 Radioactivity in Etna volcanic rocks

Studies on radioactive isotopes in volcanic rocks of Mt. Etna were among the first to be carried out on this volcano (Capaldi et al., 1976), with the aim to imply the dynamics of magma ascent during pre-eruptive periods from the radioactive disequilibria between Ra, Th and U short-lived daughters belonging to the decay chains of ^{232}Th and ^{238}U (all measurements performed with gamma spectrometry). Since the first results, it was found that Ra isotopes were in excess over equilibrium contents, especially regarding the ^{228}Ra/^{228}Th ratio, and this was modeled as a long-term (in the order of tenses to hundreds of years) injection of Ra-rich magma. Conversely, ^{230}Th/^{238}U and ^{234}U/^{238}U ratios were in substantial agreement with equilibrium conditions.

More extensive studies on a larger number of rock samples (Condomines et al., 1995) and a larger number of isotopes (^{238}U, ^{230}Th, ^{226}Ra, ^{210}Pb, ^{87}Sr, and ^{86}Sr) allowed to observe changes related with crystal fractionation over time scales of a couple of centuries, and to estimate both the residence time (max 1,500 years) of magma in the deep reservoir feeding the volcano and to infer a volume of magma in the order of 150–300 km^3. Furthermore, it was observed that since 1970 this reservoir was injected with new basaltic magma with isotopic signature suggesting crustal contamination.

A new series of measurements of the same isotopes as those surveyed by Condomines et al. (1995) was performed both in the 2001 and in the 2002–2003 lavas (Clocchiatti et al., 2004). The results fully confirmed those of Condomines et al. (1995) and strengthened the hypothesis that those two eruptions were fed by a volatile-rich magma intrusion independent of the central conduits of the volcano ("eccentric" or "peripheral" intrusion) and composed of new basaltic melt produced from a large-scale metasomatized mantle source.

Some other radioactivity measurements were recently performed in rock samples collected mostly from the SE flank of Mt. Etna (Kozłowska et al., 2016; Kozłowska et al., 2019). Radium isotopes ^{226}Ra and ^{228}Ra were measured by gamma spectroscopy, giving average values of 61.8 and 53.3 Bq/kg, respectively, thus slightly lower than those of the volcanic rocks from other nearby volcanic areas.

The only direct measurements of radon emission from volcanic rocks of Mt. Etna were carried out by Morelli et al. (2011), who performed laboratory measurements of radon exhalation rate from rock samples using the can technique (Grasty, 1997) and CR-39-based (diglycol carbonate) detectors exposed inside each can for 3 months. Both volcanic rocks of different composition and non-volcanic rocks (sedimentary and metamorphic) were analyzed, showing that higher radon exhalation values were found in volcanic rocks, following their higher uranium content, reaching about 700 m Bq m^{-2} h^{-1}. The results were propaedeutic for developing models of radon transport and release at the surface through soils.

3 ^{222}Rn in crater gas emissions and in the air

Determination of radon emission from open conduit degassing at active volcanoes during the last 40 years was mostly performed through the measurement of the last three, long-lived, radon daughters (namely, ^{210}Pb, ^{210}Bi, and ^{210}Po) in volcanic plumes (e.g., Lambert et al., 1976). Studying ^{210}Pb-^{210}Bi-^{210}Po radioactive disequilibria in magmatic gases from open-conduit persistent crater plumes has proved useful to infer degassing dynamics of active volcanoes (Lambert et al., 1976; Gauthier et al., 2000; Le Cloarec & Pennisi, 2001; Allard et al., 2016), where major gases like CO_2 and H_2O act as carriers for radon and its daughter radionuclides. On Mt. Etna, such measurements were carried out since 1988 using cellulose acetate filters to trap the airborne aerosol particles that carry those radionuclides and then measuring alpha and beta radioactivity in the collected samples (Lambert et al., 1976; Le Cloarec et al., 1988; Marty and Le Cloarec, 1992; Le Cloarec and Pennisi, 2001; Terray et al., 2018).

The basic assumption of all the above studies is that radioactive equilibrium is achieved among all of the ^{238}U daughters (e.g., Lambert et al., 1976), therefore the above long-lived decay products of radon associated with the aerosols collected are reasonably all emitted from magma. One of the first results so far obtained was to infer the degassing time of magma inside Etna's shallow conduits and to show the different proportions of fresh magma that is involved in convective processes (Le Cloarec et al., 1988). In fact, the measured activities of the above nuclides were actually found to be very different, with a marked enrichment in ^{210}Bi and ^{210}Po relative to ^{210}Pb, because of the higher volatility of the former nuclides with respect to that of the latter. Using the ratios ^{210}Bi/^{210}Pb and ^{210}Po/^{210}Pb both in the volatile phase and in the magma it was possible to model how their radioactive disequilibria in the gas phase vary in time after exsolution, thus allowing for the estimate both of the magma residence time and of the gas transfer time in the volcano conduit, especially if taking ^{222}Rn into account in the degassing models (Terray et al., 2018; Terray et al., 2020a). Other models used the above nuclides together with SO_2 crater fluxes to infer the dynamics of magma in the shallow conduits of Mt. Etna, as well as the volume of degassing magma and the proportion of non-erupted degassing magma (Le Cloarec and Pennisi, 2001). Furthermore, using elemental ratios between other magmatic gases (CO_2, He) detected in the crater plume emissions and ^{210}Po it was possible to estimate their volcanic fluxes (Marty and Le Cloarec, 1992).

The main results of the above studies were: i) assessment of the role of the South-east Crater as a "secondary" degassing vent (i.e., not directly related with the central conduit of the volcano); ii) assessment of the existence of different magma convective cells within the conduits of the volcano; iii) estimate of the proportion of degassed magma eventually erupted (e.g., 15%–20% during the period 1983–1995); iv) magma residence times within the shallow reservoirs in the order of 500–1,000 days; v) transfer times of magma to the surface shorter than 7 days.

It was only recently that the first direct measurements of in-air radon were carried out, both at the summit craters of Mt. Etna (Terray et al., 2020b) and at different altitudes around the volcano (Vaupotič et al., 2010).

Vaupotič et al. (2010) investigated radon contents in outdoor air both close to the volcano summit and in other areas along its flanks, showing radon concentrations in the range from 3.0 to 19.6 Bq m^{-3}. Higher average values were generally found in the west sector of Mt. Etna, but the highest ones (up to 93 Bq m^{-3}) were measured at high altitude (about 3,000 m asl).

In particular, Terray et al. (2020a) used a network of fixed dosimeters around the rim of the central crater of the volcano to monitor radon emissions for several months. This allowed for a better constraint of radon emission in an open-conduit volcanic plume and also for the assessment of the potential health hazard for the people working or visiting the summit area of Mt. Etna. The results indicated higher radon concentrations downwind and also close to high-flow fumaroles, thus showing substantial emission of this gas both from crater plume degassing and from fumarole emissions around the rim of the central crater of Mt. Etna. In terms of potential radon hazard in air, the radon contents in the high-concentration sites were much higher than the thresholds recommended by the WHO handbook (WHO, 2009) for 8-hour-long indoor exposure (radon values measured in 4 sites out of 41 at 1 m elevation above ground ranged from 704 to 8,827 Bq m^{-3}, compared to a maximum recommended concentration of 300 Bq m^{-3}). However, both the very short periods of exposure (normally << 8 h) and the rapid dispersion of radon in open air due to air/gas motion make this hazard low, if not negligible.

4 ^{222}Rn in groundwaters

Despite the growing interest on this subject around the world, relatively few papers (including conference materials) on radon activity in groundwater have been published on Mt. Etna area (D'Alessandro and Vita, 2003; Galli et al., 2000; Quattrocchi et al., 2000; Kozłowska et al., 2009; Kozłowska et al., 2016; Kozłowska et al., 2019; Fiore et al., 2011). This is quite surprising, considering that the groundwaters of Mt. Etna not only represents the main drinking water resource for the local population and are also distributed in the municipal water networks of the surrounding areas, but are also used both for agricultural and for industrial purposes.

Groundwater contamination from radon is a serious global concern: the major health hazard occurs due to toxic indoor air inhalation and consumption of contaminated drinking water supplied from groundwater. It is widely shared the assumption that the radon was found to be directly or indirectly responsible of about 2% of all death from cancer in Europe (Darby et al., 2005) and that indoor radon levels derived from groundwater use in the United States are thought to cause 1%–7% of fatal lung cancers (Cothern et al., 1986). Studies have been conducted in order to find the correlation between the drinking water radon contamination and gastrointestinal malignancies, but the consequences are contradictory (Auvinen et al., 2005). Epidemiological studies on the incidence of cancer in the volcanic area of Etna, cannot draw any conclusion on the association between increased exposure to ^{222}Rn and the risk of thyroid cancer (Pellegriti et al., 2009) The guidance levels for waters intended for human consumption in 24 European Union countries are 100 Bq L^{-1} (Jobbàgi et al., 2017).

The only extensive survey on Mt. Etna's groundwater for the specific determination of dissolved radon contents was performed by D'Alessandro and Vita (2003), who measured ^{222}Rn activity in 119 groundwater samples collected throughout the active volcanic area of Mt. Etna. The activity values, measured by means of a portable Lucas-type scintillation chamber, ranged from 1.8 to 52.7 Bq L^{-1}, highlighting that about 40% of the samples exceeded the maximum level of 11 Bq L^{-1} proposed by the USEPA in 1991. Samples collected from wells showed generally higher radon contents than those collected from springs and drainage galleries, probably because of radon loss at the contact with the atmosphere in the well head-space. Despite the rather uniform composition of the Etnean volcanic rocks, with a very narrow range of uranium content, the ^{222}Rn activity in groundwaters showed an uneven distribution. The highest radon levels were found in the eastern sector of Mt. Etna, the tectonically most active area of the volcano (with the maximum values clustering along the Timpe Fault System). The south-western sector, on the contrary, despite its intense geodynamic activity (high seismicity and strong magmatic degassing at the surface from both focused vents and diffuse degassing areas), displayed lower radon levels. This is probably due to the formation of a free gas phase in the groundwater (due to oversaturation of water in magmatic CO_2, which is particularly abundant in this part of the volcano) that strips the radon from the water. The gas emitted from water into the soil, therefore, would be strongly enriched in radon compared to groundwater. Moreover, comparing the data collected at Mt. Etna with those of other volcanic areas of Italy, D'Alessandro and Vita (2003) show that the two main factors controlling radon release to the aquifers are i) the content of parent elements in the aquifer rocks and ii) the temperature of the geothermal systems that interact with the sampled aquifers. The former acts when the leaching of U and other parent nuclides in the host rocks is more effective due to Eh-pH conditions in the groundwaters that favor mineral dissolution (Aiuppa et al., 2000), whereas the latter is explained by the inverse correlation between radon solubility in water and water temperature, so that higher temperature causes greater evolution of radon from water (Wilhelm et al., 1977).

Both Galli et al. (2000) and Quattrocchi et al. (2000) described the design and set-up of automated monitoring stations for the determination of many physical and chemical parameters, including dissolved radon, in Etna's groundwater. The few radon concentration data indicate background values in the same range as that shown by D'Alessandro and Vita (2003).

Kozłowska et al. (2009) investigated radioactivity in underground waters from Mt. Etna on the basis of 13 water samples. The samples were collected from springs, wells and galleries around the volcano. Water from nine out of thirteen intakes is actually used for human consumption. Activity concentration measurements of ^{222}Rn were performed with a liquid scintillation counter. Radon activity concentration was found within the range from 1 to 13 Bq L^{-1}, hence these waters can be classified as low-radon waters.

Kozłowska et al. (2016) focused on activity concentration of ^{222}Rn measured in 9 water samples from the aquifers of the eastern flank of Mt. Etna volcano. Three samples were from water drainage galleries and six from water wells, all used for human consumption. Sampling was performed three times, in 2011, 2012, and 2013. This area is a good case study because it is characterized by large volumes of groundwater and by strong interactions between groundwater, volcanic rocks, volcanic gases and some hydrothermal fluids. Moreover, it is also the area of Mt. Etna with the highest values of dissolved radon, as already shown by D'Alessandro and Vita (2003). Measurements of radon activity concentration in water were performed with a liquid scintillation technique. All water samples

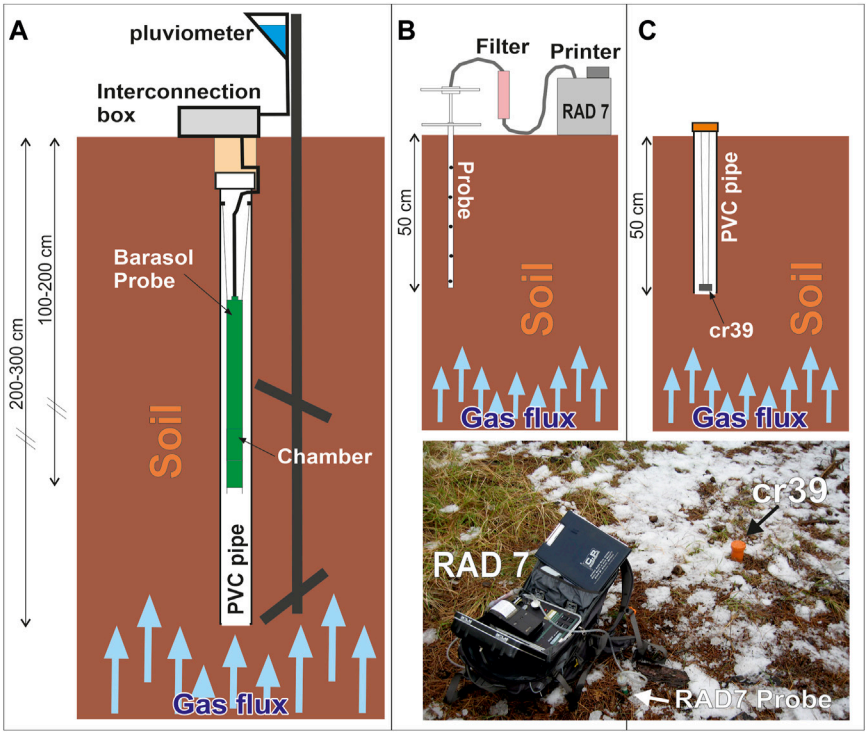

FIGURE 2
Summary of the different methods used to measure in-soil radon on Mt. Etna. Inbox **(A)** shows the typical setup of the sensors for continuous radon monitoring; **(B)** shows the field setup for discrete measurement both of ^{222}Rn and ^{220}Rn with Durridge RAD7 portable radonmeter; **(C)** shows the setup for long-term monitoring of radon using track detectors (SSNTD CR-39 type).

showed Radon activity concentration within the range from 2.91 ± 0.36 to 21.21 ± 1.10 Bq L^{-1}, hence these waters can be classified as low-radon waters.

Finally, on the basis of a radiometric survey carried out on eight rock samples from the eastern flank of Mt. Etna, representative of the average rock type of the aquifers, Kozłowska et al. (2019) made an interesting attempt to determine radionuclide transfer factors from soil to water and to calculate the radiological risk resulting from ingestion of these isotopes contained in drinking water. Based on both the results of this study and those of previous investigations (Kozłowska et al., 2016), the Authors concluded that the magmatic rocks of Mt. Etna show favorable conditions for uranium leaching by water, whereas thorium and radium remain in the host rocks of the aquifer. Furthermore, the effective radiation doses due to radionuclides ingestion via drinking water are significantly below the limit of 100 μSv/year set by WHO (2017) and the limit of 1 mSv/year set by the Italian law, and therefore represents a rather limited risk to human health.

5 ^{222}Rn and ^{220}Rn in-soil gas

5.1 General outlines

Measurements of radon (both ^{222}Rn and ^{220}Rn) in soil (Figure 2) can produce different results as a function of many factors, the most important of which are: i) the concentration of parent radionuclides in the different layers of rock in the sub-soil; ii) the grain size (i.e., the porosity) of the surface layers of the soil; iii) the presence of a pre-fractured soil, which increases the permeability of subsurface rocks; iv) the concurrent presence of other soil gases (mostly CO_2) in the sub-soil that can act as carrier for radon and thus enhance (or dampen by dilution, in case of excessive gas flow rates) radon emissions; v) the proximity of an active fault plane, which through its fractures increases the local permeability of rocks; vi) the influence of environmental parameters like humidity, wind speed and temperature, the latter both in the air and in the soil atmosphere.

In-soil radon detection can be either discrete, being performed discontinuously in time in the same location or as spot measurements in different locations over large surfaces, or near-continuous, being performed automatically in the same place at time intervals ranging from a few minutes to a few hours.

On Etna, temporal changes of in-soil ^{222}Rn activity were observed simultaneously with changes in volcanic activity (Le Cloarec et al., 1988; Alparone et al., 2005; Neri et al., 2006, 2016; Giammanco et al., 2007, Immè et al., 2005; Immè et al., 2006a; Immè et al., 2006b; Immè et al., 2014; Morelli et al., 2006; La Delfa et al., 2007; Immè and Morelli, 2012; Falsaperla et al., 2014; Falsaperla et al., 2017) and/or during increased tectonic activity in the proximity of fault planes (Burton et al., 2004; Brogna et al., 2007; La Delfa et al., 2007, 2008; Neri et al., 2007, 2011, 2014, 2016, 2019; Giammanco et al., 2009; La Delfa et al., 2010; Siniscalchi et al., 2010; Morelli et al., 2011a; Morellia et al., 2011b; Vizzini and Brai, 2012;

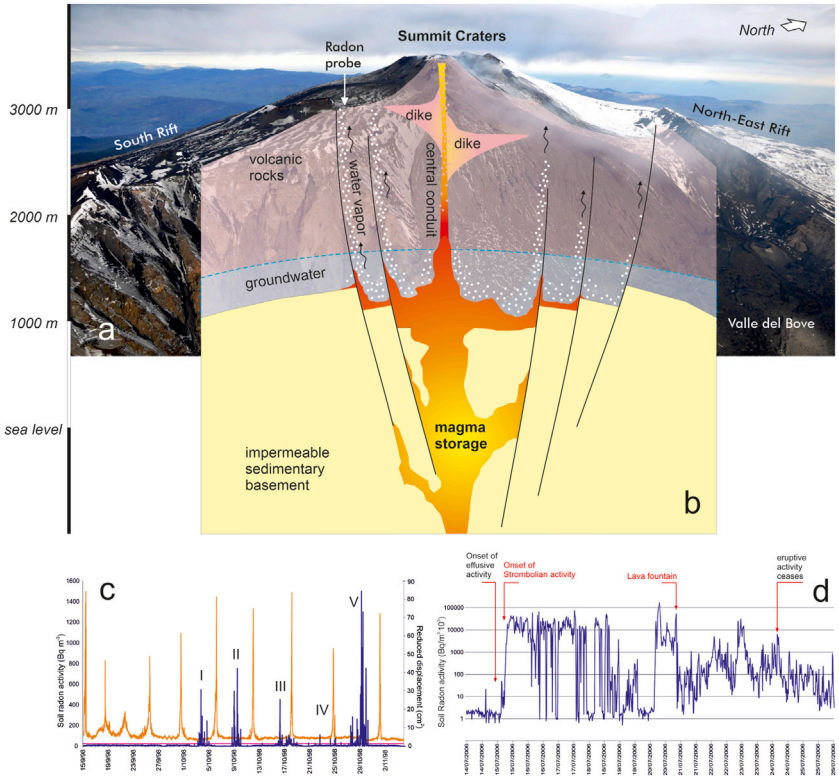

FIGURE 3
(A) Location of the continuous ^{222}Rn monitoring stations used from 1996 to 2013 in the site called "Torre del Filosofo" (TDF in Figure 1, at 2,940 m asl) along the so-called South Rift of Mt. Etna; **(B)** Schematic volcanologic and structural N-S profile of the summit of Mt. Etna, showing a model of radon degassing from magma and across the groundwater/hydrothermal system towards the radon monitoring station; **(C)** results of in-soil radon monitoring at TDF during 1998, where the blu lines is the radon signal, the orange line is the reduced displacement associated with volcanic tremor amplitude and roman numbers indicate the radon anomalies associated with lava fountain episodes (modified from Alparone et al., 2005); **(D)** radon signal at TDF during July 2006, showing the main changes associated with eruptive activity. Radon values were obtained using a BMC2 barasol probe (limit of detection = 50 Bq m^{-3}; range from 0 to 1 GBq m^{-3}) (modified from Neri et al., 2006).

Bonforte et al., 2013; Johnova et al., 2014; Woith, 2015). Moreover, some studies were aimed at verifying the correspondence between the strongest in-soil radon emissions and the indoor radon pollution in buildings located in areas with surface faulting, in order to evaluate the possible risks to human health (Brogna et al., 2007; Pellegriti et al., 2009; Neri et al., 2019).

5.2 Continuous radon measurements

The first continuous measurements of in-soil ^{222}Rn activity on Etna were performed from January 1992 to January 1993 using a probe equipped with a solid-state detector (Alphameter^{tm}—Alphanuclear Co., Canada), placed at the bottom of a 2 m-deep bore-hole at altitude of about 1,650 m asl, close to a dry fissure that formed during the 1989 flank eruption and that re-activated during the 1991–1993 flank eruption (Badalamenti et al., 1994). Anomalous variations were observed mostly in late January 1992, seemingly correlated with a magmatic intrusion along the 1989 dry fissure. Further radon monitoring was performed some months later using a similar sensor (Barasol Multisensor BMC2, Algade, France) by Pinault and Baubron (1996) and some years later also by Alparone et al. (2005). In both cases, the ^{222}Rn station was located ~1 km South of SEC, at 2,940 m altitude in a place called "Torre del Filosofo" (see Figures 1, 3). In the former, some large anomalous spikes were observed and they were interpreted as non-periodic, spasmodic ^{222}Rn emissions likely due to volcanic activity. In the latter, the Authors analyzed ^{222}Rn measurements carried out during a period of frequent eruptive episodes that occurred at South-East Crater (SEC) in September-November 1998, using the same type of solid-state sensor device as that used by Badalamenti et al. (1994), placed at the bottom of a 1 m-deep sealed bore-hole. Air temperature and air relative humidity were also measured over 1 h periods by sensors placed in the same location. According to Alparone et al. (2005), conspicuous increases of ^{222}Rn were recorded at least 46 h before each of five episodes of lava fountaining that occurred at SEC during the period of monitoring, thus demonstrating the potential use of ^{222}Rn as a precursor to strong explosive basaltic eruptions (Figure 3C).

Considering these first positive experiments, a Barasol Multisensor BMC2 (Algade, France) probe was later installed in the same site in July 2005. Since then, the ^{222}Rn probe was constantly active until 2013, when a lava flow buried the monitoring station. During the period of operation, the probe collected data useful for monitoring the volcanic activity at the summit craters of Etna, particularly during the 10-day-long July 2006 Strombolian/effusive

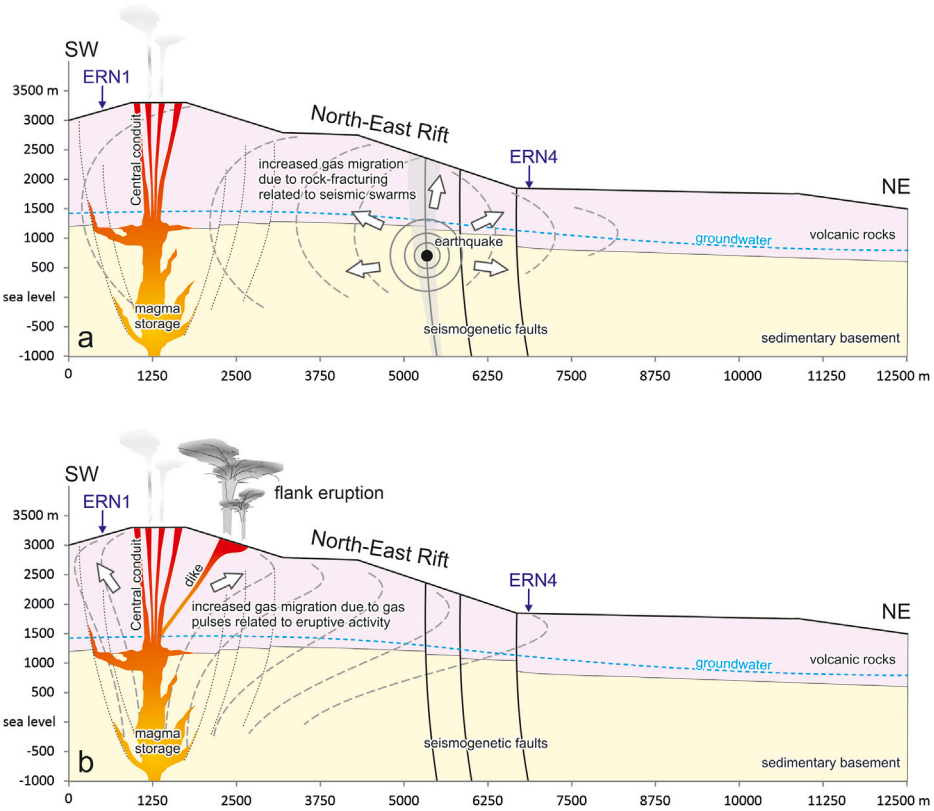

FIGURE 4
Schematic geological sections of the summit area and the NE Rift of Mt. Etna, showing a dynamic conceptual model of radon gas release and migration in case of **(A)** tectonic strain release due to earthquakes or **(B)** increase in soil gas velocity due to increased magmatic degassing during dike-fed intrusions (white arrows and dashed grey lines). Dashed red arrows indicate possible directions of magmatic intrusions into the NE rift zone. Modified from Falsaperla et al. (2017).

eruption (Neri et al., 2006). Both the onset of explosive activity and a lava fountain episode at SEC were preceded by some hours by increases in ^{222}Rn in-soil emissions. Anomalous peaks in ^{222}Rn activity were interpreted as due to micro fracturing of uranium-bearing volcanic rocks. These observations confirmed the hypothesis that in-soil ^{222}Rn measurements collected in the Etna's summit area can be strongly controlled by the state of volcano-tectonic stress within the volcano and demonstrate the usefulness of high-frequency ^{222}Rn acquisition before and during explosive-effusive eruptions (Figure 3D).

In addition to this, between February and April 2007 the ^{222}Rn probe installed at Torre del Filosofo detected some episodes of volcanic activity that were not evident at the surface, i.e., magma ascent along the central conduit, and did not culminate in an eruption. Falsaperla et al. (2014) described several of these cases, called "failed eruptions", during inter-eruptive periods between paroxysmal eruptions at the SEC. Failed eruptions were characterized by increases in volcanic tremor amplitude and simultaneous ^{222}Rn anomalies and were explained as ascending magma batches that triggered repeated episodes of gas pulses and rock fracturing, but that were not able to eventually erupt at the surface.

Also in case of long-lasting flank eruptions, the ^{222}Rn probe installed at site Torre del Filosofo demonstrated its usefulness. Falsaperla et al. (2017) analyzed ^{222}Rn data together with other seismic and environmental parameters; the triggering mechanism of ^{222}Rn anomalies was postulated to be either tectonic (promoting rock fracturing) or volcanic (promoting gas pulses) (Figure 4). During the 2008–2009 flank eruption, in particular, numerous episodes of rock fracturing, inferred from seismic swarms, both anticipated and accompanied the beginning of the eruption. Concurrently, vigorous gas pulses causing anomalous peaks in ^{222}Rn emissions testified the arrival of new magma batches at the surface during the same eruption, each one interpreted as a distinct episode of magma re-feeding following deep rock fracturing. Moreover, analyzing the temporal pattern of the anomalous ^{222}Rn emissions, Falsaperla et al. (2017) inferred that the advective ascent speed of the ^{222}Rn gas carrier (mainly water vapor) in the area of Torre del Filosofo was >>94 m/day, hence much faster than diffusive motion of the gas. In this case, the ascent speed was about double that calculated by Neri et al. (2016) in a radon monitoring site located about 7 km away from the summit crater area.

Other continuous ^{222}Rn measurement stations, equipped with Alphameter^{tm}, Barasol or AlphaGUARD (Bertin Technologies SAS, France) monitoring devices, were installed far from the summit craters of Mt. Etna and near active fault planes of the northern and eastern flanks of Etna, that are the areas of the volcano mostly affected by seismic capable faults, at altitudes ranging from ~450 m

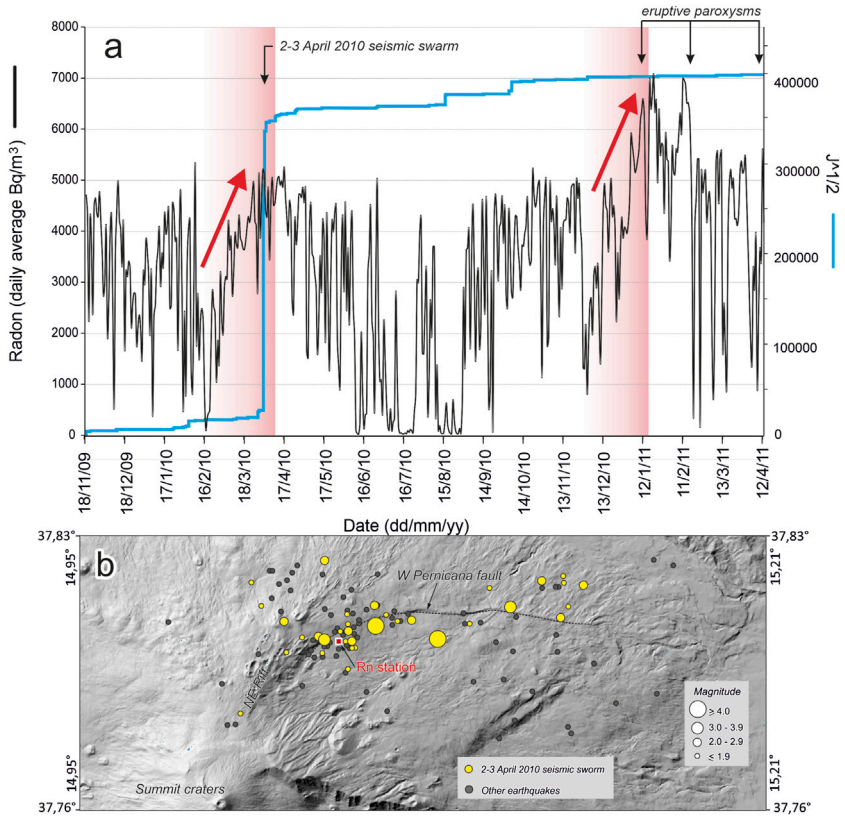

FIGURE 5
(A) Example of in-soil radon signal from the continuous monitoring station located near the Pernicana Fault from November 2009 to April 2011, showing daily average values of radon activity (black line), cumulate strain release during earthquakes (blue line) and summit eruptions of Mt. Etna during the studied period (arrows). ^{222}Rn values were obtained using a BCM2 Barasol probe (Algade, FR). The BCM2 probe integrates and stores the data collected every 20 min (limit of detection = 50 Bq m^{-3}; range from 0 to 1 GBq m^{-3}). Meteorological parameters, such as temperature (0.1°C) and atmospheric pressure (1 hPa), were simultaneously recorded. The two vertical pink bands highlight periods of steady increase in radon emissions (red arrows: each period lasted about 7 weeks) that preceded both major seismic events and summit eruptions; **(B)** earthquake epicenters distribution from 2 November 2009 to 13 April 2011, projected onto a Digital Elevation Model of the NE flank of Mt. Etna. Modified from Neri et al. (2016).

to 1800 m asl (Figure 1), in order to monitor mainly the tectonic activity of the volcano (Immè et al., 2005; Immè et al., 2006a; Immè et al., 2006b, 2014; La Delfa et al., 2008; Morelli et al., 2011a, 2011b; Neri et al., 2016; İçhedef et al., 2020). Interesting results were obtained, in particular, by Neri et al. (2016) analyzing the ^{222}Rn data acquired in 2009–2011 by a probe placed in the Piano Provenzana area, on the north-eastern flank, at 1800 m asl (Figure 1). According to the Authors, radon is released mainly from sources at depth <1,400 m, with an ascent speed of >50 m/day. Three periods of anomalous gas release were detected after filtering of the raw radon signal and they were interpreted as having either a tectonic (as in February 2010) or a volcanic (as in January and February 2011) trigger (Figure 5A). This was not a surprise, because the probe was purposely installed in a site that was both near the Pernicana fault and near the North-East Rift of the volcano, that is a volcanic-tectonic structure which intercepts the central volcanic conduit of the volcano (Figure 5B).

More recent studies (İçhedef et al., 2020) have focused on how to filter out all the periodic cycles from the radon signals recorded at different stations around the volcano using digital band-stop filters after applying the Fast Fourier Transform algorithm, assuming these were caused by non-volcanic influences (environmental parameters, Earth tides, etc.). This kind of approach is intended to avoid recording environmental parameters that are then used to filter the raw radon time series based on linear regression models. The alternative filtering procedure of İçhedef et al., 2020 helped reveal aperiodic radon changes that were interpreted and modeled in terms of gas-pressure waves that propagated away from the central conduits of the volcano during rapid pre-eruptive magma ascent episodes.

5.3 Discrete radon measurements

It is known that the measurement of in-soil radon (^{222}Rn) and thoron (^{220}Rn) emissions are greater in areas characterized by high permeability of the rocks richer in uranium and in the presence of significant fluxes of carrier gases (mostly water vapor and CO_2). These conditions often occur in areas with surface soil faulting, i.e., in the immediate proximity (from tens to hundreds of meters) to active faults. On Etna, these conditions are mainly found along the eastern and southern slopes of the volcano, where numerous and important active and capable fault systems occur (Branca et al., 2011;

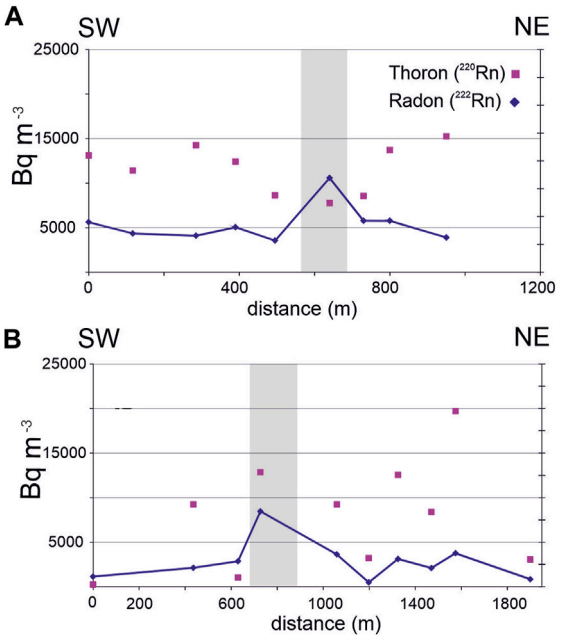

FIGURE 6
Example of profiles of in-soil ^{222}Rn and ^{220}Rn activities measured across faults (grey bands) on the southern flank of Mt. Etna: **(A)** seismogenic fault with emission of "deep" ^{222}Rn only; **(B)** shallower fault with creep motion and marked emission of "shallow" ^{220}Rn. The Durridge RAD7 instrument was used to measure radon and thoron concentrations in soils (Measurement = +/−5% absolute accuracy). According to the method suggested by Burton et al. (2004), one ^{222}Rn and ^{220}Rn measurement consists of hammering a hollow metal tube into the soil to a depth of 50 cm, inserting a plastic tube connected to the inlet of the RAD7 instrument and performing three measurements of radon and thoron activity each with 5-min integration time. The result was determined by taking the average of the second and third integrations. When the difference between these two was greater than 30% we repeated the measurement until the difference was reduced. Modified from Bonforte et al. (2013).

Barreca et al., 2013, and references therein) and dry fissures have often opened during important flank eruptions. However, these volcano-tectonic structures, or parts of them, are often buried by recent and historical lava flows, due to the high frequency of Etna eruptions and the large volumes of volcanic materials (especially tephra) emitted. In these cases, one can only guess the presence of such faults because of linear morphological flexures of the topographic surface. However, in recent decades a valid support to the identification of buried active faults has been provided by discrete surveys of in-soil radon performed with portable instruments. This approach was first tested in the field with measurements across already known tectonic systems (Chiodini et al., 1989; Badalamenti et al., 1994; Burton et al., 2004; Brogna et al., 2007; Giammanco et al., 2009; Siniscalchi et al., 2010), which provided objective evidence about the correspondence between radon anomalies and faults. After obtaining positive results with this method, in-soil radon surveys were carried out in areas apparently without evidence of tectonic dislocations on the surface, but marked by the presence of linear morphological flexures and/or characterized by numerous earthquake epicenters aligned along well-defined spatial directions, which suggested the presence of buried seismogenic faults (Neri et al., 2007, 2011, 2014; Morelli et al., 2011b; Bonforte et al., 2013; Johnová et al., 2014).

Two different types of in-soil radon measurements were used for discrete surveys: passive and spot (Figure 2). Passive measurements (only for ^{222}Rn) were performed using track detectors (SSNTD CR-39 type), while spot measurements (both for ^{222}Rn and ^{220}Rn) were made using an active portable device (model RAD7, Durridge COMPANY Inc., Bedford, United States). Moreover, in some cases (i.e., Giammanco et al., 2009; Bonforte et al., 2013) soil CO_2 effluxes were measured at the same sampling points of radon using the accumulation chamber method (Farrar et al., 1995; Chiodini et al., 1998). An example of an in-soil radon measurement profile is shown in Figure 6, that shows both ^{222}Rn and ^{220}Rn measurements performed along two profiles ~1,000–2000 m long: radon anomalies were found in correspondence of fault planes and they were always associated both with other soil gas anomalies (mostly CO_2) and with ground deformation observed from satellite (In-SAR) data. Also, the different ^{220}Rn/^{222}Rn ratios in soil gases would highlight different stress regimes in the surveyed faults driving the gas to the surface. Actually, faults characterized mostly if not exclusively by creep motion, thus producing constant fracturing in the shallow rocks, are associated with higher ^{220}Rn emissions compared to ^{222}Rn, due to the shorter half-life and hence shallower production source of the former (Burton et al., 2004).

Therefore, the radon surveys conducted on Etna showed that in-soil measurements can be a valid method to identify buried active and capable faults and to evaluate the state of stress of the tectonic structures under investigation (Burton et al., 2004; Neri et al., 2007; Neri et al., 2011; Neri et al., 2014; Bonforte et al., 2013; Johnová et al., 2014). Moreover, according to Burton et al. (2004), a high spatial resolution of radon sampling (sampling step of the order of some tenses of meters) is required to correctly map radon anomalies. The ability to identify and localize active faults using radon surveys at high spatial resolution has a strong impact on the assessment of the local risk posed by volcano-tectonic earthquakes (Brogna et al., 2007; La Delfa et al., 2008; Pellegriti et al., 2009; Neri et al., 2016).

Monitoring ^{220}Rn/^{222}Rn ratios in time along faults, if associated with concurrent soil CO_2 effluxes in the same sites, was found to be a proxy for the velocity of gas in the subsoil, which in turn is a function of the gas pressure in the volcanic system (Giammanco et al., 2007). Starting from the above assumptions, the temporal changes of a new parameter, named Soil Gas Disequilibrium Index, that incorporates the combination between CO_2 efflux and ^{220}Rn/^{222}Rn ratio, proved effective in detecting changes in the degassing regime inside Mt. Etna before eruptions (Giammanco and Sims, 2022).

In many cases, analysis of radionuclides concentration in rock samples was also undertaken in the radon survey areas (Seidel and Monnin, 1984; Condomines et al., 1995; Giammanco et al., 2009; Morelli et al., 2011a,b; Johnová et al., 2014; Catalano et al., 2015a,b; Neri et al., 2016) and in one case it was carried out in the same measuring points as the in-soil radon content, showing similar patterns of all parameters along the surveyed profiles (Johnová et al., 2014).

5.4 ^{222}Rn indoor

Since late 2007, continuous long-term (up to ~3 years) indoor radon monitoring was performed inside several buildings located in the Etna area at various altitudes (Figure 1; Brogna et al., 2007; Neri

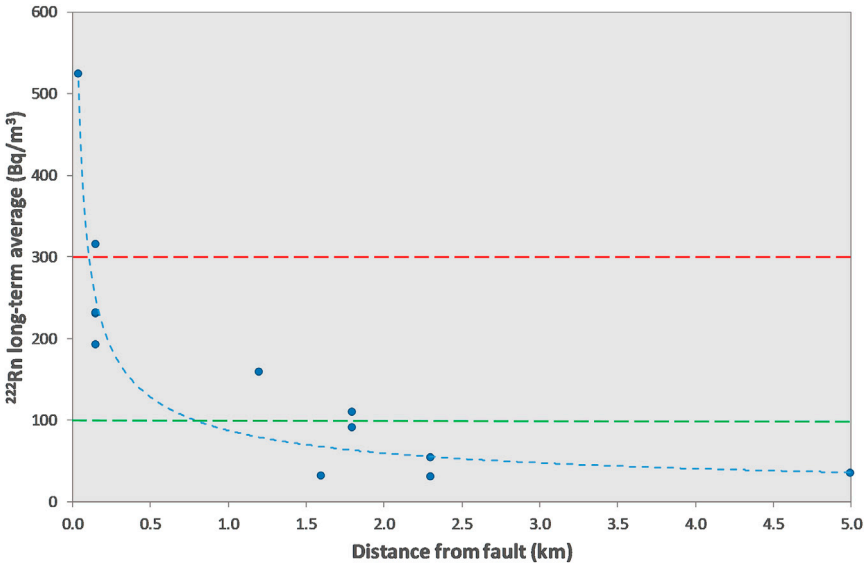

FIGURE 7
Spatial relationship between average radon indoor concentrations in houses of the southern and eastern flanks of Mt. Etna and distance from faults. The best fit model to the data (dashed blue line) follows a negative power law ($y = 3.928\ x^{-0.551}$; $R^2 = 0.8$). The dashed red line indicates the threshold value (300 Bq m^{-3}) recommended by WHO (2009), whereas the dashed green line indicates the attention threshold (100 Bq m^{-3}) suggested by WHO (2009). Modified from Neri et al. (2019).

et al., 2019), in order to evaluate the potential risk from radon pollution for the inhabitants, since radon is among the main causes of cancer of the respiratory system (Baxter, 1990; Muirhead, 1994; Baxter et al., 1999; Pellegriti et al., 2009; Rodríguez-Martínez et al., 2018). Recent studies (Darby et al., 2005; Health Protection Agency, 2009; WHO, 2009) suggest radon thresholds above which the probability of lung cancer incidence increases significantly. These thresholds correspond to 100 Bq m^{-3} (attention threshold) and to 300 Bq m^{-3} (maximum threshold recommended), both considered at an exposure time of 8 h. The starting hypothesis was that buildings placed near or on active faults are more exposed to indoor radon pollution, given the higher radon emission from faults as evidenced from in-soil radon surveys. Radon can spread from the fractured ground and diffuse into buildings mainly through their foundations, where they are in direct contact with the ground, being trapped inside the houses due to its high density.

A first study of indoor radon concentration was performed by Brogna et al. (2007), using an ionization chamber and carbon cylinders, making spot measurements in 150 sites of inhabited areas of the south-eastern slope of Mt. Etna. Higher ^{222}Rn concentrations were generally found in basements and ground floors, but the highest values were measured especially in houses built near or on faults, demonstrating that faulted areas are preferential pathways for radon migration through the ground and its emission at the surface, which in turn can cause indoor pollution.

La Delfa et al. (2012) monitored indoor radon in the east flank of Mt. Etna, near an active tectonic fault, and they found correlations between radon accumulation into buildings, type of construction materials and also Etna volcanic activity.

Neri et al. (2019) used a digital radon-monitor to measure alpha emissions with an Rn-accumulative method and their results confirmed those by Brogna et al. (2007). In particular, it was demonstrated that: i) the problem of indoor radon pollution in Etna buildings exists (indoor radon concentrations up to 3,549 Bq m^{-3} were found); ii) the most polluted buildings were those located near (from tens of meters to a few hundred meters) active and capable faults; iii) the distance of monitoring sites from faults was a key parameter in determining the accumulation of radon indoor (Figure 7), and iv) the construction features of the houses seemed to play an important role in the mitigation of indoor radon accumulation, even in the presence of intensely degassing soils.

The data acquired both by Brogna et al. (2007), La Delfa et al. (2012) and Neri et al. (2019) clearly show that it is necessary to deepen this type of study, extending the measurements of indoor radon to other, larger urban areas of Etna volcano, in order to evaluate in detail and monitor the health risk over the time for the population living on the volcano (about one million people).

6 Discussion and conclusive remarks

From the studies carried out so far on Mt. Etna, several important considerations can be outlined, which we have used to produce a comprehensive model that takes into account both the mechanisms of radon release from magma and its surrounding rocks and those of its transport to and accumulation at the surface (Figure 8).

First of all, radon parents in volcanic rocks are useful to reveal processes and evolutionary trends in the magmatic source underneath Mt. Etna; they also define the background radioactive levels that serve as the basis for the models of radon gas emission at the surface. In these senses, periodic analysis of radon and radionuclides contents in Etna lavas will certainly help monitor

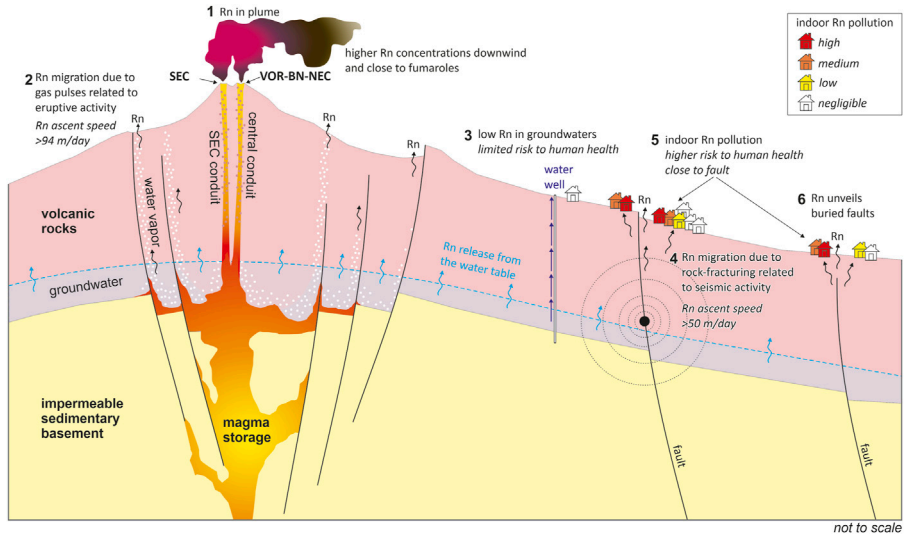

FIGURE 8
Comprehensive model of radon sources, mechanisms of transport and discharge at the surface and potential accumulation indoor at Mt. Etna.

possible long-term changes in the physical and chemical processes affecting the deep source of magma that feeds the volcano and/or to better understand shallower degassing processes the may occur within the conduits of Etna just before eruptions.

The radon emitted into the plume by the summit craters of Mt. Etna comes mainly from the outgassing of the magma residing both in the shallow magma chamber and in the overlying conduits that reach the topographic surface ("1" in Figure 8). High Rn concentrations in the air are found along the crater rims, especially near fumaroles and in downwind conditions. This produces a potential, albeit limited, risk to the health of people who constantly visit those areas and stand there for a long time (up to several hours), such as scientists, technicians working for the maintenance of volcanological equipment, volcanological and alpine guides who accompany tourists. Radon and its parents and daughters in summit crater gases help define the possible direct link of a specific crater conduit to the deep source of magma beneath the volcano and they allow for the determination of transfer times of gas from the magma reservoir to the surface, thus supporting volcano monitoring and surveillance techniques. To date, there is no continuous and prolonged measurement over time (many months, years) of radon concentration in the crater plume. It would, therefore, be useful to extend such measurements to long periods of time, so as to include more significant eruptive events than simple passive degassing. This requires equipping the measurement stations with real-time transmission systems, in order to give greater robustness to what has been observed and inferred up to now.

Magmatic outgassing in the summit area of Mt. Etna outside its open craters (>2,700 m a. s. l.) occurs mostly in diffuse form through the rocks where they are permeable to gas by porosity and/or by cracking. Radon laden magmatic gas thus reaches the surface mainly through structural discontinuities that intercept the magma ascent conduits. Such discontinuities on Mt. Etna are represented by eruptive fissures, faults, craters and caldera rims and they may also show intense fumarolic activity ("2" in Figure 8). Steam fumaroles could also occur due to the presence of a boiling shallow aquifer contained in the pile of volcanic rocks overlying the impermeable sedimentary basement. Groundwater is heated and partly vaporized near the magmatic conduits, triggering the rapid ascent of water vapor and other gases, mainly CO_2, that carry radon. By combining the $^{220}Rn/^{222}Rn$ ratio with the soil CO_2 efflux it is also possible to get information on the velocity/pressure of the gas system inside the volcano. The temporal monitoring of these parameters proved useful in revealing anomalies correlated with volcanic activity. However, although both radon and environmental data have been acquired for very long periods (several years, since 2005), until today the installed stations have not been capable of transmitting the data, a fact which limits the ability to fully exploit the potential of the acquired signals for monitoring and surveillance purposes.

In-soil radon monitoring stations located in the summit area can record the variations of the volcano's magmatic activity, and in particular those preceding explosive eruptions, more easily than elsewhere, as numerous studies have shown (Alparone et al., 2005; Neri et al., 2006; Neri et al., 2016; Giammanco et al., 2007; Falsaperla et al., 2014; Falsaperla et al., 2017). However, it has also been noted that in some cases significant increases in in-soil radon emissions occurred in the absence of visible volcanic activity on the surface, leading the phenomenon to variations in the level of magma in the central conduit of the volcano (Falsaperla et al., 2014), or to an interaction between seismic activity and movement of volcanic gases in the summit area (Falsaperla et al., 2017). In any case, it seems certain that a more rigorous understanding of radon variations can only be obtained through comparison of radon data with other types of signals acquired by seismic, deformation and gas monitoring networks. As stated above, an evident limit of the measurements carried out so far on Mt. Etna consists in the absence of automatic transmission systems of the data acquired by the radon stations installed. This allows only for an "*a posteriori*" data analysis, thus

nullifying the potential advantages deriving from following the signal variation trends and therefore the phenomena before and during their occurrence. Furthermore, for future monitoring, it will be essential to associate both radon and environmental sensors (temperature and atmospheric pressure) with the seismic and deformation stations installed in the summit area of the volcano, providing them with data transmission in order to allow for a real-time comparative analysis of all the signals acquired by the monitoring networks.

Radon in groundwaters is generally low, in contrast with the high uranium content in the volcanic host rocks, probably because of water thermalism that allows for a larger release of this gas from the water table, due to the inverse correlation between radon solubility and water temperature ("3" in Figure 8). This would also explain the high radon emissions in the subsurface soil and at the surface, because this radon would be produced both directly from the shallow rocks and also from the groundwater degassing.

Near-continuous monitoring of in-soil radon gas in stations located in the proximity (from tens to a few hundred meters) of active faults can anticipate the tectonic activity of those faults from a few weeks to a few hours, albeit with some limitations and uncertainties in the interpretation of the data ("4" in Figure 8). Indeed, in many cases the radon variations were recorded in the absence of subsequent or simultaneous seismic activity, demonstrating the current unreliability of the data in terms of seismic precursor. This unreliability decreases, however, when radon is analyzed in multi-parameter monitoring stations, i.e., when the radon signal can be directly compared with other geochemical and physical signals, which allows for a better understanding of the monitored phenomena. Therefore, also in this case the hope is to transform at least a part of the current seismic/geophysical stations installed on Mt. Etna into multi-parameter stations (in order to acquire also geochemical and environmental signals) capable of transmitting all signals in real-time.

In-soil radon surveys are extremely useful to find hidden or buried capable faults. In particular, the combined measurement both of ^{220}Rn and of ^{222}Rn allows to distinguish between deep-rooted faults, whose strain release works periodically with earthquakes, and shallow faults that are characterized by a more constant and weaker strain release through creeping ("5, 6" in Figure 8). The systematic application of in-soil radon measurements could, therefore, prove very useful when drawing up highly detailed geological maps, especially in places where recent lava flows hide surface evidence of tectonic structures, such as morphological steps or ground fractures.

Finally, indoor radon monitoring in the Mt. Etna area revealed several cases of houses with strong radon accumulation, well above the safety limits set according to the EU recommendations and regulations. Higher indoor radon levels were found generally in buildings located closer to faults and, for a specific building, during the winter period ("5, 6" in Figure 8). This means that, in future perspective, it would be useful to carry out preliminary in-soil radon degassing measurements both during general territorial planning studies and at a more detailed scale of each individual house or other building intended for human use (such as hospitals, schools, offices, etc.), in order to mitigate the risk of indoor radon pollution. The reduction of the health risk can be obtained through the implementation of adequate construction techniques, such as forced ventilation of the rooms, crawl spaces for ventilation of the foundations, laying of radon-proof coatings and sealing of cracks. The latter in particular is extremely necessary in the case of buildings located in areas with a high release of radon from the soil. Application and implementation of radon dispersion models both indoor and in the atmosphere, which is still to be done on Etna, will help assess the health hazard posed by potential accumulation of this gas into buildings and at the summit areas of the volcano (Josse et al., 2004; Zhang et al., 2021; Mancini et al., 2022).

Author contributions

SG and MN conceived the work and wrote the paper. PB described data on radon in groundwater, collected the literature cited and realized Figure 1. MN elaborated all the other Figures and the conceptual models. All authors listed have made a substantial, direct, and intellectual contribution to the work and approved it for publication.

Acknowledgments

The authors wish to thank SM and FD for their useful comments and suggestions.

Conflict of interest

The authors declare that the research was conducted in the absence of any commercial or financial relationships that could be construed as a potential conflict of interest.

Publisher's note

References

Aiuppa, A., Allard, P., D'Alessandro, W., Michel, A., Parello, F., Treuil, M., et al. (2000). Mobility and fluxes of major, minor and trace metals during basalt weathering and groundwater transport at Mt. Etna volcano (Sicily). *Geochim. Cosmochim. Acta* 64, 1827–1841. doi:10.1016/S0016-7037(00)00345-8

Allard, P., Aiuppa, A., Bani, P., Métrich, N., Bertagnini, A., Gauthier, P. .-J., et al. (2016). Prodigious emission rates and magma degassing budget of major, trace and radioactive volatile species from Ambrym basaltic volcano, Vanuatu island Arc. *J. Volcanol. Geotherm. Res.* 322, 119–143. doi:10.1016/j.jvolgeores.2015.10.004

Alparone, S., Behncke, B., Giammanco, S., Neri, M., and Privitera, E. (2005). Paroxysmal summit activity at Mt. Etna (Italy) monitored through continuous soil radon measurements. *Geophys. Res. Lett.* 32, L16307. doi:10.1029/2005GL023352

Auvinen, A., Salonen, L., Pekkanen, J., Pukkala, E., Ilus, T., and Kurttio, P. (2005). Radon and other natural radionuclides in drinking water and risk of stomach cancer: A case-cohort study in Finland. *Int. J. Cancer* 114, 109–113. doi:10.1002/ijc.20680

Badalamenti, B., Capasso, G., Carapezza, M. L., D'Alessandro, W., Di Ganci, F., Diliberto, I. S., et al. (1994). Soil gases investigations during the 1991–92 Etna eruption. *Acta Vulcanol.* 4, 135–141.

Barreca, G., Bonforte, A., and Neri, M. (2013). A pilot gis database of active faults of Mt. Etna (sicily): A tool for integrated hazard evaluation. *J. Volcanol. Geotherm. Res.* 251, 170–186. doi:10.1016/j.jvolgeores.2012.08.013

Baxter, P. J., Baudron, J. C., and Coutinho, R. (1999). Health hazards and disaster potential of ground gas emissions at Furnas volcano, Sao Miguel, Azores. *J. Volcanol. Geotherm. Res.* 92, 95–106. doi:10.1016/S0377-0273(99)00070-0

Baxter, P. J. (1990). Medical effects of volcanic eruptions: 1. Main causes of death and injury. *Bull. Volcanol.* 52, 532–544. doi:10.1007/BF00301534

Bonforte, A., Federico, C., Giammanco, S., Guglielmino, F., Liuzzo, M., and Neri, M. (2013). Soil gases and SAR measurements reveal hidden faults on the sliding flank of Mt. Etna (Italy). *J. Volcanol. Geotherm. Res.* 251, 27–40. doi:10.1016/j.jvolgeores.2012.08.010

Branca, S., Coltelli, M., and Groppelli, G. (2011). Geological evolution of a complex basaltic stratovolcano: Mount Etna. *Italy. Ital. J. Geosci.* 130. doi:10.3301/IJG.2011.13

Brogna, A., La Delfa, S., La Monaca, V., Lo Nigro, S., Morelli, D., Patane', G., et al. (2007). Measurements of indoor radon concentration on the south-eastern flank of Mount Etna volcano (Southern Italy). *J. Volcanol. Geotherm. Res.* 165, 71–75. doi:10.1016/j.jvolgeores.2007.04.012

Burton, M., Neri, M., and Condarelli, D. (2004). High spatial resolution radon measurements reveal hidden active faults on Mt. Etna: Radon Measurements Reveal Faults on Etna. *Mt. Etna. Geophys. Res. Lett.* 31. doi:10.1029/2003GL019181

Capaldi, G., Cortini, M., Gasparini, P., and Pece, R. (1976). Short-lived radioactive disequilibria in freshly erupted volcanic rocks and their implications for the preeruption history of a magma. *J. Geophys. Res.* 81, 350–358. doi:10.1029/jb081i002p00350

Catalano, R., Immé, G., Mangano, G., Morelli, D., Aranzulla, M., Giammanco, S., et al. (2015b). *In situ* and laboratory measurements for radon transport process study. *J. Radioanal. Nucl. Chem.* 306, 673–684. doi:10.1007/s10967-015-4336-6

Catalano, R., Immé, G., Mangano, G., Morelli, D., and Aranzulla, M. (2015a). Radon transport: Laboratory and model study. *Radiat. Prot. Dosim.* 164, 575–581. doi:10.1093/rpd/ncv314

Chiodini, G., Cioni, R., Guidi, M., Raco, B., and Marini, L. (1998). Soil CO_2 flux measurements in volcanic and geothermal areas. *Appl. Geochem.* 13, 543–552. doi:10.1016/S0883-2927(97)00076-0

Chiodini, G., Cioni, R., Pescia, A., Ponziani, F., Raco, B., and Taddeucci, G. (1989). Eruzione dell'Etna nell'autunno 1989: H_2, CO e ^{222}Rn nei gas del suolo in prossimità della frattura apertasi sul versante meridionale del vulcano. *Boll. del Grup. Naz. Vulcanol.* 1, 177–187.

Clocchiatti, R., Condomines, M., Guénot, N., and Tanguy, J. C. (2004). Magma changes at mount Etna: The 2001 and 2002-2003 eruptions. *Earth Planet. Sci. Lett.* 226, 397–414. doi:10.1016/j.epsl.2004.07.039

Condomines, M., Tanguy, J. C., and Michaud, V. (1995). Magma dynamics at Mt Etna: Constraints from U-Th-Ra-Pb radioactive disequilibria and Sr isotopes in historical lavas. *Earth Planet. Sci. Lett.* 132, 25–41. doi:10.1016/0012-821X(95)00052-E

Cothern, C. R., Lappenbusch, W. L., and Michel, J. (1986). Drinking-water contribution to natural background radiation. *Health Phys.* 50, 33–47. doi:10.1097/00004032-198601000-00002

D'Alessandro, W., and Vita, F. (2003). Groundwater radon measurements in the Mt. Etna area. *J. Environ. Radioact.* 65, 187–201. doi:10.1016/S0265-931X(02)00096-6

Darby, S., Hill, D., Auvinen, A., Barros-Dios, J. M., Baysson, H., Bochicchio, F., et al. (2005). Radon in homes and risk of lung cancer: Collaborative analysis of individual data from 13 European case-control studies. *Br. Med. J.* 330, 223. doi:10.1136/bmj.38308.477650.63

Falsaperla, S., Behncke, B., Langer, H., Neri, M., Salerno, G. G., Giammanco, S., et al. (2014). Failed" eruptions revealed by pattern classification analysis of gas emission and volcanic tremor data at Mt. Etna, Italy. *Int. J. Earth Sci.* 103, 297–313. doi:10.1007/s00531-013-0964-7

Falsaperla, S., Neri, M., Di Grazia, G., Langer, H., and Spampinato, S. (2017). What happens to in-soil radon activity during a long-lasting eruption? Insights from Etna by multidisciplinary data analysis. *Geochem. Geophys. Geosystems* 18, 2162–2176. doi:10.1002/2017GC006825

Farrar, C. D., Sorey, M. L., Evans, W. C., Howle, J. F., Kerr, B. D., Kennedy, B. M., et al. (1995). Forest-killing diffuse CO_2 emission at Mammoth Mountain as a sign of magmatic unrest. *Nature* 376, 675–678. doi:10.1038/376675a0

Fiore, M., Ledda, C., Conti, G. O., Fallico, R., Sciacca, S., and Ferrante, M. (2011). Radon monitoring in groundwater from the Mt. Etna area. *ISEE Conf. Abstr.* 2011. doi:10.1289/isee.2011.01783

Galli, G., Mancini, C., and Quattrocchi, F. (2000). Groundwater, radon continuous monitoring system (α -scintillation counting) for natural hazard surveillance. *Pure Appl. Geophys.* 157, 407–433. doi:10.1007/s000240050006

Gauthier, P. J., Le Cloarec, M. F., and Condomines, M. (2000). Degassing processes at Stromboli volcano inferred from short-lived disequilibria (^{210}Pb-^{210}Bi-^{210}Po) in volcanic gases. *J. Volcanol. Geotherm. Res.* 102, 1–19. doi:10.1016/S0377-0273(00)00179-7

Giammanco, S., Immè, G., Mangano, G., Morelli, D., and Neri, M. (2009). Comparison between different methodologies for detecting radon in soil along an active fault: The case of the Pernicana fault system, Mt. Etna (Italy). *Appl. Radiat. Isot.* 67, 178–185. doi:10.1016/j.apradiso.2008.09.007

Giammanco, S., and Sims, K. W. W. (2022). "Monitoring volcanic activity through combined measurements of CO_2 efflux and (^{222}Rn) and (^{220}Rn) in soil gas," in *Isotopic constraints on earth system processes*. Editors K. W. W. Sims, K. Maher, and D. P. Schrag (United States: Wiley), 167–202. doi:10.1002/9781119595007.ch7

Giammanco, S., Sims, K. W. W., and Neri, M. (2007). Measurements of ^{220}Rn and ^{222}Rn and CO_2 emissions in soil and fumarole gases on Mt. Etna volcano (Italy): Implications for gas transport and shallow ground fracture. *Geochem. Geophys. Geosystems* 8. doi:10.1029/2007GC001644

Grasty, R. (1997). Radon emanation and soil moisture effects on airborne gamma-ray measurements. *Geophys* 62, 1379–1385. doi:10.1190/1.1444242

Health Protection Agency (2009). *Radon and public health—report of the independent advisory Group on ionizing radiation*. England: Documents of the Health Protection Agency.

İçhedef, M., Giammanco, S., Neri, M., Catalano, R., Immé, G., Morelli, D., et al. (2020). In soil radon anomalies and volcanic activity on Mt. Etna (Italy). *J. Environ. Radioact.* 218, 106267. doi:10.1016/j.jenvrad.2020.106267

Immè, G., Catalano, R., Mangano, G., and Morelli, D. (2014). Radon exhalation measurements for environmental and geophysics study. *Radiat. Phys. Chem.* 95, 349–351. doi:10.1016/j.radphyschem.2013.02.033

Immè, G., La Delfa, S., Lo Nigro, S., Morelli, D., and Patanè, G. (2005). Gas radon emission related to geodynamic activity on. *Mt. Etna. Ann. Geophys.* 48. doi:10.4401/ag-3180

Immè, G., La Delfa, S., Lo Nigro, S., Morelli, D., and Patanè, G. (2006a). Soil radon concentration and volcanic activity of Mt. Etna before and after the 2002 eruption. *Radiat. Meas.* 41, 241–245. doi:10.1016/j.radmeas.2005.06.008

Immè, G., La Delfa, S., Lo Nigro, S., Morelli, D., and Patanè, G. (2006b). Soil radon monitoring in the NE flank of Mt. Etna (Sicily). *Appl. Radiat. Isot.* 64, 624–629. doi:10.1016/j.apradiso.2005.12.007

Immè, G., and Morelli, D. (2012). "Radon survey in active volcanoes," in *Handbook of radon: Properties, applications and health*. Editors Z. Li and C. Feng (New York: Nova Science Publishers Inc.), 405–416.

Jobbágy, V., Altzitzoglou, T., Malo, P., Tanner, V., and Hult, M. (2017). A brief overview on radon measurements in drinking water. *J. Environ. Radioact.* 173, 18–24. doi:10.1016/j.jenvrad.2016.09.019

Johnová, K., Thinová, L., and Giammanco, S. (2014). Revealing the hidden faults in the SE flank of Mt. Etna using radon in-soil gas measurement. *Radiat. Prot. Dosim.* 160, 70–73. doi:10.1093/rpd/ncu092

Josse, B., Simon, P., and Peuch, V.-H. (2004). Radon global simulations with the multiscale chemistry and transport model MOCAGE. *Tellus B Chem. Phys. Meteorol.* 56, 339. doi:10.3402/tellusb.v56i4.16448

Kozłowska, B., Morelli, D., Walencik, A., Dorda, J., Altamore, I., Chieffalo, V., et al. (2009). Radioactivity in waters of Mt. Etna (Italy). *Radiat. Meas.* 44, 384–389. doi:10.1016/j.radmeas.2009.05.002

Kozłowska, B., Walencik-łata, A., Giammanco, S., Immè, G., Catalano, R., and Mangano, G. (2019). Radioactivity content in volcanic rocks and radionuclides transfer from rocks to groundwater at Mt. Etna volcano. *Ann. Geophys.* 62. doi:10.4401/ag-7549

Kozłowska, B., Walencik-Łata, A., Immè, G., Catalano, R., Mangano, G., Morelli, D., et al. (2016). Natural radioactivity content in groundwater of Mt. Etna's eastern flank and gamma background of surrounding rocks. *Ann. Geophys.* 59. doi:10.4401/ag-6799

La Delfa, S., Agostino, I., Morelli, D., and Patanè, G. (2008). Soil radon concentration and effective stress variation at Mt. Etna (Sicily) in the period January 2003-April 2005. *Radiat. Meas.* 43, 1299–1304. doi:10.1016/j.radmeas.2008.02.004

La Delfa, S., Immè, G., Lo Nigro, S., Morelli, D., Patanè, G., and Vizzini, F. (2007). Radon measurements in the SE and NE flank of Mt. Etna (Italy). *Radiat. Meas.* 42, 1404–1408. doi:10.1016/j.radmeas.2007.06.004

La Delfa, S., Vizzini, F., and Patanè, G. (2010). Identification of radon anomalies at Mt. Etna (sicily) by using three different methods. *Environ. Semeiot.* 3, 1–16. doi:10.3383/es.3.1.1

La Delfa, S., Vizzini, F., and Patanè, G. (2012). Radon migration into different building types at medium and low south-eastern flank of Mt Etna (Sicily): Connection with the volcanic activity. *Environ. Earth Sci.* 66, 923–931. doi:10.1007/s12665-011-1302-7

Lambert, G., Bristeau, P., and Polian, G. (1976). Emission and enrichments of radon daughters from Etna Volcano magma. *Geophys. Res. Lett.* 3, 724–726. doi:10.1029/GL003i012p00724

Le Cloarec, M. F., Pennisi, M., Ardouin, B., Roulley, J. C. L., and Lambert, G. (1988). Relationship between gases and volcanic activity of Mount Etna in 1986. *J. Geophys. Res.* 93, 4477–4484. doi:10.1029/jb093ib05p04477

Le Cloarec, M. F., and Pennisi, M. (2001). Radionuclides and sulfur content in Mount Etna plume in 1983-1995: New constraints on the magma feeding system. *J. Volcanol. Geotherm. Res.* 108, 141–155. doi:10.1016/S0377-0273(00)00282-1

Mancini, S., Vilnitis, M., Todorović, N., Nikolov, J., and Guida, M. (2022). Experimental studies to test a predictive indoor radon model. *Int. J. Environ. Res. Public Health* 19, 6056. doi:10.3390/ijerph19106056

Marty, B., and Le Cloarec, M. F. (1992). Helium-3 and CO_2 fluxes from subaerial volcanoes estimated from polonium-210 emissions. *J. Volcanol. Geotherm. Res.* 53, 67–72. doi:10.1016/0377-0273(92)90074-N

Morelli, D., Di Martino, S., Immè, G., La Delfa, S., Lo Nigro, S., and Patanè, G. (2006). Evidence of soil radon as tracer of magma uprising in Mt. Etna. *Etna. Radiat. Meas.* 41, 721–725. doi:10.1016/j.radmeas.2006.04.026

Morelli, D., Immé, G., Altamore, I., Aranzulla, M., Cammisa, S., Catalano, R., et al. (2011a). "Radiation measurements as tool for environmental and geophysics studies on volcano-tectonic areas," in *Nuovo cimento della Società italiana di Fisica C* (Italy: Società Italiana Di Fisica), 155–165. doi:10.1393/ncc/i2011-10823-0

Morelli, D., Immè, G., Altamore, I., Cammisa, S., Giammanco, S., La Delfa, S., et al. (2011b). Radionuclide measurements, via different methodologies, as tool for geophysical studies on Mt. Etna. *Nucl. Instrum. Methods Phys. Res. Sect. A Accel. Spectrom. Detect. Assoc. Equip.* 652, 911–914. doi:10.1016/j.nima.2011.01.172

Muirhead, C. R. (1994). Radon risks. *Lancet* 344, 143–144. doi:10.1016/S0140-6736(94)92751-0

Neri, M., Behncke, B., Burton, M., Galli, G., Giammanco, S., Pecora, E., et al. (2006). Continuous soil radon monitoring during the July 2006 Etna eruption. *Geophys. Res. Lett.* 33, L24316. doi:10.1029/2006GL028394

Neri, M., Ferrera, E., Giammanco, S., Currenti, G., Cirrincione, R., Patanè, G., et al. (2016). Soil radon measurements as a potential tracer of tectonic and volcanic activity. *Sci. Rep.* 6, 24581. doi:10.1038/srep24581

Neri, M., Ferrera, E., Giammanco, S., Patanè, G., and Zanon, V. (2014). Un metodo per riconoscere faglie attive sepolte mediante misure areali di radon dal suolo. *Geol. dell'Ambiente ISSN* 1591-5352, 1–8.

Neri, M., Giammanco, S., Ferrera, E., Patanè, G., and Zanon, V. (2011). Spatial distribution of soil radon as a tool to recognize active faulting on an active volcano: The example of Mt. Etna (Italy). *J. Environ. Radioact.* 102, 863–870. doi:10.1016/j.jenvrad.2011.05.002

Neri, M., Giammanco, S., and Leonardi, A. (2019). Preliminary indoor radon measurements near faults crossing urban areas of Mt. Etna volcano (Italy). *Front. Public Heal.* 7, 105. doi:10.3389/fpubh.2019.00105

Neri, M., Guglielmino, F., and Rust, D. (2007). Flank instability on Mount Etna: Radon, radar interferometry, and geodetic data from the southwestern boundary of the unstable sector. *J. Geophys. Res. Solid Earth* 112. doi:10.1029/2006JB004756

Pellegriti, G., De Vathaire, F., Scollo, C., Attard, M., Giordano, C., Arena, S., et al. (2009). Papillary thyroid cancer incidence in the volcanic area of Sicily. *J. Natl. Cancer Inst.* 101, 1575–1583. doi:10.1093/jnci/djp354

Pinault, J. L., and Baubron, J. C. (1996). Signal processing of soil gas radon, atmospheric pressure, moisture, and soil temperature data: A new approach for radon concentration modeling. *J. Geophys. Res. Solid Earth* 101, 3157–3171. doi:10.1029/95jb03121

Quattrocchi, F., Di Stefano, G., Pizzino, L., Pongetti, F., Romeo, G., Scarlato, P., et al. (2000). Geochemical Monitoring System II prototype (GMS II) installation at the "Acqua Difesa" well, within the Etna region: First data during the 1999 volcanic crisis. *J. Volcanol. Geotherm. Res.* 101, 273–306. doi:10.1016/S0377-0273(00)00177-3

Rodríguez-Martínez, A., Torres-Durán, M., Barros-Dios, J. M., and Ruano-Ravina, A. (2018). Residential radon and small cell lung cancer. A systematic review. *Cancer Lett.* 426, 57–62. doi:10.1016/j.canlet.2018.04.003

Seidel, J. L., and Monnin, M. (1984). Mesures de Radon-222 dans le sol de l'Etna (sicile): 1980-1983. *Bull. Volcanol.* 47, 1071–1077. doi:10.1007/BF01952363

Siniscalchi, A., Tripaldi, S., Neri, M., Giammanco, S., Piscitelli, S., Balasco, M., et al. (2010). Insights into fluid circulation across the Pernicana Fault (Mt. Etna, Italy) and implications for flank instability. *J. Volcanol. Geotherm. Res.* 193, 137–142. doi:10.1016/j.jvolgeores.2010.03.013

Terray, L., Gauthier, P. J., Breton, V., Giammanco, S., Sigmarsson, O., Salerno, G., et al. (2020a). Radon activity in volcanic gases of Mt. Etna by passive dosimetry. *J. Geophys. Res. Solid Earth* 125. doi:10.1029/2019JB019149

Terray, L., Gauthier, P. J., Salerno, G., Caltabiano, T., La Spina, A., Sellitto, P., et al. (2018). A new degassing model to infer magma dynamics from radioactive disequilibria in volcanic plumes. *Geosci* 8, 27. doi:10.3390/geosciences8010027

Terray, L., Royer, L., Sarramia, D., Achard, C., Bourdeau, E., Chardon, P., et al. (2020b). From sensor to cloud: An IoT network of radon outdoor probes to monitor active volcanoes. *Sensors Switz.* 20, 2755. doi:10.3390/s20102755

Vaupotič, J., Žvab, P., and Giammanco, S. (2010). Radon in outdoor air in the Mt. Etna area. *Italy. Nukl.* 55, 573–577.

Vizzini, F., and Brai, M. (2012). In-soil radon anomalies as precursors of earthquakes: A case study in the SE slope of Mt. Etna in a period of quite stable weather conditions. *J. Environ. Radioact.* 113, 131–141. doi:10.1016/j.jenvrad.2012.05.027

WHO (2017). *Guidelines for drinking water quality*. Switzerland: World Health Organization.

WHO (2009). *WHO handbook on indoor radon: A public health*. Switzerland: World Health Organization.

Wilhelm, E., Battino, R., and Wilcox, R. J. (1977). Low-pressure solubility of gases in liquid water. *Chem. Revs.* 77, 219–262. doi:10.1021/cr60306a003

Woith, H. (2015). Radon earthquake precursor: A short review. *Eur. Phys. J. Spec. Top.* 224, 611–627. doi:10.1140/epjst/e2015-02395-9

Zhang, B., Liu, H., Crawford, J. H., Chen, G., Fairlie, T. D., Chambers, S., et al. (2021). Simulation of radon-222 with the GEOS-chem global model: Emissions, seasonality, and convective transport. *Atmos. Chem. Phys.* 21, 1861–1887. doi:10.5194/acp-21-1861-2021

frontiers | Frontiers in Earth Science

TYPE Review
PUBLISHED 25 August 2023
DOI 10.3389/feart.2023.1142649

OPEN ACCESS

EDITED BY
João Pedro Coelho,
University of Aveiro, Portugal

REVIEWED BY
Martin F. Soto-Jimenez,
National Autonomous University of Mexico, Mexico
Jorge Eduardo Marcovecchio, Instituto Argentino de Oceanografia (CONICET/UNS), Argentina

*CORRESPONDENCE
Rozane Valente Marins,
rmarins@ufc.br

RECEIVED 11 January 2023
ACCEPTED 26 July 2023
PUBLISHED 25 August 2023

CITATION
Santos TTL, Marins RV and Alves LP (2023), Review on metal contamination in equatorial estuaries in the Brazilian Northeast.
Front. Earth Sci. 11:1142649.
doi: 10.3389/feart.2023.1142649

Review on metal contamination in equatorial estuaries in the Brazilian Northeast

Thays Thayanne Luz Santos, Rozane Valente Marins* and Letícia Paulino Alves

Laboratory of Coastal Biogeochemistry (LBC), Institute of Marine Sciences (LABOMAR), Universidade Federal do Ceará, Fortaleza, Brazil

The present study provides an overview and assessment of the metals and trace metals registered in water, sediment, and biota in estuaries of the Equatorial Zone of the Brazilian Northeast (EZBN). The study aims to compare the degree of contamination and highlight necessary complementary research. The EZBN is characterized by the transition between the humid and hot Amazonian climate and the hot and dry semiarid climate. The spatial distribution identified enrichment for Cu, Pb, Zn, Hg, and Fe in the sediment, and sequential extraction of metals suggested low to medium mobility of metals along the environments. The Parnaíba River Delta, Curimataú, and the Anil and Bacanga estuaries were the environments with the lowest sediment quality for Pb, Zn, Cu, and Fe, identified by the geoaccumulation index (Igeo). The deposits in these estuaries were related to anthropogenic contributions from domestic sewage and inadequate disposal of wastewater from shrimp farms. However, more studies to determine the natural background levels based on sediment cores and metal speciation are necessary to better differentiate between natural and anthropic sources. Oysters, carnivorous fishes, and crustaceans had the best feedback as biomonitors for Cu, Pb, Zn, and Hg, but the application of biomonitoring needs to be expanded and maintained so that the potential for environmental degradation, which can have significant consequences both for the ecosystem and for human health, can be closely monitored in the EZBN estuaries.

KEYWORDS

sediments, sequential extraction, estuarine waters, biomonitor, Igeo accumulation index

1 Introduction

An estuary is a good example of a coupled system that can balance physical, chemical, and biotic components, and that consists of several subsystems intertwined and influenced by the seawater flow. Estuaries provide goods and services that are economically and ecologically indispensable as well as support the establishment of economic activities. However, to fully characterize environmental impacts in estuaries, activities located at the drainage basin upstream of the estuary need to be considered because their magnitude and changing nature can impact the support capacity of estuarine ecosystems (Santana et al., 2015). Local and upper drainage basin discharges from anthropogenic activities deposit many substances in estuaries, including trace metals. Most trace metal contamination causes serious environmental problems globally because of their toxicity, non-biodegradable properties, and accumulation and biomagnification in the food chain (Barletta et al., 2019). When contaminants enter estuaries, they can adsorb onto suspended particles,

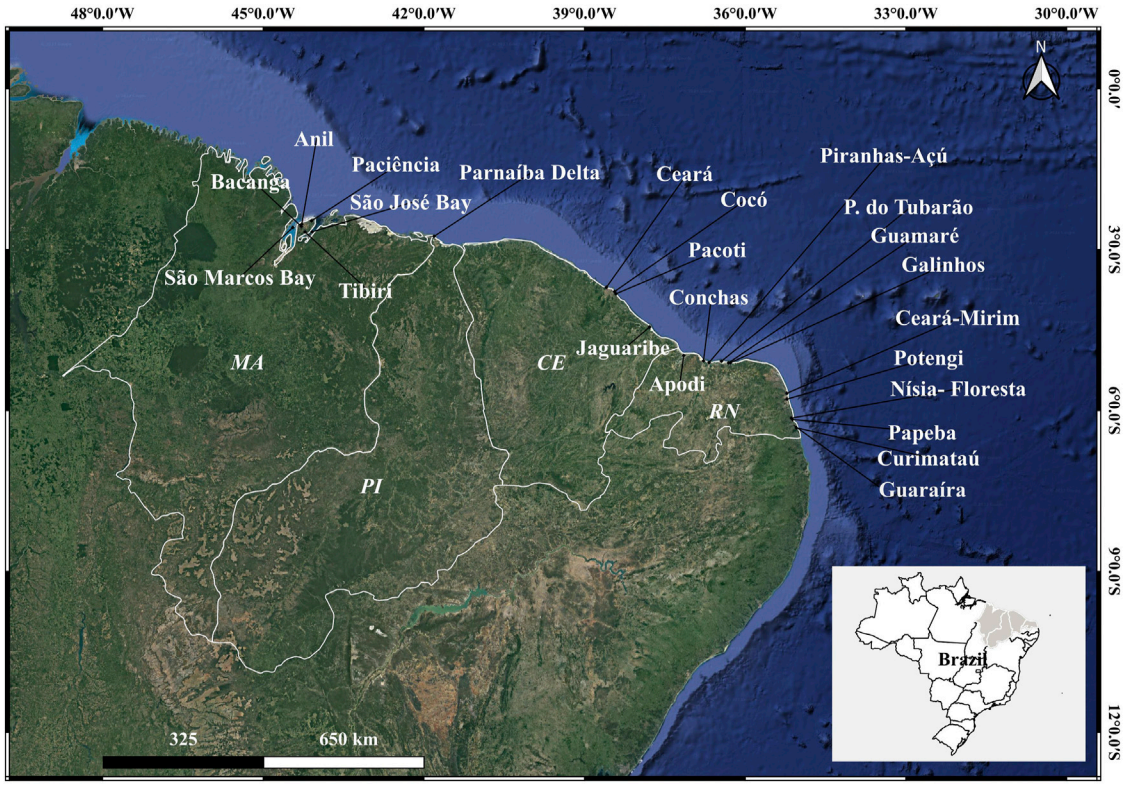

FIGURE 1
Location map of the 23 estuaries evaluated in the Equatorial Zone of the Brazilian Northeast (EZBN).

form complexes, and settle on surface sediments, where they reach contents high enough to become a risk to aquatic life (Buruaem et al., 2012; Silva et al., 2015).

There are few studies dealing with trace metal contamination in the Equatorial Zone of the Brazilian Northeast (EZBN) that characterize and quantify major sources, the spatial and temporal variability of trace metals in compartments of the estuarine environment, and the eventual risk to the biota. The present article will focus on the EZBN including the states of Maranhão (MA), Piauí (PI), Ceará (CE) and the Rio Grande do Norte (RN). This region includes more than 88 cities, totaling approximately 7.9 million inhabitants, with 85.1% of the population in urban regions and 14.9% in rural areas (IBGE, 2020).

The objective of the present study is to provide an overview of metals (Al, Fe, Mn, As, Ba, Cd, Co, Cr, Cu, Hg, Ni, Pb, Sn, and Zn) of environmental interest and the biogeochemical processes influencing their fate in water, sediment, and biota as a biomonitor, as reported previously in published research, including monographs, dissertations, thesis, scientific articles, and information from regional environmental protection agencies, in estuarine environments of the EZBN. This review identifies metal contaminations, highlights future complementary studies, and suggests necessary complementary research. The data collected are from 23 estuaries situated near the major coastal cities in the EZBN, that presents different socio-economic activities.

2 Environmental setting

The EZBN comprises the region located between 1°5′S and 46°1′W to 6°30S and 34°58′W (Figure 1). It is characterized by the transition from the humid and hot Amazonian climate to the hot and dry semiarid climate, with average annual temperatures ranging from 18.4oC to 34.9°C, considering all the EZBN and data from 1981 to 2010 (MMA, 2006; INMET, 2019). Precipitation in this region is influenced by the migration of the Intertropical Convergence Zone (ITCZ), El Niño, La Niña, and by the action of the trade winds from the Atlantic Ocean, which define the seasonal rainy and dry periods (Polzin and Hastenrath, 2014). The Amazonian region is very well-defined, with high precipitation from January to June and low precipitation from July to December, while the semiarid region shows a short rainy season from February to May and a longer dry season from June to January. There is a west-east decrease in the average accumulated rainfall along the coast with the state of MA exhibiting an average accumulated rainfall of 1,599 mm (1,177 to 2,200 mm), the state of PI 1,007 mm (635–1,423 mm), the state of CE 969 mm (599–1,669 mm), and the state of RN 904 mm (518–1,721 mm) between 1981 to 2010 (FUNCEME, 2019; INMET, 2020). Carvalho et al. (2020) detected a reduction in the number of rainy days in Northeastern Brazil in the past 30 years. For example, in Fortaleza, the capital of the state of Ceará, an annual decrease of 19 days of rain has been recorded during this period. In addition, the change in the rainfall distribution has an impact on the

occurrence of extreme events, such as drought and floods, in the EZBN, which has witnessed an increase both in frequency and extension of extreme events (Lacerda et al., 2020).

The semidiurnal tidal regime is characteristic of the coastal environments of the EZBN with amplitudes varying from macro tidal, as observed in the coast of MA (0.2–7.3 m), to mesotidal regimes found in PI (0.5–4.0 m), CE (0.6–3.5 m) and RN (0.1–3.9 m) (CHN, 2019). Tidal variation along the EZBN can influence the morphology and hydrodynamics of the coast, as well as the dispersion of sediments and contaminants (Landim et al., 2005; Aquino da Silva et al., 2019). The coastline has 1,689 km in extension, composed of complex ecosystems such as sandy beaches, mangroves, estuaries, bays, and one of the largest open-sea deltas of the Americas and the third largest in the world, the Parnaiba River Delta, which suffers periodical seawater intrusion (Paula Filho et al., 2015; Souza Silva et al., 2015). The state of Maranhão harbors the largest continuous range of protected mangroves in the world with three dominant mangrove genera: *Rhizophora, Laguncularia*, and *Avicennia.* Mangroves in the EZBN cover a total area of approximately 544,100 ha, representing 38.9% of Brazilian mangroves, and serve as the greatest natural source of organic matter (OM) for the aquatic system (ICMBio, 2018; Mounier et al., 2018).

The geology comprises several lithostratigraphic units, and the diabase dikes and sedimentary basins of the MA coastline belong to the Pre-Cambrian to the Cenozoic, with Codó, Grajaú, Itapecuru, Pirabas, and Barreira's formations (El-Robrini et al., 2006). The state of Ceará has geological characteristics from the Pleistocene to the Holocene, compounded by the Barreiras, Camocim, and Serra Grande formations (Morais et al., 2006). The geology of the state of RN consists of sedimentary rocks of the Cretaceous age, which are covered by rocks of the Barreiras Formation and Quaternary sediments (Vital et al., 2006). The driest region of the EZBN has scarce water resources and marked climatic seasonality, resulting in the presence of 235 medium to large artificial reservoirs with storage capacities varying from 571 to 18.738 hm^3; 66% of the total number of reservoirs in the EZBN are located in the state of CE (IBGE, 2020). Besides the benefits of water supply or for the generation of electric energy, these dams decrease the water and material discharge from the continent to coastal environments, altering estuarine ecosystems (Marins et al., 2003; Dias et al., 2013; Diasda et al., 2016).

3 Major anthropogenic sources of trace metals in the EZBN

Most trace metals derive from igneous rocks, simply based on the relative fraction of igneous rocks in comparison with sedimentary and metamorphic rocks in the Earth's crust. However, the EBZN shows a predominance of sedimentary and metamorphic rocks in the continent and consequently, the continental shelf differs from other Brazilian regions where igneous rocks predominate (Aguiar et al., 2014). Resuspension of soil particles by winds, salt spray, forest fires, and soil and surface runoff are among the drivers that can contribute to the natural emissions of trace metals to watersheds of rivers and potentially affect metal content in the coastal ecosystems (Marins et al., 2004; Bianchi, 2007).

The contamination process began with anthropic activities that expanded significantly as urbanization and industry increased, and the consequent rise of energy and raw materials consumption, frequently associated with deforestation and conversion of natural areas into urban regions, remobilizing soils (Oliveira and Marins, 2011).

According to Soares et al. (2021), the Brazilian semi-arid coast is one of the most densely populated areas globally. For this reason, there are many activities, such as industries, agriculture, mining operations, and aquaculture, located in coastal and adjacent areas to supply the population's needs (Pinheiro et al., 2008; Lacerda et al., 2011; Soares, 2011). Only approximately 46% of northeastern households have a domestic sewage collection network, with the states of PI and MA having the lowest percentages, 4.5% and 6.5%, respectively (IBGE, 2020). The discharge of domestic sewage and solid wastes *in natura* carries several pollutants into water bodies. Other main economic activities in the area are civil construction and industrial utilities, including pulp and paper industry, food, leather and footwear, oil and natural gas extraction, metallurgy, and the production of oil and biofuels (CNI, 2019).

Harbor activities have great economic importance in the exportation of iron ore and pellets, manganese, ferroalloys, fertilizers, oil and byproducts, wheat, and salt. Major harbors in the EZBN are Itaqui (MA), Fortaleza and Pecém (CE), and Natal and the Terminal Salineiro de Areia Branca (RN) (Lima, 1999; González-Gorbena et al., 2015). According to the National Socioeconomic Development Bank of Brazil (BNDES), the coasts of the states of CE and RN do not have many natural conditions for the implementation of new harbors due to sheltered areas and bays or estuaries with deep waters. Therefore, the Itaqui harbor (MA) is the only one located in a deep, sheltered area in São Marcos Bay (MA), and the other harbors are positioned in the open sea or offshore to receive large cargo ships, while the small estuaries allow docking of smaller fishing and tourism boats (Lima, 1999). This activity is a potential source of trace metals due to accidents with the spillage products during the loading and unloading into aquatic systems. For example, 92% of the cargo handled in the Itaqui harbor, which is the second largest in terms of tons handled in the country, corresponds to bulk ore. Harbor operation, in particular dredging to increase the depth of the navigation channels, can resuspend deposited metals from the bottom, increasing their bioavailability, as demonstrated in the Mucuripe Harbor, CE state (Maia, 2004; Lacerda et al., 2019; Moreira et al., 2021).

Another potential source of trace metals is shrimp farming, with 98.8% of the total 41 tons of shrimp produced in 2017 having come from the Brazilian northeastern. The states evaluated in the present study were responsible for the production of around 30 tons of shrimp, representing 74.6% of the entire northeastern region, with the state of RN being the largest producer (IBGE, 2020). Shrimp farming showed significant Hg and Cu emissions to the environment, as detected by bioindicators, sediment, and water analyses. Mercury is mostly derived from fish meal present in aquafeeds, whereas Cu comes mostly from the use of algaecides during pond cleaning. Emission factors for Hg ($0.03–0.04\ kg.km^{-2}.yr^{-1}$) and Cu ($38.6–59.8\ kg.km^{-2}.yr^{-1}$) are among the highest from anthropogenic sources (Lacerda et al., 2006; 2011; Lacerda and Marins, 2006; Torres, 2009; Costa et al.,

2013; Paula Filho et al., 2014; Rios et al., 2016; Moura and Lacerda, 2018).

According to Costa et al. (2015), Baptista Neto et al. (2013), and Duquesne et al. (2006), the disposal of domestic sewage and urban solid wastes, such as batteries, in unsuitable places, are important sources of Hg, Zn, Pb, Ni, Cu, and Cr, and these are the major trace metal sources to estuaries bordering metropolitan areas along the EBZN.

Industrial discharges have commonly caused contamination by As, Cd, Cr, Cu, Hg, Ni, Pb, and Zn in nearshore sediments, river channels, and coastal zones (Li et al., 2013; Souza and Silva, 2016), but the low industrialized nature of the EBZN decreases the relative importance of these sources. The emission factor determined by Vaisman and Lacerda (2003) also suggests coal burning as a significant source of As and Hg. Boats may also contribute to the trace metal inputs since some of these elements (Zn, Cd, Cu, and Pb) are contained in fossil fuel residues and have a significant correlation with the petroleum markers (Yunus and Chuan, 2009; Costa et al., 2015). Unfortunately, notwithstanding the high intensity of fisheries and recreational boat activities along the EBZN, and the evidence of biological impacts of pollutants from naval-related activities, with the exception of studies on TBT (Castro et al., 2000; 2008; Braga et al., 2006), no study, to our knowledge, has addressed the significance of this source of trace metals to the EBZN.

Emission factors of trace metals estimated to the Parnaíba River Delta (MA-PI-CE) identified significant anthropogenic contributions for Zn and Cu (117 and 71 t $year^{-1}$, respectively) derived from urban runoff and inadequate disposal of urban solid waste, while the other metals showed erosion and leaching of soils as a dominant natural source to the environment, with 65.6 t of Pb $year^{-1}$, 42.4 t of Cr $year^{-1}$, 7.4 t of Cd $year^{-1}$, and 0.6 t of Hg $year^{-1}$ (Paula Filho et al., 2014).

4 Metals and trace metals in estuarine sediments of the EZBN

Sediments act as a reservoir of metals that can account for more than 99% of trace metals that enter rivers (Huang et al., 2012), integrating the impact of the different sources to the adjacent drainage basin to the estuaries, and through relatively long periods. Most studies on trace metal concentrations in sediments were quantified in the fine grain size fraction (<63 μm) due to trace metals' preferential association with fine materials such as clays, silt, and particulate organic matter (POC), which are their major geochemical carriers in aquatic ecosystems (Marins et al., 2004; Nilin, 2008; Oliveira, 2012; Nascimento, 2013; Silva et al., 2015; Rios, 2018). Nevertheless, in estuaries with high hydrodynamic conditions, the analytical determinations were frequently performed in larger grain size fractions (<2 and <1 mm) of the sediment (Garlipp, 2006; Peres, 2012; Santos et al., 2019). Table 1 presents the average contents of metals and trace metals in sediments of different estuaries of the EZBN, as reported in the literature in the past 2 decades.

Sediments of São Marcos Bay (MA) showed higher concentrations during the dry season for Cu, Zn, Al, and Mn, while Fe was higher during the rainy season (Sousa, 2009). The author concluded that Al, Fe, and Mn were above the concentration limit allowed by the applicable Brazilian legislation (CONAMA 344/04, 2004) and also suggested a great availability of these elements. Santos et al. (2019) also found anomalous values for Mn in the same region, indicating the influence of ore shipment. Anil River and São José estuaries (MA), both located in the Maranhão Gulf, showed anomalous values, especially for Pb, resulting mainly from domestic and hospital sewage to the Anil River, while in the São José estuary, Pb was mostly derived from the lithogenic source with small anthropogenic contribution (Azevedo, 2019; Santos et al., 2019).

Paula Filho et al. (2015) established background values for trace metals in sediment cores in the largest open sea delta of the Americas, the Parnaíba River Delta (PI). Most of the metals were below two threshold levels established by sediment quality guidelines: the Probable Effect Level (PEL), in which there is a greater likelihood of adverse effects on the biota, and the Threshold Effect Level (TEL), in which there is a lower likelihood of adverse effects on the biota. However, in a more recent study in the Parnaíba River Delta, an anthropogenic influence was observed in surface sediments, classifying them as moderately to severely polluted by Cu, Zn, and Pb (Paula Filho et al., 2019). Analytical microscopy (SEM/EDS) identified pyrites in sediments from the continental shelf of the state of PI, near the Parnaíba River Delta. These pyrites were wrapped in a clay matrix and observed in a raspberry-shaped format, which is commonly found in organic-enriched marine and estuarine sediments (Aguiar, 2014). These studies collected sediment in different stations along the continental shelf, which evidences the large variability of the complex deltaic ecosystem with mangrove forest, dunes and bays under anthropogenic activities that influence contaminant inputs.

Estuaries in the state of CE have been the subject of more trace metal contamination studies than the other states listed here. In the metropolitan region of Fortaleza city (MRF), the Pacoti River, one of the most pristine in the metropolitan region, was initially not impacted by Zn, Cu, and Hg contents in estuarine sediments (Aguiar, 2005; Vaisman et al., 2005). However, this has changed in more recent years, with an evident accumulation of Fe, Cu, Pb, Zn, and Hg (Rios et al., 2016; Souza and Silva, 2016) due to intensive metal load in the misuse of water resources, whether by tourist activities and deforestation in the region previously covered by dunes and mangroves. Also in the MRF, the urbanized Cocó River exhibited Hg concentrations in bottom sediments about 112 times higher upstream than downstream of the estuarine mixing zone (Vaisman et al., 2005; Almeida, 2015). The highest values were related to urbanization and to the proximity of a decommissioned landfill that continues to be a significant point source of toxic substances to the river. In the Ceará River, also in the urban region, Cu and Hg contents in the sediment were associated with non-lithogenic sources (Aguiar, 2005; Vaisman et al., 2005). In addition, Nilin (2012) and Nilin et al. (2013) performed studies to assess the human influence on the sediment quality of these rivers. They identified high Zn and Cu accumulation near the river mouth, with Zn concentrations one order of magnitude higher than in upstream stations, and the estuary was considered moderately contaminated by Hg compared to other Brazilian coastal regions.

One of the first assessment studies in sediment cores in the Jaguaribe River, the largest basin under a semiarid climate, determined 15 ng g^{-1} of Hg as the regional background concentration for the Brazilian Northeastern Equatorial Coast

TABLE 1 Metal contents in the sediment of different estuaries in the Equatorial Zone of the Brazilian Northeast [values in μg g^{-1}, except Al and Fe (%) and Hg (ng g^{-1})]. <DL is below the detection limit.

References	Environment	Fraction	Al	Fe	Mn	As	Ba	Cd	Co	Cr	Cu	Hg	Ni	Pb	Zn
Sousa (2009)	São Marcos Bay (MA)	<63 μm	0.3	0.2	190.8	—	—	5.8	—	—	8.7	—	<DL	<DL	19.7
Nascimento (2013)	Tibiri (MA)	<63 μm	—	—	—	—	—	<DL	—	10.6	14.8	—	9.1	10.4	28.9
Carvalho et al. (2014)	Paciência (MA)	<63 μm	—	—	—	—	—	<DL	—	5.7	<DL		<DL	24.3	4.4
Silva et al. (2015)	Bacanga (MA)	<63 μm	—	—	—	—	—	0.3	—	55.0	8.9	—	6.0	62.6	50.1
Santos et al. (2019)	São Marcos Bay(MA)	<2 mm	0.3	1.0	365.0	—	—	—	—	4.7	1.1	—	2.8	3.6	7.1
	Anil (MA)	<2 mm	2.2	2.0	159.7	—	—	—	—	16.7	7.8	—	9.5	8.7	31.0
Azevedo (2019)	Arraial/São José (MA)	<63 μm	2.3	1.3	166.3	—	—	—	—	24.6	4.8	—	8.2	23.9	22.7
Paula Filho et al. (2015)	Parnaíba River Delta (PI)	<63 μm	—	1.4	633.0	—	—	—	—	18.0	6.8	—	—	5.9	13.4
Paula Filho et al. (2019)	Parnaíba River Delta (PI)	<63 μm	4.0	2.9	138.3	—	—	0.5	—	35.6	21.4	—	25.9	80.9	45.7
Marins et al. (2004)	Jaguaribe (CE)	<63 μm	—	—	—	—	—	—	—	—	—	19.0	—	—	—
	Ceará (CE)	<63 μm	—	—	—	—	—	—	—	—	—	45.0	—	—	—
Aguiar (2005)	Pacoti (CE)	<63 μm	1.3	1.5	—	—	—	—	—	—	1.3	—	—	—	3.5
	Ceará (CE)	<63 μm	1.4	1.3	—	—	—	—	—	—	4.6	—	—	—	5.2
Torres (2009)	Jaguaribe (CE)	Total	—	—	—	—	—	—	—	—	10.6	—	—	9.5	—
	Pacoti (CE)	Total	—	—	—	—	—	—	—	—	6.9	—	—	10.2	—
Oliveira (2012)	Jaguaribe (CE)	<63 μm	1.6	1.6		—	—	—	—	24.5	7.8	—	11.4	8.3	22.5
Peres (2012)	Jaguaribe (CE)	<2 mm	1.9	3.0	470.0	—	—	—	—	—	9.6	—	—	11.8	42.1
Nilin (2012)	Ceará (CE)	<63 μm	—	—	—	—	—	—	—	—	—	5.7	—	—	—
Nilin et al. (2013)	Ceará (CE)	<63 μm	0.9	1.2	—	—	—	—	—	28.1	8.8	—	—	14.2	60.2
Almeida (2015)	Cocó (CE)	<63 μm	—	—	—	—	—	—	—	—	—	86.5	—	—	—
Souza and Silva (2016)	Pacoti (CE)	Total	—	0.5	—	—	—	—	—	—	1.3	—	—	2.3	2.6
Rios (2018)	Jaguaribe (CE)	<63 μm	3.3	—	—	—	841.6	-	—	—	13.5	—	—	—	50.9
Lacerda et al. (2004)	Curimataú (RN)	<63 μm	—	—	—	—	—	0.4	—	—	0.7	—	—	7.6	17.0
	Jaguaribe (CE)	<63 μm	—	—	—	—	—	0.4	—	—	9.1	—	—	3.2	27.5
	Piranhas-Açú (RN)	<63 μm	—	—	—	—	—	0.3	—	—	15.3	—	—	6.7	31.1
Garlipp (2006)	Curimataú (RN)	<1 mm	2.4	13.2	30.0	—	62.2	—	—	6.6	64.4	—	15.7	87.7	—
Correa (2008)	Potengi (RN)	<63 μm	2.0	2.9	—	4.0	103.9	0.1	11.9	86.1	26.6	0.1	34.8	15.0	69.7

(Continued on following page)

10.3389/feart.2023.1142649

TABLE 1 (*Continued*) Metal contents in the sediment of different estuaries in the Equatorial Zone of the Brazilian Northeast [values in μg g^{-1}, except Al and Fe (%) and Hg (ng g^{-1})]. <DL is below the detection limit.

References	Environment	Fraction	Al	Fe	Mn	As	Ba	Cd	Co	Cr	Cu	Hg	Ni	Pb	Zn
Silva et al. (2017)	Apodi (RN)	<1 mm	—	—	—	—	—	0.5	—	3.2	2.3	—	—	21.4	5.4
	Conchas (RN)	<1 mm	—	—	—	—	—	<DL	—	7.0	5.1	—	—	17.1	6.0
	Guamaré (RN)	<1 mm	—	—	—	—	—	<DL	—	3.2	0.5	—	—	6.4	1.6
	Galinhos (RN)	<1 mm	—	—	—	—	—	<DL	—	3.8	1.2	—	—	18.6	4.1
	Ceará-Mirim (RN)	<1 mm	—	—	—	—	—	<DL	—	<DL	<DL	—	—	<DL	0.1
	Potengi (RN)	<1 mm	—	—	—	—	—	<DL	—	4.8	3.2	—	—	9.5	6.9
	Nísia- Floresta (RN)	<1 mm	—	—	—	—	—	<DL	—	<DL	5.1	—	—	<DL	7.6
	Papeba (RN)	<1 mm	—	—	—	—	—	<DL	—	<DL	<DL	—	—	<DL	1.1
	Guaraíra (RN)	<1 mm	—	—	—	—	—	<DL	—	<DL	<DL	—	—	<DL	<DL
Cantinho (2017)	Ponta do Tubarão (RN)	Total	—	—	—	—	—	0.4	—	0.4	1.3	3.8	1.3	—	3.4

(Marins et al., 2004). The authors also suggested the use of Hg as a proxy to indicate anthropogenic pollution for the region in reason of its absence in the local geology. Lacerda et al. (2004) compared Cu, Zn, Cd, and Pb contents in the Jaguaribe River with two other estuaries located on the coast of the state of RN: the Piranhas-Açú and Curimataú Rivers. Cd and Pb values were similar in the three rivers, whereas Zn and Cu were lower in the Curimataú and higher in the Piranhas-Açú. The authors suggest that Cd and Pb inputs were heavily driven by natural processes, such as soil denudation, while Cu and Zn emissions were due to agriculture and inadequate disposal of wastewater and solid waste. Peres (2012) found in a sediment core from the Jaguaribe River estuary that OM, Fe, and Mn acted as the main geochemical carriers of Cu and Zn, due to the suboxic conditions that favor the formation of Fe-Mn oxy-hydroxide or pyritization (FeS_2), common in this environment.

Metal (Al, Ba, Cd, Cr, Cu, Fe, Mn, Ni, Pb, and Zn) accumulation in superficial sediment and cores analyzed in the Curimataú River (RN) indicated lower concentrations compared to other estuaries, except for Mn and Cu, which showed enrichment in some stations (Garlipp, 2006). When compared to Lacerda et al. (2004), it is possible to observe the intensification of Pb and Cu inputs, with values one and two orders of magnitude higher, respectively. The observed high concentrations can result from trace metal contamination by the increase of effluent discharges from shrimp farming to rivers.

The evaporation in some estuaries in the state of RN exceeds the freshwater input, making the upstream of the river become a source of dense water, saltier than seawater. This condition characterizes the environment as negative hyper-saline estuaries, as in the Apodi and Conchas Rivers. These environments showed significantly higher contamination by Cr, Cu, Cd, and Pb than the positive Potengi estuary, also in RN state, at least for Cr (Silva et al., 2017), which exhibits salinity increases seaward. The authors also indicated anthropogenic influence on a load of trace metals in addition to the hydrodynamic conditions characterized by weak tide dispersion capacity, which increases the water resident time along the estuary. The high content of Pb and Zn was also identified in Ponta do Tubarão estuary (RN), which featured the highest metal concentrations detected near the urban area and anchoring boats, but still below the limit established by Brazilian legislation (Cantinho, 2017).

The results indicated higher levels of Zn, Cu, and Pb for at least one estuary of each state. Anomalous values for Fe were also identified in estuaries in the states of MA and CE, as well as high content of Mn in aquatic systems in the states of MA and RN. Estuaries in the CE state also showed a significant amount of Hg in their sediments, but this metal was not analyzed in the other EZBN regions. The similar Zn, Cu, and Pb contaminations among the estuaries along the EZBN may result initially from the regional and local geological characteristics associated with the Barreiras Formation (Morais, 1977; El-Robrini et al., 2006; Vital et al., 2006) and the intense increase of anthropogenic activities developed on the discharge basins, which aggravates the enrichment of metals in the coastal zone.

Xavier et al. (2017) identified that even the Capibaribe estuary, in a metropole of another Northeast state of Brazil out of the EZBN, showed good environment quality for the sediment related to Mn, Fe, Cu, Zn, Pb, and other trace metal concentrations. However, Fe,

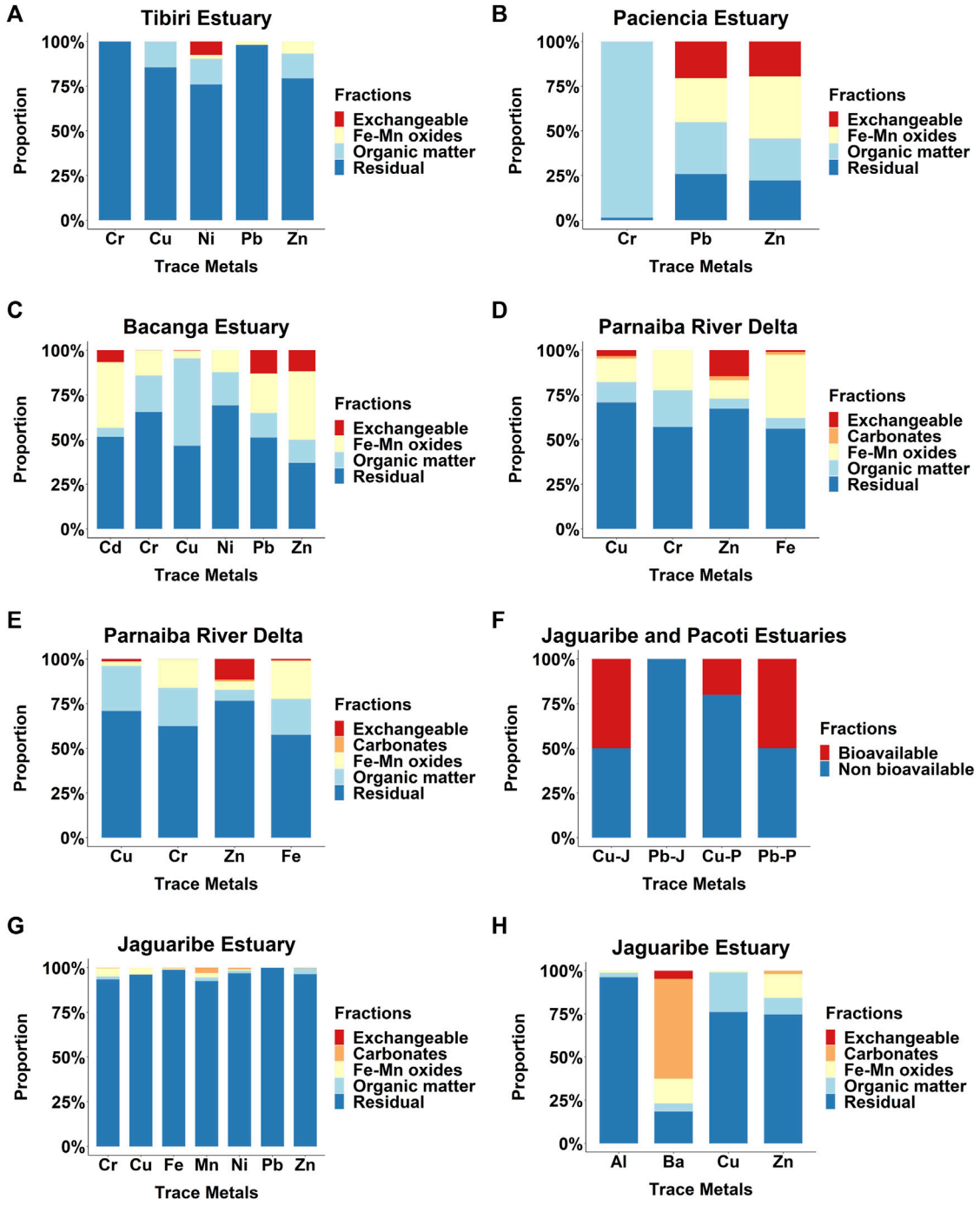

FIGURE 2
Trace metal sequential extractions (%) in estuarine sediments in the Equatorial Zone of the Brazilian Northeast. Data sources from **(A)** Nascimento (2013), **(B)** Carvalho (2014), **(C)** Silva et al. (2015), **(D,E)** Present study, **(F)** Torres (2009), **(G)** Oliveira (2012), and **(H)** Rios (2018).

Mn, Pb, and other concentrations in sediments were higher than those found in most estuaries of the EZNB. The authors affirm that the Barreiras Formation was the main source that increased metals in the environment, whereas anthropic influence was unlikely due to the low values of local sediment quality indices.

In fact, the measurement of total metals and trace metals in sediment are not satisfactory to assess the mobility and availability in the estuarine ecosystems (Passos et al., 2011; Pejman et al., 2017). However, the use of sequential extractions furnishes detailed information about metals' origin, mode of occurrence, availability, mobility, and transport (Tessier et al., 1979). Tessier et al. (1979) determined trace metals in five sediment fractions: the exchangeable fraction, which includes the metal bounded with cations that can be exchanged by ions present in water, the fraction bound to carbonates that can be mobilized by changes in pH, the reducible fraction bound to Fe-Mn oxides and released

10.3389/feart.2023.1142649

TABLE 2 Metal contents in the water of different estuaries in the Equatorial Zone of the Brazilian Northeast. D is dissolved, P is particulate, and T is the total fraction.

References	Environment	Fraction	Unit	Al	Fe	Mn	Cd	Co	Cu	Hg	Ni	Pb	Zn
Furtado (2007)	São Marcos Bay (MA)	D	mg L^{-1}	—	3.3–7.2	—	—	0.006–0.02	0.02–0.05	—	0.05–0.09	0.009–0.09	—
Sousa (2009)	São Marcos Bay (MA)	D		6.2–36.3	0.7–6.8	<DL- 0.06	<DL-0.0007	—	0.00007–0.002	—	< DL	0.009–0.02	0.005–0.7
Dias (2007)	Jaguaribe (CE)	P	mg g^{-1}	0.002	—	—	—	—	0.01	—	—	—	6.2
Dias et al. (2009)	Jaguaribe (CE)	P	mg g^{-1}	<DL-47.3	20–29	0.5–15.5	—	—	0.005–0.01	—	—	<DL-0.007	<DL-4.4
Torres (2009)	Jaguaribe (CE)	P	mg g^{-1}	26.4–46.7	—	—	—	—	0.01–0.03	—	—	<DL	—
Costa (2009)	Jaguaribe (CE)	D	ng L^{-1}	—	—	—	—	—	—	1.1–23.5	—	—	—
		P	ng L^{-1}	—	—	—	—	—	—	3.2–15.0	—	—	—
		T	ng L^{-1}	—	—	—	—	—	—	6.3–32.1	—	—	—
Soares (2011)	Jaguaribe (CE)	P	ng L^{-1}	—	—	—	—	—	—	0.1–3.8	—	—	—
		D	ng L^{-1}	—	—	—	—	—	—	0.1–11.9	—	—	—

under anoxic conditions (i.e., low Eh), the oxidizable fraction bound to OM and sulfides that are solubilized under oxidizing conditions, and the residual fraction, which holds trace metals within the crystal lattice of minerals that are not expected to mobilize easily in solution.

Unfortunately, for the region, there are few studies based on the sequential extraction mentioned above (Figure 2). In the MA state, Nascimento (2013), Carvalho (2014), and Silva et al. (2015) extracted metals present in the exchangeable (F1), reducible (F2), oxidizable (F3), and residual (F4) fractions from estuarine sediments (Figures 2A–C). The authors identified the dominance of all trace metals bound to the residual fraction, except for Cr, Pb, and Zn in the Paciência River estuary and Cu in the Bacanga River estuary, which were mostly associated with the oxidizable fraction. These results indicate the predominance of trace metals in non-labile fractions, except for Cr, Pb, Cu, and Zn, which can be mobilized from the sediment to the water column with the change of physicochemical conditions, mainly in the Paciência and Bacanga river estuaries, where some of these metals are often associated to oxidizable fraction, meaning that geochemistry of these elements can be controlled by OM.

The present study provides data about trace metal sequential extractions (Cu, Cr, Zn, and Fe) in surface sediments in two stations from the Parnaíba River Delta, sampled in 2019. The results identified the dominance of the residual fraction (circa 50%–75%) for all metals evaluated (Figures 2D, E). However, Zn was significantly associated with exchangeable fractions, whereas Fe was bounded to the reducible fraction (circa 60%) in both stations. Cu and Cr showed a large spatial geochemical variability in the sediments binding to different reducible and oxidizable fractions. The association of trace metal to labile fractions indicates the occurrence of elements from secondary sources that are adsorbed, complexed, and settled distinctly to the bottom by the influence of local hydrodynamics. Zn exhibited medium mobility by the association to the exchangeable fractions, corroborating with a previous study that suggested that untreated domestic effluent and livestock activities from the main regional urban center of Parnaíba city were the main source of this element to the environment (Paula Filho et al., 2015).

Other studies developed in the Jaguaribe River (CE) applied sequential procedures to determine metals (Figures 2G, H) in the five sediment fractions (Oliveira, 2012; Rios, 2018). Sequential extraction to determine the potentially bioavailable (F1 + F2 + F3 + F4 fractions) and non-available trace metals (F5) in the Jaguaribe and Pacoti rivers (Figure 2F) found Cu predominated associated with the non-available fraction, while Pb was available in sediment samples from the Pacoti River (Torres, 2009).

The different extractions, sediment fractions, and sampling points along the Jaguaribe estuary, the most studied in the EZBN relative to sequential extraction of metals, showed that these methodological differences produced different results, but they showed that 50%–100% of metal (Cu, Zn, Cr, Pb, Ni, Fe, Mn, and Al) concentrations were bounded to the residual fraction, suggesting a small contribution from local anthropogenic sources in the estuarine region, although aquaculture effluents and urban discharges have been found to influence the trophic state of the region (Marins et al., 2011; Marins et al., 2021). A different geochemical partitioning was observed for Ba, which is bounded to carbonates and is related to pH increase.

TABLE 3 Trace metal in organisms (wet weight) of different estuaries in the Equatorial Zone of the Brazilian Northeast (values in μg g^{-1}). (a) Indicates the maximum values of trace metals in fish set by ANVISA RDC n°42/13 (Ministério da Saúde. Agência Nacional de Vigilância Sanitária, 2013) and (b) indicates the trace metal range allowed in food in general by ANVISA n° 685/98 (Brasil, 1998).

References	Estuary	Group	Scientific name	Al	Fe	Mn	Ba	Cd	Cr	Cu	Hg	Ni	Pb	Sn	Zn
Brazilian Legislation		Fish- shellfish	—	—	—	—	—	0.05–2.0	—	0.1–10	0.5–1.0	—	0.3–1.5	—	—
Carvalho et al. (2000)	Bacanga (MA)	Oyster	*Mytella falcata*	—	—	—	—	<DL	—	1,240.0	—	—	<DL	—	11,274
Sousa (2009)	São Marcos Bay (MA)	Fish	*Arius proops*	3.3	2.2	<DL	—	<DL	—	<DL	—	<DL	<DL	—	6.0
			Arius rugispinis	1.3	4.1	0.2	—	<DL	—	0.3	—	<DL	<DL	—	43.2
			Hexanematicht hys herzbergii	0.5	2.4	0.2	—	<DL	—	0.1	—	<DL	<DL	—	29.3
			Bagre marinus	3.3	5.0	0.4	—	<DL	—	0.3	—	<DL	<DL	—	38.8
			Lophiosilurus alexandri	2.0	4.5	0.9	—	<DL	—	0.3	—	<DL	<DL	—	6.2
			Geniatremus luteus	0.5	3.4	0.4	—	<DL	—	0.2	—	<DL	<DL	—	9.1
			Micropogonias furnieri	0.3	1.5	0.4	—	<DL	—	0.1	—	<DL	<DL	—	5.7
Vaisman, Marins and Lacerda (2006)	Ceará (CE)	Oyster	*Crassostraea rhizophorae*	—	—	—	—	—	—	—	30.8	—	—	—	—
	Cocó (CE)			—	—	—	—	—	—	—	16.8	—	—	—	—
	Pacoti (CE)			—	—	—	—	—	—	—	9.0	—	—	—	—
	Jaguaribe (CE)			—	—	—	—	—	—	—	10.4	—	—	—	—
Torres (2009)	Jaguaribe (CE)	Crustacean	*Callinectes sapidus*	—	—	—	—	—	—	—	—	—	<LD	—	—
			Litopenaeus schimitti	—	—	—	—	—	—	4.2	—	—	<LD	—	—
		Oyster	*Crassostrea rhizophorae*	—	—	—	—	—	—	1.5	—	—	<LD	—	—
		Seaweed	*Ulva lactuca*	—	—	—	—	—	—	0.3	—	—	<DL	—	—
	Pacoti (CE)	Oyster	*Crassostrea rhizophorae*	—	—	—	—	—	—	1.5	—	—	0.4	—	—
			Mytella falcata	—	—	—	—	—	—	3.1	—	—	<DL	—	—
			Anomalocardia brasiliana	—	—	—	—	—	—	1.7	—	—	1.3	—	—
Costa (2009)	Jaguaribe (CE)	Fish	*Sphoeroides testudineus*	—	—	—	—	—	—	—	9.9	—	—	—	—
			Cathorops spixii	—	—	—	—	—	—	—	31.8	—	—	—	—
Lopes (2012)	Jaguaribe (CE)	Fish	*Cichla sp*	—	—	—	—	—	—	—	28.8	—	—	—	—
			Serrasalmus rhombeus	—	—	—	—	—	—	—	40.9	—	—	—	—
			Centropomus parallelus	—	—	—	—	—	—	—	25.4	—	—	—	—
			Menticirrhus americanus	—	—	—	—	—	—	—	7.6	—	—	—	—

(Continued on following page)

10.3389/feart.2023.1142649

TABLE 3 (*Continued*) Trace metal in organisms (wet weight) of different estuaries in the Equatorial Zone of the Brazilian Northeast (values in μg g^{-1}). (a) Indicates the maximum values of trace metals in fish set by ANVISA RDC n°42/13 (Ministério da Saúde. Agência Nacional de Vigilância Sanitária, 2013) and (b) indicates the trace metal range allowed in food in general by ANVISA n° 685/98 (Brasil, 1998).

References	Estuary	Group	Scientific name	Al	Fe	Mn	Ba	Cd	Cr	Cu	Hg	Ni	Pb	Sn	Zn
			Cathorops spixii	—	—	—	—	—	—	—	17.0	—	—	—	—
			Plagioscion squamosissimus	—	—	—	—	—	—	—	44.5	—	—	—	—
			Prochilodus sp	—	—	—	—	—	—	—	7.9	—	—	—	—
			Leporinus friderici	—	—	—	—	—	—	—	26.6	—	—	—	—
			Oreochromis niloticus	—	—	—	—	—	—	—	10.3	—	—	—	—
Almeida (2015)	Cocó (CE)	Fish	*Oreochromis niloticus*	—	—	—	—	—	—	—	2.1	—	—	—	—
			Hypostamus pusarum	—	—	—	—	—	—	—	3.4	—	—	—	—
			Pseudancistrus papariae	—	—	—	—	—	—	—	14.3	—	—	—	—
			Prochilodus brevis	—	—	—	—	—	—	—	8.4	—	—	—	—
Rios et al. (2016)	Ceará (CE)	Oyster	*Crassostraea rhizophorae*	—	—	—	—	—	—	—	18.6	—	—	—	—
	Jaguaribe (CE)			—	—	—	—	—	—	—	15.0	—	—	—	—
	Pacoti (CE)			—	—	—	—	—	—	—	10.4	—	—	—	—
	Cocó (CE)			—	—	—	—	—	—	—	12.2	—	—	—	—
Soares (2017)	Jaguaribe (CE)	Oyster	*Crassostrea rhizophorae*	—	—	—	—	—	—	9.6	7.7	—	—	—	—
Moura and Lacerda (2018)	Jaguaribe (CE)	Fish	*Cathorops spixii*	—	—	—	—	—	—	—	10.0	—	—	—	—
			Centropomus parallelus	—	—	—	—	—	—	—	7.8	—	—	—	—
			Elops saurus	—	—	—	—	—	—	—	21.8	—	—	—	—
			Eugerres brasilianus	—	—	—	—	—	—	—	7.6	—	—	—	—
			Gobionellus oceanicus	—	—	—	—	—	—	—	2.8	—	—	—	—
			Lutjanus jocu	—	—	—	—	—	—	—	16.8	—	—	—	—
			Lutjanus synagris	—	—	—	—	—	—	—	12.2	—	—	—	—
			Menticirrhus americanus	—	—	—	—	—	—	—	20.8	—	—	—	—
			Mugil curema	—	—	—	—	—	—	—	4.2	—	—	—	—
		Crustacean	*Callinectes bocourti*	-	-	-	-	-	-	-	40.2	—	—	—	—
			Callinectes danae	—	—	—	—	—	—	—	13.8	—	—	—	—
			Callinectes exasperatus	—	—	—	—	—	—	—	4.6	—	—	—	—

(Continued on following page)

10.3389/feart.2023.1142649

TABLE 3 (*Continued*) Trace metal in organisms (wet weight) of different estuaries in the Equatorial Zone of the Brazilian Northeast (values in μg g^{-1}). (a) Indicates the maximum values of trace metals in fish set by ANVISA RDC n°42/13 (Ministério da Saúde. Agência Nacional de Vigilância Sanitária, 2013) and (b) indicates the trace metal range allowed in food in general by ANVISA n° 685/98 (Brasil, 1998).

References	Estuary	Group	Scientific name	Al	Fe	Mn	Ba	Cd	Cr	Cu	Hg	Ni	Pb	Sn	Zn
			Callinectes larvatus	—	—	—	—	—	—	—	20.8	—	—	—	—
			Litopenaeus vannamei	—	—	—	—	—	—	—	2.8	—	—	—	—
		Oyster	*Anomalocardia brasiliana*	—	—	—	—	—	—	—	10.2	—	—	—	—
			Mytella charruana	—	—	—	—	—	—	—	10.4	—	—	—	—
		Gastropod	*Pugilina morio*	—	—	—	—	—	—	—	9.8	—	—	—	—
Silva et al. (2001)	Potengi (RN)	Oyster	*Crassostrea rhizophorae*	—	100.0	5.9	—	0.3	0.5	19.8	—	0.3	0.7	—	487.0
Carvalho et al. (2002)	Potengi (RN)	Oyster	*Tagelus plebeius*	—	—	—	0.7	<DL	0.9	0.9	—	3.0	4.2	23.8	149.0

The few studies about sequential extractions in estuaries of the EZBN suggest low to medium mobility of these metals in the environment related to the prevailing percentage in residual fractions. Although, it is notable that the associations among trace metals with Fe-Mn oxides (reducible fraction), OM, and carbonates can act as important geochemical carriers of metals along these environments. Therefore, investigation on the quantification and qualification of geochemical carriers present in the EZBN could be relevant to the comprehension of many mobilization and transport processes and the fate of contaminants along the region, as observed by the complexation of Cu-OM in the Pacoti River (Mounier et al., 2018). In addition, no study has evaluated if the estuaries in the EZBN can function as a source or sinks of contaminants to adjacent marine environments, and if the eventual mobility verified in certain estuaries is related to concentrations and distribution of these metals on the adjacent continental shelf.

5 Trace metals in estuarine waters of the EZBN

Most trace metals that enter the estuarine ecosystems are influenced by local hydrodynamic, physical, and chemical parameters, such as temperature, pH, salinity, and dissolved oxygen, usually resulting in a non-conservative behavior along the estuary (Machado et al., 2016; Wang et al., 2017; Mori et al., 2019; Mosley and Liss, 2019). The comprehension of geochemical processes that influence the partitioning of trace metals among colloidal, dissolved, and particulate fractions indicates the possible fate and transport of these contaminants in the environment (Robert et al., 2004; Machado Júnior and Macedo, 2016). Suspended particulate matter (particles with a size smaller than 63 μm) has a high capacity to carry trace metals due to the increase in specific surface area (Yao et al., 2015). Metals in particulate fractions can be associated with Fe-Mn hydroxides, carbonates, OM, silt, and clay minerals (Du Laing et al., 2009). These metal-particle associations can suffer precipitation, dissolution, complexation, absorption, and dissociation processes in the estuary. The coefficient evaluation of metal-organic complexation (<0.45 μm) and metals in colloidal forms (<0.025 μm) play a major role in metal bioavailability and the hazard posed by them (Simpson et al., 2014). Quantification of trace metals in estuarine water is scarce in the EZBN due to the necessity of methods and equipment with a low detection limit and high sensibility and selectivity, which can determine the very low concentrations of these elements found naturally in natural waters (less than 1 ppb). Available published data from the EZBN are presented in Table 2.

There is a great lack of data on metal concentration in the waters of the EZBN as demonstrated in Table 2. São Marcos Bay (MA) and the Jaguaribe River Estuary (CE) were the only environments where trace metals were determined in the water. São Marcos Bay is composed of diverse estuaries that discharge on it, with an important harbor complex with a large movement of ore and grains, which influences trace metal contamination in the region. Dissolved Cu and Ni concentrations were reported above the maximum allowed by Brazilian legislation (CONAMA nº 357,

TABLE 4 A summary of environmental conditions and the major drivers of metal contamination in estuaries of the Equatorial Zone of the Brazilian Northeast.

Hydrographic basin	Estuaries	Igeo classes	Biomonitor	Major driver	Driver tendence (2013–2035)	Responses
Piranha-Açú	**Conchas**	Pb = uncontaminated to moderately contaminated; No speciation data	No data	Natural sources, agriculture effluents and solid waste	Slow urbanization of 0.9% per year	Monitoring
	Piranhas-Açú	Cu and Zn = uncontaminated to moderately contaminated; No speciation data				
Ceará-Mirim	**Ceará-Mirim**	Zn = uncontaminated; No speciation data	No data	Natural sources, and aquaculture effluents	Fast urbanization of 1.1% per year	Monitoring
Trairi	**Nísia-Floresta**	Cu and Zn = uncontaminated; No speciation data	No data	Agriculture, aquaculture, domestic sewage	Fast urbanization of 1.5% per year	Monitoring
Northern coastline of RN	**Galinhos**	Pb = uncontaminated to moderately contaminated; No speciation data	No data	Natural sources, and aquaculture effluents	Slow urbanization of 0.9% per year	Monitoring
	Guamaré	All metal = uncontaminated; No speciation data				
	Ponta do Tubarão	All metal = uncontaminated; No speciation data				
Apodi	**Apodi**	Cr, Cu and Zn = uncontaminated; Pb = moderately contaminated; No speciation data	No data	Domestic sewage, and aquaculture effluents	Fast urbanization of 1.7% per year	Confirm Pb speciation; Monitoring and reduce the emissions; Biota monitoring
Itapecuru and Munim	**São José Bay**	Zn = uncontaminated to moderately contaminated; Pb = moderately contaminated; No speciation data	No data	Natural sources, and domestic sewage	Fast urbanization of 1.0% per year	Confirm Pb speciations; Monitoring
Mearim	**São Marcos Bay**	Cr and Zn = uncontaminated to moderately contaminated; Pb = moderately contaminated; No speciation data	High Zn value in fish; Cu below than permitted by law in fish	Harbor activities, deforestation, decommissioned landfill, industrial and domestic sewage	Fast urbanization of 1.0% per year	Confirm Pb speciations; Monitoring and reduce the emissions; Biota monitoring; Advisories on biota contamination by metals.
Jaguaribe	**Jaguaribe**	Fe, Cu and Pb = uncontaminated to moderately contaminated; Zn = moderately contaminated; Cu with 50% bioavailable and Ba with 62% in labile fractions with exchangeable and carbonates	Cu in oyster near to the maximum permitted by law	Domestic sewage, aquaculture, and deforestation	Fast urbanization of 1.2% per year	Monitoring and reduce the emissions; Biota monitoring; Advisories on biota contamination by metals.
Metropolitan basin of Fortaleza	**Ceará**	Cr and Pb = uncontaminated to moderately contaminated; Hg and Zn = moderately contaminated; No speciation data	Hg in oyster below than permitted by law	Harbor activities, tourism, deforestation, decommissioned landfill and domesticsewage	Fast urbanization of 1.1% per year	Confirm Hg, Pb,Cu, and Zn speciations; Monitoring and reduce the emissions; Biota monitoring
	Cocó	Hg = moderately contaminated; No speciation data	Hg in oyster and fishes below than permitted by law			
	Pacoti	Pb = uncontaminated to moderately contaminated; Cu with 20% and Pb with 50% bioavailable	Pb in oyster near to the maximum permitted by law			

(Continued on following page)

TABLE 4 (*Continued*) A summary of environmental conditions and the major drivers of metal contamination in estuaries of the Equatorial Zone of the Brazilian Northeast.

Hydrographic basin	Estuaries	Igeo classes	Biomonitor	Major driver	Driver tendence (2013–2035)	Responses
Potengi	**Potengi**	Hg = uncontaminated; Fe and Pb = uncontaminated to moderately contaminated; Cr, Cu and Zn = moderately contaminated; No speciation data	Cu and Pb in oyster higher than permitted by law; High Zn value in oysters	Domestic sewage, industrial and aquaculture effluents	Slow urbanization of 0.8% per year	Confirm Cr, Cu and Zn speciations; Emissions reductions; Biota monitoring; Advisories on biota contamination by metals
Maranhão Island	**Anil**	Fe, Cr and Cu = uncontaminated to moderately contaminated; Pb = moderately contaminated; Zn = moderately to heavily contaminated; No speciation data	No data	Harbor activities, domestic, hospital and industrial sewage	Slow urbanization of 0.8% per year	Confirm metals speciations; Monitoring and reduce the emissions; Biota monitoring; Advisories on biota contamination by metals
	Bacanga	Cr = moderately contaminated; Pb = moderately to heavily contaminated; Pb and Zn circa of 13 and 11% exchangeable	High Zn value in oyster			
	Paciência	Pb = moderately contaminated; Pb and Zn circa of 20% exchangeable	No data			
	Tibiri	Cu, Pb and Zn = uncontaminated to moderately contaminated; Cr, Cu and Zn residual fraction and Ni circa of 10% exchangeable	No data			
Parnaíba	**Parnaíba River Delta**	Fe and Cr = uncontaminated to moderately contaminated; Cu and Zn = moderately contaminated; Pb = heavily contaminated; Zn circa of 16% in labile fractions with exchangeable and carbonates	No data	Natural sources, domestic sewage and livestock activities	Fast urbanization of 1.1% per year	Confirm Pb speciation; Cu, Pb and Zn biota monitoring; Monitoring and reduce the emissions
Southern coastline of RN	**Curimataú**	Fe and Cu = moderately to heavily contaminated; Pb = heavily contaminated; No speciation data	No data	Domestic sewage, and shrimp farming effluents	Slow urbanization of 0.9% per year	Confirm Cu and Pb speciations; Monitoring and reduce the emissions; Biota monitoring
	Papeba	Zn = uncontaminated; No speciation data				

2005), while dissolved Al and Fe concentrations increased in the dry and rainy seasons, respectively (Furtado, 2007; Sousa, 2009), since their concentrations' variability in the water columns is related to aluminosilicates and oxyhydroxide of Fe and Mn coming from weathering in the drainage basin. These elements are associated with finer particles (related to grain size), and their concentrations should not be altered by anthropogenic sources (Barbieri, 2016). In addition to the natural sources, the variability of Al and Fe concentrations may result from bauxite mining, as in the Mearim river basin, and from ore and grain cargo ships in the city of São Luís, adjacent to São Marcos Bay (Bandeira, 2013). High values of Al and Fe in the water corroborate with values observed in the sediment compartment, as discussed previously for São Marcos Bay.

The Jaguaribe River Estuary is a negative estuary with strong shrimp farming activity in CE state. Some studies evidenced the lithogenic source for particulate Fe, Al, and Mn with the highest values upstream of the estuary, while Zn and Pb showed diffuse and point sources with enrichment near urban zones, major agriculture activities, and along the navigation routes of large fishing boats (Dias, 2007; Dias et al., 2009). Particulate Cu had an interesting variation; the first studies reported that Cu origin was mostly from lithogenic sources but increased up to an order of magnitude in

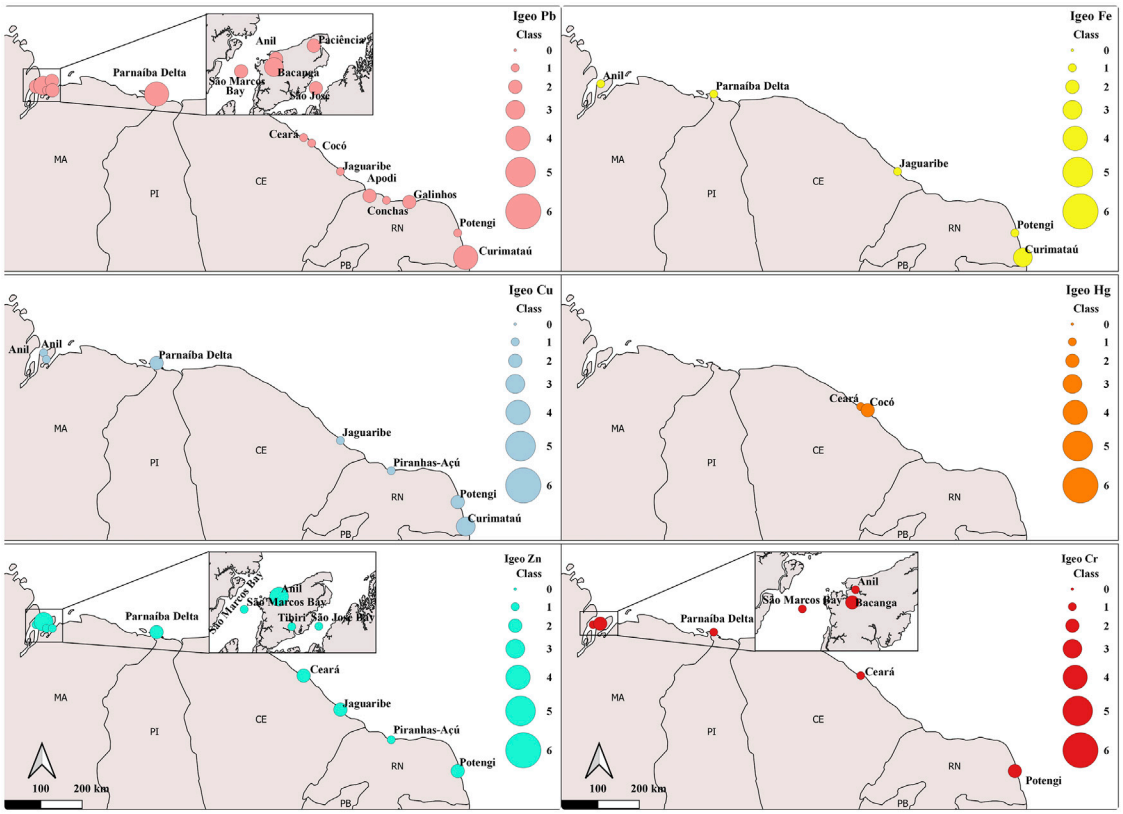

FIGURE 3
Geoaccumulation Index for Pb, Fe, Cu, Hg, Zn, and Cr in estuarine sediments along the Equatorial Zone of the Brazilian Northeast.

different locations of the estuary over time (Dias, 2007; Torres, 2009). This recent increase was associated with the increasing extension of shrimp aquaculture farms along the estuary, and the authors observed higher values near the releasing point of shrimp pond effluents. An increase in the available fraction of metals in bottom sediments affected by shrimp farm effluents has also been reported (Costa et al., 2013).

Both environments in MA and CE states present high concentrations of Cu, which may derive from the desorption of the particulate phase under salinity variation with tidal flooding, increasing the dissolved Cu fraction. Bottom sediments can be another source for Cu in the water column because even though Cu is dominantly bound to a residual fraction in the estuaries of the EZBN, the element was also found associated with an oxidizable fraction of OM and sulfides that are solubilized under oxidizing conditions in the environment, as observed in bottom sediments. Copper in estuarine environments can be found commonly complexed with dissolved and colloidal organic matter as metal-OM complex as observed in the Cocó and Pacoti river estuaries in the state of CE (Mounier et al., 2018). These complexes occur due to the attraction of the positive charge of dissolved metals to the negatively charged OM, which is bound to functional groups.

In the Jaguaribe estuary, in the CE state, Hg in particulate and dissolved forms showed a predominant positive correlation with continental geochemical tracers (Si, Ba, and suspended particulate matter), but the dissolved fraction showed some enrichment near the releasing point of the shrimp farms effluents (78.3% of the total Hg content in waters) in comparison to particulate Hg (Costa, 2009; Soares, 2011). Estuarine regions can present Hg in the most toxic species, such as methylmercury ($MeHg^{+}$), during hypoxic conditions and associated with organic particulates (Horvat, 1997). The semiarid estuaries of the EZBN present low natural continental runoff made lower due to anthropogenic influence in association with global climate change. These factors could increase the residence time of the fluvial waters entering the estuaries, in their middle section, resulting in increasing reactivity and bioavailability of metal forms. This biogeochemical estuarine process has been observed to control Hg dynamics in these semiarid estuaries (Lacerda et al., 2012; 2020).

There is no study focusing on the distribution coefficient (Kd) between dissolved and particulate fractions of trace metals in the water column of the EZBN that measured and compared metal retention capacity. High values of Kd indicate that the metal is retained by the solid phase (particulate) through adsorption reactions, whereas low values indicate that an important proportion remains soluble (dissolved) (Yang and Wang, 2017). This parameter has valuable information to allow the evaluation of metal-related pollution in a water body and the identification of sites where waste management decisions need to be remediated.

Comparing the range of dissolved trace metals to other Brazilian tropical estuaries under anthropogenic pressure, such as Tapacurá River (Pernambuco), Rio Una (Bahia), Sepetiba Bay (Rio de Janeiro), and Lagoa dos Patos (Rio Grande do Sul), and the Brazilian legislation (CONAMA nº 357, 2005 we can recognize high values

for most metals found in estuaries of the EZBN, except dissolved Cd and Mn, which were 7.1 and 1.6 times lower than CONAMA values for brackish water, respectively (CONAMA nº 357, 2005; Molisani et al., 2007; Aprile and Bouvy, 2010; Barbosa et al., 2012; Jesus and Cruz, 2019). Tapacurá River and Rio Una identified enrichment of dissolved Cu, Zn, and Cd as a result of surrounding anthropic activities such as domestic sewage and agriculture runoff (Aprile and Bouvy, 2010; Jesus and Cruz, 2019). These elements are probably available to aquatic organisms and cause harm due to high metal toxicity. The concentrations of dissolved Hg from lithogenic sources in Sepetiba Bay (Molisani et al., 2007) are 11 times lower than the concentration found in the Jaguaribe estuary. However, there are no significant sources of Hg in the Jaguaribe estuary, but there are seasonal geochemical processes that increase the Hg mobility and solubility in the EZBN (Lacerda et al., 2012; 2020). The effects of these processes were not evaluated for other metals rather than Hg.

The frequent sediment dredging in harbor areas decreases the concentration of dissolved Pb, Cu and Zn by the dilution and dispersion of the metals accumulated in the environment over time, in the harbor zone in Lagoa dos Patos, located at the southern end of the Brazilian coast. However, it was not observed for Cd due to the abundance of chloride ions from seawater intrusion that forms soluble complexes in the water column with Cd from domestic effluent and fertilizer industries (Barbosa et al., 2012). However, the value of dissolved Cd in Sao Marcos Bay, also with an important harbor, Itaqui Harbor, was five times lower than in Lagoa dos Patos.

The particulate Zn in the EZBN estuaries was the only element with high concentrations in comparison to other Brazilian tropical estuaries, such as Rio Una (Bahia) and Paraíba do Sul (Rio de Janeiro) (Carvalho et al., 2002; Gonçalves and Carvalho, 2006; Jesus and Cruz, 2019). The Jaguaribe estuary showed particulate Cu and Pb concentrations two and five times lower, respectively, than Rio Una, while particulate Al and Fe were three times lower than concentrations observed in the Paraíba do Sul. In general, the concentration of trace metals in the dissolved fraction of the EZBN estuaries was higher than the particulate fraction when compared to other tropical urban estuaries. It points to the high desorption of trace metals from the solid to liquid phase in the water column of the EZBN estuaries resulting from changes in physicochemical conditions associated with saline intrusions in the flood tide. There is, therefore, a need for more studies on the distribution coefficient in environmental compartments and how it may impact local aquatic biota, especially those of commercial value for human consumption.

6 Organisms of the EZBN as biomonitors

Metals can be classified as essential (Fe, Mn, Zn, Cr, and Cu) depending on their concentrations or toxicity (Hg) to organisms, but when present in the environment in high concentrations, most of them can cause the death of organisms (Abessa et al., 2005). For this reason, some biomonitors, living organisms that accumulate trace metals in their tissues, are utilized to monitor the process of bioaccumulation of bioavailable contaminants present in riverine, estuarine, or coastal ecosystems through time (Rainbow and Phillips, 1993). In addition, biomagnification can be a serious problem due to the contaminant transfer along the food chain, especially if the concentrations reach toxic levels in top organisms, such as humans.

As observed in the few studies about the water compartment of the EZBN estuaries there is potential mobility of trace metals from the particulate to the dissolved fraction, due to the change of physicochemical conditions, which suggests the presence of available trace metals species contaminate the aquatic organisms. Therefore, the National Sanitary Surveillance Agency-ANVISA (Ministério da Saúde. Agência Nacional de Vigilância Sanitária, 2013) developed the Resolution RDC n° 42/13 derived from the Ordinance n° 685/98, which determined the maximum levels of chemical contaminants in food that may constitute a risk to human health (Table 3). Considering this legislation, the present study examined the trace metal contents in the wet weight of the organisms to better comparison. When concentrations reported in a given study were in dry weight, they were converted to wet weight, using the percentage of water reported for a given organism, or considering 80% humidity when humidity data were not available (Kütter et al., 2021).

Aquatic organisms in the state of MA, such as oysters (*Mytella falcata)* and fishes (*Arius props, Arius rugispinis, Hexanematicht hys herzbergii, Bagre marinus, Lophiosilurus alexandri, Geniatremus luteus*, and *Micropogonias furnier)* exhibited concentrations for Cd, Cu, and Pb below to the level set by ANVISA n° 42/13 (Carvalho et al., 2000; Sousa, 2009; Ministério da Saúde. Agência Nacional de Vigilância Sanitária, 2013), but Zn in oysters was identified with contents one or two orders of magnitude above the contents compared to the oyster from the other environments (Table 3). This result corroborates the lability of Zn identified in the MA sediments discussed in the previous section. The assimilation of Zn in the oyster muscles may result from the resuspension of this element from the sediment to the water column that uses the suspended material contaminated with Zn in their filter-feeding diet.

Trace metal accumulation was also identified in another oyster in estuaries from the state of CE. The mangrove oyster (*Crassostrea rhizophorae)* usually acts as a consistent Hg regional biomonitor, reflecting the degree of anthropogenic impact on estuary systems. In the Metropolitan basin of Fortaleza (CE), this organism showed a greater bioaccumulation of Hg in the estuary of the urban Ceará River than in other estuaries. However, it does not present a significant correlation with the size and sediment contents, which vary due to the influence of the hydrodynamics on this estuarine compartment (Vaisman et al., 2005; Rios et al., 2016). Notwithstanding, Almeida (2015) identified higher Hg in detritivores fish species (*Pseudancistrus papariae* and *Prochilodus brevis*) than in omnivores species (*Oreochromis niloticus* and *Hypostamus pusarum*) at the Cocó Estuary, something the author associated to the largest size observed in the first group. Organisms present in the Jaguaribe Estuary showed Hg biomagnification, most in genera of carnivorous fish (*Sphoeroides testudineus, Cathorops spixii, Elops saurus, Menticirrhus americanus,* and *Plagioscion squamosissimu)* and in carnivorous crustaceans (*Callinectes bocourti, Callinectes Larvatus,* and *Callinectes Danae*) (Costa, 2009; Torres, 2009; Lopes, 2012; Costa and Lacerda, 2014; Moura and Lacerda, 2018). These contents were correlated to biological factors, such as weight, size, feeding habits, and trophic level. As

mentioned previously, in the water and sediment sections, Hg was dominantly from the input from shrimp farming effluents, but despite the biomagnification process, its contents do not present a risk for human health as values were in the range accepted by ANVISA n° 42/13 (Ministério da Saúde. Agência Nacional de Vigilância Sanitária, 2013). In addition, Pb contents in oysters from the Pacoti estuary were observed near the maximum value permitted by the legislation (Torres, 2009).

Torres (2009) identified low values of Cu in oysters (*C. rhizophorae*) and cockles (*Anomalocardia brasiliana*) in the Jaguaribe River estuary, but the contents of Cu in the crustacean's exoskeleton (*Callinectes sapidus*) were up to twice higher than obtained in their muscles. This variation demonstrates that crustaceans may be subject to anomalous Cu levels exceeding their physiological needs, thus resulting in the export of Cu to the carapace prior to ecdysis, as a detoxification process. A few years later, Cu contents in the muscles of oysters (*C. rhizophorae*) exhibited values closer to the limit for food in general allowed by ANVISA n° 685/98 (Soares, 2017). It was also notable that the study by Torres (2009) found that the increased Cu concentrations in the water column were associated with the high content in the sediment, typical also to almost all the EZBN estuaries, as noticed in the previous sections. Cu is associated with OM as identified in the sediment partition and is easily available to filter-feeding organisms.

A study developed in the Potengi Estuary (RN) reported bioaccumulation of Fe, Zn, Cu, Cr, Pb, Cd, Ni, and Ag in oysters (*C. rhizophorae)*, as a consequence of discharges of sewage and industrial effluents (Silva et al., 2001) where Cu and Pb were higher than those allowed by ANVISA n° 685/98 and ANVISA RDC n° 42/13 (Brasil, 1998; Ministério da Saúde. Agência Nacional de Vigilância Sanitária, 2013). Besides, there is no limit value for Zn determined by Brazilian legislation; however, Zn concentrations were an order magnitude higher than observed in São Marcos Bay.

It is remarkable that oysters and carnivorous fish and crustaceans had the best feedback as biomonitors of trace metals, especially for Hg, Cu, Zn, and Pb, in the estuaries of the EZBN. Oysters are widely used as biomonitors due to their filter-feeding and sedentary habits, which incorporate the bioavailable trace metals species from the environment (Rainbow and Phillips, 1993; Góngora-Gómez et al., 2017; Lu et al., 2017). The bioaccumulation of Hg, Cu, Zn, and Pb in the organisms of oysters may result from element availability in the water column of EZBN estuaries, as mentioned previously. Carnivorous fishes are affected by feeding habits and high trophic levels (Bisi et al., 2012). These species are highly consumed by the local population, and although most values were below the legal limit, the constant consumption of these organisms throughout someone's life can lead to toxicity and deleterious effects.

The accumulation occurs when the rate of metal uptake into the body exceeds the combined rate of excretion and detoxification of the metabolically available metal. As a consequence, some aquatic organisms can present changes in the metabolic regulatory processes in the biological system, at molecular, cellular, or physiological levels (NRC, 1987; Rainbow, 2002). Geochemical partitioning showed medium mobility to Pb, Cu, and Zn in sediments and efficient desorption of Pb, Cu, Zn, and Hg from particulate to dissolved fraction in the water column in the EZBN estuaries (Torres, 2009; Carvalho, 2014; Silva et al., 2015; Rios, 2018). These trace metals' mobility reflects on the bioaccumulation and biomagnification in oysters, carnivorous fish, and crustaceans, especially for Pb, Cu, Zn, and Hg. This process may occur due to environmental availability, in which the metal interacts with other environmental matrices that influence their fate and transport processes (Drexler et al., 2003). For example, dissolved Cu can be available for interaction with the gills of an invertebrate, binding to dissolved OM, whereas Cu bound to sulfide in sediments is not (Drexler et al., 2003). Therefore, the monitoring and assessment of aquatic biota with trace metal bioaccumulation and biomagnification is helpful to examine the environmental quality. However, to better understand the processes that act on the reactivity of metals to promote incorporation by biota, it is necessary to expand the collection of data on the metals partition in the EZBN estuarine waters.

7 Assessment of the environmental quality of the EZBN's estuaries

Currently, trace metal studies utilize the sediment quality index as an important tool to evaluate and classify the contamination degree of sediments. It indicates anomalous values in the region originated from natural and/or anthropogenic sources and allows for the comparison of different sedimentary matrices. The most common indexes are the Enrichment Factor (EF) and Geoaccumulation Index (Igeo) (Marins et al., 2004; Buruaem et al., 2012; Nilin et al., 2013; Paula Filho et al., 2015; Barbieri, 2016; Santos et al., 2019). In the present study, Igeo was applied to the metal's contents (Figure 3). This index was proposed by Müller (1986) to measure the level of sediment contamination by environmentally relevant inorganic contaminants. It is determined by the following equation Igeo = $\log_2$(Cn/1.5*Bn), in which Cn is the content of the element in the clay fraction of the sediment, 1.5 is a factor to include the natural fluctuations and even in low anthropogenic inputs, and Bn is the geochemical background value of the element. The Igeo classes and scales range in six degrees of contamination: Class 0: <0 suggests an uncontaminated environment and Class 6: >5 indicates very heavily contaminated sediment.

There are only a few elements with regional background values determined in two estuaries of the EZBN, as mentioned previously. Therefore, these values will be considered representative for all the regions to evaluate the sediment contamination due to the similarity observed in the spatial distribution of metals along with the sediments of the EZBN. The background values utilized were 1.4% for Fe, 633 $\mu g.g^{-1}$ for Mn, 18 $\mu g.g^{-1}$ for Cr, 6.8 $\mu g.g^{-1}$ for Cu, 15 $ng.g^{-1}$ for Hg, 5.9 $\mu g.g^{-1}$ for Pb, and 13.4 $\mu g.g^{-1}$ for Zn (Marins et al., 2004; Paula Filho et al., 2015). The maximum metal concentrations of each estuary were used to determine the index, because some of the studies showed only the minimum and maximum range, and others just the average values.

In Supplementary Material—Supplementary Table S1, Pb and Zn showed Igeo values higher than moderately contaminated (Class 2) in 53% and 25% of the EZBN estuaries, respectively. While for Mn all estuaries were considered uncontaminated. Pb was classified as moderately contaminated (Class 2) in the Anil, São Marcos, São José, Paciencia River, Apodi, and Galinhos estuaries. The Bacanga estuary was indicated as moderately to heavily contaminated (Class 3), while the Parnaíba River Delta and Curimataú estuary were found heavily contaminated for this element (Class 4). Pb is a toxic metal to aquatic biota and humans (Jesus and Cruz, 2019; Kütter et al., 2021),

but the main source of Pb for the region is mainly from natural contribution, urban runoff, inadequate disposal of solid waste, and Pb present in aerosols resulting from the burning of fossil fuels. Pb can be correlated with suspended particulate material, which may favor the co-precipitation of Pb with Fe–Mn oxyhydroxides and $PbCO_3$ in an environment with pH > 6 (Nascimento, 2013; Paula Filho et al., 2014; Azevedo, 2019; Santos et al., 2019), explaining the large spatial distribution of Pb in these estuarine sediments. The anomalous concentrations of Pb reflect its bioaccumulation in oysters with values higher than the limits allowed by the Brazilian legislation ANVISA RDC n° 42/13 (Ministério da Saúde. Agência Nacional de Vigilância Sanitária, 2013).

The Parnaíba River Delta, Ceará, Jaguaribe, and Potengi estuaries were classified as moderately contaminated for Zn (Class 2), while the Anil estuary was considered moderately to heavily contaminated (Class 3). This element is an essential element that participates in the metabolism of proteins, nucleic acids, carbohydrates, and lipids in organisms (Kütter et al., 2021). These high values of Zn in sediments are mostly from lithogenic sources with anthropogenic enrichment from urban runoff and inadequate disposal of solid waste observed in the Parnaíba River Delta (Paula Filho et al., 2014), as identified by the sediment partitioning of Zn associated mainly to residual fraction and secondly to Fe-Mn oxides (Oliveira, 2012; Silva et al., 2015; Rios, 2018). Therefore, Zn from anthropogenic activities that are found bound to the reducible forms in the sediments may be available as soluble species under anoxic conditions (Tessier et al., 1979). As previously mentioned, Zn was also found desorbed in the water column and led to bioaccumulation in oysters of the EZBN estuaries.

Sediments of the Parnaíba River Delta and Potengi estuary were classified as moderately contaminated for Cu (Class 2), and the Curimataú estuary was classified as moderately to heavily contaminated (Class 3). The presence of Cu in high concentrations in water and sediments facilitate bioaccumulation and biomagnification in aquatic organisms (oyster and crustaceans) as observed in the EZBN estuaries. The main sources of Cu observed for the region were natural processes of soil denudation, electroplating, iron smelting, mining, agriculture, and inadequate disposal of wastewater and solid waste (Correa, 2008; Torres, 2009; Paula Filho et al., 2014).

The Curimataú estuary was considered moderately to heavily contaminated by Fe (Class 3). Iron is necessary to the circulatory system of organisms and it is commonly found in high concentrations in soils and sediments in the Earth's crust (Salomons and Förstner, 1984). The presence of Fe in the sediments may be related to the lithogenic source from the Barreiras Formation, which is rich in Fe, Mn, Co, and Cu (Xavier et al., 2017). Igeo for Cr classified Bacanga and Potengi estuaries as moderately contaminated (Class 2). The presence of Cr is related to emissions from agriculture, untreated sewage, and fossil fuels from anchoring boats. Cr is an essential metal to fish metabolism and algal photosynthesis but can be highly toxic when present as soluble species as a result of pH variation (Jesus and Cruz, 2019).

The Ceará and Cocó estuaries, in the state of CE, were the only environments that were uncontaminated and moderately contaminated by Hg, presenting class 1 among all the EZBN estuaries evaluated. Hg is a non-essential metal that is bioaccumulated in oysters and possibly biomagnified in detritivores and omnivores fishes (Vaisman et al., 2005; Almeida, 2015; Rios et al., 2016). Stronger seawater intrusion facilitates the mobilization of Hg from the sediment to the water column and Hg methylation increases its bioavailability (Marins et al., 2004; Dias et al., 2009; Lacerda et al., 2012). This element was found bioaccumulated in oysters and biomagnified in carnivorous fishes and crustaceans in estuaries of the EZBN (Vaisman et al., 2005; Costa, 2009; Torres, 2009; Lopes, 2012; Costa and Lacerda, 2014; Rios et al., 2016; Moura and Lacerda, 2018).

Table 4 shows an overview of the environmental conditions considering the metal contamination, lability indicated by sequential extractions, influence on the aquatic biota, and other major drivers. The estuaries were grouped into 13 hydrographic units according to the National Water Resources Plan (PNRH) to determine the urban population by municipalities (ANA, 2006; ANA, 2017). The annual urbanization rate through population growth, between 2013 and 2035, was estimated according to the United Nations guideline (2018) to estimate the growth of the main anthropogenic factors of contamination by residual metals. Rate urbanization with values below 1% present slow growth, and above 1% demonstrate fast growth. The Anil, Tibiri, Paciência, and Bacanga estuaries are located in the Maranhão Island basin. Ceará, Cocó, and Pacoti estuaries belong to the Metropolitan basin of Fortaleza. Conchas and Piranha-Açu belong to the Piranha-Açu basin. Galinhos, Guamaré, and Ponta do Tubarão estuaries compose the Northern coastline with a diffuse flow of the RN basin, while Papeba and Curimataú estuaries are located in the southern coastline with a diffuse flow of the RN basin. The other environments represent their own hydrographic unit.

The Piranha-Açu, Ceará-Mirim, Nísia-Floresta, and the northern coastline of the RN basin have been found to exhibit low trace metal contamination with uncontaminated to moderately contaminated levels. However, there is no available data about metal speciation and the potential influence of these trace metals on the local biota. The Igeo results suggest trace metal contents are from natural sources, but it should be noted that the margins of these estuaries are home to many aquaculture farms and urban centers. While the rate of urbanization in the estuaries from the northern coastline of the RN and Piranha-Açú basins is slow, with an increase of 0.9% per year between 2013 and 2035, the other basins are experiencing fast growth, with an increase of more than 1% per year.

This indicates that anthropogenic activities in Ceará-Mirim and Nísia-Floresta will increase, leading to a potential rise of metal loads to these environments. While the trace metal contents are not a significant concern, it is essential to monitor the aquatic organisms and the other compartments of these estuaries to evaluate the possible increase of contamination. The monitoring will help to detect any potential risks to the ecological health of these estuaries and help the development of effective management strategies to protect these ecosystems.

The Apodi, São José Bay, and São Marcos Bay environments have been classified as uncontaminated or uncontaminated to moderately contaminated for Cr, Cu, and Zn, while surface sediments are commonly found to be moderately contaminated for Pb. Among these three environments, only São Marcos Bay has reported high concentrations of Zn in fish, and Pb values were not detectable. Its main drivers of metal contamination are natural

sources and domestic sewage. Additionally, São Marcos Bay has intense harbor activities for ore loading, while the Apodi estuary has diverse aquaculture farms on its margins. All basins experience fast growth at a rate of more than 1% per year, suggesting a potential rise of trace metal sources. Therefore, it is crucial to identify the lability of Pb through sequential extractions and monitor and reduce its emissions. Developing biota monitoring is also essential to provide information on the bioaccumulation and biomagnification of metals through the food chain, which is necessary for understanding the potential risks to human health.

The Jaguaribe basin and Metropolitan basin of Fortaleza have been commonly classified as uncontaminated to moderately contaminated for Pb, while Zn and Hg have been identified as the trace metals of most concern, with moderate contamination levels. Although the Jaguaribe estuary is classified as uncontaminated to moderately contaminated for Cu, approximately 50% of Cu in the surface sediments is bioavailable. This bioavailability has a significant impact on the bioaccumulation of Cu in oysters, with concentrations nearing the maximum limit allowed by law. The presence of Ba is also a concern due to its lability, circa 62% in the sediment bounded to exchangeable and carbonates fractions.

Besides the values of Hg in the Ceará and Cocó estuaries, the oysters and fishes did not accumulate this element in their tissues. The Pacoti estuary is classified as uncontaminated to moderately contaminated for Pb, with approximately 50% of the Pb in the surface sediments being bioavailable. This high bioavailability has a notable impact on the oyster population, as they are absorbing the Pb and reaching concentrations close to the maximum limit allowed by law. All basins estimate fast growth at a rate of more than 1% per year, suggesting a potential expansion of trace metal loadings. So, it is important to develop strategies to monitor and reduce the emissions from domestic sewage, aquaculture, and harbor activities because the biota is showing evidence of environmental degradation due to the potential availability of metals. This condition can have significant consequences for both the ecosystem and human health, as oysters are a common food source for many people in the region.

Sediment from the Potengi estuary was classified as moderately contaminated for Cr, Cu, and Zn, but there were no speciation data to estimate the lability of these elements. However, oysters were showing evidence of the availability of Cu and Pb with concentrations higher than what is permitted by Brazilian law. Additionally, while there is no specific legislation on the permitted amount of Zn for seafood consumption, the values of Zn observed in oysters were an order of magnitude greater than those found in oysters from São Marcos Bay. A total of 90% of the population of the Potengi Basin was already living in urban areas in 2013, however, the basin has had a slow rate of urbanization, at 0.8% per year between 2013 to 2035, suggesting stabilization of trace metal emissions that can be considered high. So, it is necessary to warn the population about aquatic organisms that are not appropriate for consumption, conduct more studies to confirm metal speciation for Cu and Pb, and increase monitoring of the local biota, as well as develop strategies to reduce the trace metal emissions from domestic sewage and industrial and aquaculture effluents.

Nevertheless, the environments with the highest concerned contamination in sediment conditions are located in the Maranhão Island basin, the Southern coastline of the RN basin, and the Parnaíba River Delta. The estuaries in Maranhão Island demonstrated moderate contamination and were moderately contaminated to heavily contaminated for Pb, except the Tibiri estuary, which was uncontaminated to moderately contaminated. Some lability of trace metals (Pb, Zn, and Ni) was observed in the sediment of these estuaries, except in the Anil estuary, which did not feature in any of the studies. The Bacanga estuary was the only environment with some data about trace metal bioavailability. The oysters presented Zn in an order of magnitude higher than oysters found in the Potengi estuary. Besides the slow rate of urbanization, 0.8% from 2013 to 2035, Maranhão Island presented more than 80% of the urban population in its area in 2013. Therefore, the metal loads from harbor activities and from domestic, hospital, and industrial sewage must be controlled, and monitoring of the biota quality consumed by the population should begin.

The Curimataú estuary, located on the southern coastline of the state of RN, and the Parnaíba River Delta have shown significant levels of metal contamination. The Curimataú estuary was found to be moderately to heavily contaminated with Fe and Cu, and heavily contaminated with Pb. The presence of Fe in the sediment may be attributed to a lithogenic source from the Barreiras Formation, while Cu and Pb are the result of effluent discharges from shrimp farming and domestic sewage. The Parnaíba River Delta is designated as an Environmental Protection Area, but sediment from the area also shows metal enrichment similar to that of the Curimataú estuary for Pb. Unfortunately, there have been no studies conducted on Pb speciation or contamination in organisms in both environments. However, Zn was found to be present in labile fractions, with 16% bound to exchangeable carbonates in the Parnaíba River Delta. The urbanization rate is estimated to increase moderately from 2013 to 2035 for the protected area and it is expected to remain low for the estuaries in the southern coastline of the state of RN. Therefore, it is strongly recommended that metal speciation is conducted as well as monitoring and reducing metal emissions in these areas.

In general, most of the environments present a lack of information about metal speciation in sediments that exhibited an enrichment of contaminations, as well as there were little data about the biomonitoring of the local organisms. The major drivers of contamination include natural sources, agriculture and aquaculture effluents, domestic and industrial sewage, harbor activities, deforestation, and landfill. Most of the estuaries present an increase of urbanization at a rate of more than 1% per year, suggesting a potential rise of trace metal loadings and anthropogenic contaminations. So, the main responses to these contaminations include identifying and reducing emissions, monitoring the biotic and abiotic compartments, and public warnings on biota contamination by metals that can be a risk to human health. Sediment from the Curimataú estuary, the Parnaíba River Delta, and the Anil and Bacanga estuaries presented the highest metal contaminations for Pb, Zn, Cu, and Fe.

Compared to other urban estuaries located in tropical zones, the EZBN estuaries exhibited Igeo values for Hg, Cu, and Zn below those observed in the Vembanad estuary in India, which is deemed extremely contaminated (Class 6) (Sruthi et al., 2018). However, the Parnaíba River Delta and the Curimataú estuary showed a similar classification for Pb as the Bumbu River and Kokolo

Canal in the Democratic Republic of the Congo, which are considered heavily contaminated (Class 4). The Anil estuary received a similar classification of moderate to heavily contaminated (Class 3) for Zn as the Pearl River Estuary (China) (Kayembe et al., 2018; Chai et al., 2019). In addition, the Igeo value of Pb, Cu, and Zn in the Saigon River Estuary in Vietnam and the Capibaribe Estuary in Brazil exhibited a classification below that observed in the EZBN estuarine sediments, with uncontaminated to moderately contaminated (Class 1) and moderately contaminated (Class 2), respectively (Xavier et al., 2017; Noncent et al., 2020). These comparisons show the similarity of trace metal enrichment in the EZBN estuaries and other tropical estuaries under anthropogenic pressures.

Igeo results have a limitation that needs to be taken into consideration since the reviewed estuaries present some different geological aspects that may affect metal concentrations (El-Robrini et al., 2006; Morais et al., 2006; Vital et al., 2006). Therefore, it is necessary to conduct more studies to determine the natural background levels based on sediment cores and better differentiate between natural and anthropic sources through the Igeo index. Sequential extractions of metals in sediment, and distribution coefficients between the soluble phase (dissolved) and solid phase (particulate and sediment) are necessary to evaluate the mobility of these elements in the environments and their potential for biota intoxication. On the other hand, these assessments accompanied by biomonitoring include all the properties of the estuarine systems and can qualify these systems. However, this review has provided a snapshot of metal contamination in the EZBN, which may help the development of new investments in environmental research in the region as well as assist authorities in their decision-making processes to diminish trace metal inputs from anthropogenic sources, thus reducing the bioaccumulation and biomagnification of metals and reducing risks to human health.

8 Final considerations

Trace metals in the Equatorial Zone of the Brazilian Northeast were more intensively studied in the state of CE, which was distinct from the other three states. Most of the environments showed some anthropogenic enrichment of trace metals (Cu, Pb, Zn, and Hg) either from shrimp farming effluents or domestic and industrial discharges, all of which can alter the environmental quality of the estuaries. Sequential extractions in the sediment suggested low to medium mobility of metals, and that Fe-Mn oxides, OM, and carbonates can act as geochemical carriers of trace metals along the estuarine gradient. These results pointed to the importance of monitoring the main anthropogenic activities in the region, such as shrimp farming effluents and domestic and industrial discharges.

However, compared with studies in other Brazilian estuaries, metals data in EZBN sediments, such as Sr, V, and Mg, are still scarce. The observed metal concentration in water for Cu, Pb, Zn, Hg, and Fe varies over two orders of magnitude in the same large-scale geological province, highlighting the influence of the anthropogenic uses of drainage basins.

Most of the organisms presented trace metal values below the maximum limit established by the Brazilian legislation, but, remarkably, oysters, carnivorous fishes, and crustaceans were the most dependable biomonitors of Cu, Pb, Zn, and Hg, in agreement with the sediment contamination degree evidenced by Igeo. Igeo exhibited anomalous values in the Curimataú estuary, Parnaíba River Delta, and the Anil and Bacanga estuaries for Pb, Zn, Cu, and Fe with a classification of moderately to heavily contaminated and heavily contaminated. Anomalous values may be related to lithogenic sources, domestic sewage, and inadequate disposal of wastewater from aquaculture and solid waste. In addition, more studies to determine the natural background levels, based on cores sampled in different estuaries, and metal speciation are necessary to better differentiate between natural and anthropic sources.

Author contributions

TS was responsible for the analyses of metals from the Parnaíba River Delta and part of São Marcos Bay, for the supervision of LA, literature review, preparation of graphs and tables, and writing of the manuscript. RM was responsible for guidance of practical work and preparation of the article, writing of the manuscript, and funding. LA made the sequential analyses of metals in the sediments and discussion of results from the Parnaíba River Delta mentioned in the manuscript. All authors contributed to the article and approved the submitted version.

Funding

This work was supported by the Coordination for the Improvement of Higher Education Personnel (CAPES) through a Ph.D. grant to TS and the Cearense Foundation for Scientific and Technological Development Support (FUNCAP)/Programme of Support to Centers of Excellence (PRONEX; PR2-0101-00052.01.00/15) coordinated by RM.

Conflict of interest

The authors declare that the research was conducted in the absence of any commercial or financial relationships that could be construed as a potential conflict of interest.

Publisher's note

Supplementary material

The Supplementary Material for this article can be found online at: https://www.frontiersin.org/articles/10.3389/feart.2023.1142649/full#supplementary-material

References

Abessa, D. M. de S., Carr, R. S., Rachid, B. R. F., Sousa, E. C. P. M. de, Hortelani, M. A., and Sarkis, J. E. de S. (2005). Influence of a Brazilian sewage outfall on the toxicity and contamination of adjacent sediments. *Mar. Pollut. Bull.* 50, 875–885. doi:10.1016/j.marpolbul.2005.02.034

Aguiar, J. E. (2014). Contribuição ao estudo da mineralogia de sedimentos na plataforma continental dos estados do Ceará, Piauí e Maranhão através da microscopia analítica SEM/EDS. Available at: http://www.repositorio.ufc.br/handle/riufc/8508.

Aguiar, J. E. (2005). *Geoquímica de metais-traço em sedimentos superficiais nos estuários dos Rios Ceará E Pacoti, CE.* Ceará: Federal University of Ceará. [undergraduate monography]. [Fortaleza].

Aguiar, J. E., Lacerda, L. D. de, Miguens, F. C., and Marins, R. V. (2014). The geostatistics of the metal concentrations in sediments from the eastern Brazilian continental shelf in areas of gas and oil production. *J. South Am. Earth Sci.* 51, 91–104. doi:10.1016/j.jsames.2013.12.005

Almeida, B. F. M. A. D. (2015). Determinação da concentração de mercúrio total e do valor econômico ambiental no trecho do Rio Cocó-CE. *Bull. Environ. Contam. Toxicol.* 8 (2), 8. doi:10.6008/2179-6858.2017.002.0024

Almeida, B. F. M. A. de. (2017). Valoração e percepção ambiental: estudo de caso no baixo curso do rio Cocó, Fortaleza, Ceará, Brasil. *Ibero-Am. J. Environ. Sci.* 8 (2), 8. doi:10.6008/2179-6858.2017.002.0024

ANA (2021). in *Bacias e Divisões Hidrográficas do Brasil*. Editor A. N. d. Á. e. S. B. ANA (Rio de Janeiro: Instituto Brasileiro de Geografia e Estatística).

Ana (2017). *ATLAS Esgotos - informações por Município. Agência Nacional de Águas e Saneamento Básico*. Indira Paryavaran Bhawan Jorbagh Road, New Delhi: Secretaria Nacional de Saneamento Ambiental. Ministério do Meio Ambiente. Available at: https://metadados.snirh.gov.br/geonetwork/srv/api/records/1d8cea87-3d7b-49ff-86b8-966d96c9eb01/attachments/ATLAS_Esgotos_Tabela_Completa_por_Municipio.xlsx.

Ana (2006). Nível 2 de Sub-bacias do Plano Nacional de Recursos Hídricos. Agência Nacional de Águas e Saneamento Básico, Ministério do Meio Ambiente. Available at: https://metadados.snirh.gov.br/geonetwork/srv/api/records/f50527b9-24ed-41d5-b063-b5acfb25e10d (Accessed January 3, 2023).

Aprile, F. M., and Bouvy, M. (2010). Heavy metal levels in surface waters from a tropical river basin, Pernambuco State, northeastern Brazil. *Acta Sci. - Biol. Sci.* 32, 357–364. doi:10.4025/actascibiolsci.v32i4.5231

Aquino da Silva, A. G., Stattegger, K., Vital, H., and Schwarzer, K. (2019). Coastline change and offshore suspended sediment dynamics in a naturally developing delta (Parnaíba Delta, NE Brazil). *Mar. Geol.* 410, 1–15. doi:10.1016/j.margeo.2018.12.013

Azevedo, I. H. R. (2019). Dinâmica e distribuição de metais no complexo estuarino Arraial/São José, Maranhão. Available at: https://tedebc.ufma.br/jspui/handle/tede/tede/2787.

Bandeira, I. C. N. (2013). *Geodiversidade do estado do Maranhão*. 1. Teresina, Brasil: CPRM Serviço Geológico do Brasil.

Baptista Neto, J. A., Peixoto, T. C. S., Smith, B. J., Mcalister, J. J., Patchineelam, S. M., Patchineelam, S. R., et al. (2013). Geochronology and heavy metal flux to guanabara bay, Rio de Janeiro state: a preliminary study. *An. Acad. Bras. Cienc.* 85, 1317–1327. doi:10.1590/0001-3765201394612

Barbieri, M. (2016). The importance of enrichment factor (EF) and geoaccumulation index (Igeo) to evaluate the soil contamination. *J. Geol. Geophys.* 5, 1–4. doi:10.4172/2381-8719.1000237

Barbosa, F. G., Wallner-Kersanach, M., and Baumgarten, M. D. G. Z. (2012). Metais traço nas águas portuárias do estuário da Lagoa dos Patos, RS. *Rs. Braz. J. Aquat. Sci. Technol.* 16, 27–36. doi:10.14210/bjast.v16n2.p27-36

Barletta, M., Lima, A. R. A., and Costa, M. F. (2019). Distribution, sources and consequences of nutrients, persistent organic pollutants, metals and microplastics in South American estuaries. *Sci. Total Environ.* 651, 1199–1218. doi:10.1016/j.scitotenv.2018.09.276

Bianchi, T. S. (2007). *Biogeochemistry of estuaries*. New York: OXFORD University Press.

Bisi, T. L., Lepoint, G., Azevedo, A. D. F., Dorneles, P. R., Flach, L., Das, K., et al. (2012). Trophic relationships and mercury biomagnification in Brazilian tropical coastal food webs. *Ecol. Indic.* 18, 291–302. doi:10.1016/j.ecolind.2011.11.015

Braga, A. R. C., Castro, Í. B. de, and Rocha-barreira, C. D. A. (2006). Compostos Organoestânicos: um risco potencial para contaminação do pescado marinho. *Bol. Técnico-científico do CEPENE Compost.* 14, 103–107.

Brasil (1965). *Decreto no 55871, de 26 de março de 1965. Modifica o Decreto no 50.040, de 24 de janeiro de 1961, referente a normas reguladoras do emprêgo de aditivos para alimentos, alterado pelo Decreto no 691, de 13 de março de 1962*. Nairobi, Kenya: united nations environment programme.

Brasil (1998). *Portaria no 685, de 27 de agosto de 1998. Aprova o Regulamento Técnico: princípios Gerais para o Estabelecimento de Níveis Máximos de Contaminantes Químicos em Alimentos" e seu Anexo: limites máximos de tolerância para contaminantes inorgânicos*. Available at: http://bvsms.saude.gov.br/bvs/saudelegis/anvisa/1998/prt0685_27_08_1998_rep.html.

BrasilMinistério da Saúde. Agência Nacional de Vigilância Sanitária (2013). *Dispõe sobre o Regulamento Técnico MERCOSUL sobre Limites Máximos de Contaminantes Inorgânicos em Alimentos*. Available at: https://bvsms.saude.gov.br/bvs/saudelegis/anvisa/2013/rdc0042_29_08_2013.pdf.

Buruaem, L. M., Hortellani, M. A., Sarkis, J. E., Costa-Lotufo, L. V., and Abessa, D. M. S. (2012). Contamination of port zone sediments by metals from Large Marine Ecosystems of Brazil. *Mar. Pollut. Bull.* 64, 479–488. doi:10.1016/j.marpolbul.2012.01.017

Cantinho, K. M. C. R. (2017). *Caracterização e avaliação da qualidade ambiental do estuário Ponta Do Tubarão (RN) com base na água, sedimento e macroalgas marinhas*. Available at: https://repositorio.ufrn.br/handle/123456789/26958.

Carvalho, A. A. De, Montenegro, A. A. D. A., Silva, H. P., Lopes, I., Morais, J. E. F. d., and Silva, T. G. F. d. (2020). Trends of rainfall and temperature in Northeast Brazil. *R. Bras. Eng. Agríc. Ambient.* 24 (1), 15–23. doi:10.1590/1807-1929/agriambi.v24n1p15-23

Carvalho, C. E. V. de, Salomão, M. S. M. de B., Molisani, M. M., Rezende, C. E. de, and Lacerda, L. D. (2002). Contribution of a medium-sized tropical river to the particulate heavy-metal load for the South Atlantic Ocean. *Sci. Total Environ.* 284, 85–93. doi:10.1016/S0048-9697(01)00869-5

Carvalho, G. P., Cavalcante, P. R., de Castro, A. C., and Rojas, M. O. (2000). Preliminary assessment of heavy metal levels in Mytella falcata (Bivalvia, Mytilidae) from Bacanga River estuary, São Luís, state of Maranhão, northeastern Brazil. *Rev. Bras. Biol.* 60, 11–16. doi:10.1590/S0034-71082000000100003

Carvalho, L. M. da S. (2014). A biogeoquímica de metais em sedimentos de manguezal na ilha do maranhão. Available at: https://tedebc.ufma.br/jspui/handle/tede/tede/993.

Castro, Í. B. De, Cascon, H. M., and Fernandez, M. A. (2000). Imposex em Thais Haemastoma (Linnaeus, 1767) (Mollusca: gastropoda), uma indicação da contaminação por organoestânicos na costa do município de Fortaleza – ceará – brasil. *Arq. Ciências do Mar.* 33, 143–148. doi:10.32360/acmar.v33i1-2.11806

Castro, Í. B. D., Meirelles, C. A. O. D., Matthews-Cascon, H., Almeida Rocha-Barreira, C. D., Penchaszadeh, P., and Bigatti, G. (2008). Imposex in endemic volutid from Northeast Brazil (Mollusca: gastropoda). *Braz. Arch. Biol. Technol.* 5, 1065–1069. doi:10.1590/s1516-89132008000500024

Chai, M., Li, R., Tam, N. F. Y., and Zan, Q. (2019). Effects of mangrove plant species on accumulation of heavy metals in sediment in a heavily polluted mangrove swamp in Pearl River Estuary, China. *Environ. Geochem. Health* 41, 175–189. doi:10.1007/s10653-018-0107-y

CHN (2019). Porto de Luís Correia (Estado do Piauí) - 2019. Cent. Hidrogr. da Mar., 2. Available at: https://www.marinha.mil.br/chm/tabuas-de-mare (Accessed December 1, 2019).

CNI (2019). Perfil da Indústria nos Estados. Confed. Nac. da Indústria, 4. Available at: http://perfildaindustria.portaldaindustria.com.br/ (Accessed July 15, 2019).

CONAMA no 357 (2005). *Resolução CONAMA N° 357, de 17 de março de 2005* (retificada)*. Available at: https://www.icmbio.gov.br/cepsul/images/stories/legislacao/Resolucao/2005/res_conama_357_2005_classificacao_corpos_agua_rtfcda_altrd_res_393_2007_397_2008_410_2009_430_2011.pdf.

CONAMA, C. N. do M. A (2004). *Resolução CONAMA no 3444/04*, 53. Cambridge: Cambridge University Press, 1689–1699. doi:10.1017/CBO9781107415324.004

Correa, T. L. (2008). *Impactos Geoquímicos e Sócio-Ambientais do Estuário do Rio Potengi - região Metropolitana da Grande Natal/RN [dissertation/master's thesis]*. Natal: Federal University of Rio Grande do Norte. Available at: https://repositorio.ufrn.br/jspui/bitstream/123456789/18187/1/TatianaLC.pdf.

Costa, B. G. B. (2009). *Distribuição de mercúrio (Hg) em sedimento, água e biota da região de influencia dos efluentes da carcinicultura, na Gamboa do Cumbe- Rio Jaguaribe- Ceará- Brasil*. doi:10.2174/138920312803582960

Costa, B. G. B., and Lacerda, L. D. (2014). Mercury (Hg) in fish consumed by the local population of the Jaguaribe River lower basin, Northeast Brazil. *Environ. Sci. Pollut. Res.* 21, 13335–13341. doi:10.1007/s11356-014-3297-6

Costa, B. G. B., Soares, T. C. M., Torres, R. F., and Lacerda, L. D. (2013). Mercury distribution in a mangrove tidal creek affected by intensive shrimp farming. *Bull. Environ. Contam. Toxicol.* 90, 537–541. doi:10.1007/s00128-012-0957-4

Costa, E. S., Grilo, C. F., Wolff, G. A., Thompson, A., Figueira, R. C. L., and Neto, R. R. (2015). Evaluation of metals and hydrocarbons in sediments from a tropical tidal flat estuary of Southern Brazil. *Mar. Pollut. Bull.* 92, 259–268. doi:10.1016/j.marpolbul.2014.11.028

DiasdaS, F. J. (2007). *Hidrodinâmica das descargas fluviais para o estuário do Rio Jaguaribe (CE). [dissertation/master's thesis]. [Fortaleza]*. Ceará, Brazil: Federal University of Ceará. Available at: https://repositorio.ufc.br/bitstream/riufc/1358/3/2007_dis_fjsdias.pdf.

Dias, F. J., da, S., Castro, B. M., Lacerda, L. D., Miranda, L. B., and Marins, R. V. (2016). Physical characteristics and discharges of suspended particulate matter at the continent-ocean interface in an estuary located in a semiarid region in northeastern Brazil. *Estuar. Coast. Shelf Sci.* 180, 258–274. doi:10.1016/j.ecss.2016.08.006

Dias, F. J. D. S., Lacerda, L. D. D., Marins, R. V., and Peres, T. F. (2009). *Descargas de metais particulados ao longo do estuário do Rio Jaguaribe (CE) durante um ciclo de maré de sizígia 2000–2003*. Available at: http://www.sbgq.org.br/index.php?option=com_phocadownload&view=category&download=287&id=20:hidrogeoquimica.

Dias, F. J. D. S., Marins, R. V., and Maia, L. P. (2013). Impact of drainage basin changes on suspended matter and particulate copper and zinc discharges to the ocean from the Jaguaribe River in the semiarid NE Brazilian coast. *J. Coast. Res.* 290, 1137–1145. doi:10.2112/jcoastres-d-12-00115.1

Drexler, J., Fisher, N., Henningsen, G., Lanno, R., Mcgeer, J., and Sappington, K. (2003). *Issue paper on the bioavailability and bioaccumulation of metals*. Washington: United States Environmental Protection Agency.

Du Laing, G., Rinklebe, J., Vandecasteele, B., Meers, E., and Tack, F. M. G. (2009). Trace metal behaviour in estuarine and riverine floodplain soils and sediments: a review. *Sci. Total Environ.* 407, 3972–3985. doi:10.1016/j.scitotenv.2008.07.025

Duquesne, S., Newton, L. C., Giusti, L., Marriott, S. B., Stark, H.-J., and Bird, D. J. (2006). Evidence for declining levels of heavy-metals in the Severn Estuary and Bristol Channel, U.K. and their spatial distribution in sediments. *Environ. Pollut.* 143, 187–196. doi:10.1016/j.envpol.2005.12.002

El-Robrini, M., Valter Marques, J., Silva, M. A. M. A. D., Robrini, M. H. S. E., Feitosa, A. C., Tarouco, J. E. F., et al. (2006). "Maranhão," in *Erosão e Progradação do Litoral Brasileiro*. Editor D. Muehe (Brasília: The Federal University of Viçosa is a Federal University), 87–130. doi:10.13140/RG.2.1.1916.8723

FUNCEME (2019). *Fundação Cearense de Meteorologia. Calendário das Chuvas no Estado do Ceará*. Available at: http://www.funceme.br/app-calendario/diario/municipios/maxima/2023/1.

Furtado, J. G. C. (2007). *Estudo De Impactos Ambientais Causados Por Metais Pesados Em Água Do Mar Na Baía De São Marcos: correlações e Níveis Background*. Available at: https://www.ufpb.br/ppgq/contents/documentos/teses-e-dissertacoes/dissertacoes/2007/Dissertacao_Jethania_G_C_Furtado.pdf.

Garlipp, A. B. (2006). Variação Espacial E Sazonal De Elementos Maiores E Traços No Estuário Do Rio Curimataú (Rn), Através De Dados Geoquímicos e de Sensoriamento Remoto. Available at: https://repositorio.ufrn.br/handle/123456789/18370.

ICMBio (2018). in *Atlas dos manguezais do brasil*. Editor M. A. Gonçalves Brasília Available at: https://ava.icmbio.gov.br/pluginfile.php/4592/mod_data/content/14085/atlas%20dos_manguezais_do_brasil.pdf.

Gonçalves, G. M., and Carvalho, C. E. V. de (2006). Particulate heavy metal dynamics in a tropical estuary under distinct river discharge and tidal regimes, southeastern, Brazil. *J. Coast. Res.* Special Issue No. 39. Proceedings of the 8th International Coastal Symposium (ICS 2004) 2, 1032–1035.

Góngora-Gómez, A. M., García-ulloa, M., Muñoz-sevilla, N. P., Domínguez-orozco, A. L., Paulina, B., Hernández-sepúlveda, J. A., et al. (2017). Heavy-metal contents in oysters (*Crassostrea gigas*) cultivated on the southeastern coast of the Gulf of California, Mexico. *Hidrobiológica* 27, 219–227. doi:10.24275/uam/izt/dcbs/hidro/2017v27n2/garcia

González-Gorbena, E., Wilson Junior, G., Rosman, P. C. C., and Qassim, R. Y. (2015). Effects of hydrokinetic energy turbine arrays on sediment transport at São Marcos Bay, Brazil 9th Symp River, Coast Estuar Morphodynamics, 2. Available at: http://www.macrothink.org/journal/index.php/ast/article/view/6544.

Hadlich, H. L., Venturini, N., Martins, C. C., Hatje, V., Tinelli, P., Gomes, L. E. de O., et al. (2018). Multiple biogeochemical indicators of environmental quality in tropical estuaries reveal contrasting conservation opportunities. *Ecol. Indic.* 95, 21–31. doi:10.1016/j.ecolind.2018.07.027

Horvat, M. (1997). Mercury behavior in estuarine and coatal environment. *Trans. Ecol. Environ.* 14, 547–556.

Huang, J., Ge, X., and Wang, D. (2012). Distribution of heavy metals in the water column, suspended particulate matters and the sediment under hydrodynamic conditions using an annular flume. *J. Environ. Sci. (China)* 24, 2051–2059. doi:10.1016/S1001-0742(11)61042-5

IBGE (2020). Paronama. Inst. Bras. Geogr. e Estatística IBGE. Available at: https://cidades.ibge.gov.br/brasil/panorama.

INMET (2019). *Normais climatológicas do brasil. Inst. Nac. Meteorol., 1*. Available at: http://www.inmet.gov.br/portal/index.php?r=clima/normaisClimatologicas.

INMET (2020). *Normal climatológica do brasil 1981-2010. Inst. Nac. Meteorol.* Available at: https://portal.inmet.gov.br/servicos/normais-climatol%C3%B3gicas.

Jesus, S. B. de, and Cruz, M. J. M. (2019). Caracterização geoquímica do estuário do rio Una, BA, brasil. *Geochim. Bras.* 33, 286–302. doi:10.21715/gb2358-2812.2019333286

Kayembe, J. M., Sivalingam, P., Diz, C., Ngelinkoto, P., Otamonga, J., Mulaji, C. K., et al. (2018). Assessment of water quality and time accumulation of heavy metals in the sediments of tropical urban rivers: case of Bumbu River and Kokolo Canal, Kinshasa City, Democratic Republic of the Congo. *J. Afr. Earth Sci.* 147, 536–543. doi:10.1016/j.jafrearsci.2018.07.016

Kütter, V. T., Moreira, V. A., Kütter, M. T., Silva-Filho, E. V., Marques, E. D., Garnier, J., et al. (2021). Metal bioavailability and distribution in the fish community in a tropical estuary, Sepetiba Bay, Rio de Janeiro, Brazil. *Geochim. Bras.* 35, 17–38. doi:10.21715/gb2358-2812.2021351017

Lacerda, L. D. De, Belmino, I. K. B., Moreira, L. B., and Marins, R. V. (2019). Effect of dredging on Hg distribution in water and sediments in the Mucuripe Harbor, Fortaleza, NE Brazil. *Arq. Ciências do Mar.* 52, 77–84. doi:10.32360/acmar.v52i2.42167

Lacerda, L. D. de, Marins, R. V., and Dias, F. J. da S. (2020). An arctic paradox: response of fluvial Hg inputs and bioavailability to global climate change in an extreme coastal environment. *Front. Earth Sci.* 8. doi:10.3389/feart.2020.00093

Lacerda, L. D. De, Marins, R. V., Vaisman, A. G., Maia, S. R. R., and Aguiar, J. E. (2004). Contaminação por metais pesados e pesticidas nas bacias inferiores dos Rios Curimataú e Açu (RN) e Rio Jaguaribe (CE). *Assoc. Bras. Criadores Camarão* 1–59.

Lacerda, L. D., Marins, R. V., Dias, F. J. S., and Soares, T. M. (2012). The arctic paradox: impacts of climate changes on rivers from the arctic and the semiarid increase mercury export to the ocean. *Oceano. Rev. Virtual quim.* 4, 456–463. doi:10.5935/1984-6835.20120034

Lacerda, L. D., and Marins, R. V. (2006). Geoquímica de sedimentos e o monitoramento de metais na Plataforma Continental Nordeste Oriental do Brasil. *Geochim. Bras.* 20, 123–135.

Lacerda, L. D., Santos, J. A., Madrid, R. M., and Jay, J. A. (2006). Total and methylmercury in three species of sea turtles of Baja California Sur. *Mar. Pollut. Bull.* 52, 1816–1823. doi:10.1016/j.marpolbul.2006.09.019

Lacerda, L. D., Soares, T. M., Costa, B. G. B., and Godoy, M. D. P. (2011). Mercury emission factors from intensive shrimp aquaculture and their relative importance to the Jaguaribe River Estuary, NE Brazil. *Bull. Env. Contam. Toxicol.* 87, 657–661. doi:10.1007/s00128-011-0399-4

Landim, M., Bittencourt, P., Martin, L., and Reima, I. (2005). Longshore transport on the northeastern Brazilian coast and implications to the location of large scale accumulative and erosive zones: an overview. *Mar. Geol.* 219, 219–234. doi:10.1016/j.margeo.2005.06.006

Li, X., Wang, Y., Li, B., Feng, C., Chen, Y., and Shen, Z. (2013). Distribution and speciation of heavy metals in surface sediments from the Yangtze estuary and coastal areas. *Environ. Earth Sci.* 69, 1537–1547. doi:10.1007/s12665-012-1988-1

Lima, E. T. (1999). *Diretrizes estratégicas para os Portos do Nordeste*. Rio de Janeiro: National Bank for Economic and Social Development. Available at: https://web.bndes.gov.br/bib/jspui/bitstream/1408/2922/1/BS%2010%20Diretrizes%20estrategicas%20para%20os%20portos%20do%20Nordeste_P.pdf.

Lopes, D. N. M. (2012). Mércúrio Total em Peixes do RIo Jaguaribe-jusante do dique de Itaiçaba/CE. Available at: http://www.dt.co.kr/contents.html?article_no=2012071302010531749001.

Lu, G. Y., Ke, C. H., Zhu, A., and Wang, W. X. (2017). Oyster-based national mapping of trace metals pollution in the Chinese coastal waters. *Environ. Pollut.* 224, 658–669. doi:10.1016/j.envpol.2017.02.049

Machado, A. A. de S., Spencer, K., Kloas, W., Toffolon, M., and Zarfl, C. (2016). Metal fate and effects in estuaries: a review and conceptual model for better understanding of toxicity. *Sci. Total Environ.* 541, 268–281. doi:10.1016/j.scitotenv.2015.09.045

Machado Júnior, J., and Macedo, J. (2016). A relação do turismo no Delta do Parnaíba com comunidades locais. *Cult. Rev. Cult. Tur.* 10, 71–88.

Maia, S. R. R. (2004). Distribuição e partição geoquímica de metais traço na costa norte de Fortaleza, CE. Available at: http://www.repositorio.ufc.br/handle/riufc/1628.

Marins, R. V., Lacerda, L. D. De, Abreu, I. M., and Dias, F. J. da S. (2003). Efeitos da açudagem no rio Jaguaribe. *Ciência Hoje* 33, 66–70.

Marins, R. V., Paula Filho, F. J. De, Rodrigues Maia, S. R., De Lacerda, L. D., and Marques, W. S. (2004). Distribuição de mercúrio total como indicador de poluição urbana e industrial na costa Brasileira. *Quim. Nova* 27, 763–770. doi:10.1590/S0100-40422004000500016

Marins, R. V., Paula Filho, F. J., Eschrique, S. A., and Lacerda, L. D. (2011). Anthropogenic sources and distribution of phosphorus in sediments from the Jaguaribe River estuary, NE, Brazil. *Braz. J. Bio.* 71 (3), 673–678. doi:10.1590/S1519-69842011000400011

Molisani, M. M., Kjerfve, B., Barreto, R., and Lacerda, L. D. D. (2007). Land-sea mercury transport through a modified watershed, SE Brazil. *Water Res.* 41, 1929–1938. doi:10.1016/j.watres.2007.02.007

Molisani, M. M., Esteves, F. de A., Lacerda, L. D., and Rezende, C. E. de (2013). Emissões naturais e antrópicas de nitrogênio, fósforo e metais para a bacia do Rio Macaé (Macaé, RJ, Brasil) sob influência das atividades de exploração de petroleo e gás na Bacia de Campos. *gás Bacia Campos* 36, 27–66. doi:10.1590/s0100-40422013000100006

Morais, J. O. de, Freire, G. S. S., Pinheiro, L. D. S., Souza, M. J. N. de, Carvalho, A. M. De, Pessoa, P. R. S., et al. (2006). "Ceará," in *Erosão e progradação do litoral brasileiro*. Editors D. Muehe and D. F. Brasília, 131–154.

Morais, J. O. de (1977). Processos de Sedimentação na baía de São Marcos. *Estado do Maranhão, Bras. Arq. Ciencias Mar.* 17, 153–164.

Moreira, L. B., Braga Castro, Í., Fillmann, G., Peres, T. F., Cavalcante Belmino, I. K., Sasaki, S. T., et al. (2021). Dredging impacts on the toxicity and development of sediment quality values in a semi-arid region (Ceará state, NE Brazil). *Environ. Res.* 193, 110525. doi:10.1016/j.envres.2020.110525

Mori, C., Santos, I. R., Brumsack, H., Schnetger, B., Dittmar, T., and Seidel, M. (2019). Non-conservative behavior of dissolved organic matter and trace metals (Mn, Fe, Ba) driven by porewater exchange in a subtropical mangrove-estuary. *Front. Mar. Sci.* 6, 1–21. doi:10.3389/fmars.2019.00481

Mosley, L. M., and Liss, P. S. (2019). Particle aggregation, pH changes and metal behaviour during estuarine mixing: review and integration. *Mar. Frenshwater Res.* 71, 300–310. doi:10.1071/mf19195

Mounier, S. J. L., Marins, R. V., Lacerda, L. D. de, and de Lacerda, L. D. (2018). "Determining the influence of urbanization on mangrove zones of northeastern Brazil: characterization of Ceará state coastal zone organic matter inputs," in *Threats to mangrove forests*. Editors C. Makowski and C. W. Finkl (Cham: Springer), 199–222. doi:10.1007/978-3-319-73016-5

Moura, V. L., and Lacerda, L. D. De (2018). Contrasting mercury bioavailability in the marine and fluvial dominated areas of the Jaguaribe River basin, Ceará, Brazil. *Bull. Environ. Contam. Toxicol.* 0, 0. doi:10.1007/s00128-018-2368-7

MMA (2006). in *Erosão e progradação no litoral brasileiro*. Editors D. Muehe Brasília and DF. doi:10.1016/S0920-4105(01)00162-0

Müller, V. G. (1986). Schadstoffe in sedimenten - sedimente als schadstoffe von. *Mittl. Österreichischen Geol. Ges.* 79, 107–126. doi:10.1055/s-2007-1023171

Nascimento, A. S. do (2013). Distribuição e fracionamento de metais em sedimento do Rio Tibiri na Ilha do Maranhão. Available at: https://tedebc.ufma.br/jspui/handle/tede/tede/960.

Nilin, J. (2008). Avaliação da qualidade do sedimento do estuário do Rio Ceará. Available at: http://www.repositorio.ufc.br/handle/riufc/18362.

Nilin, J. (2012). Biomarcadores em estudos ambientais: a vigilia dos bivalves na ria de Aveiro (Portugal) e no rio Ceará (brasil). Available at: http://www.dt.co.kr/contents.html?article_no=2012071302010531749001.

Nilin, J., Moreira, L. B., Aguiar, J. E., Marins, R., Denis, M. de S. A., Tito, M., et al. (2013). Sediment quality assessment in a tropical estuary: the case of Ceará River, Northeastern Brazil. *Mar. Environ. Res.* 91, 89–96. doi:10.1016/j.marenvres.2013.02.009

Noncent, D., Strady, E., Némery, J., Thanh-Nho, N., Denis, H., Mourier, B., et al. (2020). Sedimentological and geochemical data in bed sediments from a tropical river-estuary system impacted by a developing megacity, Ho Chi Minh City - Vietnam. *Data Br.* 31, 105938. doi:10.1016/j.dib.2020.105938

NRC (1987). Biological markers in environmental health research. *Environ. Health Perspect.* 74, 3–9. doi:10.2307/3430428

Oliveira, R. C. B. de (2012). Investigação do comportamento geoquímico de metais-traços em solos e sedimentos da bacia inferior do Rio Jaguaribe, Nordeste do Brasil. Available at: https://repositorio.ufc.br/bitstream/riufc/19782/1/2012_tese_rcbdeoliveira.pdf.

Oliveira, R. C. B. de, and Marins, R. V. (2011). Trace metals dynamics in soil and estuarine sediment as a major factor controlling contaminants contribution to the aquatic environment: review. *Rev. Virtual Quím.* 3. doi:10.5935/1984-6835.20110014

Passos, E. D. A., Alves, J. D. P. H., Garcia, C. A. B., and Costa, A. C. S. (2011). Metal fractionation in sediments of the sergipe river, northeast, Brazil. *J. Braz. Chem. Soc.* 22, 828–835. doi:10.1590/s0103-50532011000500004

Paula Filho, F. J. de, Marins, R. V., Aguiar, J. E., Peres, T. F., and Lacerda, L. D. de (2014). "Emisiones Naturales y antrópicas de Zn, Cu, Pb, Cr, Cd y Hg al Delta de Río Parnaíba/NE/Brasil," in *Procesos geoquímicos de la superficie en América Latina*. Editors J. E. Marcovecchio, S. E. Botté, and H. Freije (Bahía Blanca: Sciedad Iberoamericana de Física y Química Ambiental), 251–278.

Paula Filho, F. J. de, Marins, R. V., Lacerda, L. D. de, Aguiar, J. E., and Peres, T. F. (2015). Background values for evaluation of heavy metal contamination in sediments in the Parnaíba River Delta estuary, NE/Brazil. *Mar. Pollut. Bull.* 91, 424–428. doi:10.1016/j.marpolbul.2014.08.022

Paula Filho, F. J. de, Marins, R. V., Santos, D. V., and Menezes, J. M. (2019). "Acumulation of heavy metals in sediments of the Parnaíba River Delta," in *Actas de la V Reunión Argentina de Geoquímica de la Superficie*. Editors B. Guido, S. Lucía, T. Carolina, and C. Eleonora (La Plata: Asociación Argentina de Sedimentología), 138–141.

Pejman, A., Nabi Bidhendi, G., Ardestani, M., Saeedi, M., and Baghvand, A. (2017). Fractionation of heavy metals in sediments and assessment of their availability risk: a case study in the northwestern of Persian Gulf. *Mar. Pollut. Bull.* 114, 881–887. doi:10.1016/j.marpolbul.2016.11.021

Peres, T. F. (2012). Influência da biota na acumulação de metais pesados nos sedimentos superficiais do estuário do rio Jaguaribe, praia de Ponta Grossa e praia de Arpoeira, Ceará. Available at: http://www.repositorio.ufc.br/handle/riufc/11468.

Pinheiro, L. de S., Coriolano, L. N., da Costa, M. F., and Dias, J. A. (2008). Prefácio - O Nordeste brasileiro e a Gestão Costeira. *Rev. Gestão Costeira Integr.* 8, 5–10. doi:10.5894/rgci58

Polzin, D., and Hastenrath, S. (2014). Climate of Brazil's nordeste and tropical Atlantic sector: preferred time scales of variability. *Rev. Bras. Meteorol.* 29, 153–160. doi:10.1590/s0102-77862014000200001

Rainbow, P., and Phillips, D. J. H. (1993). Cosmopolitan biomonitors of trace metals. *Mar. Pollut. Bull.* 26, 593–601. doi:10.1016/0025-326x(93)90497-8

Rainbow, P. S. (2002). Trace metal concentrations in aquatic invertebrates: why ans so what? *Environ. Pollut.* 120, 497–507. doi:10.1016/S0269-7491(02)00238-5

Rios, J. H. L. (2018). *Distribuição e Fracionamento Geoquímico de Metais em Sedimento Estuarino do Semiarido Barasileiro sob Diferentes Estações Climáticas*. Available at: http://www.repositorio.ufc.br/handle/riufc/32410.

Rios, J. H. L., Marins, R. V., Oliveira, K. F., and Lacerda, L. D. (2016). Long-term (2002–2015) changes in mercury contamination in NE Brazil depicted by the mangrove oyster crassostraea rhizophorae (guilding, 1828). *Bull. Environ. Contam. Toxicol.* 97, 474–479. doi:10.1007/s00128-016-1855-y

Robert, S., Blanc, G., Schafer, J., Lavaux, G., and Abril, G. (2004). Metal mobilization in the Gironde Estuary (France): the role of the soft mud layer in the maximum turbidity zone. *Mar. Chem.* 87, 1–13. doi:10.1016/S0304-4203(03)00088-4

Salomons, W., and Förstner, U. (1984). *Metals in the hydrocycle*. Cham: Springer. doi:10.1007/978-3-642-69325-0

Santana, L. M. B. M., Lotufo, L. V. C., and Abessa, D. M. S. (2015). A contaminação antrópica e seus efeitos em três estuários do litoral do Ceará, Nordeste do Brasil-Revisão. *Arq. Ciências do Mar.* 48, 93–115. doi:10.32360/acmar.v48i2.5853

Santos, T. T. L., Marins, R. V., and Dias, F. J. da S. (2019). Carbon influence on metal distribution in sediment of Amazonian macrotidal estuaries of northeastern Brazil. *Environ. Monit. Assess.* 191, 1–16. doi:10.1007/s10661-019-7626-6

Silva, G. S. da, Côrrea, L. B., Marques, A. L. B., Marques, E. P., De Nunes, M. L. F., De Sousa, E. R., et al. (2015). The role of metals and their fractions in the Bacanga River estuary: an example of the anthropogenic interference in a tropical ecosystem. *Rev. Virtual Quim.* 7, 1130–1144. doi:10.5935/1984-6835.20150063

Silva, C. A. R. e., Da Fonseca, E. M., Grotto, B. W., De Souza, F. E. S., and Baptista Neto, J. A. (2017). Potentially mobile of heavy metals on the surface sediments in tropical hyper-saline and positive estuaries. *An. Acad. Bras. Cienc.* 89, 2597–2607. doi:10.1590/0001-3765201720170110

Silva, C. A. R., Rainbow, P. S., Smith, B. D., and Santos, Z. L. (2001). Biomonitoring of trace metal contamination in the Potengi Estuary, Natal (Brazil), using the oyster Crassostrea Rhizophorae, a local food source. *Water Res.* 35, 4072–4078. doi:10.1016/s0043-1354(01)00144-0

Simpson, S. L., Vardanega, C. R., Jarolimek, C., Jolley, D. F., Angel, B. M., and Mosley, L. M. (2014). Metal speciation and potential bioavailability changes during discharge and neutralisation of acidic drainage water. *Chemosphere* 103, 172–180. doi:10.1016/j.chemosphere.2013.11.059

Soares, M. O., Campos, C. C., Carneiro, P. B. M., Barroso, H. S., Marins, R. V., Teixeira, C. E. P., et al. (2021). Challenges and perspectives for the Brazilian semi-arid coast under global environmental changes. *Perspect. Ecol. Conserv.* 19, 267–278. doi:10.1016/j.pecon.2021.06.001

Soares, R. G. M. (2017). *Bioacumulação dos metais mércúrio e cobre na ostra do mangue Crassostrea rhizophorae (Guilding, 1828) na bavia inferior do rio Jaguaribe (CE)*. Available at: http://www.repositorio.ufc.br/handle/riufc/34007.

Soares, T. C. M. (2011). Variação sazonal, transporte e partição de Hg no gradiente fluviomarinho do rio Jaguaribe - CE. Available at: http://www.repositorio.ufc.br/handle/riufc/14929.

Sousa, J. K. C. (2009). Avaliação de impactos ambientais causados por metais traço em água, sedimento e material biológico na Baia de São Marcos, São Luís - maranhão. Available at: https://repositorio.ufpb.br/jspui/handle/tede/7102.

Souza, I. S. de, and Silva, P. A. da (2016). Geochemical and ecotoxicological evaluation of an estuarine sediment section at Pacoti River/Ce, Brazil. *Holos* 7, 151–170. doi:10.15628/holos.2016.4741

Souza Silva, M. F., Mayo, S. J., and De Andrade, I. M. (2015). Ocorrência de Crenea maritima (Lythraceae) para o Delta do Parnaíba, Brasil. *Rodriguesia* 66, 931–937. doi:10.1590/2175-7860201566321

Sruthi, S. N., M S, S., Mohan, M., and Ramasamy, E. V. (2018). Distribution of priority pollutants in the sediment of Vembanad estuary, peninsular India. *Mar. Pollut. Bull.* 133, 294–303. doi:10.1016/j.marpolbul.2018.05.033

Tessier, A., Campbell, P. G. C., and Bisson, M. (1979). Sequential extraction procedure for the speciation of particulate trace metals. *Anal. Chem.* 51, 844–851. doi:10.1021/ac50043a017

Torres, R. F. (2009). Disponibilidade dos metais cobre e chumbo em um canal de maré receptor de efluentes de carcinicultura. Available at: http://www.repositorio.ufc.br/handle/riufc/1571.

United Nations (2018). *World urbanization prospects 2018: highlights. United Nations*. Available at: https://population.un.org/wup/.

Vaisman, A. G., Marins, R. V., and Lacerda, L. D. (2005). Characterization of the mangrove oyster, Crassostrea rhizophorae, as a biomonitor for mercury in tropical estuarine systems, northeast Brazil. *Bull. Environ. Contam. Toxicol.* 74, 582–588. doi:10.1007/s00128-005-0623-1

Vaisman, A. G., and Lacerda, L. D. (2003). Estimated heavy metal emissions to the atmosphere due to projected changes in the Brazilian energy generation matrix. *Reg. Environ. Chang.* 3, 140–145. doi:10.1007/s10113-002-0053-0

Vital, H., Silveira, I. M., Amaro, V. E., Melo, F. T. L. de, Souza, F. E. S. de, Chavesdos, M. S., et al. (2006). "Rio Grande do norte," in *Erosão e progradação do litoral brasileiro* (Minas Gerais, Brazil: The Federal University of Viçosa), 155–172.

Wang, W., Chen, M., Guo, L., and Wang, W. X. (2017). Size partitioning and mixing behavior of trace metals and dissolved organic matter in a South China estuary. *Sci. Total Environ.* 603–604, 434–444. doi:10.1016/j.scitotenv.2017.06.121

Xavier, D. de A., Schettini, C. A., França, E. J., Figueira, R. C., and Barcellos, R. L. (2017). Determination of geochemical background values on a tropical estuarine system in a densely urban area. Case study: capibaribe estuary, Northeastern Brazil. *Mar. Pollut. Bull.* 123, 381–386. doi:10.1016/j.marpolbul.2017.09.007

Yang, X., and Wang, Z. L. (2017). Distribution of dissolved, suspended, and sedimentary heavy metals along a Salinized River continuum. *J. Coast. Res.* 33, 1189–1195. doi:10.2112/JCOASTRES-D-16-00120.1

Yao, Q., Wang, X., Jian, H., Chen, H., and Yu, Z. (2015). Characterization of the particle size fraction associated with heavy metals in suspended sediments of the yellow river. *Int. J. Environ. Res. Public Health* 12, 6725–6744. doi:10.3390/ijerph120606725

Yunus, K., and Chuan, O. M. (2009). Geochemical proxy of some chemical elements in sediments of Kemamn river Estuary, Terengganu, Malaysia. *Sains Malays.* 38, 631–636.

frontiers | Frontiers in Earth Science

TYPE Review
PUBLISHED 25 August 2023
DOI 10.3389/feart.2023.1141209

OPEN ACCESS

EDITED BY
Qingqiang Meng,
SINOPEC Petroleum Exploration and Production Research Institute, China

REVIEWED BY
Zeyu Yang,
Environment and Climate Change Canada, Canada
Taohua He,
Yangtze University, China

*CORRESPONDENCE
Guoyi Hu,
huguoyi69@petrochina.com.cn

RECEIVED 10 January 2023
ACCEPTED 10 July 2023
PUBLISHED 25 August 2023

CITATION
Fang C, Hu G, Yuan Y and Gong D (2023), Review on detection method, main source and geological application of diamondoids in crude oil.
Front. Earth Sci. 11:1141209.
doi: 10.3389/feart.2023.1141209

Review on detection method, main source and geological application of diamondoids in crude oil

Chenchen Fang, Guoyi Hu*, Yilin Yuan and Deyu Gong

Petro China Research Institute of Petroleum Exploration and Development, Beijing, China

Diamondoids are alkanes with cage-like structure. Their diamond-like structure makes them have high stability and anti-biodegradability, and can be preserved and enriched in complex and long geological processes. Therefore, the continuous development of quantitative detection methods for diamondoids in crude oil has deepened the research of these compounds and made them more widely used in crude oil cracking evaluation, maturity evaluation, biodegradation evaluation and other aspects.

KEYWORDS

diamondoids, detection method, main source, geological application, crude oil

1 Introduction

Since the 21st century, exploration work in China has changed significantly. Specifically, exploration targets have gradually shifted from structural hydrocarbon reservoirs to subtle strata and from shallow to deep strata. In addition, exploration objects have been transformed from oil to natural gas. Such changes have triggered a series of new problems in the field of oil and gas exploration, and posed great challenges to the research on oil and gas geochemistry, but also rendered a good opportunity for the development of oil and gas geochemistry.

Increasing attention has been paid to deep oil and gas reservoirs as a new exploration target. Oil and gas geochemical experts have extensively investigated natural gas, light hydrocarbons, and biomarkers, accumulated rich experience, and achieved fruitful theoretical and practical results. However, deep oil and gas reservoirs are often prone to the loss of biomarkers, or equilibrium has been reached. In the meanwhile, light hydrocarbon components are highly susceptible to secondary alteration and mixed sources, which adds to the uncertainty in their practical application. Therefore, it is urgent to develop more stably structured geochemical parameters adaptive to the high degree of evolution.

Among geological organic matter, diamondoids are small molecular alkanes with a cage-like diamond structure (Wingert, 1992; Dahl et al., 1999). Based on the number of three-dimensional (3D) cyclic structures, diamondoids are divided into adamantane, diamantane, triamantane, tetramantane, pentamantane (Figure 1), etc. Diamondoids, which generally refer to adamantane and its alkyl substitutes with strong biodegradation resistance and high thermal stability, widely exist in coal and hydrocarbon source rocks (Imuta and Ouchi, 1973; Aczel et al., 1979; Schulz et al., 2001; Wei et al., 2006b), crude oil (Bender et al., 1986; Williams et al., 1986; Wingert, 1992; Chen et al., 1996; Grice et al., 2000; Dahl et al., 2003; Azevedo et al., 2008; Ma et al., 2009), petroleum products (Wang et al., 2006), and condensate gas (Lin and Wilk, 1995; Stout and Douglas, 2004; Sassen and Post, 2008). Diamondoids have attracted much

attention since they can be preserved and enriched in long and complicated geological processes, with relevant geological information carried and rendered. As revealed by previous studies, diamondoids are applicable to evaluating the thermal maturity of crude oil (Zhao et al., 1995; Chen et al., 1996; Zheng et al., 1998; Li et al., 2000; Zhang et al., 2005; Ma et al., 2017; Jiang et al., 2019, 2021, 2022; Akinlua et al., 2020; Goodwin et al., 2020; Huang et al., 2022b), judging the migration direction and charging period of oil and gas (Duan et al., 2007; Huang et al., 2022a, 2022b), assessing the cracking degree of crude oil (Dahl et al., 1999; Chai et al., 2022; Peng et al., 2022), identifying lithofacies (Schulz et al., 2001; Chai et al., 2020), evaluating the secondary alteration of oil reservoirs (Jiang et al., 2020), researching oil-source correlation (Forkner et al., 2021), assessing residual of migration fractionation (Zhu et al., 2021), exploring the thermochemical sulfate reduction reaction (Wei et al., 2011), and identifying in the sources of oil (Stout and Douglas, 2004; Wang et al., 2006; Spaak et al., 2020), especially at the over-mature stage in case of relative equilibrium reached among other biomarkers, or their failure resulting from low content.

Among geological organic matter, easily detectable high-content adamantane and diamantane compounds have been the focus in the present research and discussion regarding oil and gas geochemistry. Therefore, this paper focuses on adamantanes and diamantanes. The following diamondoids are also used to refer to the total of adamantanes and diamantanes.

2 Quantitative detection method of diamondoids

In 1933, the most simply structured adamantane was detected in petroleum for the first time (Landa and Machacek, 1933). Since then, increasingly abundant diamondoids have been detected in natural gas (Fu and Yu, 1998; Fu and Li, 2001), crude oil and condensate gas (Wingert, 1992; Chen et al., 1996; Grice et al., 2000; Dahl et al., 2003; Stout and Douglas, 2004), petroleum products (Wang et al., 2006), and coal and hydrocarbon source rocks (Schulz et al., 2001; Wei et al., 2006b). Moreover, some diamondoids with higher molecular weights (containing three or more diamond lattice structures) have been successfully separated and identified from petroleum (Dahl et al., 2003; Atwah et al., 2021; Gadzhiev et al., 2021).

Though being detected in nearly all crude oils and most petroleum products (Wang et al., 2006), only low-concentration (several ppm or sub-ppm) diamondoids are generally contained in normal oils (Fort and Schleyer, 1964; Wingert, 1992; Dahl et al., 1999; Wei Z. B. et al., 2007), and they exist in the highly complex matrix of petroleum hydrocarbons. Therefore, high-selectivity and high-sensitivity detection methods are required for quantitatively detecting and analyzing trace components in normal crude oils and describing their minor variation characteristics.

At present, three methods have been mainly adopted to quantitatively detect and analyze diamondoids in crude oil and hydrocarbon source rock samples: the separation of group components from crude oil samples or hydrocarbon source rock extracts in combination with gas chromatography-mass spectrometry (GC-MS) (Figure 2A), the solvent dilution of crude oil samples or hydrocarbon source rock extracts in combination with GC-triple quadrupole tandem MS (GC-MS-MS) (Figure 2B), and the separation of group components from crude oil samples or hydrocarbon source rock extracts in combination with comprehensive 2D GC-time of flight-MS (GC×GC-TOFMS) (Figure 2C).

2.1 A quantitative method integrating group component separation with GC-MS

The first method, a combination of chromatographic column-aided extract separation from actual crude oil samples and hydrocarbon source rock samples with GC-MS, is a qualitative and quantitative analysis method for diamondoids, which has been developed earliest and widely applied (Wingert, 1992; Chen et al., 1996; Grice et al., 2000; Li et al., 2000; Schulz et al., 2001; Zhang et al., 2005).

Crude oil or hydrocarbon source rock samples are usually accompanied by the interference of complex matrix components. Despite high selectivity of GC-MS, the signal of target analytical compounds will still be obscured by the interference of complex matrix components in the analysis results of samples, especially in case of the low concentration of target analytical compounds. Before the actual crude oil samples and hydrocarbon source rock extracts are analyzed via GC-MS, therefore, the interference of the complex

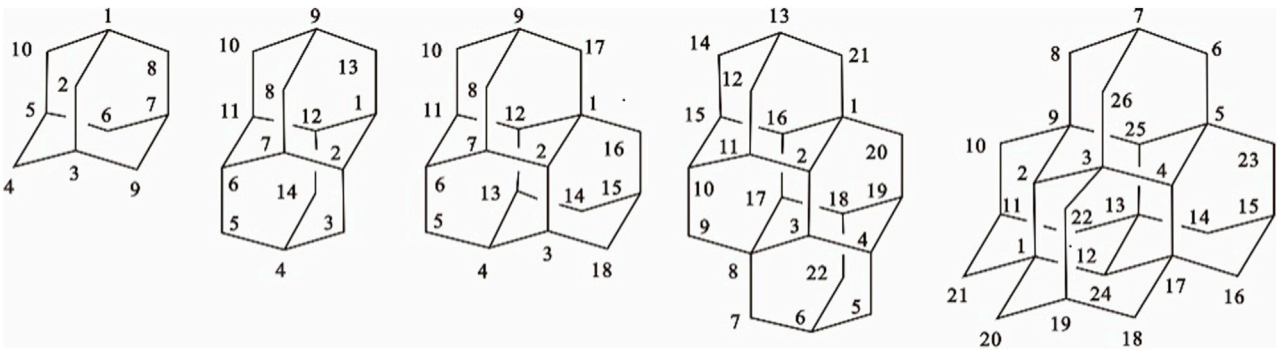

FIGURE 1
Main types of diamondods and their structure (from left to right is adamantane, diamantane, triamantane, tetramantane, pentamantane).

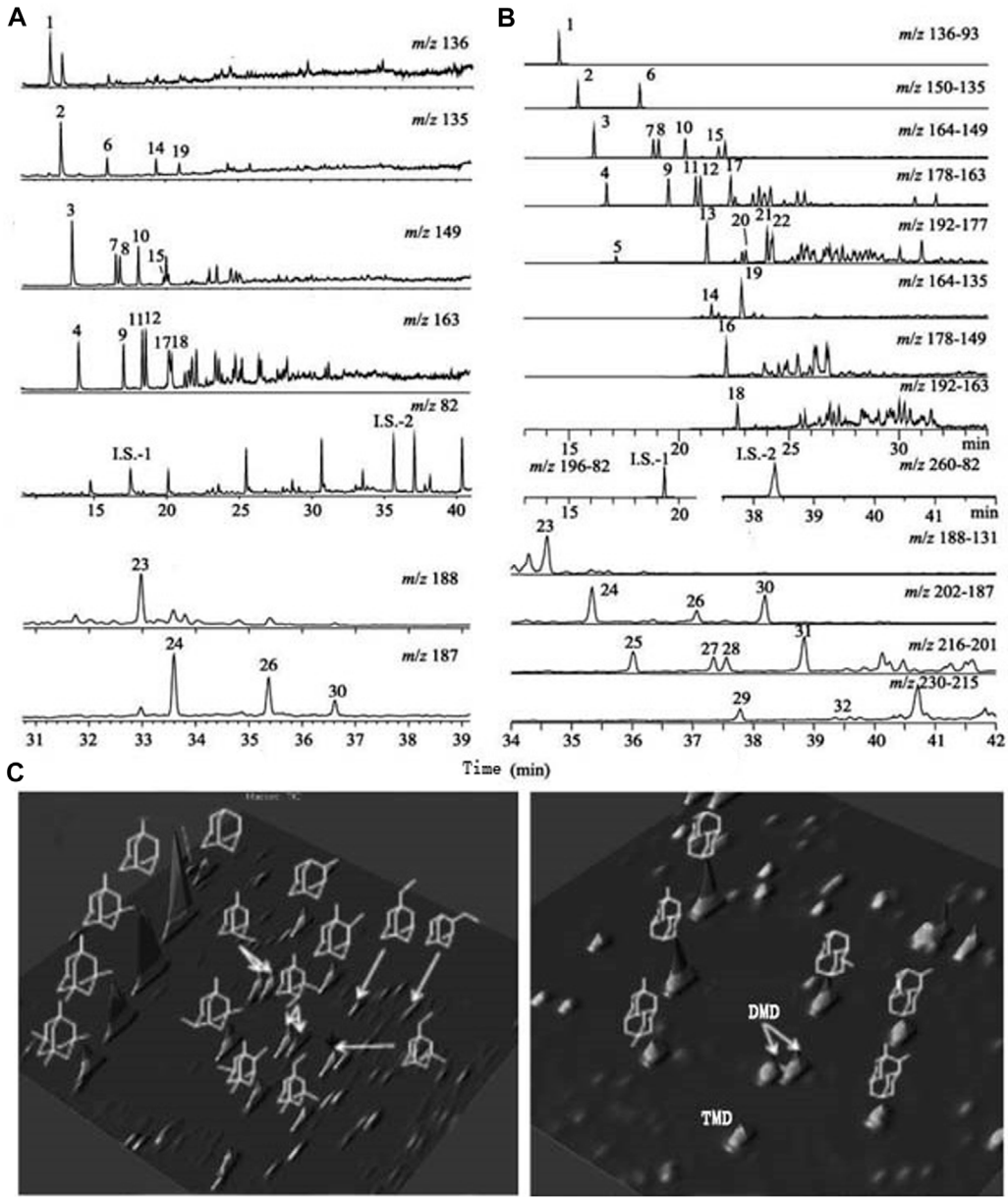

FIGURE 2
Spectrogram of diamondoids in **(A)** LN14 oil by GC-MS (Liang et al., 2012a), **(B)** LN14 oil by GC-MS-MS (Liang et al., 2012a), **(C)** KL205 oil by GC×GC-TOFMS (Wang et al., 2019). (1: adamantane, 2: 1-methyladamantane, 3: 1,3-dimethyladamantane, 4: 1,3,5-trimethyladamantane, 5: 1,3,5,7-tetramethyladamantane, 6: 2-methyladamantane, 7: 1,4-dimethyladamantane(cis), 8: 1,4-dimethyladamantane(trans), 9: 1,3,6-trimethyladamantane, 10: 1,2-dimethyladamantane, 11: 1,3,4-trimethyladamantane(cis), 12: 1,3,4-trimethyladamantane(trans), 13: 1,2,5,7-tetramethyladamantane, 14: 1-ethyladamantane, 15: 2,6- + 2,4-dimethyladamantane, 16: 1-ethyl-3-methyladamantane, 17: 1,2,3-trimethyladamantane, 18: 1-ethyl-3,5-dimethyladamantane, 19: 2-ethyladamantane, 20: 1,3,5,6-tetramethyladamantane, 21: 1,2,3,5-tetramethyladamantane, 22: 1-ethyl-3,5,7-trimethyladamantane, 23: diamantane, 24: 4-methyldiamantane, 25: 4,9-dimethyldiamantane, 26: 1-methyldiamantane, 27: 1,4- + 2,4-dimethyldiamantane, 28: 4,8-dimethyldiamantane, 29: 1,4,9-Trimethyldiamantane, 30: 3-methyldiamantane, 31: 3,4-dimethyldiamantane, 32: 3,4,9-trimethyldiamantane, I.S.-1: n-dodecane-d_{26}, I.S.-2: n-hexadecane-d_{34}).

matrix is usually eliminated by separating their group components through chromatographic column separation technology, while the target analytical compounds are concentrated and enriched using solvent volatilization (Wingert, 1992; Chen et al., 1996; Grice et al., 2000; Li et al., 2000; Schulz et al., 2001; Zhang et al., 2005). During instrumental analysis, the selective ion monitoring (SIM) mode in GC-MS can enhance the detection signal of diamondoids and improve the sensitivity of target compound analysis. Therein, ions with m/z of 136, 135, 149, 163, 177, and 191 are commonly applied to detect diamantane compounds, those with m/z of 188, 187, 201, 215, and 229 to diamantane compounds, and those with m/z of 240 and 239 to triamantane compounds.

During the separation of group components, condensate gas and gasoline can be directly injected under natural conditions, aiming to avoid the possible volatilization loss of diamondoids. The spectrogram results reveal that in the nonpolar chromatographic

column, adamantane peaks earlier than n-C11 (Stout and Douglas, 2004). However, the injection system and chromatographic column of GC-MS will be polluted by complex matrix components and non-paraffinic components with high molecular weights in crude oil samples and hydrocarbon source rock extracts, leading to the reduction of column efficiency. Therefore, this detection and analysis means for diamondoids, i.e., direct injection, does not apply to crude oil and hydrocarbon source rock samples.

2.2 A quantitative method combining solvent dilution with GC-MS-MS

During chromatographic column separation and sample concentration, moreover, evaporation may result in the loss of diamondoids, or cause the deviation of quantitative results, thus affecting the analytical research based on the concentration of diamondoids. Hence, developing the quantitative detection and analysis method integrating the nondestructive pretreatment method with the high-selectivity and high-sensitivity detection method is essential for describing and exploring low-concentration diamondoids in crude oil and hydrocarbon source rock samples.

GC-MS-MS, a highly sensitive and selective instrumental analysis method, eliminates the interference of matrix ions mainly through the selected-reaction monitoring (SRM) mode, without needing any complicated sample pretreatment or purification and separation technology before injection (Frenich et al., 2005; Hernandez et al., 2005). Under the SRM mode of GC-MS-MS, the parent ion of the set target compound is selected when passing through the first quadrupole and then collides with argon molecules in the second quadrupole. Afterward, the resulting fragment ions pass through the third quadrupole, followed by the selection, detection, and analysis of daughter ions corresponding to the target compound in the fragment ions. Thanks to this selection and detection process of GC-MS-MS, the limit of quantification (LOQ) and limit of detection (LOD) of the instrument are reduced, leading to the analysis and detection results of target compounds as low as several ppb (Hernandez et al., 2005; Qu et al., 2010).

For diamondoid detection and analysis, methyl diamantane (MD) compounds in crude oil were quantitatively detected and analyzed at the earliest by monitoring the m/z202+-187+ conversion process (Dahl et al., 1999).

Afterward, Liang et al. (2012b) optimized GC-MS-MS parameters like parent and daughter ions, collision energy, and scanning time using standard diamondoid samples, and then established a complete GC-MS-MS quantitative analysis method for diamondoids. Under the optimal operating parameters of the instrument, good linear relationships were manifested in the standard curves of 10 standard diamondoid samples, and the correlation coefficient (R2) characterizing linear correlations was always higher than 0.9980. In this process, all target diamondoids presented good repeatability, with a relative standard deviation of 1.3%–5.1% (n = 5). The LODs and LOQs of all target diamondoids in oil samples obtained by this method were 0.02–0.11 and 0.08–0.37 μg/g, respectively. The above data manifested the good applicability of this method to quantitative detection and analysis of diamondoids, especially for samples with a low concentration of diamondoids.

Under the SRM mode and optimal operating parameters, GC-MS-MS displays the maximum sensitivity and selectivity for the quantitative analysis of diamondoids in crude oil samples. Besides, this technology can eliminate the interference of co-eluted compounds in crude oil samples and hydrocarbon source rock extracts by monitoring the transformation process of paired parent ions and daughter ions, with high selectivity. In the meanwhile, its high sensitivity can compensate for the low concentration of diamondoids in samples due to the absence of concentration and enrichment pretreatment. Therefore, GC-MS-MS can serve as an effective means for the reliable quantitative analysis of diamondoids in actual samples, only needing simple sample dilution.

2.3 A quantitative method combining group component separation with comprehensive 2D GC×GC-TOFMS

As a new technology developing on the basis of the traditional 2D technology in the 1990s, comprehensive 2D GC×GC characterized by good sensitivity, high resolution, large peak capacity (the product of the peak capacities of two chromatographic columns), fast analysis speed, qualitative analysis with rules to follow, family separation, and tile effect (Frysinger and Gaines, 1999; Lu et al., 2005; Ruan et al., 2002) can be used to separate complex mixtures. Specifically, this technology connects two relatively independent chromatographic columns differing in the separation mechanism and stationary phase (e.g., nonpolar column and chiral column or polar column) in series to form a 2D GC column system by using a modulator with the functions of trapping, focusing, and transmission.

TOFMS, a common MS technique, realizes separation and determination based on different time taken by moving ions with different mass-to-charge ratios and the same kinetic energy in a steady electric field to reach the receiver. This technique is characterized by a wide detectable mass range, fast response speed, and high sensitivity (Zhao and Shen, 2006). If combined with GC×GC, TOFMS is applicable to qualitative and quantitative analysis of compounds in complex systems (Lu et al., 2004b).

GC×GC and GC×GC-TOFMS have been applied to such fields as tobacco, food, wine making, petroleum geology, refined oil products, and environmental monitoring (Schoenmakers et al., 2000; Frysinger and Gaines, 2001; Hua et al., 2002; Frysinger et al., 2003; Lu et al., 2004a; Lu et al., 2007; Ventura et al., 2008). On this basis, Wang et al. (2010) established an analytical detection method for diamondoids in actual crude oil samples by optimizing parameters like column system selection, temperature program, modulation period, hot-air blowing time, and the flow rate of the carrier gas.

However, the pretreatment method can not only remove the interference of other compounds on diamondoids, but also improve the concentration of diamondoids. Therefore, scholars are also constantly improving the pretreatment process of this method to reduce the loss of adamantanes in the pretreatment process (Wang et al., 2019). In addition, scholars have been developing quantitative analysis of diamondoids with higher carbon number (such as triamantane, tetramantane) and more complex structure (such as ethanodiamondoids) (Wang et al., 2019; Ma et al., 2022).

3 Main sources of diamondoids

Diamondoids have been extensively valued, investigated, and applied in oil and gas geochemistry because of the nature and characteristics vested in their own stable structures. Nevertheless, the source, origin, and evolutionary characteristics of diamondoids in geological bodies remain unclear yet. Diamondoids are considered to be abiotic since they have not been detected in modern organisms and sediments (Wei et al., 2006c; Wei et al., 2007 Z. B.). It is guessed that diamondoids are produced in the early diagenetic stage of organic matter because they have been detected in immature and low-mature peats and sedimentary rocks (Schulz et al., 2001; Wei et al., 2006c, Wei et al., 2007 Z. B.). Dahl et al. (1999) thought that once formed, diamondoids will be neither destroyed nor produced again. With the deepening research, however, scholars have proved by laboratory simulations that diamondoids can be generated and cracked in the process of high-temperature thermal evolution, with highly extensive sources of parent materials (Giruts et al., 2006; Giruts and Gordadze, 2007; Fang et al., 2012), and their cracking products include their own isomers and liquid hydrocarbons such as aromatics (Wei et al., 2006b). In the meanwhile, it has been verified by the above research that the formation mechanism of diamondoids is not only restricted to the early proposed catalytic rearrangement of polycyclic naphthenes (Dahl et al., 2010) but also includes high-temperature cracking.

As revealed by predecessors' results, diamondoids with lower molecular weights are formed mainly through two mechanisms: The first is Lewis acid-catalyzed rearrangement of polycyclic hydrocarbons (Schneide et al., 1966; Wingert, 1992; Lin and Wilk, 1995). The second is high-temperature cracking of higher-molecular-weight components (Giruts et al., 2006; Giruts and Gordadze, 2007; Gordadze and Giruts, 2008). As verified by laboratory thermal cracking simulation experiments, diamondoids with lower molecular weights can be formed in immature sedimentary rocks and peats (Wei et al., 2006c; Wei et al., 2007 Z.), kerogen (Gordadze, 2002), crude oil (Fang et al., 2012), as well as their different family components (Fang et al., 2013), including saturated hydrocarbon components (Giruts et al., 2006) and polar components (nonhydrocarbons and asphaltenes) (Giruts and Gordadze, 2007), and other compounds, such as C16, C19, C22, C34, and C36 (Gordadze and Giruts, 2008) and β-aryl ketone (Berwick et al.). Moreover, all possible isomers of adamantane and diamantane compounds can be detected in the cracking products of the above components. Furthermore, it has been experimentally found that adamantane compounds with lower molecular weights, such as adamantane and diamantane compounds, will crack at high temperatures (Wei et al., 2006b; Fang et al., 2012).

Some thermal cracking experiments manifest that the formation of diamondoids in modern sedimentary rocks is catalyzed or inhibited by minerals under water-bearing conditions, and those in ketone can be catalyzed or inhibited by such minerals as montmorillonite, aluminosilicate, kaolinite, and illite (Wei et al., 2006a, c, 2007b). Some pyrolysis experiments, moreover, show that diamondoids can be produced in the thermal cracking of crude oil samples and their high-molecular-weight components, saturated hydrocarbon components, aromatic hydrocarbon components, and polar components even in the absence of catalysts (Giruts et al., 2006; Giruts and Gordadze, 2007; Fang et al., 2012; Fang et al., 2013).

Through the gold tube thermal simulation experiments of saturated hydrocarbon, aromatic hydrocarbon, asphaltene and nonhydrocarbon in crude oil, it is proved that diamondoids mainly derive from the thermal cracking of saturated hydrocarbon components (Figure 3), as proved by gold tube thermal simulation experiments on saturated hydrocarbons, aromatic hydrocarbons, asphaltenes, and nonhydrocarbons (Fang et al., 2013). Light hydrocarbon components make certain contributions to the formation of diamondoids, as demonstrated by gold tube thermal simulation experiments on the original crude oil and the crude oil after the volatilization of light hydrocarbon components (Fang et al., 2016). In addition, existing studies have shown that diamondoids can be produced during the thermal cracking of kerogen with different types of sedimentary organic matter, but their content and composition characteristics are different (Jiang et al., 2018). In the meanwhile, it has been found through simulation experiments that the content of diamondoids in geological bodies is influenced by volatilization and dissipation (Fang et al., 2016) and biodegradation of crude oil in the early formation stage.

In addition, it has been proved through the gold tube thermal simulation experiment on soluble organic matter components in marine shale and kerogen after extraction that diamondoids in organic matter are mainly attributed to the thermal cracking of soluble organic matter components (Figure 4), and the same to coal measures (Fang et al., 2015; Zhai et al., 2022). Furthermore, a thermal cracking experiment was continued on the same kerogen sample after the soluble organic matter was extracted and removed under easy reflectance of vitrinite (EasyRo) of 0.8%, 1.0%, and 1.3%. On this basis, the staged cumulative generation results of diamondoids in kerogen and its resulting asphalt in three stages (EasyRo0.8%–1.0%, 1.0%–1.3%, and 1.3%) were discussed. The results showed that diamondoids were mainly produced in the secondary cracking of asphalt, and the upper limit of the contribution of kerogen thermal cracking to diamondoids was EasyRo1.3% (Li et al., 2015).

4 Application of diamondoids in the geochemical field

Diamondoids in crude oil are applied in the geochemical field mainly through their concentration and parameters.

4.1 Evaluation of crude oil cracking degree

The concentration of diamondoids in crude oil and source rock extracts has been investigated in oil and gas geochemistry. For instance, the relative abundance of diamondoids in light oil and condensate gas can serve as an important "fingerprint" tool to identify the sources of oil spill events (Stout and Douglas, 2004).

According to the theory of Dahl et al. (1999), moreover, once formed, diamondoids will be neither destroyed nor produced again. It is believed, therefore, that the increase in the concentration of

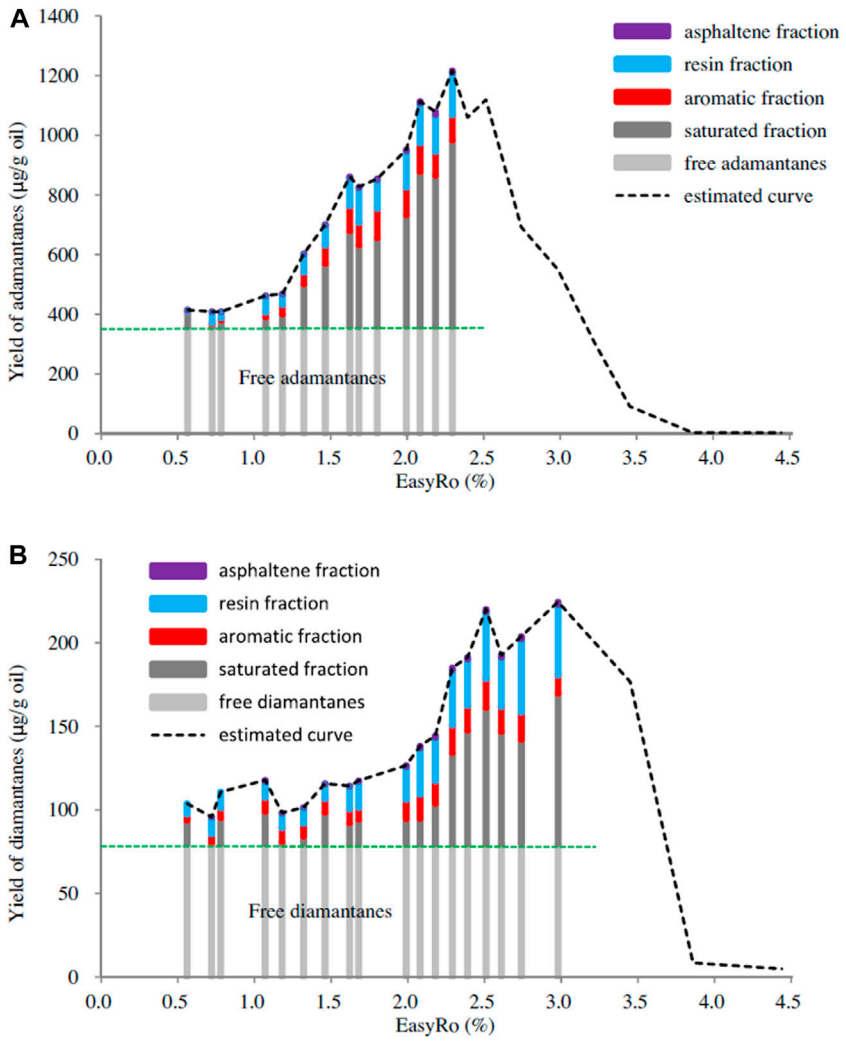

FIGURE 3
The calculated yield curves and source contributions of adamantanes and diamantanes generated from the Tarim oil. **(A)** Adamantanes; **(B)** diamantanes (Fang et al., 2013).

diamondoids in oil results from the thermal degradation of most other non-diamondoids in oil (Dahl et al., 1999). Given this, Dahl et al. (1999) proposed that the cracking degree of crude oil can be evaluated by an effective index, the concentration of 3-+4-MD (Figure 5) (Dahl et al., 1999), which has been applied in some studies (Wei Z. B. et al., 2007; Springer et al., 2010). Here, we need to pay attention to the selection of baseline concentration for different regions (Springer et al., 2010).

However, Wei et al. (2006b) explored the thermal maturity-dependent changes in the concentration of diamondoids in a set of coal and sedimentary rock samples with a maturity range of Ro=0.20%–6.40%. The quantitative results of diamondoids in coal and source rock extracts manifested that the concentration of diamondoids began to decrease after Ro>4.0% (Wei et al., 2006b). It was also found that some diamondoids can also be thermally cracked to aromatic hydrocarbons under high temperatures (Oya et al., 1981; Schoell and Carlson, 1999; Wei et al., 2006b). As the research deepens, scholars have found that the diamondoids continuously enriched in the cracking process of crude oil may be ascribed to two aspects: the cracking of relatively unstable hydrocarbons in crude oil (Dahl et al., 1999), and the sustained production of diamondoids (Wei et al., 2006c; Fang et al., 2012). Dahl et al. (1999) evaluated the cracking degree of crude oil based on the cracking of relatively unstable hydrocarbons in crude oil, in which the total amount of diamondoids is assumed to be constant. Therefore, this parameter is still applicable at the stage of constant content (EasyRo<2.0%) (Fang et al., 2013), while it needs to be carefully judged at the stage of changing content.

4.2 Maturity evaluation

Among diamondoids, the homologous compounds differing in thermal stability are formed due to the different substitutions on each substituent. For homologous diamondoids formed by the same alkyl substitution, for example, the compounds substituted at “bridge” carbon positions (positions 1, 3, 5, and 7 of adamantane in Figure 1) display higher thermal stability than those substituted at

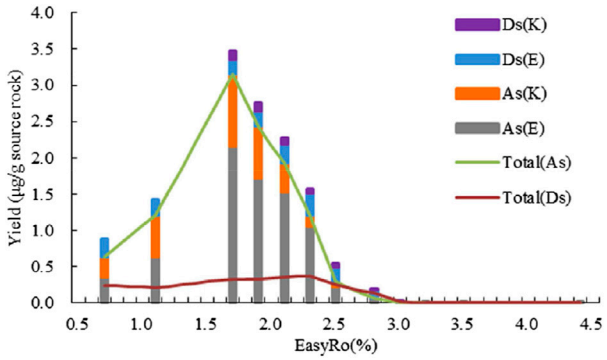

FIGURE 4
Estimated yields (mg/g) of different types diamondoids during source rock maturation. As(K) and As(E) stand for the adamantane contributions from the kerogen pyrolysate and extract pyrolysate, respectively. Ds(K) and Ds(E) stand for the diamantine contributions from the kerogen pyrolysate and extract pyrolysate, respectively (Fang et al., 2015).

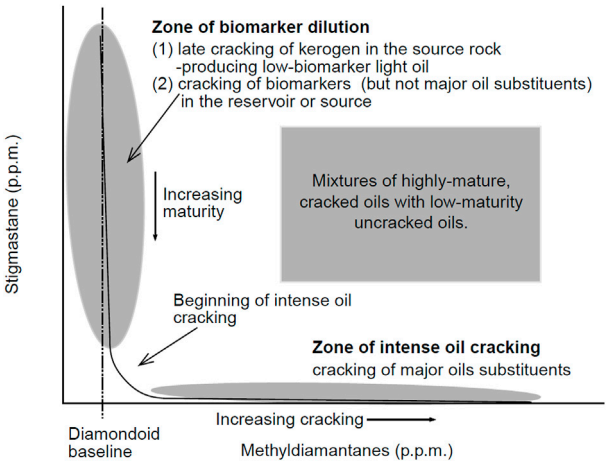

FIGURE 5
Diagram from the concentrations of methyldiamantanes(3-+4-methyldiamantane) and stigmastane (Dahl et al., 1999).

the corresponding "quaternary" carbon positions (positions 2, 4, 6, and 8 of adamantane in Figure 1). In other words, for adamantane compounds with the same methyl substitution, 1- methyl adamantane (MA) formed by methyl substitution at the "bridge" carbon position shows higher thermal stability than 2-MA (Wingert, 1992) (Figure 1). For diamantane compounds with the same methyl substitution, 4-MD formed by methyl substitution at the "bridge" carbon position presents better thermal stability than the other two homologous isomers (1-MD and 3-MD) (Wingert, 1992; Chen et al., 1996).

Based on the aforesaid thermal stability relationships, Chen et al. (1996) also established the ratio parameters of diamondoids, namely, MA index [MAI=1-MA/(1-MA + 2-MA)] and MD index [MDI=4-MD/(1-MD + 3-MD + 4-MD)]. In the meanwhile, they pointed out that these ratios increased with the increase in the thermal maturity of crude oil and hydrocarbon source rocks. Then, such indexes were used to evaluate the maturity of condensate oil samples with a high evolutionary degree in Tarim Basin, and the corresponding Ro was 1.6%–1.7%. The Ro of condensate oil in Ying-Qiong Basin was obtained in a similar fashion as 1.6%–2.0%.

Following this rule, many adamantane maturity parameters have been established in the existing studies and applied in practice. For instance, MAI and MDI have been adopted to evaluate crude oil and hydrocarbon source rocks (Chen et al., 1996; Schulz et al., 2001; Wei et al., 2006b, Wei et al., 2007 Z.). In addition, dimethyl adamantane index-1 (DMAI-1), DMAI-2, ethyl adamantane index (EAI), trimethyl adamantane index-1 (TMAI-1), TMAI-2, dimethyl diamantane index-1 (DMDI-1), and DMDI-2 have been applied in simulation experiments and actual geological samples (Schulz et al., 2001; Zhang et al., 2005; Wei Z. et al., 2007). According to the simulation results of crude oil cracking, the relative changes in TMAI-1 and DMA/MD (DMA stands for DMA compounds, including the sum of adamantane compounds formed by dimethyl substitution at different positions. MD denotes MD compounds, including the sum of diamantane compounds formed by methyl substitution at different positions), and DMAI-1 and DMA/MD are also applicable parameters for crude oil maturity (Figure 6) (Fang et al., 2013).

Taking advantages of diamondoids in maturity evaluation, Duan et al. (2007) investigated the distribution characteristics of diamantane parameters of crude oil in Tahe Oilfield, Tarim Basin, analyzed and discussed the charging period and migration direction of oil and gas in this oilfield, and explored the migration direction of crude oil. Bao et al. (2015) analyzed the distribution characteristics of alkyl adamantane and alkyl diamantane compounds in condensate oil in Zhujiadun, Yancheng Depression, Subei Basin, and that in upper Cretaceous mature hydrocarbon source rocks in Taizhou Formation, as well as their parameters. On this basis, the source of condensate oil was explored, and the comparison with the measured Ro showed that adamantane compounds are practical, to some extent, in the maturity evaluation of crude oil and hydrocarbon source rocks.

Problems exist despite the extensive practical application of adamantane parameters in maturity evaluation. As suggested by the existing studies, MAI and MDI are only applicable in a narrow range of Ro. Li et al. (2000) analyzed the adamantane parameters obtained from the extracts of the hydrocarbon source rocks in lower Ordovician Majiagou Formation in the central gas field of Ordos Basin, China, and thought that MDI changes within 44%–65%, without obvious changes in the area of Ro>2.0%, so it is only applicable in a Ro range of 0.9%–2.0%. However, Schulz et al. (2001) and Wei Z. B. et al. (2007) conducted thermal cracking experiments on actual samples under water-bearing conditions, and held that MAI and MDI are only applicable to the maturity evaluation of samples with Ro>1.3%.

On the other hand, Li et al. (2000) also pointed out no obvious correlation between MDI and sample depth or Ro, which contradicts with the previous conclusion drawn by Chen et al. (1996). As discovered through laboratory simulation of MDI-Ro correlation thermal maturation of hydrocarbon source rocks in different horizons of Ying-Qiong Basin, samples from different horizons are correlated with maturity differently, which also highlights the reliability problem and limitations of adamantane parameters in practical application (Li et al., 2000; Wei Z. et al., 2007).

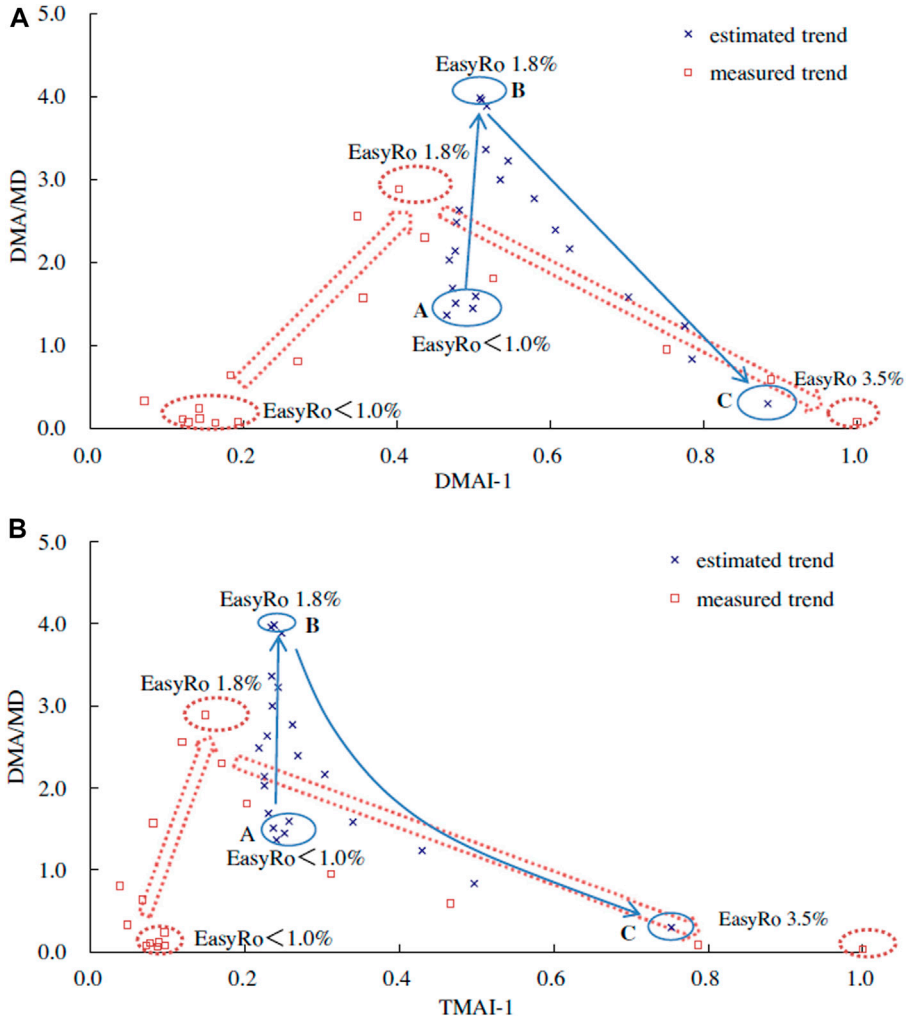

FIGURE 6
The plots of concentration ratios vs. isomerization ratios of diamondoids for the Tarim oil cracking. **(A)** DMA/MD vs. DMAI-1; **(B)** DMA/MD vs. TMAI-1 (Fang et al., 2013).

4.3 Identification of genetic types

At present, the research on the genetic types of organic matter in diamondoids is still insufficient. Schulz et al. (2001) proposed for the first time that dimethyl diamantane compounds (4,9-dimethyl diamantane, 4,8-dimethyl diamantine, and 3,4-dimethyl diamantane) show different distribution characteristics in different types of hydrocarbon source rocks (Figure 7). To be specific, marine siliceous clastic rocks of type II kerogen are rich in 4,9-dimethyl diamantane and carbonate rocks are rich in 4,8-dimethyl diamantine, while type III carbon mudstone and coal contain abundant 3,4-dimethyl diamantane. Accordingly, it was pointed out that different types of organic matter can be distinguished using a triangle diagram characterizing the relative content of dimethyl diamantane compounds.

With this triangle diagram, which was considered an effective identification method, Chen et al. (2008) identified the genetic types of organic matter of condensate oil in Jiyang Depression, and concluded that the condensate oil in Jiyang Depression originates from the mixture of coal bed and lake facies.

The existing studies have shown that the difference in some maturity parameters may result from different sources or causes of organic matter during hydrocarbon generation (Li et al., 2015; Jiang et al., 2018). For instance, DMAI-1 and DMAI-2 may be different due to the primary cracking of kerogen at different stages and the secondary cracking of its resulting asphalt (Li et al., 2015). Among the gold tube thermal cracking products of type I and type II kerogen, two bivariant parameters (DMA/MD and TMAI-1, and DMA/MD and DMAI-1) of diamondoids also display different evolutionary characteristics. Even the loss of volatile components of crude oil in the low-mature stage will generate an influence on the maturity parameters of adamantane in the later stage (Fang et al., 2016).

Some scholars have suggested that the application of diamondoids can be extended by deeply exploring their evolutionary characteristics during the thermal evolution of different types of hydrocarbon source rocks (Ma, 2016). As aforementioned, the influence of organic matter types on the composition characteristics of diamondoids has been analytically investigated through gold tube cracking simulation experiments on

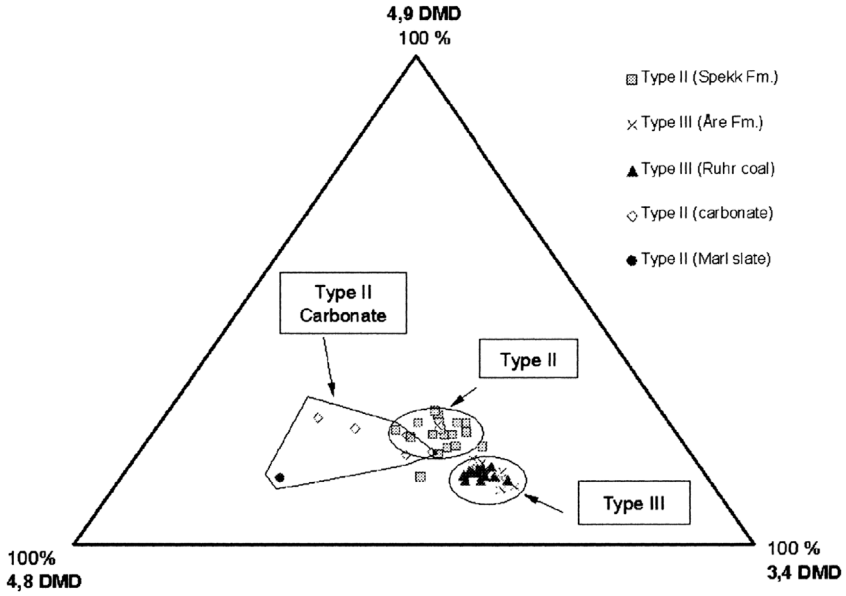

FIGURE 7
Triangular plot of the relative distribution of 4,9-dimethyldiamantane (4,9-DMD), 4,8-dimethyldiamantane (4,8-DMD) and 3,4-dimethyldiamantane (3,4-DMD) (Schulz et al., 2001).

different types of kerogens (Jiang et al., 2018). However, the difference in composition characteristics is attributed to the combined effects of the primary cracking of kerogen and the secondary cracking of asphalt, which goes against the situation under actual geological conditions. Efforts have been made to distinguish the two effects, but what has been obtained is the staged cumulative generation result of diamondoids in kerogen and its resulting asphalt in three stages: EasyRo0.8%–1.0%, 1.0%–1.3%, and >1.3% (Li et al., 2015).

4.4 Evaluation of biodegradation degree

Biodegradation, a significant transformation process of crude oil in underground oil and gas-bearing basins (Connan, 1984; Peters and Moldwan, 1993; Head et al., 2003), will influence the physical and chemical molecular characteristics of crude oil (Winters and Williams, 1969; Hunt, 1979; Connan, 1984; Peters and Moldowan, 1993) and further affect oil exploitation and refining costs. Moreover, biodegradation can generate important economic impacts on oil (Connan, 1984; Wilhelms et al., 2001; Larter et al., 2006) and strategic impacts on oil exploration (Larter et al., 2012).

A few studies regarding the biodegradation process and degree of crude oil by diamondoids have been reported. Generally, hydrocarbons present consistent overall variation trends and different individual rates in the process of biodegradation (Larter et al., 2006). Accordingly, the evaluation indexes of biodegradation degree have been established in past studies based on the differences in relative abundance and sequentially sensitive structures among different series of compounds (Volkman et al., 1984; Peters and Moldowan, 1993). Following the same principle, Grice et al. (2000) quantitatively detected diamondoids in actual crude oil samples with different degrees of biodegradation, and the results manifested that MA/A (MA stands for MA compounds, including the sum of MA at each substitution position, and A denotes adamantane) will change regularly with the variation of the biodegradation degree, which can serve as an evaluation index of the biodegradation degree and can also be used to identify the mixture of severely biodegradable oil and non-biodegradable oil. Besides, MA/A will not be significantly influenced by the difference in maturity. Wei Z. B. et al. (2007) already applied this parameter in related studies.

Wang et al. (2006), Yang et al. (2013), Grice et al. (2000), Wei Z. B. et al. (2007), and Chai et al. (2022) quantitatively detected diamondoids in crude oil biodegradation products during indoor and outdoor simulations and those in actual crude oil biodegradation products. Results revealed that diamondoids will be affected by biodegradation in actual oil reservoirs, with their content presenting an overall declining trend (Grice et al., 2000; Wang et al., 2006; Wei Z. B. et al., 2007; Yang et al., 2013; Chai et al., 2022). Therein, the decreasing trend of the content of adamantane resembles that of total diamondoids, which is decided by the dominant position of adamantane compounds in diamondoids. The content of diamantane compounds, however, shows a less obvious decreasing trend than that of adamantane compounds, reflecting the better anti-biodegradation ability of diamantane compounds than adamantane compounds. In the meanwhile, triamantane compounds are subjected to minor content changes (Wang et al., 2006; Wei Z. B. et al., 2007). Even if the biodegradation degree reaches the eighth grade defined by Peters and Moldowan (1993), crude oil will still contain diamondoids with a certain concentration (Wei Z. B. et al., 2007), which also effectively guarantees the application of diamondoids in biodegradable oils, especially in highly biodegradable oils.

The application of other parameters in biodegradable oils has also been studied by scholars. Dahl et al. (1999) proposed an effective index, namely, the concentration of 3-+4-MD, to evaluate the cracking degree of crude oil and mixed oil. This method is considered immune to biodegradation (Wei Z. B.

et al., 2007). Grice et al. (2000) calculated the MAI and MDI in actual crude oil samples biodegraded to different degrees, and found that the MAI is consistent well, reflecting their similar maturity. However, the MDI varies a lot, which may be associated with the mineral content in source rocks (Grice et al., 2000). In addition, Xu (2007) tested the stability of MAI and MDI in biodegradation, both of which indicated a good anti-biodegradation ability. And the research results of Chai et al. (2022) indicate that no significant biodegradation impact on MAI, EAI, MDI, DMDI-1 and DMDI-2.

5 Summary

This paper summarizes the research of adamantanes in crude oil. (1) There are three main methods for quantitative analysis of diamondoids in crude oil, pretreatment combined with GC-MS, crude oil dilution combined with GC-MS-MS, and pretreatment combined with GC×GC-TOFMS. (2) The main sources of diamondoids in crude oil are the thermal cracking of saturated hydrocarbon components or the soluble organic matter components in source rocks. (3) Diamondoids can be applied to evaluate the crude oil cracking degree, maturity degree, biodegradation degree, and identificate the genetic types. However, attention should also be paid to the scope of application and assumptions.

Author contributions

CF: writing—original draft preparation, validation. GH: conceptualization, writing—reviewing and editing, validation. YY: investigation, arrangement. DG: investigation, supervision. All authors contributed to the article and approved the submitted version.

Funding

This work was financially supported by the National Natural Science Foundation of China (Grant Nos 42172184 and 42272188), the Scientific Research and Technological Development Project of China National Petroleum Corporation (Grant No. 2021DJ0601), Basic research and strategic reserve technology research fund project of institutes directly under CNPC (Grant No. 2020D-5008-02).

Conflict of interest

The authors were employed by Petro China Research Institute of Petroleum Exploration and Development.

Publisher's note

All claims expressed in this article are solely those of the authors and do not necessarily represent those of their affiliated organizations, or those of the publisher, the editors and the reviewers. Any product that may be evaluated in this article, or claim that may be made by its manufacturer, is not guaranteed or endorsed by the publisher.

References

Aczel, T., Gorbaty, M. L., Maa, P. S., and Schlosberg, R. H. (1979). Stability of adamantane and its derivatives to coal-liquefaction conditions, and its implications toward the organic structure of coal. *Fuel* 58, 228–230. doi:10.1016/0016-2361(79)90123-6

Akinlua, Akinsehinwa, Ibeachusim, B. I., Adekola, S. A., Adedosu, T. A., Li, Y., and Xiong, Y. Q. (2020). Diamondoid geochemistry of Niger delta source rocks: Implication for petroleum exploration. *Energy Sources, Part A Recovery, Util. Environ. Eff.*, 1–11. doi:10.1080/15567036.2020.1840672

Atwah, I., Moldowan, J. M., Koskella, D., and Dahl, J. (2021). Application of higher diamondoids in hydrocarbon mudrock systems. *Fuel* 284, 118994. doi:10.1016/j.fuel.2020.118994

Azevedo, D. A., Tamanqueira, J. B., Dias, J. C. M., Carmo, A. P. B., Landau, L., and Goncalves, F. T. T. (2008). Multivariate statistical analysis of diamondoid and biomarker data from Brazilian basin oil samples. *Fuel* 87, 2122–2130. doi:10.1016/j.fuel.2007.11.005

Bao, J. P., Liang, X. Y., Zhu, C. S., and Jiang, X. C. (2015). Diamondoid hydrocarbons and their geochemical significances in condensate from the Zhujiadun gas reservoir in the Yancheng sag. *Nat. Gas. Geosci*. 26 (3), 513–523.

Bender, A. O., Said, E. Z., and Abdulsada, A. K. (1986). Gas chromatographic identification of adamantanes in some Iraqi crude oils. *Analyst* 111, 575–576. doi:10.1039/an9861100575

Chai, Z., Chen, Z. H., Liu, H., Cao, Z. C., Cheng, B., Wu, Z. P., et al. (2020). Light hydrocarbons and diamondoids of light oils in deep reservoirs of shuntuoguole low uplift, Tarim Basin: Implication for the evaluation on thermal maturity, secondary alteration and source characteristics. *Mar. Petroleum Geol.* 117, 104388. doi:10.1016/j.marpetgeo.2020.104388

Chai, Z., Chen, Z., Patience, R., Wen, Z., Tang, Y., Cheng, B., et al. (2022). Light hydrocarbons and diamondoids in deep oil from tabei of Tarim Basin: Implications on petroleum alteration and mixing. *Mar. Petroleum Geol.* 138, 105565. doi:10.1016/j.marpetgeo.2022.105565

Chen, J., Fu, J., Sheng, G., Liu, D., and Zhang, J. (1996). Diamondoid hydrocarbon ratios: Novel maturity indices for highly mature crude oils. *Org. Geochem.* 25 (3), 179–190. doi:10.1016/s0146-6380(96)00125-8

Chen, Z. L., Liu, X., Jin, H. R., Wang, Z., and Zhang, L. Y. (2008). Study on condensate maturity and type using methyl diamantane parameter. *Acta Sedimentol. Sin.* 26 (4), 705–708. doi:CNKI:SUN:CJXB.0.2008-04-025

Connan, J. (1984). "Biodegradation of crude oils in reservoirs," in *Advances in petroleum geochemistry*. Editors J. Brooks and D. H. Welte (London, UK: Academic Press), 299–335.

Dahl, J. E., Liu, S. G., and Carlson, R. M. K. (2003). Isolation and structure of higher diamondoids, nanometer-sized diamond molecules. *Science* 299 (5603), 96–99. doi:10.1126/science.1078239

Dahl, J. E., Moldowan, J. M., Peters, K. E., Claypool, G. E., Rooney, M. A., Michael, G. E., et al. (1999). Diamondoid hydrocarbons as indicators of natural oil cracking. *Nature* 399 (6731), 54–57. doi:10.1038/19953

Dahl, J. E. P., Moldowan, J. M., Wei, Z. B., Lipton, P. A., Denisevich, P., Gat, R., et al. (2010). Synthesis of higher diamondoids and implications for their formation in petroleum. *Angew. Chemie-International Ed.* 49, 9881–9885. doi:10.1002/anie.201004276

Duan, Y., Wang, C. Y., Zheng, C. Y., and Wu, B. X. (2007). Diamantane distribution characteristics in crude oil from Tahe Oilfield in Tarim Basin and oil and gas migration. *Nat. Gas. Geosci.* 18 (5), 693–696. doi:10.1016/S1872-5813(07)60034-6

Fang, C. C., Xiong, Y. Q., Li, Y., Chen, Y., and Tang, Y. J. (2015). Generation and evolution of diamondoids in source rock. *Mar. Petroleum Geol.* 67, 197–203. doi:10.1016/j.marpetgeo.2015.05.018

Fang, C. C., Xiong, Y. Q., Li, Y., Liang, Q. Y., Wang, T. S., and Li, Y. X. (2016). The effect of volatile components in oil on evolutionary characteristics of diamondoids during oil thermal pyrolysis. *Sci. China Earth Sci.* 59, 362–370. doi:10.1007/s11430-015-5163-x

Fang, C., Xiong, Y., Li, Y., Chen, Y., Liu, J., Zhang, H., et al. (2013). The origin and evolution of adamantanes and diamantanes in petroleum. *Geochimica Cosmochimica Acta* 120, 109–120. doi:10.1016/j.gca.2013.06.027

Fang, C., Xiong, Y., Liang, Q., and Li, Y. (2012). Variation in abundance and distribution of diamondoids during oil cracking. *Org. Geochem.* 47, 1–8. doi:10.1016/j.orggeochem.2012.03.003

Forkner, R., Fildani, A., Ochoa, J., and Moldowan, J. M. (2021). Linking source rock to expelled hydrocarbons using diamondoids: An integrated approach from the northern gulf of Mexico. *J. Petroleum Sci. Eng.* 196, 108015. doi:10.1016/j.petrol.2020.108015

Fort, R. C., and Schleyer, P. V. (1964). Adamantane: Consequences of the diamondoid structure. *Chem. Rev.* 64, 277–300. doi:10.1021/cr60229a004

Frenich, A. G., Gonzalez-Rodriguez, M. J., Arrebola, F. J., and Vidal, J. L. M. (2005). Potentiality of gas chromatography-triple quadrupole mass spectrometry in vanguard and rearguard methods of pesticide residues in vegetables. *Anal. Chem.* 77, 4640–4648. doi:10.1021/ac050252o

Frysinger, G. S., and Gaines, R. B. (1999). Comprehensive two-dimensional gas chromatography with mass spectrometric detection (GC × GC/MS) applied to the analysis of petroleum. *J. High Resolut. Chromatogr.* 22 (5), 251–255. doi:10.1002/(sici)1521-4168(19990501)22:5<251:aid-jhrc251>3.0.co;2-v

Frysinger, G. S., and Gaines, R. B. (2001). Separation and identification of petroleum biomarkers by comprehensive two-dimensional gas chromatography. *J. Sep. Sci.* 24 (2), 87–96. doi:10.1002/1615-9314(20010201)24:2<87:aid-jssc87>3.0.co;2-0

Frysinger, G. S., Gaines, R. B., Xu, L., and Reddy, C. M. (2003). Resolving the unresolved complex mixture in petroleum-contaminated sediments. *Environ. Sci. Technol.* 37 (8), 1653–1662. doi:10.1021/es020742n

Fu, N., and Li, Y. C. (2001). Diamondoid hydrocarbon ratios as indicators of maturity in natural gas. *Acta Sedimentol. Sin.* 19 (1), 145–149. doi:10.3969/j.issn.1000-0550.2001.01.025

Fu, N., and Yu, X. G. (1998). Detection and application of diamondoids in natural gas. *Petroleum Geol. Exp.* 20 (3), 267–271.

Gadzhiev, G. A., Badmaev, C. M., Gordadze, G. N., and Giruts, M. V. (2021). Thermal diffusion separation of petroleum diamondoids and protodiamondoids. *Pet. Chem.* 61, 147–151. doi:10.1134/s0965544121020110

Giruts, M. V., and Gordadze, G. N. (2007). Generation of adamantanes and diamantanes by thermal cracking of polar components of crude oils of different genotypes. *Pet. Chem.* 47 (1), 12–22. doi:10.1134/s0965544107010021

Giruts, M. V., Rusinova, G. V., and Gordadze, G. N. (2006). Generation of adamantanes and diamantanes by thermal cracking of high-molecular-mass saturated fractions of crude oils of different genotypes. *Pet. Chem.* 46 (4), 225–236. doi:10.1134/s0965544106040025

Goodwin, N. R. J., Abdullayev, N., Javadova, A., Volk, H., and Riley, G. (2020). Diamondoids and basin modelling reveal one of the world's deepest petroleum systems, south caspian basin, Azerbaijan. *J. Petroleum Geol.* 43 (2), 133–149. doi:10.1111/jpg.12754

Gordadze, G. N., and Giruts, M. V. (2008). Synthesis of adamantane and diamantane hydrocarbons by high-temperature cracking of higher n-alkanes. *Pet. Chem.* 48, 414–419. doi:10.1134/s0965544108060029

Gordadze, G. N., 2002. *Termoliz organicheskogo veshchestva v neftegazopoiskovoĭ geokhimii*. Institut geologii i razrabotki goriru Chikh iskopaemykh IGiRGI, Moskva.

Grice, K., Alexander, R., and Kagi, R. I. (2000). Diamondoid hydrocarbon ratios as indicators of biodegradation in Australian crude oils. *Org. Geochem.* 31 (1), 67–73. doi:10.1016/s0146-6380(99)00137-0

Head, I. M., Jones, D. M., and Larter, S. R. (2003). Biological activity in the deep subsurface and the origin of heavy oil. *Nature* 426 (6964), 344–352. doi:10.1038/nature02134

Hernandez, F., Portoles, T., Pitarch, E., Lopez, F. J., Beltran, J., and Vazquez, C. (2005). Potential of gas chromatography coupled to triple quadrupole mass spectrometry for quantification and confirmation of organohalogen xenoestrogen compounds in human breast tissues. *Anal. Chem.* 77, 7662–7672. doi:10.1021/ac050874+

Hua, R. X., Ruan, C. H., Wang, J. H., Lu, X., Liu, J., Xiao, K., et al. (2002). Research of group separation of petroleum fractions by comprehensive two-dimensional gas chromatography. *Acta Chim. Sin.* 12, 2185–2191. doi:10.3321/j.issn:0567-7351.2002.12.018

Huang, W., Yu, S., Zhang, H., Xiao, Z., Liu, D., and Pan, C. (2022a). Diamondoid fractionation and implications for the kekeya condensate field in the southwestern depression of the tarim basin, nw China. *Mar. Petroleum Geol.* 138, 105551. doi:10.1016/j.marpetgeo.2022.105551

Huang, W., Zhang, H., Xiao, Z., Yu, S., and Pan, C. (2022b). Generation, expulsion and accumulation of diamondoids, aromatic components and gaseous hydrocarbons for gas fields in Kuqa Depression of the Tarim Basin, NW China. *Mar. Petroleum Geol.* 145, 105893. doi:10.1016/j.marpetgeo.2022.105893

Hunt, J. M. (1979). *Petroleum geochemistry and geology*. San Francisco, CA, USA: W. H. Freeman.

Imuta, K., and Ouchi, K. (1973). Isolation of adamantane from coal extract. *Fuel* 52, 301–302. doi:10.1016/0016-2361(73)90062-8

Jiang, W., Chen, C., Long, Z., Li, Y., Yang, C., and Xiong, Y. (2022). Geochemical characteristics and possible sources of crude oils in the baiyun deep-water area of the pearl river mouth basin, south China sea. *Mar. Petroleum Geol.* 135, 105410. doi:10.1016/j.marpetgeo.2021.105410

Jiang, W., Li, Y., Fang, C., Yu, Z., and Xiong, Y. (2021). Diamondoids in petroleum: Their potential as source and maturity indicators. *Org. Geochem.* 160, 104298. doi:10.1016/j.orggeochem.2021.104298

Jiang, W., Li, Y., and Xiong, Y. (2020). Reservoir alteration of crude oils in the junggar basin, northwest China: Insights from diamondoid indices. *Mar. Petroleum Geol.* 109, 104451. doi:10.1016/j.marpetgeo.2020.104451

Jiang, W., Li, Y., and Xiong, Y. (2019). Source and thermal maturity of crude oils in the junggar basin in northwest China determined from the concentration and distribution of diamondoids. *Org. Geochem.* 128, 148–160. doi:10.1016/j.orggeochem.2019.01.004

Jiang, W., Li, Y., and Xiong, Y. (2018). The effect of organic matter type on formation and evolution of diamondoids. *Mar. Petroleum Geol.* 89, 714–720. doi:10.1016/j.marpetgeo.2017.11.003

Landa, S., and Machacek, V. (1933). Sur l'adamantane, nouvel hydrocarbure extrait du naphte. *Collect. Czechoslov. Chem. Commun.* 5, 1–5. doi:10.1135/cccc19330001

Larter, S., Huang, H., Adams, J., Bennett, B., Jokanola, O., Oldenburg, T., et al. (2006). The controls on the composition of biodegraded oils in the deep subsurface: Part II—geological controls on subsurface biodegradation fluxes and constraints on reservoir-fluid property prediction. *AAPG Bull.* 90 (6), 921–938. doi:10.1306/01270605130

Larter, S., Huang, H., Adams, J., Bennett, B., and Snowdon, L. R. (2012). A practical biodegradation scale for use in reservoir geochemical studies of biodegraded oils. *Org. Geochem.* 45, 66–76. doi:10.1016/j.orggeochem.2012.01.007

Li, J. G., Paul, P., and Cui, M. Z. (2000). Methyl diamantane index (MDI) as a maturity parameter for Lower Palaeozoic carbonate rocks at high maturity and overmaturity. *Org. Geochem.* 31 (4), 267–272. doi:10.1016/s0146-6380(00)00016-4

Li, Y., Chen, Y., Xiong, Y. Q., Wang, X. T., Fang, C. C., Zhang, L., et al. (2015). Origin of adamantanes and diamantanes in marine source rock. *Energy & Fules* 29, 8188–8194. doi:10.1021/acs.energyfuels.5b01993

Liang, Q., Xiong, Y., Fang, C., and Li, Y. (2012a). Comparison of two methods for the determination of diamondoids in crude oil. *Geochemica* 41, 433–441. doi:10.1007/s11783-011-0280-z

Liang, Q., Xiong, Y., Fang, C., and Li, Y. (2012b). Quantitative analysis of diamondoids in crude oils using gas chromatography–triple quadrupole mass spectrometry. *Org. Geochem.* 43, 83–91. doi:10.1016/j.orggeochem.2011.10.008

Lin, R., and Wilk, Z. A. (1995). Natural occurrence of tetramantane ($C_{22}H_{28}$), pentamantane ($C_{26}H_{32}$) and hexamantane ($C_{30}H_{36}$) in a deep petroleum reservoir. *Fuel* 74, 1512–1521. doi:10.1016/0016-2361(95)00116-m

Lu, H. L., Zhao, M. Y., Liu, H. M., and Bo, Y. C. (2005). Principle and application of comprehensive two dimensional gas chromatography-mass spectroscopy: A review. *Tob. Sci. Technology/Tobacco Chem.* 3, 22–25. doi:CNKI:SUN:YCKJ.0.2005-03-007

Lu, H. L., Zhao, M. Y., Liu, H. M., Gong, A. D., Yu, J., Zheng, H. N., et al. (2007). Determination of neutral chemical constituents in flue-cured tobacco by comprehensive two-dimensional gas chromatography and time-of flight mass spectrometry. *Chin. J. Chromatogr.* 25 (1), 30–34. doi:10.3321/j.issn:1000-8713.2007.01.006

Lu, X., Cai, J. L., Wu, J. F., Kong, H. W., Zhao, M. Y., Hua, R. X., et al. (2004a). Characterization of phenols in cigarette mainstream smoke condensate by using comprehensive two-dimensional gas chromatography/time-of-flight mass spectrometry. *Acta Chim. Sin.* 62 (8), 804–810. doi:10.3321/j.issn:0567-7351.2004.08.011

Lu, X., Wu, J. F., Wu, J. H., Kong, H. W., Hua, R. X., Tao, W. S., et al. (2004b). Characterization and quantitative determination of diesel fractions by comprehensive two-dimensional gas chromatography/time of flight mass spectrometry. *Chin. J. Chromatogr.* 22 (1), 5–11. doi:10.3321/j.issn:1000-8713.2004.01.002

Ma, A. L., Jin, Z. J., and Zhu, C. S. (2017). Maturity and oil-cracking of the ordovician oils from Tahe oilfield, Tarim Basin, NW China. *Nat. Gas. Geosci.* 28 (2), 313–323. doi:10.1016/j.jnggs.2017.12.001

Ma, A. L., Jin, Z. J., Zhu, C. S., Peng, S. T., and Zhang, W. B. (2009). Quantitative analysis on absolute concentration of diamondoids in oils from Tahe Oilfield. *Acta Pet. Sin.* 30 (2), 214–218. doi:10.7623/syxb200902009

Ma, A. L., Lin, H. X., Yun, L., Qiu, N. S., Zhu, X. X., and Wu, X. (2022). Detection of ethanodiamantanes in the Ordovician crude oil from Shuntuoguole area in Tarim Basin and its significance. *Acta Pet. Sin.* 43 (6), 788–803. doi:10.7623/syxb202206004

Ma, A. L. (2016). New advancement in application of diamondoids on organic geochemistry. *Nat. Gas. Geosci.* 27 (005), 851–860. doi:10.11764/j.issn.1672-1926.2016.05.0851

Oya, A., Nakamura, H., Otani, S., and Marsh, H. (1981). Carbonization of adamantane to a graphitizable carbon. *Fuel* 60, 667–669. doi:10.1016/0016-2361(81)90215-5

Peng, Y., Cai, C., Fang, C., Wu, L., Liu, D., Sun, P., et al. (2022). Diamondoids and thiadiamondoids generated from hydrothermal pyrolysis of crude oil and TSR experiments. *Sci. Rep.* 12, 196. doi:10.1038/s41598-021-04270-z

Peters, K. E., and Moldowan, J. M. (1993). *The biomarker guide: Interpreting molecular fossils in petroleum and ancient sediments*. Englewood Cliffs, NJ, USA: Prentice Hall.

Qu, L. J., Zhang, H., Zhu, J. H., Yang, G. S., and Aboul-Enein, H. Y. (2010). Rapid determination of organophosphorous pesticides in leeks by gas chromatography-triple quadrupole mass spectrometry. *Food Chem.* 122, 327–332. doi:10.1016/j.foodchem.2010.02.038

Ruan, C. H., Ye, F., Kong, H. W., Lu, X., and Xu, G. W. (2002). Separation characteristics of comprehensive two-dimensional gas chromatography in analyzing petroleum sample. *Chin. J. Anal. Chem.* 30 (5), 548–551. doi:10.1016/S0956-5663(01)00303-7

Sassen, R., and Post, P. (2008). Enrichment of diamondoids and 13C in condensate from hudson canyon, US atlantic. *Org. Geochem.* 39, 147–151. doi:10.1016/j.orggeochem.2007.10.004

Schneide, A., Warren, R. W., and Janoski, E. J. (1966). Formation of perhydrophenalenes and polyalkyladamantanes by isomerization of tricyclic perhydroaromatics. *J. Org. Chem.* 31, 1617–1625. doi:10.1021/jo01343a070

Schoell, M., and Carlson, R. M. K. (1999). Diamondoids and oil are not forever. *Nature* 399, 15–16. doi:10.1038/19847

Schoenmakers, P. J., Oomen, J. L. M. M., Blomberg, J., Genuit, W., and Velzen, G. V. (2000). Comparison of comprehensive two-dimensional gas chromatography and gas chromatography-mass spectrometry for the characterization of complex hydrocarbon mixtures. *J. Chromatogr. A* 892, 29–46. doi:10.1016/s0021-9673(00)00744-5

Schulz, L. K., Wilhelms, A., Rein, E., and Steen, A. S. (2001). Application of diamondoids to distinguish source rock facies. *Org. Geochem.* 32 (3), 365–375. doi:10.1016/s0146-6380(01)00003-1

Spaak, G., Edwards, D. S., Grosjean, E., Scarlett, A. G., and Grice, K. (2020). Identifying multiple sources of petroleum fluids in browse basin accumulations using diamondoids and semi-volatile aromatic compounds. *Mar. Petroleum Geol.* 113, 104091. doi:10.1016/j.marpetgeo.2019.104091

Springer, M. V., Garcia, D. F., Goncalves, F. T. T., Landau, L., and Azevedo, D. A. (2010). Diamondoid and biomarker characterization of oils from the llanos orientales basin, Colombia. *Org. Geochem.* 41, 1013–1018. doi:10.1016/j.orggeochem.2010.03.002

Stout, S. A., and Douglas, G. S. (2004). Diamondoid hydrocarbons—Application in the chemical fingerprinting of natural gas condensate and gasoline. *Environ. Forensics* 5 (4), 225–235. doi:10.1080/15275920490886734

Ventura, G. T., Kenig, F., Reddy, C. M., Frysinger, G. S., Gaines, R. B., Mooy, B. V., et al. (2008). Analysis of unresolved complex mixtures of hydrocarbons extracted from Late Archean sediments by comprehensive two-dimensional gas chromatography (GC×GC). *Org. Geochem.* 39, 846–867. doi:10.1016/j.orggeochem.2008.03.006

Volkman, J. K., Alexander, R., Kagi, R. I., Rowland, S. J., and Sheppard, P. N. (1984). Biodegradation of aromatic hydrocarbons in crude oils from the Barrow Sub-basin of Western Australia. *Org. Geochem.* 6, 619–632. doi:10.1016/0146-6380(84)90084-6

Wang, H. T., Weng, N., Zhang, S. C., Chen, J. P., and Wei, C. Y. (2010). Characteristics and identification of saturated hydrocarbons by comprehensive two-dimensional gas chromatography coupled to time-of-flight mass spectrometry. *J. Chin. Mass Spectrom. Soc.* 31, 18–27. doi:10.1016/S1872-2067(10)60128-3

Wang, H. T., Weng, N., Zhang, S. C., Wei, C. Y., and Zhang, C. J. (2019). A novel method for quantitative analysis of diamondoids in petroleum samples. *Petroleum Geol. Exp.* 41 (3), 443–450. doi:10.11781/sysydz201903443

Wang, Z., Yang, C., Hollebone, B., and Fingas, M. (2006). Forensic fingerprinting of diamondoids for correlation and differentiation of spilled oil and petroleum products. *Environ. Sci. Technol.* 40 (18), 5636–5646. doi:10.1021/es060675n

Wei, Z. B., Moldowan, J. M., Peters, K. E., Wang, Y., and Xiang, W. (2007a). The abundance and distribution of diamondoids in biodegraded oils from the San Joaquin Valley: Implications for biodegradation of diamondoids in petroleum reservoirs. *Org. Geochem.* 38, 1910–1926. doi:10.1016/j.orggeochem.2007.07.009

Wei, Z., Mankiewicz, P., Walters, C., Qian, K., Phan, N. T., Madincea, M. E., et al. (2011). Natural occurrence of higher thiadiamondoids and diamondoidthiols in a deep petroleum reservoir in the Mobile Bay gas field. *Org. Geochem.* 42 (2), 121–133. doi:10.1016/j.orggeochem.2010.12.002

Wei, Z., Michael Moldowan, J., Dahl, J., Goldstein, T. P., and Jarvie, D. M. (2006a). The catalytic effects of minerals on the formation of diamondoids from kerogen macromolecules. *Org. Geochem.* 37 (11), 1421–1436. doi:10.1016/j.orggeochem.2006.07.006

Wei, Z., Moldowan, J. M., Jarvie, D. M., and Hill, R. (2006b). The fate of diamondoids in coals and sedimentary rocks. *Geology* 34 (12), 1013–1016. doi:10.1130/g22840a.1

Wei, Z., Moldowan, J. M., and Paytan, A. (2006c). Diamondoids and molecular biomarkers generated from modern sediments in the absence and presence of minerals during hydrous pyrolysis. *Org. Geochem.* 37 (8), 891–911. doi:10.1016/j.orggeochem.2006.04.008

Wei, Z., Moldowan, J. M., Zhang, S., Hill, R., Jarvie, D. M., Wang, H., et al. (2007b). Diamondoid hydrocarbons as a molecular proxy for thermal maturity and oil cracking: Geochemical models from hydrous pyrolysis. *Org. Geochem.* 38 (2), 227–249. doi:10.1016/j.orggeochem.2006.09.011

Wilhelms, A., Larter, S. R., Head, I., Farrimond, P., Di-Primio, R., and Zwach, C. (2001). Biodegradation of oil in uplifted basins prevented by deep-burial sterilization. *Nature* 411 (6841), 1034–1037. doi:10.1038/35082535

Williams, J. A., Bjoroy, M., Dolcater, D. L., and Winters, J. C. (1986). Biodegradation in south Texas eocene oils — effects on aromatics and biomarkers. *Org. Geochem.* 10, 451–461. doi:10.1016/0146-6380(86)90045-8

Wingert, W. S. (1992). GC-MS analysis of diamondoid hydrocarbons in Smackover petroleums. *Fuel* 71 (1), 37–43. doi:10.1016/0016-2361(92)90190-y

Winters, J. C., and Williams, J. A. (1969). "September Microbiological alteration of crude oil in the reservoir," in *Symposium on petroleum transformation in geologic environments* (Washington, D.C, United States: American Chemical Society), E22–E31.

Xu, X. Q. (2007). *Analysis and tracer technology of organic pollutants in the marine environment. Xiamen, college of chemistry and chemical engineering*. Xiamen, China: Xiamen University.

Yang, B. J., Zheng, L., Cui, Z. S., Gao, W., Li, Q., and Wang, X. R. (2013). Changes of diamondoid compounds in crude oil from the west of Bohai sea by biodegradation in shorelines. *Mar. Environ. Sci.* 4, 481–485. doi:CNKI:SUN:HYHJ.0.2013-04-001

Zhai, J., Cao, Z., Fang, C., Yuan, Y., Wu, W., and Liu, J. (2022). The evolution characteristics of diamondoids in coal measures and their potential application in maturity evaluation. *Front. Earth Sci.* 10. doi:10.3389/feart.2022.1031799

Zhang, S., Huang, H., Xiao, Z., and Liang, D. (2005). Geochemistry of palaeozoic marine petroleum from the Tarim Basin, NW China. Part 2: Maturity assessment. *Org. Geochem.* 36 (8), 1215–1225. doi:10.1016/j.orggeochem.2005.01.014

Zhao, B., and Shen, X. J. (2006). The development of TOFMS analysis technique. *Mod. Sci. Instrum.* 4, 30–33. doi:10.3969/j.issn.1003-8892.2006.04.006

Zhao, H., Wang, P. R., Chen, Q., Yao, H. X., and Zhu, J. Z. (1995). Adamantane and its application to studying the maturity of crude oils from Tarim Basin. *J. Jianghan Petroleum Inst.* 17 (3), 24–30.

Zheng, L. J., Cao, J. P., Xue, J. H., and Bie, D. Z. (1998). A new index for the maturity of crude oil and hydrocarbon source rocks-methyl diamantane index. *Petroleum Geol. Exp.* 20 (4), 411–416.

Zhu, G., Chen, J., Zhang, C., Wang, Y., Liu, K., and Zhang, T. (2021). Effects of evaporative fractionation on diamondoid hydrocarbons in condensates from the xihu sag, east China sea shelf basin. *Mar. Petroleum Geol.* 126, 104929. doi:10.1016/j.marpetgeo.2021.104929

Frontiers in Earth Science

Investigates the processes operating within the major spheres of our planet

Advances our understanding across the earth sciences, providing a theoretical background for better use of our planet's resources and equipping us to face major environmental challenges.

Discover the latest Research Topics

See more →

Frontiers

Avenue du Tribunal-Fédéral 34
1005 Lausanne, Switzerland
frontiersin.org

Contact us

+41 (0)21 510 17 00
frontiersin.org/about/contact